APPLICATION OF SOLID-STATE TRACK RECORDERS TO FAST NEUTRON MEASUREMENTS

by

Anwar Ul Haque

B.Sc.,M.Sc.,D.I.C.

A thesis submitted for the degree of

Doctor of Philosophy (Ph.D)

in the University of London.

Nuclear Power Section,
Department of Mechanical Engineering,
Imperial College of Science and Technology,
London, SW7 2BX.

September 1980

ACKNOWLEDGEMENTS

The author wishes to express his gratitude to Dr. C.B. Besant who has taken a close interest in the work, for his moral support, advice and correction of the manuscript.

The author is deeply indebted to Dr. B.W. Hooton of the Nuclear Physics Division, Atomic Energy Research Establishment, Harwell, for having proposed the investigation, for his continuous interest in the work, and for many useful discussions and suggestions.

The author would like to thank Professor P.J. Grant, Professor of Nuclear Power at Imperial College for his support and encouragement during this research.

Sincere thanks are due to Dr. J.G. Williams of the University of London Reactor Centre, for his advice and comments with respect to the experiments on the reactor 'CONSORT'. Thanks are also due to Professor G.N. Walton and Dr. P.G. Clay of the Nuclear Technology Section of the Chemical Engineering Department at Imperial College for providing gamma ray irradiation facilities and for many useful discussions.

Many thanks to the following, for their help and advice on the efficient use of the automatic track counting system: Mr. J.A. Mason of the University of London Reactor Centre, Dr. D. Thompson of the CAD Group, Nuclear Power Section and Dr. C.S. Ow of the Thermal Power Section.

Sincere thanks are also due to many persons at Imperial College who have been associated with the project at different stages; in particular Mr. G.W. Briers and Miss P. Martins of the Metallurgy and Material Science Department and Mr. L.W. Eggleston of the Nuclear Power Laboratory.

The author wishes to express his appreciation of the talented efforts of Mrs. E.M. Noel in the typing of his manuscript into a legible and presentable form.

Finally, the author is indebted to the Atomic Energy Research Establishment, Harwell for awarding the research studentship.

ABSTRACT

Both, experimental and theoretical results are presented from a detailed study of CA80-15, CR-39 and Makrofol K.G Solid State Track Recorders (SSTRs) for the selective detection of fast neutrons in the presence of a high flux of gamma rays. This interest stems from a requirement to measure the fissile content of spent reactor fuel elements and the assay of fissile material for safeguards.

A theoretical model has been developed to calculate the sensitivity of SSTRs to neutrons as a function of neutron energy. Results are reported from this model for CA80-15 and Makrofol K.G SSTRs in the case of thermal and fast neutrons.

Results from a series of irradiations involving particle accelerators, reactor and different charged particle sources are presented. These irradiations were performed to characterise the track density in CA80-15, CR-39 and Makrofol K.G as a function of neutron energy.

The sensitivities of CA80-15 and CR-39 are measured for the registration of charged particle tracks resulting from the interaction of fast neutrons, of energies ranging from 0.50 to 17 MeV with the constituents of the SSTR. The optimisation of etching times and the effect of counting the 'front' or 'back' surface of the detector are discussed.

For a fission neutron source the sensitivity of CA80-15 without any 'converter' foil is 1.20×10^{-5} tracks per neutron which is in agreement to within $\pm$ 15% of the theoretical results.

Effects of high gamma doses on SSTRs have also been investigated and underline the importance of proper etching conditions for the selective detection of fast neutrons in the presence of a high flux of gamma rays.

Automatic track counting technique has been applied to neutron induced track measurements and should help to overcome the subjective nature of human decisions on the number of tracks seen in an etched SSTR.

Finally, an attempt has been made to utilise the SSTR technique in the neutron interrogation of reactor fuel assemblies.

CONTENTS

	Page
ABSTRACT	3
TABLE OF CONTENTS	5
LIST OF FIGURES	11
LIST OF TABLES	17
NOTATIONS	19
CHAPTER 1: OBJECTIVES AND GENERAL CONSIDERATIONS	20
1.1 Introduction	20
1.2 Review of Previous Work on SSTRs	21
1.3 Track Registration Criteria	23
1.3.1 The Total Energy Loss Rate Criterion	24
1.3.2 The Primary Ionization Criterion	24
1.3.3 The Restricted Energy Loss Criterion	26
1.3.4 The δ-ray Criterion (Katz and Kobetich)	27
1.3.5 The δ-ray Criterion (Monnin)	28
1.3.6 Remarks	28
1.4 Methods of Latent Track Revelation	30
1.4.1 Transmission Electron Microscopy	30
1.4.2 Track Decoration Techniques	31
1.4.3 Chemical Etching	33
1.4.4 Electrochemical Etching	34
1.5 Applications of SSTRs	35
1.5.1 Radiation Dosimetry	35
1.5.2 Reactor Physics Applications	38
1.5.3 Miscellaneous Applications	39
1.6 The Present Work	39
1.6.1 Objectives	41

		Page
CHAPTER 2:	RESPONSE OF SSTRs TO NEUTRONS; THEORY AND ASSESSMENT	43
	2.1 Introduction	43
	2.2 Response of 'Intrinsic' SSTRs to Neutrons	44
	2.2.1 Response Function	46
	2.2.2 Thermal Neutrons	49
	2.2.3 Elastic Scattering	50
	2.2.4 Nuclear Reactions	54
	2.2.5 Etching Effects	57
	2.2.6 Neutrons in Cellulose Nitrate (CA80-15 SSTR)	57
	(i) Track Parameters	57
	(ii) Response of CA80-15 SSTR	60
	2.3 Response of SSTRs with a 'Converter Foil' to Neutrons	63
	2.3.1 SSTRs with a (n,f) 'Converter Foil'	63
	(i) Response of ^{238}U foil in contact with Makrofol K.G SSTR	72
	2.3.2 SSTRs with a (n,α) 'Converter Foil'	74
	(i) Response of CA80-15 type B SSTR	74
	2.4 Conclusions	77
CHAPTER 3:	MATERIALS AND PRELIMINARY EXPERIMENTS	79
	3.1 Introduction	79
	3.2 SSTR Materials for Neutron Detection	80
	3.2.1 Polymers (Chemistry and radiation effects)	83
	(i) Cellulose nitrate (CA80-15 SSTR)	83
	(ii) Polycarbonates (Makrofol and CR-39 SSTRs)	89
	3.2.2 Effects of Radiation on Polymers	91

Page

3.2.3 Alkaline Etching of Polymers 95

(i) Alkaline etching of cellulose nitrate 95
(ii) Alkaline etching of polycarbonates 96

3.3 Chemical Etching of Latent Tracks 98

3.3.1 Critical Angle for Track Detection 101

3.3.2 Etching Efficiency 103

3.3.3 Etching Experiments 103

(i) The etching apparatus 103
(ii) The etching procedure 105
(iii) Measurement of bulk and track etch rates 106

3.3.4 Results and Discussion 108

(i) Cellulose nitrate (CA80-15 SSTR) 108
(ii) Polycarbonates (CR-39 and Makrofol SSTRs) 122

3.4 Track Observation and Counting 129

3.4.1 Optical Techniques 129

(i) Bright-field transmitted light illumination 131
(ii) Dark-field illumination 132
(iii) Phase-contrast microscopy 135
(iv) Incident light illumination 135

3.4.2 The Microscope Equipment 136

3.4.3 Track Counting Conventions 137

3.5 Conclusions 138

CHAPTER 4: EXPERIMENTS 140

4.1 Introduction 140

4.2 Experiments on the Van de Graaf Accelerator 142

4.2.1 Description of Experimental Set-up on Van de Graaf 143

4.2.2 Experimental 147

(i) Protons 148
(ii) Alpha-particles 148
(iii) Heavy ions 149
(iv) Etchings 149

	Page
4.2.3 Results and Discussion	150
(i) CA80-15 SSTR	150
(ii) CR-39 SSTR	158
4.3 Experiments on the Reactor 'Consort'	169
4.3.1 Description of the Vertical Thermal Column Facility	169
4.3.2 Experimental	172
4.3.3 Results and Discussion	175
4.4 Experiments on the 'IBIS' Accelerator	179
4.4.1 Description of 'IBIS' Accelerator	180
4.4.2 Experimental	180
4.4.3 Results and Discussion	185
(i) CA80-15 SSTR	185
(ii) Makrofol K.G SSTR	193
4.5 Neutrons in CR-39 SSTR	197
4.5.1 Results and Discussion	198
4.6 Conclusions	202
CHAPTER 5: SYSTEMATIC ERRORS AND SUMMARY OF THEORETICAL AND EXPERIMENTAL EVIDENCE	204
5.1 Sources of Systematic Errors	204
5.1.1 Chemical Etching	204
5.1.2 Manual Track Scanning	206
5.1.3 Time and Position of Irradiation Exposure	208
5.1.4 Quality of (n,f) 'Converter Foils'	208
5.1.5 Summary	208
5.2 Comparison Between Theoretical and Experimental Results	209
5.2.1 Response of CA80-15 to Thermal and Fast Neutrons	209
5.2.2 Response of Makrofol (in contact with 1.23 mg/cm^2 Natural Uranium Foil) to Neutrons	213

	Page
CHAPTER 6: EFFECTS OF HIGH GAMMA DOSES ON SSTRs	216
6.1 Introduction	216
6.2 Experiments	217
6.2.1 Irradiations	217
6.2.2 Chemical Etching	218
6.3 Results and Discussion	219
6.3.1 Errors	232
6.4 Conclusions	232
CHAPTER 7: AUTOMATIC COUNTING OF TRACKS IN SSTRs	234
7.1 Introduction	234
7.2 System Hardware	236
7.2.1 The Digitiser	238
7.2.2 Extensions to the Digitiser Hardware	243
7.3 System Software	244
7.3.1 Definitions	246
7.3.2 Program and Data Structure on PDP-11	247
(i) Routine 'CAMERA'	247
(ii) Data Structure	248
7.3.3 Routine 'LEVEL'	248
7.3.4 Routine 'DIS 2'	249
7.3.5 Routine 'DOT 2'	249
7.3.6 Routine 'CARIK'	249
7.3.7 Routine 'SORT'	250
7.3.8 Routine 'SEARCH'	251
7.3.9 Routine 'TENTU'	251
7.4 Calibration of the System	251
7.4.1 Grey-Level Setting	251
7.4.2 Size Setting	252
7.4.3 Overlap Correction	256

		Page
	7.5 Data Analysis and Results	256
	7.5.1 Errors	258
	7.6 Conclusions	258
CHAPTER 8:	APPLICATION OF SSTRs IN NUCLEAR FUEL SAFEGUARDS	261
	8.1 Introduction	261
	8.2 Experimental Arrangement	263
	8.3 Results	265
	8.4 Conclusions	268
CHAPTER 9:	SUMMARY OF CONCLUSIONS AND PROPOSALS FOR FUTURE WORK	270
	9.1 Summary of Conclusions	270
	9.2 Proposals for Future Work	273
REFERENCES		276
APPENDIX A:	KINEMATICS OF NUCLEAR REACTIONS AND SCATTERING	283
	A.1 Nuclear Reactions	283
	A.1.1 Non-relativistic kinematics	283
	A.1.2 Relativistic kinematics	286
	A.2 Elastic Scattering	287
APPENDIX B:	RANGE-ENERGY AND ENERGY LOSS RELATIONS	290
	B.1 Introduction	290
	B.2 Method of Calculation	291
	B.2.1 General Expressions	291
	B.2.2 The adjusted mean ionization potential	293
	B.2.3 The ideal proton range and its derivative	294
	B.2.4 The range extension and its derivative	295
	B.3 Discussion of the Method	300
APPENDIX C:	NEUTRON CROSS SECTIONS	306

LIST OF FIGURES

Figure		Page
2.1	Important features of neutron induced tracks in 'intrinsic' SSTRs	45
2.2	Kinematics of fast neutron elastic scattering	51
2.3	Form of observable track length 'L' as a function of particle energy	53
2.4	Kinematics of nuclear reactions	55
2.5(a)	Energy loss rate, dE/dx in cellulose nitrate as a function of proton and alpha-particle energy	59
(b)	Energy loss rate, dE/dx in cellulose nitrate as a function of ^{12}C and ^{16}O ion energy	61
2.6	Range of protons, alpha-particles, carbon and oxygen ions in cellulose nitrate as a function of particle energy	62
2.7	The contribution of elastic scattering to the neutron sensitivity of CA80-15, as a function of neutron energy	64
2.8	The contribution of nuclear reactions to the neutron sensitivity of CA80-15, as a function of neutron energy	65
2.9	The contribution of elastic scatterings and nuclear reactions to the neutron sensitivity of CA80-15 and total neutron sensitivity of CA80-15, as a function of neutron energy	66
2.10	Integral ranges of fission products of ^{235}U in uranium metal as a function of mass number	68
2.11	The geometry factor for 'thick' fission foils	69
2.12	Microscopic fission cross sections, σ_F for various isotopes as a function of neutron energy	73
2.13	Theoretical neutron sensitivity of a 'thick' ^{238}U fission foil in good contact with a SSTR	75
3.1(a)	The structural formula for cellulose	85
(b)	The structural formula for cellulose tri-nitrate	85
3.2	The structural formula for polycarbonate	90
3.3	Cross-sectional view of a typical track after different etching times	100

Figure		Page
3.4	Diagrammatic representation of an etched track	102
3.5	The fraction of a random distribution of tracks that is revealed by a short etch as a function of the depth of the lower end of the track	104
3.6	High resolution thickness measuring machine used to measure the change in the film thickness to determine the bulk etch rates	107
3.7(a)	Average bulk etch rate of CA80-15 as a function of NaOH concentration at 19°C, 31°C and 60°C	109
(b)	Average bulk etch rate of CA80-15 as a function of KOH concentration at 19°C, 31°C and 60°C	110
3.8(a)	Dependence of the average bulk etch rate of CA80-15 on the etchant temperature at different NaOH concentrations	114
(b)	Dependence of the average bulk etch rate of CA80-15 on the etchant temperature at different KOH concentrations	115
3.9	The time required to etch out fission fragment tracks in CA80-15 as a function of NaOH concentration at 60°C	116
3.10(a)	Dependence of the track etch rate and the etch rate ratio for 6 MeV alpha-particles in CA80-15, on NaOH concentration at 19°C	118
(b)	Dependence of the etch rate ratio for 6 MeV alpha-particles in CA80-15, on the etchant temperature (2.5N NaOH)	119
3.11	A free energy diagram of irradiated and un-irradiated CA80-15	120
3.12(a)	Average bulk etch rate of CR-39 as a function of NaOH concentration at different temperatures	123
(b)	Average bulk etch rate of CR-39 as a function of KOH concentration at different temperatures	124
3.13	Average bulk etch rate of Makrofol K.G as a function of NaOH and KOH concentrations at 60°C	126
3.14	Dependence of the track etch rate for 6 MeV alpha-particles in CR-39 on the etchant temperature and concentration	127

Figure		Page
3.15	Dependence of the average bulk etch rate of CR-39 on the etching temperature at different etchant concentrations	128
4.1(a)	Accelerator vacuum box	144
(b)	SSTR rotator system showing rotator with 12 recorders, back plate with motor and semi-conductor detector, and housing with beam entrance hole	145
(c)	Beam tube assembly terminating in the rotator system containing SSTRs and semi-conductor particle detector	146
4.2(a)	Proton track diameter in CA80-15 as a function of the layer removed from the film surface by etching	152
(b)	Track diameter in CA80-15 as a function of proton incident energy	152
4.3(a)	0.45 MeV proton tracks in CA80-15	154
(b)	0.5 MeV proton tracks in CA80-15	154
4.4(a)	Track diameter distributions of 0.6 MeV protons in CA80-15	155
(b)	Track diameter distributions of 0.7 MeV protons in CA80-15	155
4.5(a)	Alpha-particle track diameter in CA80-15 as a function of the removed layer thickness	157
(b)	Alpha-particle track diameter in CA80-15 as a function of particle energy	157
4.6	Tracks of 2 MeV normally incident alpha-particles in CA80-15	159
4.7	3.5 MeV nitrogen-14 tracks in CA80-15	160
4.8	Proton tracks in CR-39	162
4.9	Proton track diameter in CR-39 as a function of energy and removed layer thickness	165
4.10	Diameter distributions of normally incident protons in CR-39	166
4.11	Track diameter in CR-39 as a function of alpha-particle energy	167
4.12	3 MeV alpha-particle tracks in CR-39	168

Figure		Page
4.13(a)	Cross sectional side elevation on the thermal column extension	170
(b)	Arrangement of vertical thermal column graphite stack	171
4.14	Flux distribution at 100 kW in the vertical thermal column facility	173
4.15(a)	Track density in CA80-15 exposed to thermal neutrons as a function of the removed layer thickness	177
(b)	Track diameter distributions in CA80-15 exposed to thermal neutrons	177
4.16	Proton tracks from $^{14}N(n,p)^{14}C$ reaction in CA80-15 exposed to thermal neutrons	178
4.17	Experimental set-up at 'IBIS' site Harwell	181
4.18	Track density in CA80-15 exposed to fast neutrons, as a function of etching time	186
4.19	Density of triple tracks in CA80-15 as a function of etching time	187
4.20	Neutron sensitivity of CA80-15 as a function of energy	190
4.21	Tracks in CA80-15 exposed to 3 MeV neutrons from the 'IBIS' accelerator	192
4.22	Neutron sensitivity of Makrofol K.G (in contact with 1.23 mg/cm^2 natural uranium foil) as a function of energy	194
4.23	Fission fragment tracks in Makrofol K.G	195
4.24	Angular dependence of track densities in CA80-15 and Makrofol K.G	196
4.25	Neutron sensitivity of CR-39 as a function of etching time	199
4.26	Neutron induced tracks in CR-39	200
5.1	Comparison between theoretical and experimental neutron sensitivities of CA80-15	210
5.2	Comparison between theoretical and experimental neutron sensitivites of Makrofol K.G in contact with 1.23 mg/cm^2 natural uranium foil	214

Figure		Page
6.1	The ratio of average values of fission fragment track widths in CA80-15 at gamma doses of 'D-megarads' and 'zero-megarads' as a function of absorbed gamma dose	220
6.2	The ratio of average values of fission fragment track widths in CA80-15 at gamma doses of 'D-megarads' and 'zero-megarads' as a function of absorbed gamma dose	221
6.3	Average bulk etch rate of CA80-15 as a function of absorbed gamma dose	224
6.4	Average bulk etch rate of CA80-15 as a function of absorbed gamma dose	225
6.5	The ratio of average values of bulk etch rates of CA80-15 at gamma doses of 'D-megarads' and 'zero-megarads' as a function of absorbed gamma dose	226
6.6	The ratio of average values of bulk etch rates of CA80-15 at gamma doses of 'D-megarads' and 'zero-megarads' as a function of absorbed gamma dose	227
6.7	Average bulk etch rate of Makrofol K.G as a function of gamma dose	228
6.8	Track density in CA80-15 exposed to 17 MeV neutrons as a function of absorbed gamma dose	230
6.9	1 MeV alpha-particle tracks in CA80-15 subjected to a high gamma dose	231
7.1	Block diagram of automatic track counting system hardware	237
7.2	Automatic track counting system set-up	239
7.3	Block diagram of the digitiser	241
7.4	Flow of information through automatic track counting system	245
7.5	Track count in CA80-15 exposed to fast neutrons, as a function of grey level	253
7.6	Digitised tracks displayed on Tektronix 611 screen	254
7.7	Frequency histogram of the number of tracks in CA80-15 as a function of track area	255

Figure		Page
8.1	Experimental set-up used in the neutron interrogation of reactor fuels at A.E.R.E, Harwell	264
8.2	Track density in CA80-15 as a function of fuel pin enrichment and the number of pins	267
A.1	Kinematics of nuclear reactions	284
A.2	Kinematics of elastic scattering	288
B.1(a)	Empirically derived curve relating the range extension term to the velocity of the ion in units of the k-electron velocity	298
(b)	Empirically derived curve relating the quantity $C_z(\beta/z)$ to the velocity of the ion in units of k-electron velocity	299
B.2	The fractional effective charge, z^*/z as a function of the reduced velocity of the ion	301
B.3	The range extension functions, $C_z(\beta/z)$ as a function of $(\beta/z) \times 10^{-3}$	303
C.1	Microscopic fission cross sections, σ_F for various isotopes as a function of neutron energy	308

LIST OF TABLES

Table		Page
1.1	Various track registration criteria with their adjustable parameters and methods of calculation	29
2.1	The fast neutron interactions considered in the theoretical efficiency calculations of cellulose nitrate (CA80-15 SSTR)	47
2.2	Energies of the reaction products from (n,α) reactions in case of ^{12}C, ^{14}N and ^{16}O, as a function of neutron energy	56
2.3	Elementary composition of cellulose nitrate: $C_6H_7O_2(NO_3)_3$	58
2.4	Maximum observable track lengths 'L_M' and corresponding energies in cellulose nitrate	58
3.1	Approximate relation between the viscosity, molecular weight and the degree of polymerization of cellulose nitrate	88
3.2	Mechanical, physical and electrical properties of plasticized cellulose nitrate films	88
3.3	Mechanical, physical and electrical properties of polycarbonate films	92
3.4	Some effects of high energy radiation on polymers	92
3.5	Some parameters of Na^+ and K^+ ions	112
3.6	Solubility of camphor at 40°C	112
3.7(a)	Some characteristics of optical microscope objectives	133
(b)	The approximate limits of useful magnification and resolution of optical microscopes	134
4.1	Main characteristics of various irradiations performed (CA80-15, Makrofol K.G and CR-39)	141
4.2	Tracks from protons incident on CA80-15 films at 90°	151
4.3	Tracks from α-particles incident on CA80-15 films at 90°	156
4.4	Tracks from protons incident on CR-39 films at 90°	161

Table		Page
4.5	Relative transverse flux distributions at 61.5 cm from the top face	174
4.6	Main characteristics of the monoenergetic fast neutron irradiations, using the 'IBIS' accelerator at A.E.R.E., Harwell	184
5.1	Sources of systematic errors in neutron measurements using SSTRs	205
5.2	Comparison between theoretical and experimental sensitivities of CA80-15 as a function of neutron energy	211
5.3	Comparison between theoretical and experimental sensitivities of Makrofol K.G in contact with a 1.23 mg/cm^2 natural uranium foil, as a function of neutron energy	211
6.1	The average bulk etch rates and irradiation mass losses for CA80-15. The etchant was 6N KOH at (60 $\pm$ 0.1) ^{o}C	223
6.2	The 'k-values' for different etching conditions in the case of CA80-15	223
7.1	Comparison of track counting by eye - and by the 'digitiser', for CA80-15 exposed to 2 MeV neutrons	257
8.1	Track densities and neutron fluxes (measured with a CA80-15 SSTR) as a function of number of fuel pins and fuel enrichment in the neutron interrogation of fuel experiment	266
A.1	Non-relativistic expressions for the energetics and solid-angle relations for nuclear reactions	285
A.2	Non-relativistic expressions for the energetics and solid-angle relations for elastic scattering	289
B.1	Coefficients for $\lambda(\tau)$ in the low energy region	296
B.2(a)	Energy loss rate of different particles in cellulose nitrate	304
(b)	Range of different particles in cellulose nitrate	305
C.1	Elastic scattering and (n,α) reaction cross sections for ^{1}H, ^{12}C, ^{14}N and ^{16}O as a function of neutron energy	307

NOTATIONS

The following is a table of definitions of quantities used in the thesis.

V_B	bulk etch rate (μm/h)
V_T	track etch rate (μm/h)
V_T/V_B	etch rate ratio
N	etchant concentration in normals
θ_c	critical angle for track detection
L	'observable track length' in SSTR (μm)
L_M	'maximum observable track length' in SSTR (μm)
E	particle energy
E_n	neutron energy
$_xE_i$	particle energy associated with the 'maximum observable track length' in a SSTR
$_NE_i$	minimum particle energy required to produce a detectable track in a SSTR
dE/dx	energy loss rate
R	particle range in SSTR (μm)
η	neutron detection sensitivity of a SSTR (in tracks per neutron)
η_{th}	theoretical neutron detection sensitivity
η_{exp}	experimental neutron detection sensitivity
ρ_t	track density in SSTR (tracks/cm^2)
D_γ	absorbed gamma-dose (x 10^6 Rads)
W_D	track width in SSTR at a gamma-dose of 'D-megarads'
W_O	track width in SSTR at a gamma-dose of 'zero-megarads'
$V_{B,D}$	bulk etch rate at a gamma-dose of 'D-megarads'
$V_{B,O}$	bulk etch rate at a gamma-dose of 'zero-megarads'

CHAPTER 1

OBJECTIVES AND GENERAL CONSIDERATIONS

1.1 INTRODUCTION

Solid State Track Recorders (SSTRs) have found increasing use in neutron measurements in recent years[1,2]. The technique has a number of advantages over the older methods of counting recoil protons in emulsions or measuring the radioactivity of a fissile foil or other neutron absorber; among these the following are worth mentioning: insensitivity to γ-, x- and β-radiations, permanent recording of tracks with no deterioration, convenience due to small size and weight, ease of "development" and evaluation, wide range of doses amenable to measurement, small detectors give small flux perturbation, detectors can be easily switched "on" or "off".

Two types of detector systems utilising SSTRs have been developed. In the first type, SSTRs are placed adjacent to 'converter foils' which contain either fissile or alphagenic materials, so that the charged products of either (n,f) or (n,α) reactions are recorded by the SSTR[3,4]. In the second type, the SSTRs are used without 'converter foils', so that the fast neutrons are detected by means of the ionising products of a number of nuclear reactions between the neutrons and the constituents of the SSTRs themselves[5]; such SSTRs are called 'intrinsic SSTRs'.

The latent tracks in SSTRs can be etched so that they can be seen using an optical microscope and subsequently counted by eye and/or automatically.

This chapter contains a review of previous work on SSTRs including several of the important track registration criteria and track revelation methods. A summary of applications of SSTRs to radiation dosimetry and nuclear reactor physics is presented. Finally, the objectives of the research carried out on the application of SSTRs to fast neutron measurements, are discussed.

1.2 REVIEW OF PREVIOUS WORK ON SSTRs

Although credit for the first intentional etching of particle tracks in 1958 belongs to Young[6], his work escaped notice until later. It was Silk and Barne's electron microscopic work on rapidly fading tracks in natural micas in 1959[7], that was noted by Price and Walker in 1962 and pursued by them firstly to observe more stable tracks in synthetic micas and shortly thereafter to take the critical step of chemical etching. These workers reasoned that the damage trail of a charged particle is similar to that of a dislocation; the free energy of the trail should be higher than that of the surrounding undamaged material and thus should be preferentially attacked by a suitable etchant. Fleischer and Price subsequently showed that tracks could be enlarged and made visible by etching in a wide variety of dielectrics including minerals[8], natural and artificial inorganic glasses[9], and organic polymers[10]. The last category proved to be the most sensitive, permitting the detection not only of heavy densely ionising particles, but also of light particles such as alphas and protons.

The next step was the characterisation of track registration in different materials. The first picture that emerged was a simple one indeed. Above a damage threshold that differs from one substance to another, all particles are recorded; below that level none are.

The above properties are highly desirable ones for a particle detector, and their recognition led promptly to many applications, most of which derived from the twin features of the threshold property of particle registration and the basic simplicity of the magnification provided by chemical etching. Chemical analysis, dosimetry, nuclear physics studies, and geological dating are all applications of this sort. In addition, a few of the early uses depended on another characteristic: an extensively etched track is a hole, so that solids of special geometries can be made. Filters, virus counters, and a number of methods of track counting utilise this feature. These wide ranging applications have been the subject of two books[1, 11].

Track etching entered a second, more sophisticated phase in 1969, when Fleischer, Price and Walker found that, because the track etch rate varied with the ionisation rate, particle tracks are sufficiently distinctive that the individual nuclei that produced them can be identified. Among 'solid' track detectors such identification had been the unique province of nuclear emulsions, but it soon became clear that in many cases - for atomic nuclei track-etched solids provided a simpler technique and more precise particle identification. These techniques have received

widespread use in cosmic ray and solar particle studies, nuclear physics, and in searches for new heavily ionising particles[11].

Relatively little effort has gone into modifying the structure of these detectors because of the wide range of available SSTRs with different sensitivities. The favourite detectors today are ordinary glass, muscovite mica and various polymers.

1.3 TRACK REGISTRATION CRITERIA

The ability to predict which particles will produce latent (etchable) tracks in a given SSTR is a basic requirement to the understanding and to the practical utilisation of these detectors. In the last decade or so, several track registration criteria have been proposed. These criteria are reviewed here, and an attempt is made to analyse these approaches, pointing out their positive and negative aspects.

The parameters which influence track etching can be separated into five broad categories;

(i) the material parameters (which include the chemical composition, molecular weight, the extent of crystallinity, solvent content, etc.),

(ii) the particle parameters (charge, z, mass, M, velocity, v),

(iii) the irradiation environmental parameters (temperature, atmosphere, etc.),

(iv) the pre-etch storage parameters (atmosphere, temperature, storage time, etc.), and

(v) the etching parameters (type of etchant, temperature, etc.).

The question considered here is, given a particular SSTR, how does track registration depend upon the particle parameters, when all other etch-influencing parameters remain fixed? In other words, what function of z, M and v best predicts the condition $V_T/V_B > 1$, where V_T = track etch rate, and V_B = bulk etch rate.

1.3.1 The Total Energy Loss Rate, $(dE/dx)_T$ Criterion

The first criterion proposed postulated that for etchable track formation the total rate of energy loss by the bombarding particle must exceed a critical value which is characteristic of the particular detecting material[12]. This is a single adjustable parameter criterion, the adjustable parameter being the $(dE/dx)_{crit}$. It was found to work over a narrow region of particle velocities. It failed when applied to relativistic particles. The reason being that the energetic δ-electrons tend to be multiply scattered away from the latent track region and deposit their energy to the side of the path.

1.3.2 The Primary Ionisation, PI Criterion

This criterion postulates that an etchable track will result if the rate of primary ionisation of the bombarding particle exceeds a critical value which is characteristic of the detecting material[13]. The PI criterion makes use of an expression of Bethe in order to calculate the rate of primary ionisation (as defined by Bethe, PI = the average

number of collisions/g-cm^2 that result in an ejection of the least tightly bound electron from an atom)[14]. Two adjustable parameters are utilised: I_o, the ionisation potential of the outermost shell of the stopping atoms (as defined by Bethe) and $(PI)_{crit}$, the critical rate of primary ionisation. Since the formula utilised is simple, the PI criterion is easy to use and its parameters can be adjusted to produce agreement with most experimental data on track registration.

The Bethe formula utilised also contains dimensionless parameters r and s, which have been calculated only for one stopping material (hydrogen). Because of this, absolute values of PI in plastic SSTRs are not known, relative values must be utilised in detector calibration. A value of I_o = 2 eV has been utilised in order to fit the experimental data[13]. This value appears to be too low to fit the physical meaning given to it by Bethe. Optical absorption measurements indicate that one of the materials, Lexan is highly transparent to λ = 6200 ^oA (2 eV) photons. This implies the absence of allowed electronic energy levels for these low energies. The lowest allowed electronic excitation levels for Lexan lie above about 4.1 eV (3000 ^oA) with the onset of strong optical absorption occurring at about 4.4 eV (2800 ^oA). Consequently a value of $I_o \simeq 4.4$ eV appears to be more realistic. Since for ionisation in plastics, energies of 9-15 eV are required[15], the name 'primary excitation' rather than 'primary ionisation' seems more appropriate for this criterion.

1.3.3 The Restricted Energy Loss, REL Criterion

The quantity REL is simply the rate of energy loss of the bombarding particle due to the distant collisions with electrons of the stopping material[16]. The distant collisions are defined as those resulting in the ejection of electrons of energy, w, less than some predetermined value, w_o. In order to make use of the expression of Bethe to calculate REL rates, w_o must fall in the range such that the stopping atomic electrons can be treated as free particles. This criterion postulates that latent track formation takes place when the REL rate of the particle exceeds a critical value, characteristic of the detecting material. Both the energy going into the primary ionisation and into ionisations of higher order are included in REL. The energy deposited by the energetic δ-rays ($w > w_o$) as they leave the latent track region is neglected. Two adjustable parameters are utilised, w_o the average energy of the recoil electrons that delineates the boundary between those electrons which contribute and those that do not contribute to latent track formation, and $(REL)_{crit}$, the critical value of REL.

Absolute values of REL rates can easily be calculated. The criterion works well for incident ion energies $\gtrsim$ 3.5 MeV/nucleon. Since the term, C/Z (the tight binding shell correction has not been calculated for energies < 8 MeV/nucleon, calculation of REL rates at low energies becomes more complex[17]. Also the value of $w_o = 10^3$ eV previously used appears to be too high[18].

By adjusting REL_{crit}, lower values of w_o can be used, however better experimental data on track registration is needed in order to find optimum values of these parameters.

1.3.4 The δ-ray Criterion (Katz and Kobetich)

A new approach to this problem was taken by Katz and Kobetich[19]. They calculate the spatial energy distribution in the vicinity of the particle path by combining the δ-ray energy spectra and the range-energy relation for these electrons. It is proposed that etchable track damage results when a critical dose is deposited at a critical distance from the ion's path by the secondary electrons. The critical distance is taken to be approximately 20 ^{o}A, as is appropriate for the passage of the etchant along the track and the diffusion of reaction products back to the surface. It is postulated that at the critical radius the dose required for etchable damage formation approximates doses producing bulk damage under γ-irradiation. This criterion also, uses two adjustable parameters, the critical radius, R_{crit} and the critical dose, D_{crit}.

This criterion can be fitted to most of the experimental data. It is difficult to evaluate this approach in detail, since the results strongly depend upon the correctness of the basic assumptions, namely (i) the contributions of the 'primary excitations' can be completely neglected, (ii) the exact form of range-energy relation for electrons in eV energy region, and (iii) other assumptions in the calculation (such as the form of the angular distribution of the ejected electrons).

1.3.5 The δ-ray Criterion (Monnin)

A similar approach to that described in Section 1.3.4 is taken here[18]. However, no minimum critical radius is initially assumed. Calculations are made of the doses deposited within cylinders of increasing radii. It is postulated that etchability is created when the absorbed dose exceeds a specific value within a cylinder of a certain radius (the two adjustable parameters).

One particularly significant result of the calculations shows that the dose falls off quickly as a function of distance from the trajectory. For example, for particles near the threshold of registration in cellulose nitrate, the dose near the centre of the trajectory (< 10 ^{o}A) is found to be about 400 megarads. It falls to < 1 megarad at distance of ∿ 100 ^{o}A. Bulk etch rate measurements of γ-irradiated cellulose nitrate show that doses above 1 megarad are required to produce significant etch rate enhancement above the value found for the normal, unirradiated material (see Chapter 6). The calculations have been refined to include electron multiple scattering, the angle of emission of electrons, and a Monte Carlo method of simulating the electron trajectories in the polymer.

1.3.6 Remarks

A list of the track registration criteria, discussed in the preceding sections, along with their adjustable parameters and methods of calculation is given in Table 1.1. All of the criteria postulate a threshold or 'critical' value of the parameters, above which value the charged

TABLE 1.1

VARIOUS TRACK REGISTRATION CRITERIA WITH THEIR ADJUSTABLE PARAMETERS AND METHODS OF CALCULATION

Criterion	Adj. Parameters	Method of Calculation
$(\frac{dE}{dx})_T$	$(\frac{dE}{dx})_{crit}$	$(\frac{dE}{dx})_T = \frac{2\pi n (z^*)^2 r_o^2 m_o C^2}{\beta^2} \left[\ell n \frac{2m_o C^2 \beta^2 \gamma^2 w_{max}}{I_{adj}^2} - 2\beta^2 - 2C/Z_{-\delta} \right]$
$PI = \frac{dJ}{dx}$	$I_o, (PI)_{crit}$	$(\frac{dJ}{dx}) = \frac{2\pi n (z^*)^2 r_o^2 m_o C^2}{\beta^2} \frac{r}{I_o} \left[\ell n \frac{2m_o C^2 \beta^2 \gamma^2}{I_o} + S - \beta^2 \right]$
$REL=(\frac{dE}{dx})_{w<w_o}$	$w_o, (REL)_{crit}$	$(\frac{dE}{dx})_{w < w_o} = \frac{2\pi n (z^*)^2 r_o^2 m_o C^2}{\beta^2} \left[\ell n \left(\frac{2m_o C^2 \beta^2 \gamma^2 w_o}{I_{adj}^2} \right) - \beta^2 - 2C/Z_{-\delta} \right]$
Delta-ray(KK)	$R_{crit}, (dose)_{crit}$	
Delta-ray(M)	$Zone, (dose)_{crit}$	

particle forms a track which can be revealed; they take no account of the differing sensitivities of different track revelation techniques. The material properties enter only in determining the threshold or 'critical' value. All of these criteria have had a fair amount of success in correlating data, indeed it is often hard to differentiate between them in their predictions. They should be regarded as phenomenological attempts to correlate data, which may be useful for certain experimental purposes, but which do not yet rest upon a secure conceptual foundation.

1.4 METHODS OF LATENT TRACK REVELATION

The quality and quantity of information which can be acquired from the tracks left by the passage of charged particles in a SSTR depends on the methods of revelation and observation. Different track revelation techniques have different sensitivities (i.e. for charged particles of differing stopping power or linear energy transfer, LET). Each method of revelation has its particular advantages and disadvantages.

1.4.1 Transmission Electron Microscopy

The observations fall into two classes; (i) tracks in ultra thin (< 100 ^{o}A) polycrystalline layers and thin polymer films, (ii) tracks in bulk insulating monocrystals. In the first case the tracks are visible by enhanced transmission due to the removal of material by evaporation along a line 50-100 ^{o}A wide. A furrow is formed along the track, the removed material being deposited on both sides as small particles of $\sim$ 50 ^{o}A diameter. In the second case the

contrast is due to diffraction effects, suggesting a radial displacement field of cylindrical symmetry; the track core of diameter $\sim$ 100 ^{o}A is probably rich in vacancies and interstitials are shot out radially.

This technique has a number of severe limitations; extremely thin specimens are required with large track densities, only a small track length can be examined, observations are limited to tracks of heavy particles, track fading due to the electron beam occurs in certain substances. However, since electron microscopy is a direct method, it provides fundamental information on latent track structure, unobtainable by other means. In addition, it is of advantage when very large track densities ($> 10^{5}/cm^{2}$) are to be measured[20].

1.4.2 Track Decoration Techniques

Various methods have been used to nucleate precipitates of a second phase along the latent tracks. These methods allow tracks to be displayed throughout a large volume, even when they do not intersect the surface. Often, however, the sensitivity varies in an erratic manner, depending on a few impurities in the detector material. In crystals the precipitation is caused by the strain field along the track, which favours the presence of either over or undersized atoms near the track centre. An analogous phenomena is observed in the strain field of dislocations.

The most successful track decoration procedure involves the deposition of silver along tracks in silver chloride[21],

which renders them visible in the optical microscope. Ultra-violet light creates free photo-electrons, which are pulsed through the crystal via an electric field and react with silver ions to convert them into silver atoms. The sensitivity of cadmium doped silver chloride detectors is greater than any of the etched track detectors so far developed, which is not surprising, since the process involved is similar to photography (sensitive nuclear emulsion can reveal even the weakest ionising electron track). Latent tracks in these AgCl detectors are unstable and fade with time; they can be stabilised for months by illumination in light during or just after the passage of a particle[22]. This feature offers a simple method of switching the detector "on" or "off".

In polymeric SSTRs, tracks can be decorated by the grafting method, which utilises the high concentration along damage trails of free radicals and reactive groups (such as peroxy groups) to initiate graft copolymerisation[23]. Fission fragment tracks in cellulose triacetate have been revealed by this method[24,25]. The method involves three main track processing steps; (i) swelling in a weak alkaline solution, (ii) sensitisation in maleic acid, and finally (iii) dyeing in Rhodamine B to improve optical contrast. The technique needs more development before it can be reliably applied.

1.4.3 Chemical Etching

The most widely used technique for revealing charged particle tracks in SSTRs is the method of preferential etching, which enlarges tracks large enough to be easily visible under an optical microscope. The etchant attacks the damage trail faster than the detector surface. The technique is very simple; ordinary acids and bases are used as etchants. Moreover, it is the only procedure that has succeeded in revealing tracks of extremely low energy heavy nuclei such as solar wind ions and recoil nuclei from alpha decay[11].

Optimised etching conditions have to be established empirically for each detector material. More for convenience than for scientific reasons, simple etchants such as KOH, NaOH and HF have dominated etching work for a long time. Only in recent years have more sophisticated procedures such as multi-step treatments and more complex etchants (e.g. oxidising agents) been studied[17]. Much remains to be done along this line.

The etching rate along the track depends mainly on the following variables; (i) charge and velocity of the particle, (ii) etchant composition, (iii) nature of etchant (temperature and concentration), (iv) detector pre- and post-irradiation treatments, (v) the environment of the detector foil during irradiation. Under point (iii) should be included the fluid motion of the etchant around the detector; stirring and agitation often increases the bulk etch rate. As an example of point (v), the presence of

oxygen during irradiation of cellulose nitrate increases the sensitivity substantially[23].

If only track densities are required, the etching conditions do not have to be precisely controlled; however, accurate measurements of track dimensions require precise reproducibility of etching conditions and control of changes in etchant activity during etching. Precise measurements of the track dimensions have been used for particle type and energy identification. The high resolution of the method permits close neighbours like ^{10}B and ^{11}B to be distinguished [26].

1.4.4 Electrochemical Etching

In this method, the irradiated SSTR is placed between two Teflon cells containing the etchant, and a high voltage is applied ($\sim$ 1000 volts) through the SSTR by two platinum electrodes placed in the etchant. A good contact between the SSTR and the dividing wall of the containers ensures electrical isolation of the two electrolytes[27].

At the beginning of the etching, the etchant rapidly diffuses in the pre-existing fine channels resulting from the passage of the incident charged particles, producing a conductive path. This damage area is increased by the passage of the current, thus producing well defined tracks[28].

Compared with the chemical etching the etching rate is much higher. The conduction currents due to the mobile ions, and other forms of dielectric loss generate heat

continuously in the electrically stressed insulator, which raises the temperature of the SSTR, thus increasing the chemical action of the etchant. It is possible to enlarge tracks to a size observable by the unaided eye, which is desirable in the study of low yield nuclear processes[29].

1.5 APPLICATIONS OF SSTRs

Among the most important applications of SSTRs are fission track dating (geochronology, geophysics, palaeontology, archaeology), cosmic ray and solar flare studies, tracks in meteorites and lunar rocks and soil, nuclear fission studies, radiation dosimetry, and element mapping and isotopic analysis in various specimens. These applications as well as many others are extensively treated in a book by Fleischer, Price and Walker[11]. Here, the discussion is mainly confined to some of the closely related applications of SSTRs to neutron dosimetry and nuclear reactor physics.

1.5.1 Radiation Dosimetry

Neutron detection and neutron fluence measurements have been made mainly by using tracks from (n,f) reactions. The neutron fluence is measured by counting the fission tracks recorded in a thin SSTR in contact with a foil of fissionable material. The main problem is in preparing uniform, thin layers of fissionable materials; this problem can be avoided by using a layer thicker than the range of fission fragments so that fragments from zero to the maximum energy strike the detector. The sensitivity of a SSTR in contact with a 'thick' fission foil is given by;

$$\rho(\text{tracks/cm}^2) = 1.3 \times 10^{-5}\ \phi(\text{neutrons/cm}^2)\,\sigma(\text{barns}) \quad (1.1)$$

because all fissionable isotopes emit fission fragments with roughly the same range and the same detection efficiency in sensitive SSTRs (see Section 2.3.1, Chapter 2).

It is possible to obtain a histogram of the neutron energy distribution by employing either fissionable materials with different thresholds or the same material encapsulated in different neutron shields. For example, a ^{10}B spherical shell eliminates thermal and resonance neutrons and provides a cut off of $\sim$ 10 keV for the neutron spectrum[4]. By using foils of ^{235}U, ^{239}Pu, ^{237}Np, ^{238}U and ^{232}Th, the neutron flux can be determined in the following five energy intervals (in MeV)[30]: 0-0.1; 0.1-0.6; 0.6-1.5; 1.5-3; 3-6. For personnel dosimetry of fast neutrons ^{237}Np has the best characteristics because of its low threshold, high cross section and absence of high energy γ-sensitivity.

Thermal and epi-thermal neutrons can be best measured by employing the (n,α) reactions of ^{10}B and ^{6}Li whose cross sections go as v^{-1}. For a thermal neutron distribution the cross section are 3837 barns for ^{10}B and 940 barns for ^{6}Li, both of which are sufficiently higher than the fission cross section of ^{235}U. A sensitivity of 1.3×10^{-2} tracks/neutron has been attained using a thick ^{10}B layer with a cellulose nitrate detector[31]. The technique is attractive as it avoids the disadvantages of fissionable materials.

Fast neutron fluences can be measured by counting the tracks caused by elastically recoiled nuclei and also by (n',α) and other reactions in the detector material itself ('Intrinsic SSTRs'). Spectral information on high energy neutrons can be obtained from the track density changes by employing energy degrading foils of different thicknesses[32]. Measurements consist of track counting and do not involve the relatively complex procedures of track dimension measurements. For a fission neutron source, the sensitivity of cellulose nitrate SSTRs is $\sim 1.4 \times 10^{-5}$ tracks/neutron, which is comparable to that of a natural uranium radiator, next to a fission track detector.

The sensitivity of plastic SSTRs can be increased by a factor of ~ 13 by employing a helium atmosphere as the radiator. Neutrons of energy greater than 10 MeV can be distinguished from lower energy neutrons by detecting three-prong stars from the break up reaction $^{12}C(n,n')3\alpha$, the sensitivity is $\sim 8 \times 10^{-8}$ tracks/neutron at 17 MeV. 'Intrinsic SSTRs' are by far the least expensive and simplest fast neutron detectors available.

Alpha particle dosimetry is important in certain environments. Alphas represent a hazard at very high altitudes and also in uranium mines, where radon gas and its daughters emit high energy alphas (5.5 to 7.7 MeV). Sensitive plastic SSTRs such as cellulose nitrate are in present use in personnel dosimeters[11,33].

1.5.2 Reactor Physics Applications

In reactor physics SSTRs have been used for fission rate, neutron flux and nuclear fission cross-section measurements[11]. The major advantage being the insensitivity of these detectors to β- and γ-radiations and a minimum flux perturbation.

SSTRs have been used inside reactors for fission density distribution measurements in fuel elements and near interfaces. Intracell and axial fast neutron flux distributions have been measured via recoil and (n,α) reaction tracks in a Makrofol polycarbonate film[34]. Mica has been used extensively for flux measurements via fission tracks[35]. The neutron flux distribution near boron containing "grey" control rods and the microscopic distribution of boron in steel were investigated by recording alphas from the $^{10}B(n,\alpha)^{7}Li$ reaction[36]. The fast advantage factor was calculated from measurements of the fast neutron flux inside fuel elements and in the moderator. The ^{238}U:^{235}U fission ratio was measured in a fast reactor using fission tracks in Lexan (polycarbonate) film[37]. Delayed neutrons were measured in a research reactor to detect the failure of a fuel element[38]. When the track density is greater than $10^{5}/cm^{2}$, it has been measured directly in very thin Lexan films with an electron microscope, without preliminary etching[20]. This technique also permits very high spatial resolution.

When reactor fluxes are measured via fission tracks from a uranium radiator, the use of plastics rather than mica improves visibility because of longer track lengths in organic material. However, sometimes mica is more reliable,

track fading in certain plastics may occur under conditions of high temperature and a very high background radiation (α, β and γ).

1.5.3 Miscellaneous Applications

SSTRs have been used to determine the concentration of various elements in a specimen. The application is based on the fact that the number of tracks produced per unit area is proportional to the concentration of the element emitting the particles which produce the tracks[39].

Another recent interesting application of SSTRs is in the technique of heavy ion radiography which involves shooting a monoenergetic beam of charged particles (e.g. ^{16}O ions) through the object to be imaged and bringing the beam to rest in a stack of plastic sheets[40]. Particles traverse about the same mass thickness (g/cm^2) before coming to rest in a particular sheet, which gives information about the mass density along their path. The technique seems capable of becoming a practical tool of tumour diagnosis[41]. Alpha radiography may also be of interest, however because of smaller straggling and scattering, radiographs of higher resolution can be produced with heavy ions. The application of this technique is restricted by the need for high energy particles (several hundreds of MeV/nucleon).

1.6 THE PRESENT WORK

The initial impetus for the present work grew out of a definite interest which exists in nuclear industry in techniques for detecting fast neutrons in the presence of a

high flux of gamma rays and low energy neutrons[42]. This interest stems from a requirement to measure the fissile content of spent reactor fuel elements and the assay of fissile material for safeguards.

The neutron dosimetry measurements with spent fuel elements would serve two broad purposes, namely to characterise the composition and radiation environment. This first purpose, includes the need to understand and quantify spent fuel fissile isotopic compositions for reasons of economics, safeguards, or reactor physics. The second purpose encompasses health and safety requirements created by the spent fuel radiation environment.

Passive neutron dosimetry techniques to characterise composition can be based upon spontaneously-generated neutron emission from the plutonium and higher actinide content of the fuel. Neutrons are emitted from spontaneous fission as well as from (α,n) reactions in the irradiated fuel. Consequently, the presence of these spontaneously-generated neutrons is strongly correlated with the higher actinide content. At the same time, the neutron observations will contribute to characterising the radiation environment in that fast neutrons are an important component of this environment.

SSTRs would have three important advantages over other neutron detection methods in this application.

(i) The detector would be so small that it could be quite easily mounted without upsetting the fuel storage arrangement and would therefore introduce a small experimental perturbation.

(ii) It would produce a permanent record of the experimental results, making it unnecessary for them to be counted immediately after irradiation. This is a great advantage when dealing with a large number of measurements taken simultaneously and also when the foils are in a highly active assembly and therefore difficult to retrieve quickly. Furthermore, the gamma counting of foils with short half-lives can prove to be a problem.

(iii) The detectors would be insensitive to gamma radiation.

1.6.1 Objectives

To investigate the feasability of the SSTR technique in nuclear fuel safeguards, a thorough research on the application of SSTRs to fast neutron measurements was carried out. The objectives of the present work were:

(1) Designing a neutron detector based on the tracks from elastically recoiled nuclei ('Intrinsic SSTRs') or fission-fragments;

(2) Calculating the response of detectors to neutrons in the energy range 0-15 MeV;

(3) Verification of the calculated detector response by measurements using mono-energetic neutrons;

(4) Measuring the effect of a high gamma dose (if any) on the detector performance;

(5) A thorough investigation of possible systematic errors;

(6) The application of automatic track counting techniques, which would help to overcome the subjective nature of human decisions on the number of tracks seen in an etched SSTR;

(7) Performing a scoping experiment to measure neutrons from a reactor fuel assembly.

CHAPTER 2

RESPONSE OF SSTRs TO NEUTRONS; THEORY AND ASSESSMENT

2.1 INTRODUCTION

The interaction of neutrons with SSTRs, and the tracks caused by secondary charged particles has been studied for many years [1,5]; but the quantitative response function for detection efficiency as a function of neutron energy, particularly in the case of 'intrinsic' SSTRs has not previously been considered. In order to explore the utility of SSTRs in nuclear reactor physics and other areas, it is essential to know the response of a particular SSTR as a function of neutron energy. Therefore, it was necessary to develop a theoretical model to calculate the neutron sensitivity of 'intrinsic' SSTRs. It was decided, first to treat the problem generally, and second to specialise with the cellulose nitrate (CA80-15) SSTRs, in the case of thermal and fast neutrons, which is of predominant importance to the present work. It was thought that in this way a handy method would be provided so that the present considerations could easily be applied to any other SSTR, by replacing the physical parameters.

In this chapter, equations are also derived to calculate the neutron sensitivity of SSTRs with a (n,f) or (n,α) 'converter' foil. These expressions are applied to calculate the neutron sensitivity of a Makrofol KG SSTR in contact with a thick ^{238}U fission foil and of a cellulose nitrate (CA80-15, type B) SSTR coated with lithium tetraborate.

Finally, some conclusions are drawn on the response of SSTRs to neutrons.

2.2 RESPONSE OF 'INTRINSIC' SSTRs TO NEUTRONS

In this type of SSTRs, the secondary charged particles produced by neutron interactions cause the ionisation damage, which is made visible following a suitable etching procedure. There are several ways in which neutron induced tracks are considerably different from those observed in the more conventional utilisation of SSTRs i.e. SSTRs with a (n,f) or (n,α) 'converter' foil. These differences are illustrated in Figure 2.1 and can be summarised as follows:

(1) The tracks originate from all points within the volume of the SSTR in an uniformly distributed manner.

(2) The tracks appear in all directions but do not have an isotropic distribution.

(3) Some tracks are caused by the particles leaving the surface of the SSTR. In this situation the direction of etching is opposite to the direction of increasing ionisation damage.

(4) The tracks are caused by different nuclear particles, protons, alpha particles and recoil ions.

(5) At any stage of etching the observation plane will intersect tracks at all stages of production, ranging from the beginning of a track to the end of its range.

The consequences of these important differences between neutron induced tracks and conventional charged particle observations in SSTRs can be summarised by two statements on the production and observation of neutron induced tracks in SSTRs.

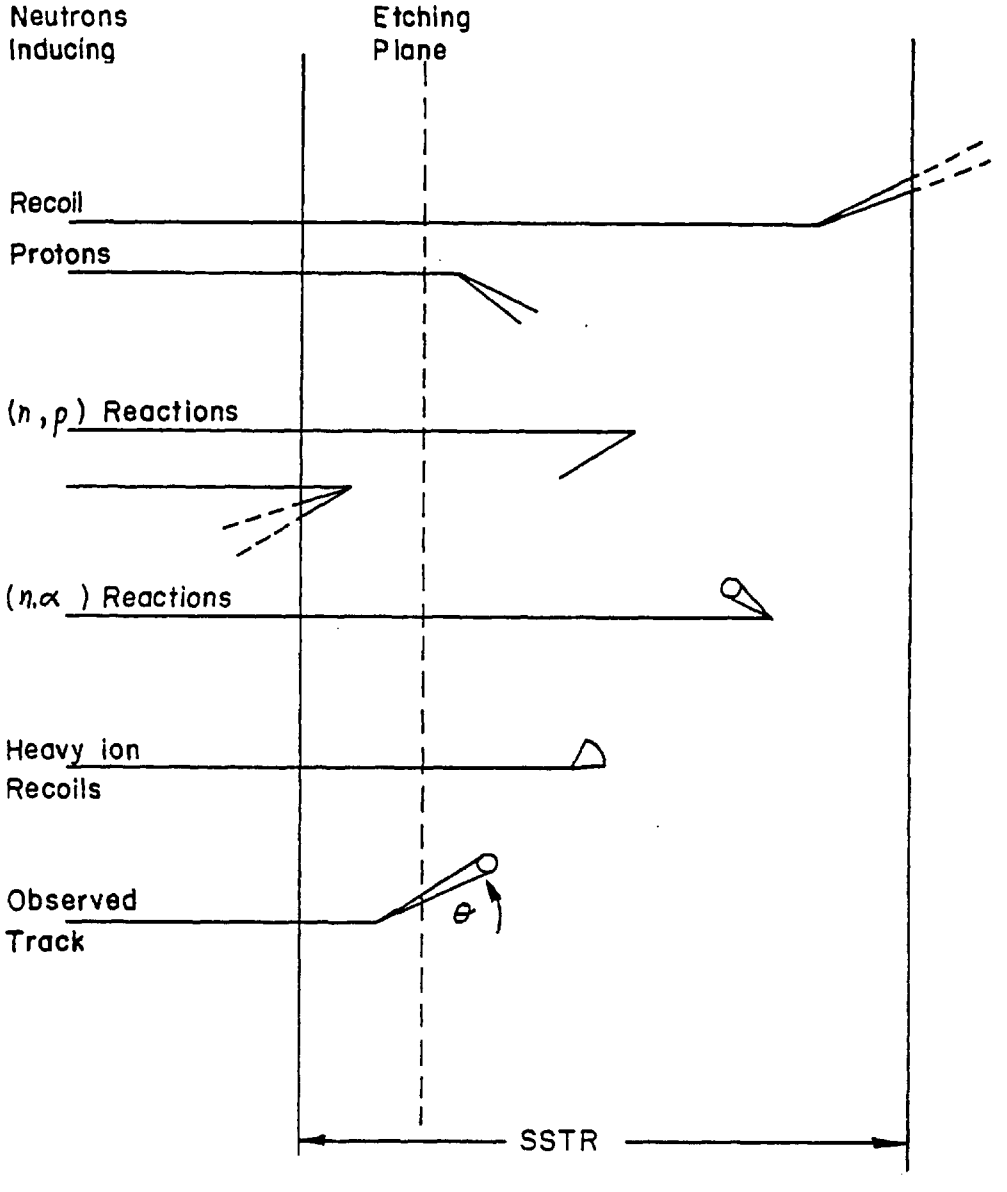


Figure 2.1 Important features of neutron induced tracks in 'intrinsic' SSTRs

(1) The secondary charged particles in the SSTR are produced by a variety of nuclear reactions in the basic constituents of the material. The production of each type of charged particle, proton, alpha or recoil ion depends on the neutron energy.

(2) The observation of an etched SSTR which has been exposed to neutrons will reveal tracks which are, in general, a complicated mixture of different sizes and appearance.

2.2.1 Response Function

The fast neutron interactions that can occur and result in detectable tracks in SSTRs containing hydrogen, carbon, nitrogen and oxygen are given in Table 2.1. The only interaction with thermal neutrons is the $^{14}N(n,p)^{14}C$ reaction, which produces protons of energy 0.584 MeV. As the neutron energy is increased then hydrogen recoils (protons) have sufficient energy to be seen and (n,α) and (n,p) reactions become possible. Eventually, at high neutron energies recoil carbon, nitrogen and oxygen ions may also be observed.

The observation of these particles in a cellulose nitrate SSTR (say) is determined by the damage produced as the ion loses energy and comes to rest. The damage per unit length depends on the particle type and its energy. Two energies can be defined; $_{N}E_{i}$ the minimum energy, below which a particle of type 'i' does not produce enough damage to be observed, and $_{X}E_{i}$ the maximum energy, above which a particle of type 'i' does not produce enough damage to be observed. In case of cellulose nitrate $_{X}E_{i}$ only applies to protons and might be $_{X}E_{i} \simeq 0.70$ MeV for a typical etching condition.

TABLE 2.1

THE FAST NEUTRON INTERACTIONS CONSIDERED IN THE THEORETICAL EFFICIENCY CALCULATIONS OF CELLULOSE NITRATE (CA80-15 SSTR)

^{1}H	$^{1}H(n,n)^{1}H$	Elastic Scattering
^{12}C	$^{12}C(n,n)^{12}C$	Elastic Scattering
	$^{12}C(n,\alpha)^{9}Be$	Q = - 5.70 MeV
	$^{12}C(n,n')3\alpha$	Q = - 7.28 MeV
^{14}N	$^{14}N(n,n)^{14}N$	Elastic Scattering
	$^{14}N(n,p)^{14}C$	Q = 0.626 MeV
	$^{14}N(n,\alpha)^{11}B$	Q = - 0.16 MeV
	$^{14}N(n,2\alpha)^{7}Li$	Q = - 8.82 MeV
	$^{14}N(n,t)3\alpha$	Q = - 11.29 MeV
^{16}O	$^{16}O(n,n)^{16}O$	Elastic Scattering
	$^{16}O(n,\alpha)^{13}C$	Q = - 2.21 MeV
	$^{16}O(n,n')4\alpha$	Q = - 14.50 MeV

Consider now the concept of the observable track length $L_i(E)$ of a particle of type 'i' and energy E. This observable length is the range between ${}_XE_i$ and ${}_NE_i$. The observable length $L_i(E)$ can also be parameterised in terms of the incident neutron beam energy E_o and the direction of the particle with respect to that of the incident beam. $L_i(\theta,E_o)$ is related to $L_i(E)$ through the kinematic equations given in Sections 2.2.3 and 2.2.4. The track length depends on the density of the medium. Its observation depends on etching conditions and the criteria used to recognise a track. To some extent, the quality of the etch, in terms of uniformity of the etching plane (Fig.2.1) plays a part in track recognition.

Consider the etching plane shown in Fig.2.1. The number of tracks recognised consists of those 'observable' tracks which intersect the plane. In order to calculate this number, consider first the total number of tracks per unit volume per normally incident neutron from the reaction 'i' produced into an element of solid angle $d\Omega$. This number is given by

$$N_i \left(\frac{d\sigma}{d\Omega}\right)_i d\Omega$$

where N_i is the number of atoms per unit volume and $\left(\frac{d\sigma}{d\Omega}\right)_i$ is the differential cross section appropriate to the reaction under consideration. Some of these tracks intersect the etching plane and the number per unit area is given by

$$N_i \left(\frac{d\sigma}{d\Omega}\right)_i d\Omega \; L_i(\theta,E_o)\cos\theta$$

The total number of tracks 'T' of type 'i' at neutron energy E_o is given by

$$E_o T_i = \int N_i \left(\frac{d\sigma}{d\Omega}\right)_i L_i(\theta, E_o) \cos\theta \, d\Omega \qquad (2.1)$$

The equation (2.1) is the basis for all calculations on the neutron sensitivity of 'intrinsic' SSTRs. For SSTRs which do not record tracks at shallow angles to the surface, equation (2.1) should be multiplied by $\cos^2 \theta_c$ (θ_c is the critical angle for particle detection, as explained in Chapter 3). The function $L_i(\theta, E_o)$ can be determined by combining the kinematics of the reaction with the basic effective length response function $L_i(E)$.

The angular dependence of the differential cross section is also required for determination of the integral. It can be expressed as

$$\left(\frac{d\sigma}{d\Omega}\right)_i = \frac{\sigma_i}{4\pi} W(\theta, \phi)$$

where $W(\theta, \phi)$ is the angular distribution in the laboratory coordinate system and σ_i is the integrated microscopic reaction cross section.

2.2.2 Thermal Neutrons

In the case of cellulose nitrate SSTRs, thermal neutrons produce 0.584 MeV protons from the $^{14}N(n,p)^{14}C$ reaction, $Q = + 0.626$ MeV. There is no centre of mass motion associated with thermal neutron capture[43], so that the isotropic distribution can be written as

$$\left(\frac{d\sigma}{d\Omega}\right)_i = \frac{\sigma_i}{4\pi}$$

Therefore, in the present case equation (2.1) reduces to

$$T_i = \frac{N_i \sigma_i}{4\pi} \int_{\phi=0}^{2\pi} \int_{\theta=0}^{\pi} L \cos\theta \sin\theta \, d\theta d\phi \qquad (2.2)$$

where 'L' is the observable track length for 0.584 MeV protons. Now, equation (2.2) after integration becomes

$$T_i = \frac{N_i \sigma_i L}{2} \qquad (2.3)$$

The equation (2.3) is used in the thermal neutron sensitivity calculations of 'intrinsic' SSTRs.

2.2.3 Elastic Scattering

The kinematics of elastic scattering are illustrated in Fig.2.2[44,45]. The centre of mass motion can have considerable effect on the laboratory measured energy and angular distribution. The laboratory energy of the recoil, as described in Appendix A, can be expressed as

$$E_R = FE_o \cos^2\theta \quad , \theta \leq \pi/2$$

where,

$$F = \frac{4 M_1 M_2}{(M_1 + M_2)^2}$$

The intensity at laboratory angle 'θ' is given by

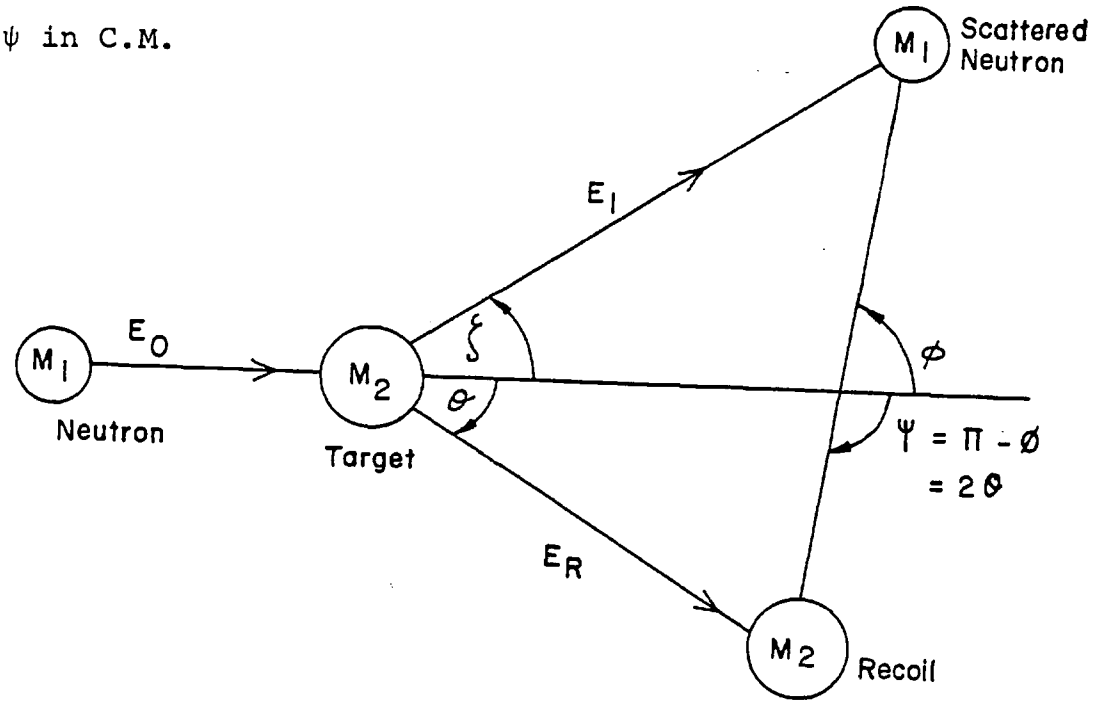
$$I(\theta) = I(\psi) 4 \cos \theta$$

where $I(\psi)$ is the intensity at an angle in centre of mass (CM) coordinate system.

If the elastic scattering is taken to be isotropic in the CM system, then

ξ, θ in lab.

ϕ, ψ in C.M.



$$\frac{E_1}{E_o} = \frac{M_1^2}{(M_1+M_2)^2} \left\{\cos\xi + \left[(M_2/M_1)^2 - \sin^2\xi\right]^{\frac{1}{2}}\right\}^2$$

$$\frac{E_R}{E_o} = \frac{4M_1M_2}{(M_1+M_2)^2} \cos^2\theta, \quad \theta \leq \pi/2$$

Figure 2.2 Kinematics of fast neutron elastic scattering

$$\left(\frac{d\sigma}{d\Omega}\right)_i = \frac{\sigma_i}{4\pi} \; 4 \cos\theta$$

Therefore, in the present case equation (2.1) becomes

$$E_o T_i = \frac{N_i \; \sigma_i}{4\pi} \int L_i \; (\theta, E_o) 4 \cos^2\theta \; d\Omega \qquad (2.4)$$

The function $L_i(\theta, E_o)$ is determined by considering the relation

$$E_R = F \; E_o \cos^2\theta$$

and the form of $L_i(E)$ given in Fig.2.3. The integral in equation (2.4) can be evaluated by considering the angles appropriate to the energies ${}_N E_i$ and ${}_X E_i$; these are given by

$$\theta_X = \cos^{-1} \left({}_X E_i / F \; E_o\right)^{\frac{1}{2}}$$

and

$$\theta_N = \cos^{-1} \left({}_N E_i / F \; E_o\right)^{\frac{1}{2}}$$

Now, the two non-zero parts of the integral in equation (2.4) are

$$I_1 = \frac{N_i \; \sigma_i}{2} \int_0^{\theta_X} 4 \; L_M \cos^2\theta \; d(\cos\theta) \qquad (2.5)$$

for the region where $L_i(E,\theta) = L_M$; where L_M is the maximum observable track length (see Fig.2.3). In the region where $L_i(E)$ varies with energy and can be expressed as

$$L_i(E,\theta) = G(E_R - {}_N E_i)$$

where

$$G = L_M / ({}_X E_i - {}_N E_i)$$

the second part of the integral in equation (2.4) becomes

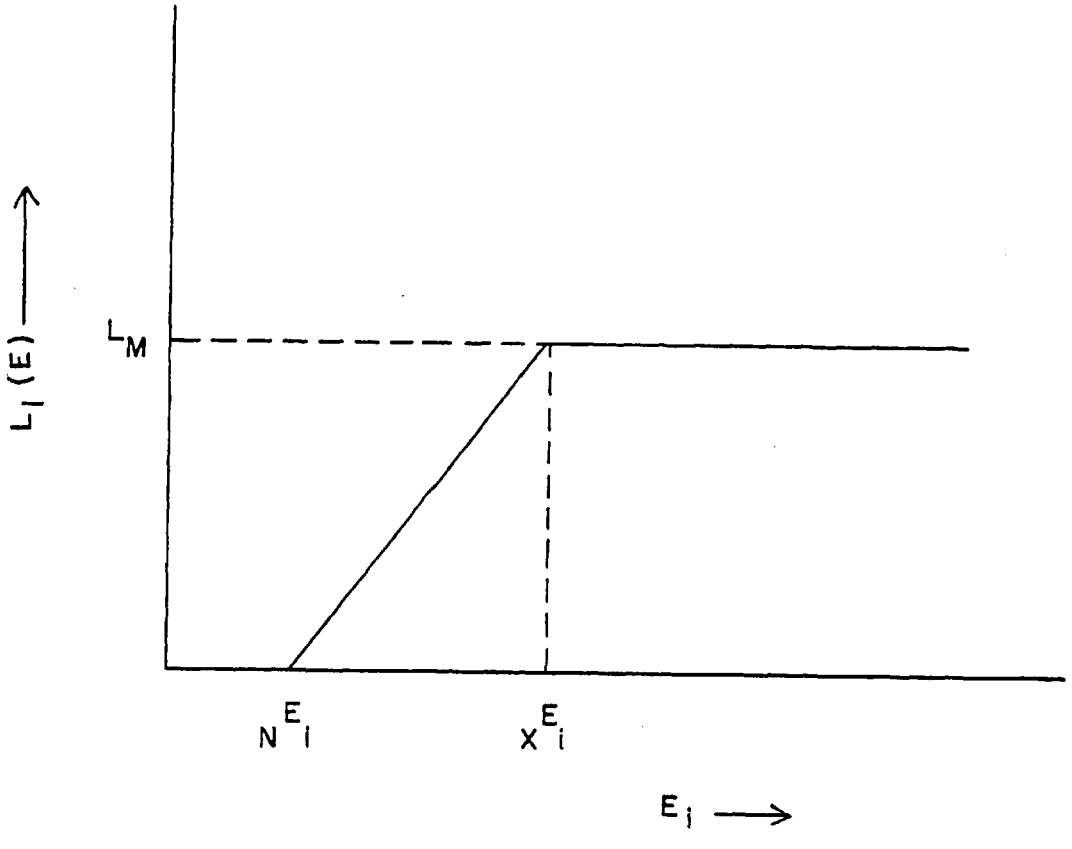


Figure 2.3 Form of observable track length, L as a function of particle energy, L_M is the maximum observable track length

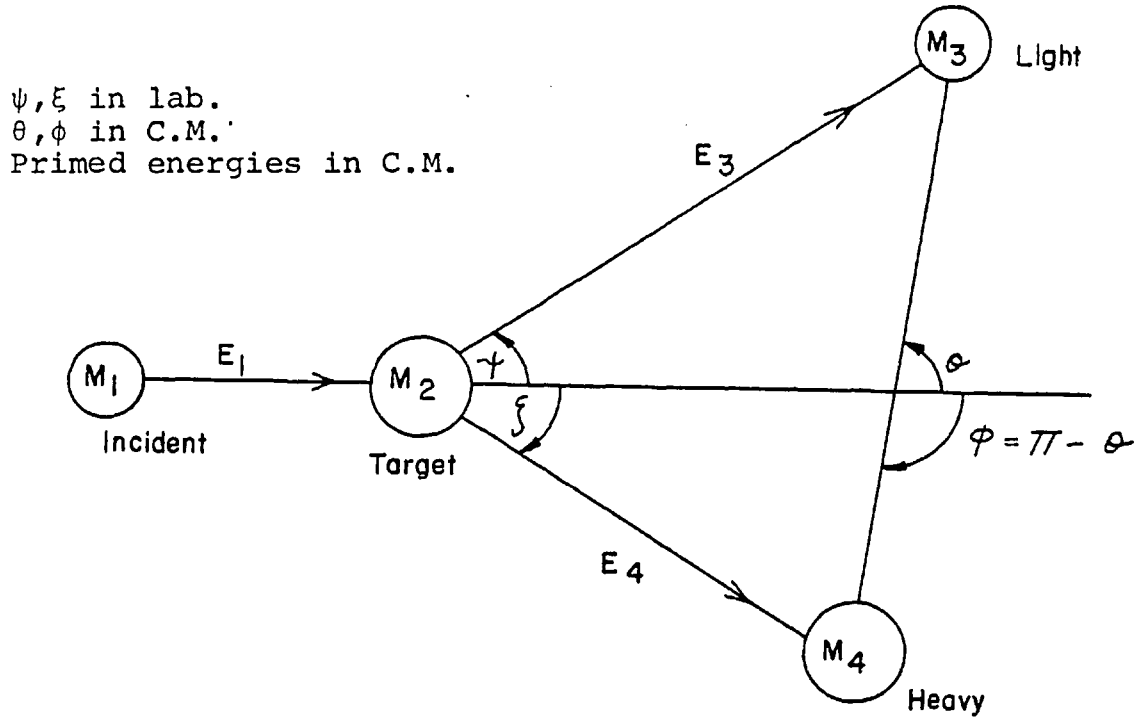
$$I_2 = \frac{N_i \sigma_i}{2} \int_{\theta_x}^{\theta_N} G\ 4\ \cos^2\theta\ ({}_XE_i - {}_NE_i)\ d\ (\cos\theta) \qquad (2.6)$$

The sum of integrals I_1 and I_2 determines the response of 'intrinsic' SSTRs in the case of elastic scattering.

2.2.4 Nuclear Reactions

Nuclear Reactions can be treated in a similar manner to elastic scattering except that the reaction product energy will not be related to the neutron energy in a simple manner. The kinematics of nuclear reactions along with the expressions for the energies of the light and heavy reaction products in the laboratory frame of reference (as described in Appendix A) are illustrated in Fig.2.4[46]. It is clear that an exact calculation, taking into account all the details of the reaction product energies, including the effect of excited states in ^{11}B, ^{9}Be and ^{13}C is hardly justified in view of the limitations of the experimental results. A number of approximations could be considered and the one chosen for comparison with experiments in the present case is to assume an isotropic distribution of light particles with a fixed energy equal to that of the particles emitted at 90°. The reaction product energies for the $^{14}N(n,\alpha)^{11}B$, $^{12}C(n,\alpha)^{9}Be$ and $^{16}O(n,\alpha)^{13}C$ reactions, calculated using equations described in Appendix A are given in Table 2.2. In this case the development of equation 2.1 follows that given in the section 2.2.2 with the appropriate value for the observable track length 'L'.

At neutron energies greater than 5 MeV besides heavy ion recoils which have sufficient energy to be observed, many



$$Q(\text{MeV}) = 931.16(M_1 + M_2 - M_3 - M_4) \text{ (a.m.u.)}$$

$$E_T = E_1 + Q = E_3 + E_4$$

$$E_3 = B\left[\cos\psi + (D/B - \sin^2\psi)^{\frac{1}{2}}\right]^2 E_T$$

$$E_4 = A\left[\cos\xi + (C/A - \sin^2\xi)^{\frac{1}{2}}\right]^2 E_T$$

where

$$\sin\xi = (M_3E_3/M_4E_4)^{\frac{1}{2}} \sin\psi$$

$$A = \frac{M_1M_4(E_1/E_T)}{(M_1+M_2)(M_3+M_4)} \quad ; \quad B = \frac{M_1M_3(E_1/E_T)}{(M_1+M_2)(M_3+M_4)}$$

$$C = \frac{M_2M_3}{(M_1+M_2)(M_3+M_4)}\left(1 + \frac{M_1Q}{M_2E_T}\right) = \frac{E'_4}{E_T}$$

$$D = \frac{M_2M_4}{(M_1+M_2)(M_3+M_4)}\left(1 + \frac{M_1Q}{M_2E_T}\right) = \frac{E'_3}{E_T}$$

Figure 2.4 Kinematics of nuclear reactions

TABLE: 2.2

ENERGIES OF THE REACTION PRODUCTS FROM (n,α) REACTIONS IN CASE OF ^{12}C, ^{14}N AND ^{16}O AS A FUNCTION OF NEUTRON ENERGY

E_n (MeV)	$^{12}C(n,\alpha)^{9}Be$		$^{14}N(n,\alpha)^{11}B$		$^{16}O(n,\alpha)^{13}C$	
	^{9}Be (MeV)	α (MeV)	^{11}B (MeV)	α (MeV)	^{13}C (MeV)	α (MeV)
1.0			0.18	0.66		
1.5			0.35	0.99		
2.0			0.52	1.32		
2.5			0.69	1.65		
3.0			0.86	1.98	0.24	0.55
3.5			1.03	2.31	0.39	0.90
4.0			1.20	2.64	0.54	1.25
4.5			1.37	2.97	0.69	1.60
5.0			1.53	3.31	0.84	1.95
5.5			1.70	3.64	0.99	2.30
6.0			1.87	3.97	1.14	2.65
6.5	0.28	0.52	2.04	4.30	1.29	3.0
7.0	0.47	0.83	2.21	4.63	1.44	3.35
7.5	0.65	1.15	2.38	4.96	1.59	3.70
8.0	0.83	1.47	2.55	5.29	1.74	4.0
8.5	1.01	1.79	2.72	5.62	1.89	4.35
9.0	1.19	2.11	2.89	5.95	2.04	4.70
9.5	1.37	2.43	3.06	6.28	2.19	5.05
10.0	1.55	2.75	3.22	6.62	2.34	5.40

other reactions are also possible. These tracks may cause additional tracks from deuterons, tritons, ^{3}He and also from $^{12}C(n,n')3\alpha$ reactions[47].

2.2.5 Etching Effects

The enlargement of tracks by the etching process is an inherent part of the SSTR technique, without which the tracks could not be seen using an optical microscope. The number of neutron induced tracks and hence the sensitivity increases with the etching time in the relatively early period of etching due to a number of reasons as discussed in Chapters 3 and 4. After some time, which depends on the neutron energy and the etching conditions, the track density reaches a plateau. In the derivation of the response function (equation 2.1), this plateau condition is assumed. Therefore, in cases when the etching conditions are such that the track density is not on the plateau, the theoretical response should be multiplied by a factor which can be obtained from the shape of the curve (track density as a function of etching time)[11]. These effects which are discussed in detail in Chapters 3 and 4 are to be taken into account, while comparing the theoretical and experimental results.

2.2.6 Neutrons in Cellulose Nitrate (CA80-15 SSTR)

(i) Track parameters

The elementary composition of cellulose nitrate is given in Table 2.3. The form of the observable track length, $L_i(E)$ for protons can be estimated by considering the energy loss of protons in cellulose nitrate, as shown in Fig.2.5(a). The

TABLE: 2.3

ELEMENTARY COMPOSITION OF CELLULOSE NITRATE: $C_6H_7O_2(NO_3)_3$

Element	Concentration	
	%	g/cm^3
^{1}H	2.40	0.036
^{12}C	24.20	0.36
^{14}N	14.10	0.21
^{16}O	59.20	0.90
		$\rho = 1.506$

TABLE: 2.4

MAXIMUM OBSERVABLE TRACK LENGTHS 'L_M' AND CORRESPONDING ENERGIES IN CELLULOSE NITRATE

Particle/Ion	L_M (μm)	Corresponding Energy (MeV)
^{1}H	5	0.60
^{4}He	15	3.60
^{12}C	330	120
^{14}N	530	190
^{16}O	660	256

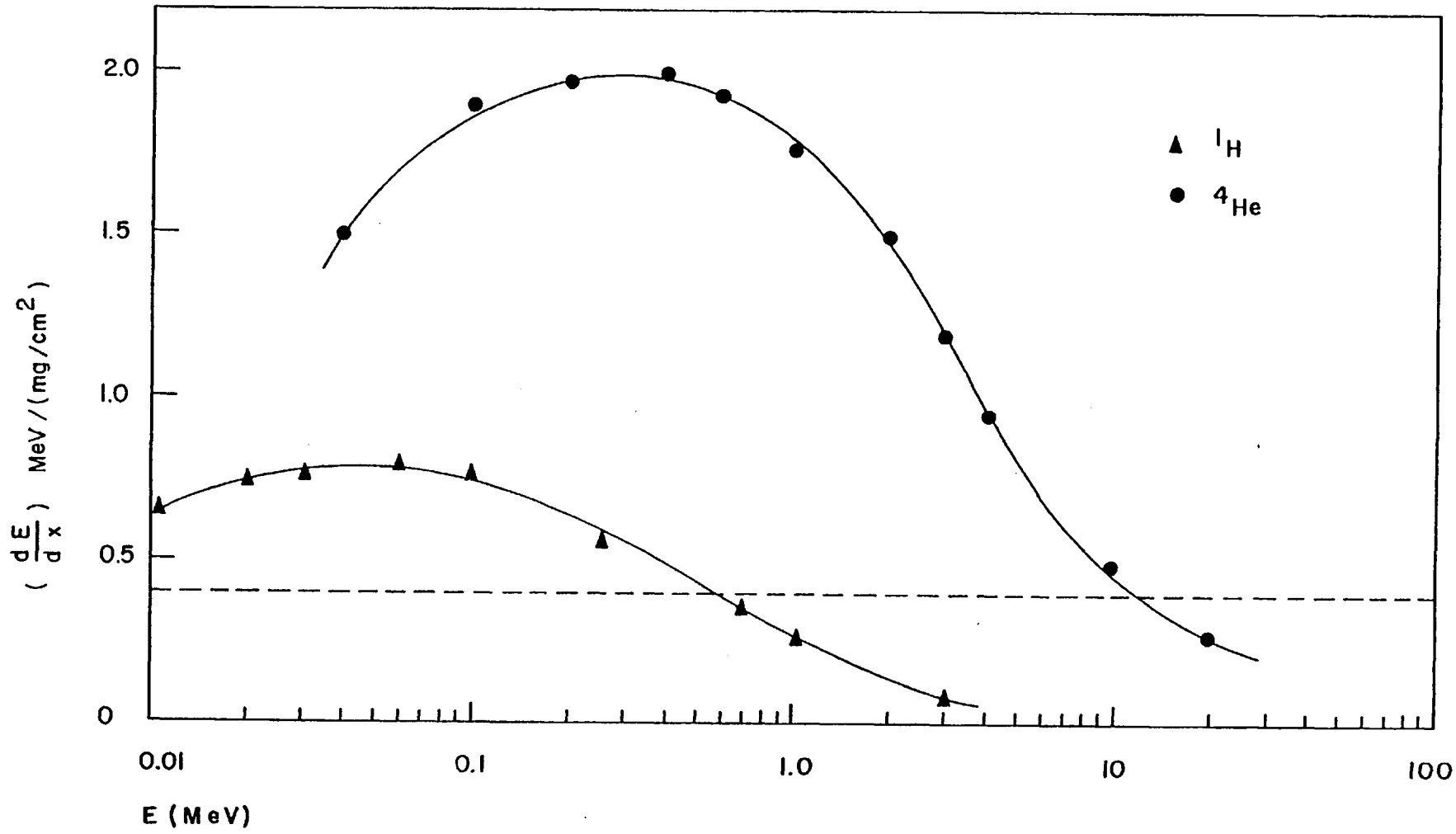


Figure 2.5(a) Energy loss rate, dE/dx in cellulose nitrate as a function of proton and alpha particle energy. The threshold for track registration is $\sim$ 0.40 MeV/(mg/cm^2)

methods used for calculating dE/dx and range for different particles are described in Appendix B. If the damage threshold applicable to the registration of a track is taken to be 0.40 MeV/(mg/cm^2); then $_NE_i$ < 0.01 MeV and $_XE_i$ = 0.75 MeV. However, in order to produce a detectable track in an optical microscope, a charged particle in addition to sufficiently high energy loss, must have a minimum range which is estimated to be 1.5 μm[12]. Therefore, taking this limitation into account in case of protons $_NE_i$ = 0.15 MeV. These values agree with the experimentally observed thresholds obtained by measuring monoenergetic protons (see Chapter 4). The value of $L_i(E)$ between 0.15 to 0.75 MeV can be obtained from the range/energy relation given in Fig.2.6. A similar procedure was adopted to obtain track parameters for alpha particles and recoil ions from Figs.2.5 and 2.6. The maximum observable track lengths L_M in case of ^1H, ^4He, ^{12}C, ^{14}N and ^{16}O in cellulose nitrate are given in Table 2.4[17]. The microscopic neutron cross section data for various reactions applicable in the present case is given in Appendix C.

(ii) Response of CA80-15 SSTR

The theoretical response of CA80-15 SSTR which is a cellulose nitrate film was calculated as a function of the neutron energy using the equations derived in the preceeding sections of this chapter. In the case of thermal neutrons, a sensitivity value of (4.0×10^{-6}) tracks per neutron is obtained from equation (2.3).

The contribution of fast neutron elastic scattering from ^1H, ^{12}C, ^{14}N and ^{16}O nuclei to the sensitivity, as a function

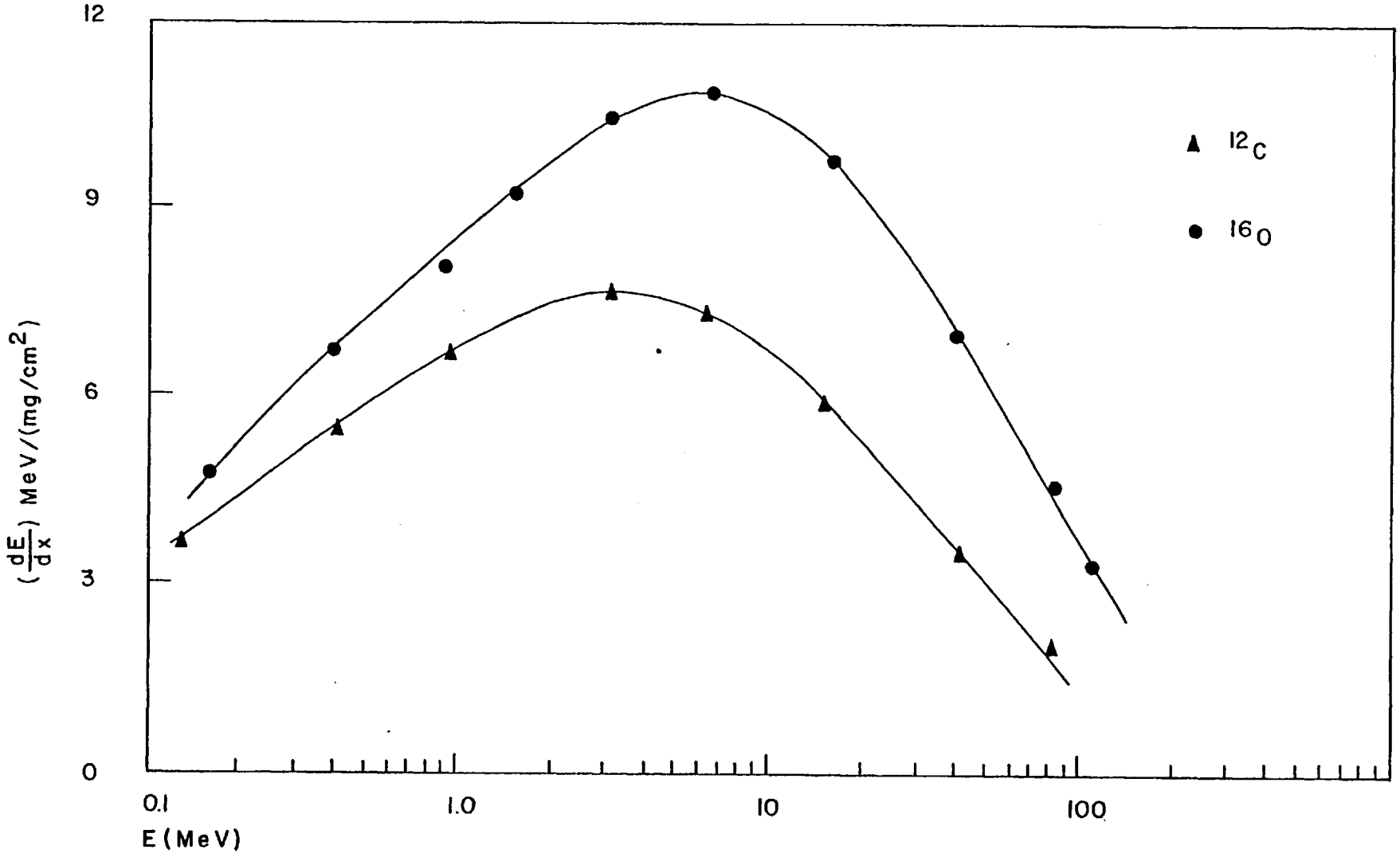


Figure 2.5(b) Energy loss rate, dE/dx in cellulose nitrate as a function of ^{12}C and ^{16}O ions energy

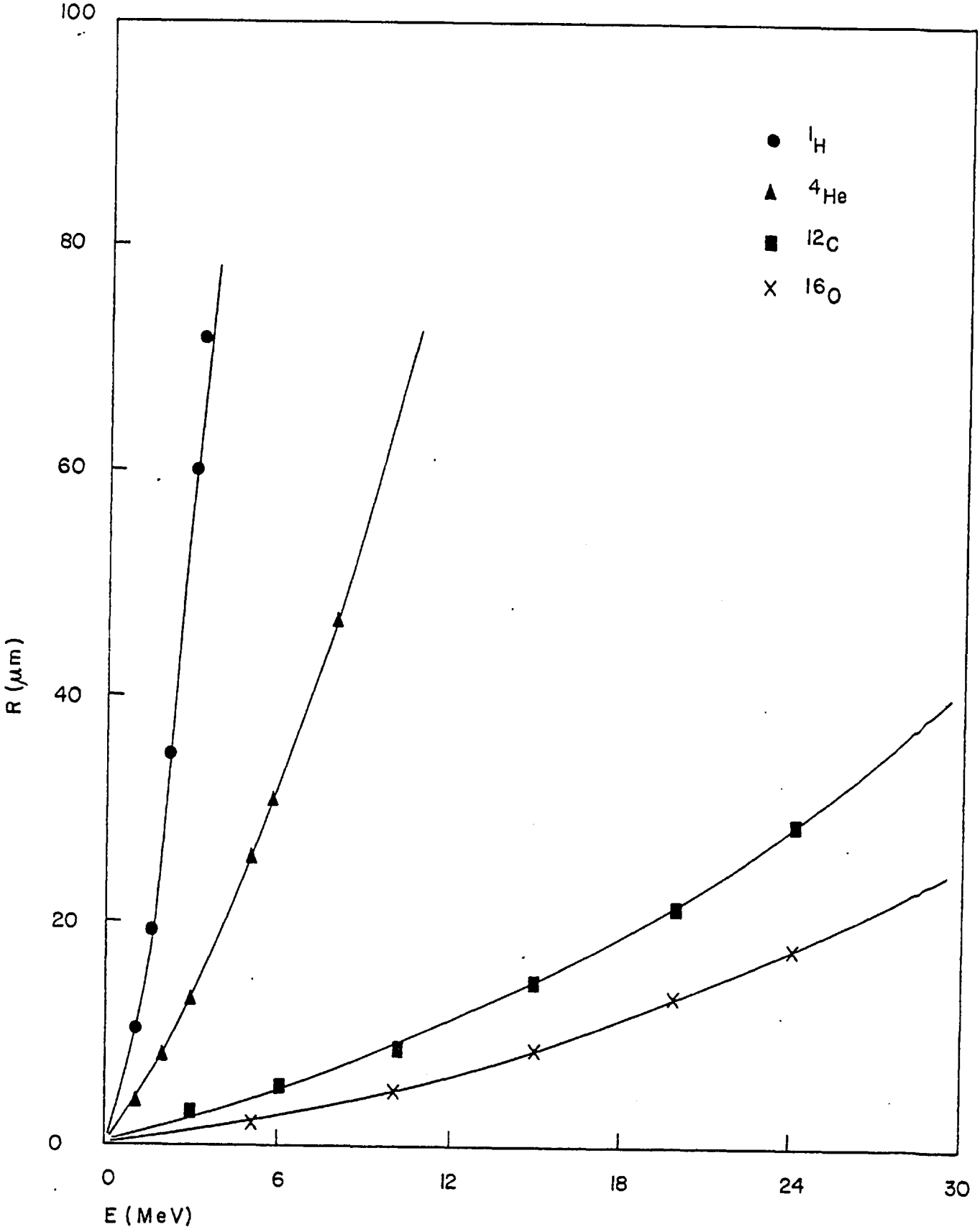


Figure 2.6 Range, R of protons, alpha particles, carbon and oxygen ions in cellulose nitrate as a function of particle energy

of neutron energy is plotted in Fig.2.7. It can be seen that even at E_n = 17 MeV recoil protons contribute significantly to the overall theoretical sensitivity 'η_{th}'. Fig.2.8 shows the contribution of different nuclear reactions to the sensitivity as a function of neutron energy. Although at $E_n \lesssim 5$ MeV, nitrogen has a high cross section for the (n,α) reaction, oxygen also contributes significantly to the sensitivity due to its high concentration in cellulose nitrate. The $^{12}C(n,n')3\alpha$ reaction has an effective threshold at about 11 MeV and appears to peak at about 17 MeV. The total neutron sensitivity of CA80-15 SSTR along with sensitivities due to different reactions is plotted in Fig.2.9. The drop in the sensitivity curve at E_n = 5 MeV is due to the $^{16}O(n,\alpha)^{13}C$ resonance.

2.3 RESPONSE OF SSTRs WITH A 'CONVERTER FOIL' TO NEUTRONS

In this section response functions for neutron detection using SSTRs based on (n,α) or (n,f) reactions are considered. The situation in these cases is not as complex as one usually finds in the case of 'intrinsic' SSTRs, because the tracks are usually produced by only one or two types of particles, either by fission fragments or alpha particles, and also the tracks are not uniformly distributed throughout the volume of the SSTR.

2.3.1 SSTRs with a (n,f) 'Converter' Foil

In this case the track density at neutron energies encountered in the reactor environments can be equated to the neutron fluence by a constant weighted by the fission cross

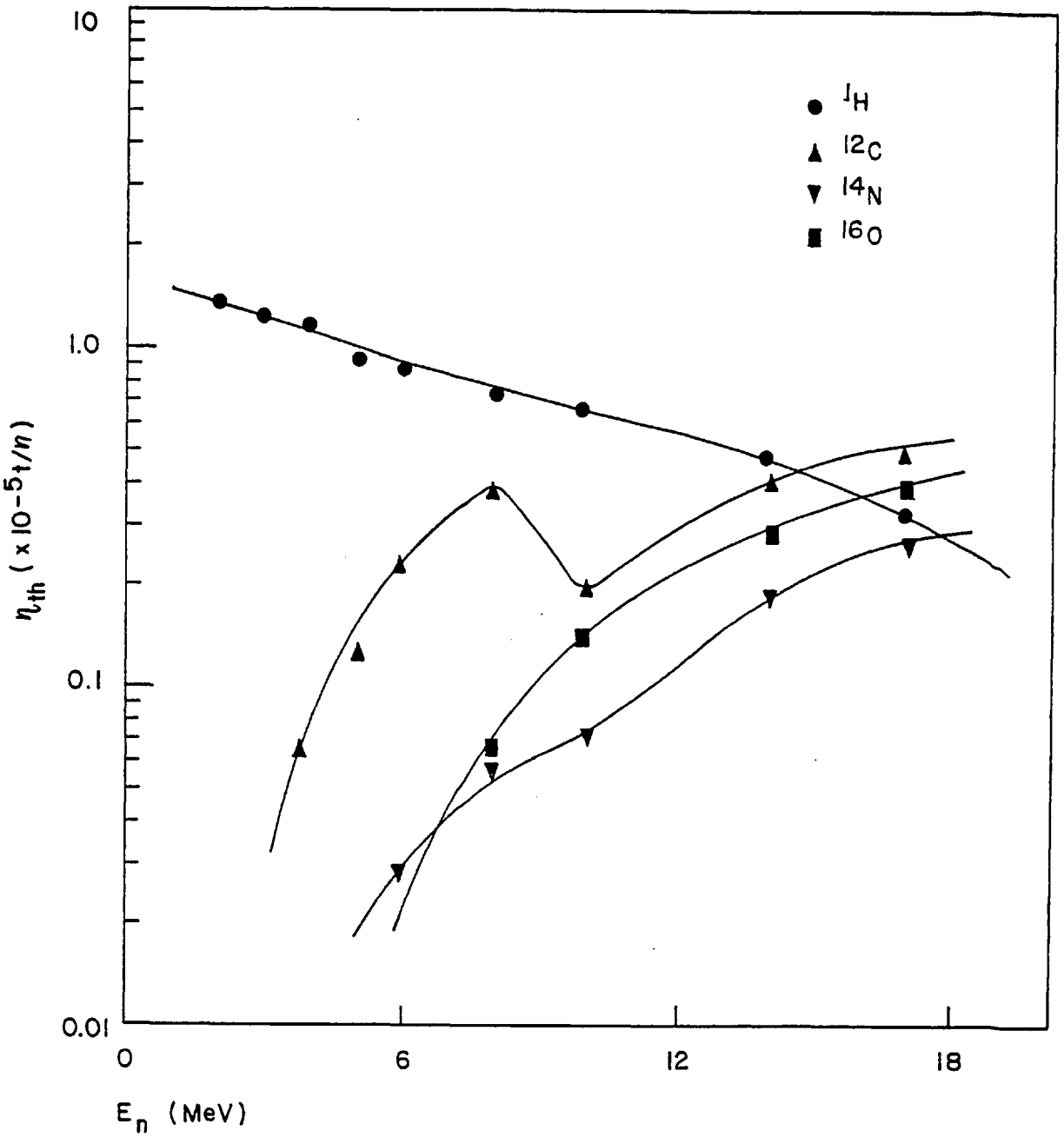


Figure 2.7 The contribution of elastic scatterings to the neutron sensitivity, η_{th} (in tracks per neutron) of CA80-15 as a function of neutron energy

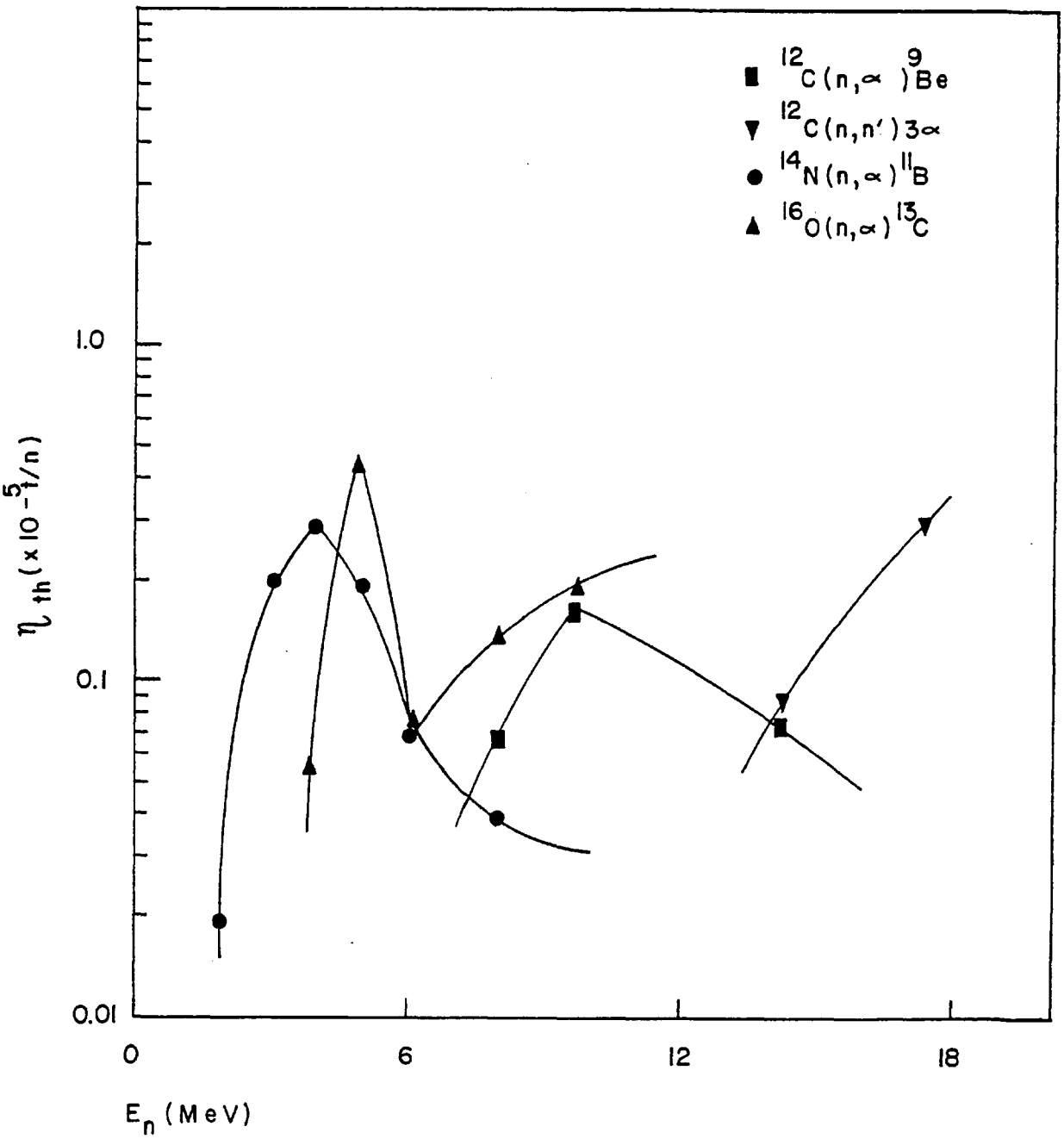


Figure 2.8 The contribution of nuclear reactions to the neutron sensitivity, η_{th} (in tracks per neutron) of CA80-15 as a function of neutron energy

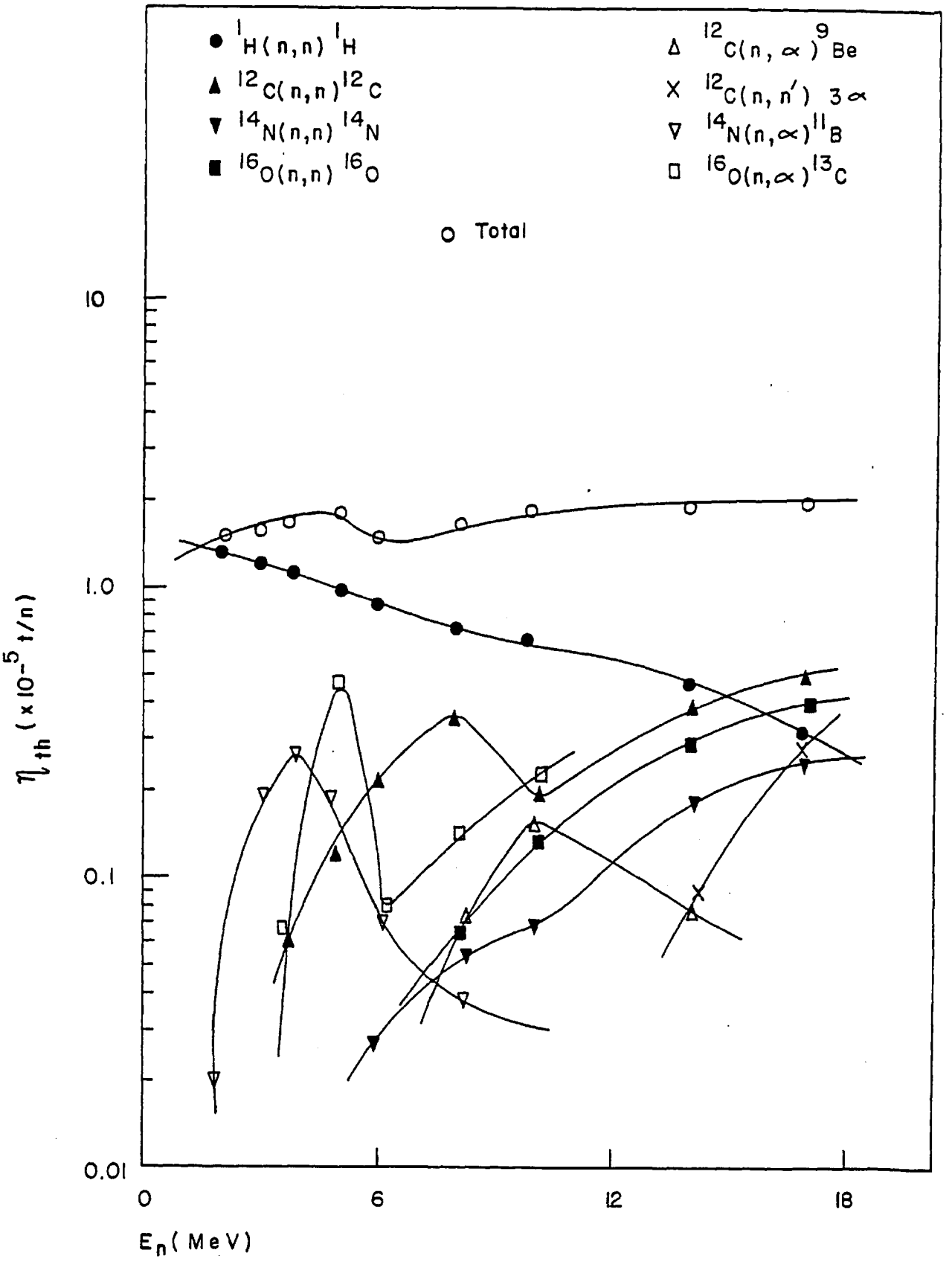


Figure 2.9 The contributions of elastic scatterings and nuclear reactions to the neutron sensitivity, η (in tracks per neutron) and total neutron sensitivity of CA80-15 as a function of neutron energy

section of the fissile material[48,49]. This relationship between track density and neutron fluence arises from the fact that the fission fragment registration efficiency of most SSTRs with a small value of θ_c (critical angle for particle detection), as well as the range and energy distribution of the fission products in the common fissile materials, are quite constant.

The ranges of fission fragments in uranium metal as a function of mass number are shown in Fig.2.10[50]. From this data it is possible to calculate the neutron sensitivity of thick fission foils. Consider an uranium target of 1 cm^2 area and a thickness R equal to the range of fission fragments. This target has $\frac{NR}{A}$ atoms/cm^2. Thus the number of induced fissions will be

$$\frac{N}{A} \frac{R_L + R_H}{2} r = 2.7 \times 10^{-5} \frac{\text{fissions}}{\text{neutron-barn}} \qquad (2.7)$$

where R_L is the range of light fission fragments in uranium ($\simeq$ 11.5 mg/cm^2); R_H is the range of heavy fission fragments in uranium ($\simeq$ 9.5 mg/cm^2); N is Avogadro's number (6.025×10^{23} atoms/mole); A is the atomic weight of uranium metal (238.1 g/mole) and r is a conversion factor (10^{-24} cm^2/barn).

Referring to Fig.2.11, if one fission occurs at point F (producing two fission fragments) the probability that one fission fragment will emerge at the lower surface is

$$\frac{2\pi\ Rh}{4\pi\ R^2} \qquad (2.8)$$

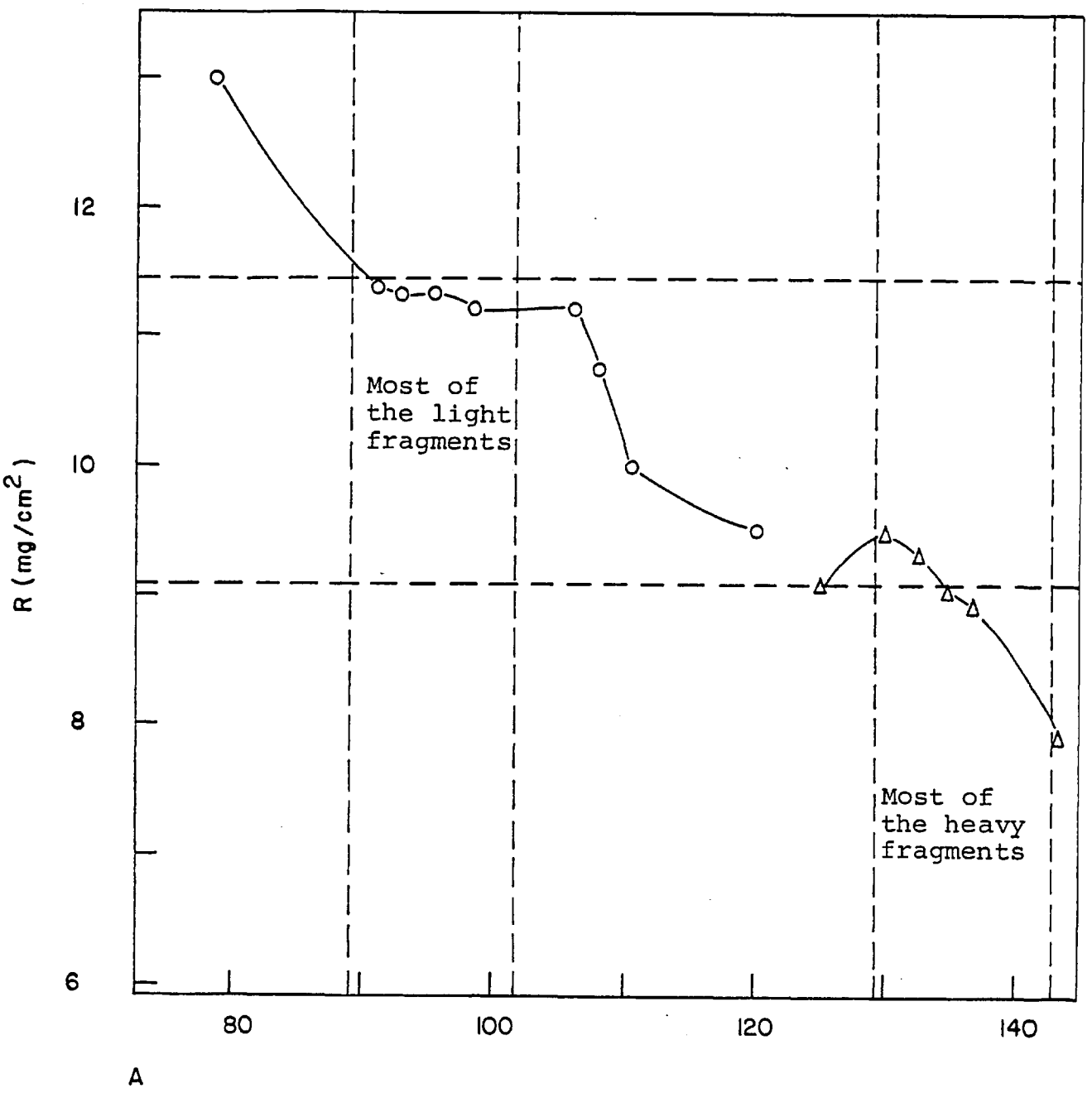


Figure 2.10 Integral range, R of fission products of ^{235}U in uranium metal as a function of mass number, A

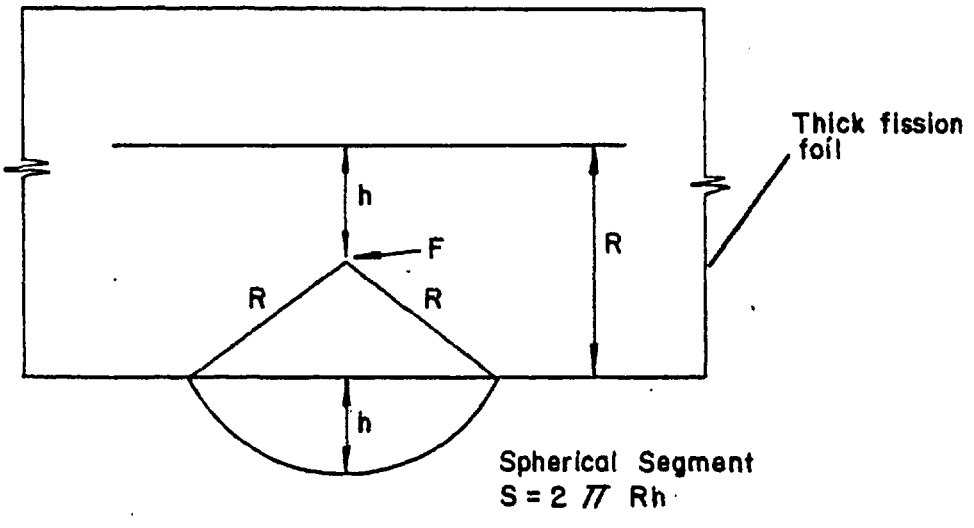


Figure 2.11 The geometry factor for thick fission foils. One fourth of all fission fragments produced within the thickness R will emerge at the surface

Assuming a uniform distribution of the fission events within this foil; the total geometry factor is

$$\frac{\int_0^R 2\pi\, Rh\, dh}{\int_0^R 4\pi\, R^2\, dh} = \frac{1}{4} \qquad (2.9)$$

The number of fission fragments which will emerge out of this thick fission foil is

$$\frac{N}{A}\ \frac{R_L + R_H}{4}\ r$$

$$= 1.4 \times 10^{-5}\ \frac{\text{emerging fission fragments}}{\text{neutron-barn}} \qquad (2.10)$$

However, not all emerging fission fragments will produce observable tracks, as due to the self absorption in the fission foil, the fragments reaching the SSTR will have a spread of energies and the tracks corresponding variety of ranges from zero up to the maximum possible. Assuming that the etching process dissolves approximately 1 μm of the plastic surface and that the fission fragment tracks must be at least 1 μm in depth to be observed, therefore in order to produce an observable track, the emerging fission fragments must have enough energy to penetrate at least 2 μm deep in the plastic. It is observed that some 90% of the emerging fission fragments fulfil this requirement[51]. Thus the neutron sensitivity of a 'thick' fission foil can be expressed as

$$1.3 \times 10^{-5}\ \frac{\text{fission fragment tracks}}{\text{neutron-barn}} \qquad (2.11)$$

The constant in the above equation has been confirmed experimentally and has also been used for the measurements of neutron cross sections[52,53].

The advantages offered by using a 'thick' foil are that the constant in equation (2.11) can be directly applied independent of fission material (^{235}U, ^{238}U or ^{238}Th) independent of neutron energy and reasonably independent of the SSTRs (assuming that fission fragment registration efficiency is about 100%; which is the case for most SSTRs). However, reduction of the thickness by a factor of five (say); will reduce the neutron sensitivity by much less than this factor due to the reduced self-absorption. A 'thickness factor' (the ratio of sensitivities of the thin and thick fission foils) can be determined from the foils less thick than the maximum range of the fission fragments and can be applied in equation (2.11) where applicable.

For SSTRs which do not record tracks at shallow angles to the surface, the numerical factor in equation (2.11) should be multiplied by $\cos^2\theta_c$. For high energy neutrons the factor is likely to be somewhat different, but uncertainties in cross sections are more serious.

Because of this proportionality between neutron detection efficiency and fission cross section, the known microscopic fission cross sections may be used for neutron energy dependence calculations of various detector combinations.

Dependence of the neutron sensitivity on the direction of neutron incidence, usually is not much of a problem.

There is some disagreement in the results reported in the literature, but the error which is introduced due to directional dependence appears to be small. According to some calculations[54], fast neutrons incident at a grazing instead of perpendicular angle result in a sensitivity drop of ≃ 12% and values up to 17 to 19% have been measured for neutrons in the 4.5 to 15 MeV range[55,56]. The directional dependence is less pronounced with polymers than with inorganic SSTRs because of the differences in the critical angle for particle detection. No directional dependence has been found for thermal neutrons, but a flux depression in thick ^{235}U foils may lead to self-shielding errors.

(i) Response of ^{238}U foil in contact with Makrofol KG SSTR

Fig.2.12 shows the microscopic fission cross sections of various isotopes for neutron energies up to 10 MeV[57]. ^{238}U has a threshold of 1 MeV but it is difficult to obtain ^{238}U completely free of ^{235}U, but only depleted. ^{232}Th has a threshold of 1.2 MeV but its cross section is even smaller than is that in the case of ^{238}U. ^{235}U and ^{239}Pu are very sensitive to thermal and epi-thermal neutrons. ^{237}Np has the best characteristics for neutron dosimetry. Its cross section falls sharply below ≃ 0.4 MeV, but has a finite cross section even for 0.1 MeV neutrons. The main drawback is its tendency to oxidise and flake in air.

One method for the detection of fast neutrons from a fission neutron source is to surround the Makrofol KG SSTR (which does not record the α-particles from the fissile material) in contact with a natural uranium foil by neutron

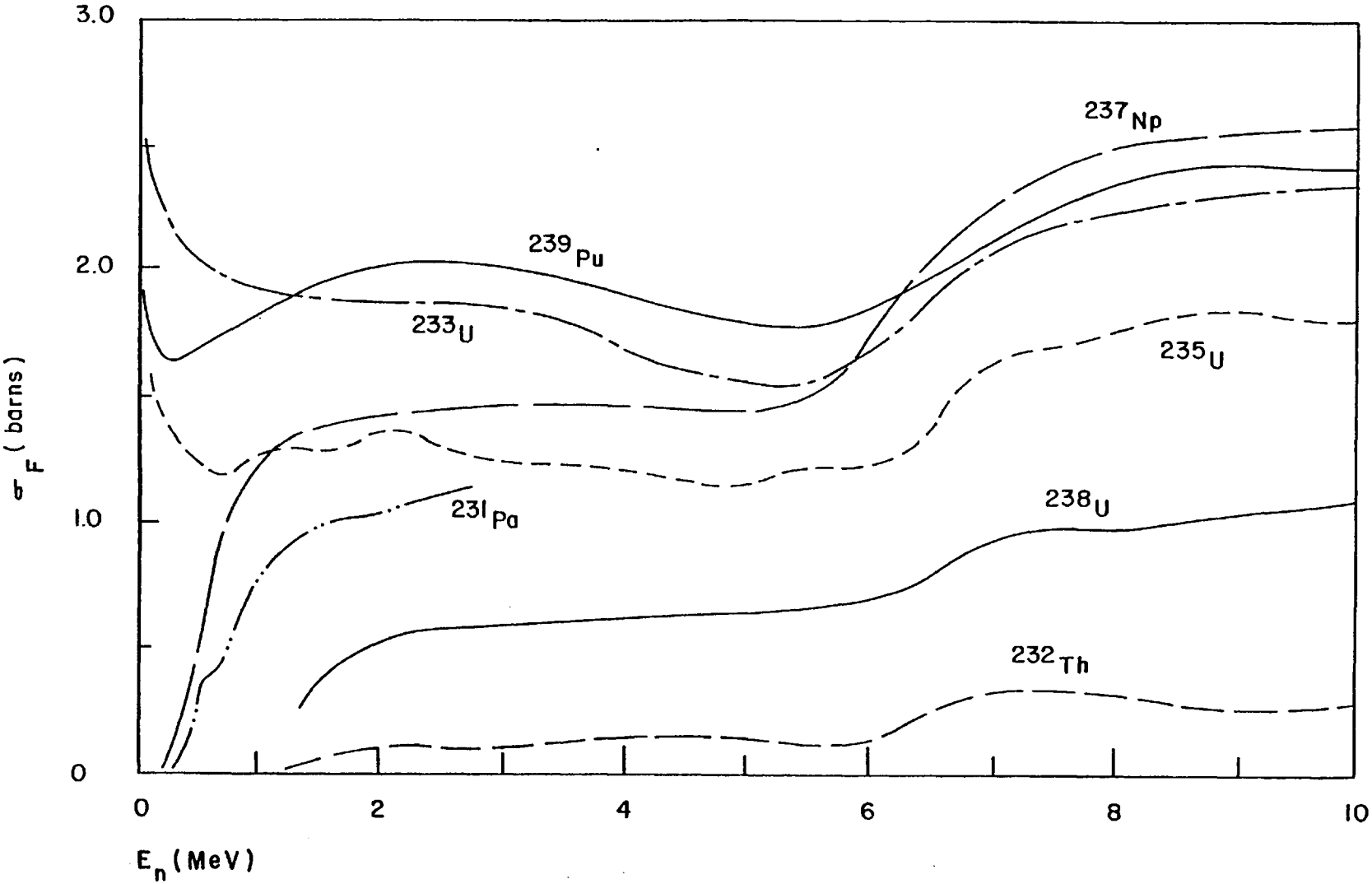


Figure 2.12 *Microscopic fission cross sections,* σ_F for various isotopes as a function of neutron energy. Data from BNL 325

absorbers. For instance by a simple cadmium shield of 0.25 to 1 mm thickness, the thermal neutron oversensitivity of such a detector can be reduced by a factor of about 12. The fission spectrum sensitivity is still reasonably high because of the contribution of resonance neutrons and neutrons above the ^{238}U-threshold.

Fig.2.13 shows the fast neutron sensitivity of ^{238}U detector combination, which was calculated using equation (2.11). The sensitivity varies according to the variation in the microscopic fission cross section of ^{238}U.

2.3.2 SSTRs with a (n,α) 'Converter Foil'

SSTRs with (n,α) 'converter foil' are not suitable for fast neutron measurements ($E_n \simeq 0.1$ MeV) due to:

(i) a rapid fall in the (n,α) reaction cross sections of the materials commonly used,

(ii) the background produced by the recoil tracks.

However, thermal and epi-thermal neutrons can be best measured by employing (n,α) reactions of ^{10}B and ^{6}Li, whose cross sections go as $(\text{velocity})^{-1}$. For a thermal neutron distribution, the cross sections are 3840 barns for ^{10}B and 940 barns for ^{6}Li.

The response function in the case of a B_4C pellet in contact with a cellulose nitrate film, in case of thermal neutrons has been studied in detail[58,59].

(i) Response of CA80-15 type B SSTR

A suitable SSTR which can be used for thermal and epi-thermal neutron dosimetry is the cellulose nitrate

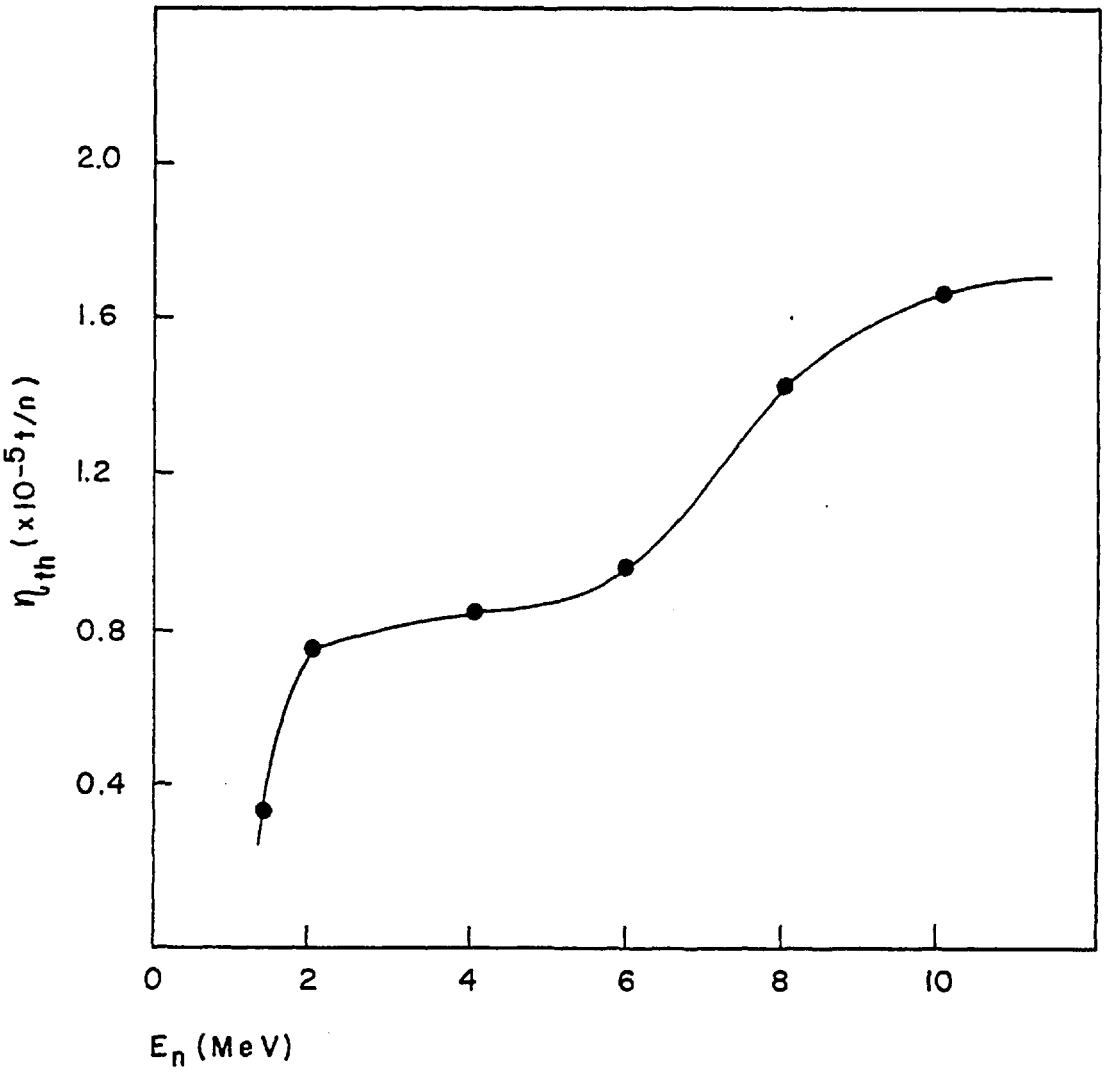


Figure 2.13 Theoretical neutron sensitivity, η_{th} (in tracks per neutron) of a 'thick' ^{238}U fission foil in good contact with a SSTR

(CA80-15, type B) film which is coated on both sides with 45 μm thick layer of lithium (natural) tetraborate ($Li_2B_4O_7$-5 H_2O). This material serves as the neutron converter with the following reactions

(i) $^{6}Li(n,\alpha)^{3}H$ Q = 4.8 MeV

(ii) $^{10}B(n,\alpha)^{7}Li$ Q = 2.3 MeV, excited state

Q = 2.8 MeV, ground state

A certain percentage of the charged particles produced as a result of these reactions reaches the cellulose nitrate film. The sensitivity to thermal and epi-thermal neutrons depends on the absorption cross sections and the energy of the particles reaching the surface of the film. The response functions in this case are quite similar to those described in Sections 2.2.2 and 2.2.4. The neutron sensitivity in the case of thermal neutrons expressed as tracks per neutron can be written as

$$T = C\left[N_B\sigma_B(th) + N_{Li}\ \sigma_{Li}(th)\right] \qquad (2.12)$$

where, σ_B and σ_{Li} are the microscopic absorption cross sections for ^{10}B and ^{6}Li at thermal energy. N_B and N_{Li} represent the number of atoms of ^{10}B and ^{6}Li per unit volume. The coefficient 'C' takes into account the distance in the converter at which the α-particle is emitted and the efficiency of α-particle detection in cellulose nitrate.

It is quite evident that only those particles reach the cellulose nitrate film which are ejected within a cone of side equal to the range of the particles and its basal

plane on the detector-converter interface. This makes the coefficient 'C' equal to half the range of particles in the converter material.

The neutron sensitivity in case of epi-thermal neutrons expressed as tracks per unit area can be written as

$$T = C \left[N_B \int_{0.4\ eV} \sigma_B(E_n)\,\phi(E_n)\,dE_n + N_{Li} \int_{0.4\ eV} \sigma_{Li}(E_n)\,\phi(E_n)\,dE_n \right] \qquad (2.13)$$

where the lower energy limit corresponds to the cadmium cut off for thermal neutrons. The upper energy limit depends on the neutron spectrum and the cross sections of the reactions.

Equations (2.12) and (2.13) give sensitivites of 1.2×10^{-3} and 3.65×10^{-4} tracks per neutron, in the case of thermal and epi-thermal neutrons (0.4 eV to 1 keV) respectively.

2.4 CONCLUSIONS

With reference to the response of SSTRs to neutrons, the following summarised conclusions can be drawn from the present theoretical treatment.

(i) The response function for the neutron detection efficiency in the case of 'intrinsic' SSTRs has been shown to be due to a large number of different neutron interactions. Clearly the presence of hydrogen in the detector is important since recoil protons make a

significant contribution to the total response even at high neutron energies. If a particular SSTR is to be used in the field of reactor physics for reaction rate measurements then some knowledge of neutron spectrum would be required since the response is energy dependent.

(ii) The energetical dependence of response functions of the SSTRs with 'converter foils' are given by the energetical evolutions of (n,f) or (n,α) reaction cross sections, which makes it easier to analyse this type of SSTRs as a function of neutron energy.

(iii) For a fission neutron source an 'intrinsic' CA80-15 SSTR has higher neutron sensitivity than a Makrofol KG SSTR in contact with a 'thick' ^{238}U foil. On the other hand it is easy to evaluate an etched SSTR with fission fragment tracks than with a mixture of different tracks (discussed in detail in Chapters on experimental results).

CHAPTER 3

MATERIALS AND PRELIMINARY EXPERIMENTS

3.1 INTRODUCTION

This chapter is divided into three major sections. The first section deals with preliminary experiments to select a dielectric material capable of recording the particles of interest. The latter had to provide under certain etching conditions, with tracks clear enough, so that automatic counting techniques were feasible with high accuracy. Various properties of the selected materials namely cellulose nitrate and polycarbonates are discussed with a view to understanding the effects of radiation and the important process of track formation, as well as the chemical etching of latent tracks. Alkaline degradation is treated in addition because of its great importance in the alkaline etching process, which is the standard technique for revelation of charged particle tracks in the various polymers employed in track recorder work.

The second section of this chapter deals with the track development by means of chemical etching. The studies reported in this section were motivated by the need to better understand the variables that control the track etch process. The major part of this work centres around cellulose nitrate (CA80-15) and polycarbonate (CR-39) which were chosen for this study.

Different optical techniques for the observation of tracks and the track counting conventions are described in the third section of this chapter. Finally, some conclusions

are drawn on chemical etching of latent tracks which could be used to optimise the etching conditions for a particular application of SSTRs.

3.2 SSTR MATERIALS FOR NEUTRON DETECTION

A wide variety of dielectrics, including minerals such as mica[8], natural and artificial inorganic glasses[9], and organic polymers[10] have been used as SSTRs. Polymers such as cellulose acetate, cellulose nitrate and polycarbonate have proved to be the most sensitive, permitting the detection not only of heavy, densely ionizing particles, but also of light particles such as alphas and protons. Only if the stopping power is greater than $\sim$ 15 MeV cm^2/mg can tracks be detected by etching in inorganic media. By contrast, all organic polymers which have been tested record particles of stopping power less than $\sim$ 4 MeV cm^2/mg and some cellulose derivatives as low as $\sim$ 0.35 MeV cm^2/mg. Therefore, it was decided to use polymers as the SSTR material for fast neutron detection.

Four polymers were studied with regard to their suitability for fast neutron detection, viz:

(a) Cellulose acetate butyrate (CAB)

(b) Cellulose tri acetate (CTA)

(c) Cellulose nitrate (CN)

(d) Makrofol polycarbonate (PC)

Films were irradiated using a ^{252}Cf-neutron source and they were compared according to the following criteria:

Reproducibility of tracks:

The low stopping power, (dE/dx) for recoil protons and alpha particles places them close to the limit of detectability for charged particles. Any change in the material composition or mode of manufacture is likely to change the sensitivity to the particles of interest. CAB was found to be particularly prone to variability of this type and was eventually rejected for this reason.

Clarity of tracks and ability to count the tracks automatically:

The proton and other recoil tracks produced in 'intrinsic' SSTRs are mostly an order of magnitude smaller than fission-fragment tracks, which makes their observation and counting difficult. This is valid as long as the same plastic and standard etching conditions are employed. The tracks in CTA were found to have insufficient contrast for reproducible automatic counting (see Chapter 7). In addition CTA films had a tendency to buckle severely after etching which made automatic counting almost impossible.

Low background count:

The quality of the etched surface must also be considered. In some materials etch-pits form during etching that are not caused by ionizing particles. These pits may be indistinguishable from short recoil tracks. Where accurate counting is desired (as in the present work), such materials are not adequate. Further, the latent tracks must etch out such that $V_T/V_B >> 1$, where V_T is the etch rate along the particle path in the SSTR, and V_B is the bulk etch rate of the SSTR. If the above condition is not

met, two significant things occur. First, track registration becomes a strong function of the angle of impingement of the particle on the SSTR. Detector sensitivity is impaired and mathematical handling (see Chapter 2) of the problem becomes difficult. Second, the tracks which are recorded may be in poor microscopic relief, making track counting less reliable.

The material found to closely meet the above critera for fast neutron detection without using any 'converter foil' is the cellulose nitrate, CA80-15[60], a Kodak-Pathé film, which is of 100 μm thickness and is weakly coloured red. The low registration threshold value ($dE/dx \simeq 0.4$ MeV cm^2/mg) makes it sensitive to a wide range of particles produced in neutron interactions with its constituents, thus leading to a high sensitivity. (Kodak-Pathé has recently introduced a colourless cellulose nitrate film, CN-85[61], which has the same chemical composition as CA80-15 films).

CA80-15 films are not suitable for neutron detection using (n,f) reaction, as they also record alpha particles from the fissile foil in contact with the film, which sometimes exceeds the number of fission-fragment tracks thus making counting difficult. Therefore, in the case of (n,f) reactions, it was decided to use Makrofol K.G polycarbonate, a Bayer film, which is of 60 μm thickness and is weakly coloured green[62].

A recently discovered SSTR, CR-39 polycarbonate[63] (colourless, 600 μm thick and manufactured by Pershore

Mouldings) was also included in the investigation in the latter stages of the programme.

3.2.1 Polymers (Cellulose Nitrate and Polycarbonate SSTRs) Chemistry and Radiation Effects

A polymer is a large molecule built up by the repetition of small simple chemical units. The word itself, is derived from the Greek roots 'meros' meaning parts, and 'poly' meaning many. In some cases the repetition of the chemical units is linear, such as a chain is built up from its links. In other cases the chains are 'branched' or interconnected to form three-dimensional networks. The 'repeat unit' of the polymer is usually equivalent or nearly equivalent to the 'monomer' or starting material from which polymer is formed. The length of the polymer chain is specified by the number of repeat units in the chain. This is called the degree of polymerisation (DP). The molecular weight of the polymer is the product of molecular weight of the repeat unit and the degree of polymerisation[64].

In terms of chemical composition, there are two broad types of polymers, one having the same repeating building-block unit throughout their molecules, and the others have two or more different building-block units regularly or irregularly distributed throughout their length[64].

(i) Cellulose Nitrate (CA80-15 SSTR)

Cellulose

Cellulose is a naturally occurring carbohydrate which is present as the chief constituent of the cell wall in all

plants. The main sources of commercial cellulose are cotton linters and wood pulp[65]. The empirical formula of cellulose is $\left[C_6H_7O_2(OH)_3\right]_n$. The structural formula is shown in Fig.3.1(a). Cellulose is thus composed of a large number 'n' of anhydroglucose units joined together by ether linkages. The molecular weight of the anhydroglucose units is taken as 162 with end groups and trace substituents in the cellulose assumed to be negligible. The average number of anhydroglucose units in the molecule is several thousand for most native celluloses[66]. Cellulose is considered to be a long, linear polymer of united rings as shown in Fig. 3.1(a). It occurs in a fibrous form having a specific gravity of about 1.50-1.55, and an index of refraction of 1.6 along the fibre and 1.5 perpendicular to it. It is thought that the cellulose fibres are built up of bundles of long molecules, held together in a more or less parallel alignment by intermolecular secondary valence forces due to the highly polar hydroxyl groups. The electric field configuration between neighbouring chains is conductive to their parallel orientation. The crystallites are called micelles. The minimum dimensions of the micelle are thought to be 60-70°A wide and 600°A long. Individual chain molecules may traverse many micelles, resulting in an interlocking assembly of parallel micelles or submicroscopic crystallites. According to x-ray measurements cellulose is about 70 percent crystalline. Cellulose is insoluble in all organic solvents, has no melting point, and is fairly resistant to thermal degradation.

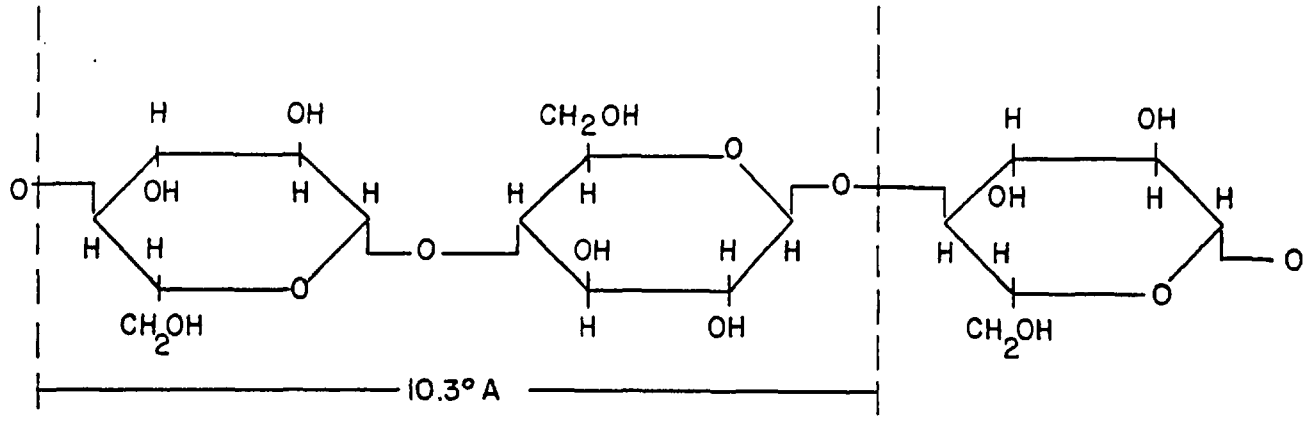


Figure 3.1(a) The structural formula for cellulose. Three hydroxyl groups are shown in each of the anhydroglucose units, the latter being joined by ether linkages

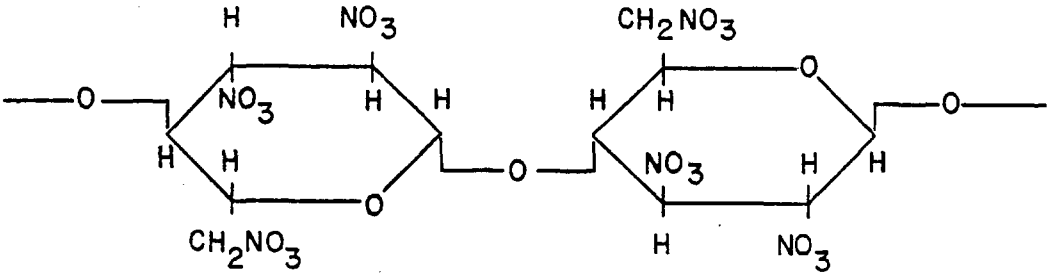


Figure 3.1(b) The structural formula for cellulose trinitrate

Cellulose Nitrate

(a) Chemical composition

Cellulose nitrate is a condensation polymer produced by the esterification of cellulose with nitric acid in the presence of a catalyst, usually sulphuric acid. The hydroxyl ions are replaced by the nitrate ions, according to the following formula for complete nitration.

$$C_6H_7O_2(OH)_3 + 3HNO_3 \xrightarrow{H_2SO_4} C_6H_7O_2(NO_3)_3 + 3H_2O \qquad (3.1)$$

The most important function of sulphuric acid is its role as a dehydrating agent for the additional undesirable water formed in the nitration reaction. Sulphuric acid also functions as a swelling agent, allowing initial entry of the nitrate groups and influences the degree of substitution or nitrogen content.

The structural formula of cellulose nitrate is shown in Fig.3.1(b). The degree of substitution (DS) is defined as the average number of hydroxyl groups replaced per anhydroglucose unit and varies between 0 and 3. In principle it should be possible to replace all three hydroxyl groups in each anhydroglucose unit with nitrate groups to give cellulose trinitrate. Such a product having a DS = 3, would contain 14.14% nitrogen. In practice, the practical upper limit for substitution is about 2.9, corresponding to a nitrogen content of 13.8%. Cellulose nitrate with a nitrogen content of about 11% is used in plastics. If the nitrogen content is less than 10%, the material is insoluble and not useful.

(b) Physical structure

The physical state of cellulose nitrate is intimately related to the forces between molecules and to the molecular length, shape and symmetry. The covalent atomic bonds confer electrical and thermal resistance, rigidity and hardness. Commercially available cellulose nitrate varies in viscosity from 18 cps to about 7.4×10^7 cps. The approximate relation between viscosity in centipoises (cps), molecular weight and DP is given in Table 3.1.

Although considerably less crystalline than the parent cellulose, cellulose nitrate possesses, in general, short range order. X-ray and electron diffraction studies amply support this view[67]. The extent of crystallinity depends on many factors, such as the degree of nitration and the exact conditions and manner of sample preparation. Cellulose nitrate is more naturally crystalline in the trinitrate state than in the less nitrated states. However, as the degree of nitration is increased towards the pure cellulose form, the polymer becomes more crystalline again. The extent of crystallinity has a definite influence on the mechanical properties of the material.

(c) Cellulose nitrate plastic

Cellulose nitrate is only one of the constituents of cellulose nitrate plastics. In order to improve or otherwise, alter the properties of the basic material, various modifiers, such as plasticizers, resins and pigments are added. Small amounts of solvent, left over from sample preparation, are also generally present. The presence of these substances affects the chemical and physical behaviour of the plastic.

TABLE 3.1

APPROXIMATE RELATION BETWEEN THE VISCOSITY, MOLECULAR WEIGHT AND THE DEGREE OF POLYMERIZATION OF CELLULOSE NITRATE

Viscosity (Cps)	Molecular Weight	Degree of Polymerization
92.5	22,000	74
11,100- 14,800	68,000	229
222,000-370,000	140,000	471

TABLE 3.2

MECHANICAL, PHYSICAL AND ELECTRICAL PROPERTIES OF PLASTICIZED CELLULOSE NITRATE FILMS

Specific gravity	1.35 - 1.60
Refractive index	1.5
Thermal conductivity	(3.1-5.1) x 10^{-4} (cal/sec cm ^{o}C)
Electrical resistivity at 30°C	(0.106-0.32) x 10^{10} ohm-cm
Specific heat	0.34 - 0.38 cal/^{o}C-g
Softening point	70° - 90°C
Effect of heat	Decomposition at 100-150°C
Burning rate	Very high
Effects of UV light	Discolouration, embrittlement
Effect of water	Very slight swelling

The function of the plasticizers is based on the fact that it contains groups capable of solvating particular polymer groups. The polar bond from the plasticizer is believed to be capable of neutralising or sufficiently weakening the van der Walls forces that exist between the polymer chains[65]. The addition of a plasticizer also produces swelling, the secondary valence forces are released, permitting flexing of the long linear polymer chains. The addition of these lower molecular weight materials (generally organics) to high polymers changes a hard, brittle, glass-like solid to a softer, more flexible material.

The plasticizer used in the Kodak-Pathé cellulose nitrate films (CA80-15, CN-85 and LR-115) is camphor, which is believed to be ideal in that the nitrate groups of the former interact with the ketone groups of the latter to form a molecular complex[65]. The rigid camphor molecule enforces a high degree of separation between the chains. Some of the physical properties of plasticized cellulose nitrate films are listed in Table 3.2.

(ii) Polycarbonates (Makrofol and CR-39 SSTRs)

Polycarbonate polymers are characterised by the - OCOO- heterochain unit and can be made either from phosgene and bisphenol A (4,4'-dihydroxy-diphenyl-2,2'-propane) or by ester exchange between bisphenol A and diphenyl carbonate. The structural formula of polycarbonate is shown in Fig.3.2. CR-39 polycarbonate is prepared from allyl-diglycol carbonate by polymerization in the form of highly cross-linked copolymers or intermediate products. The monomer

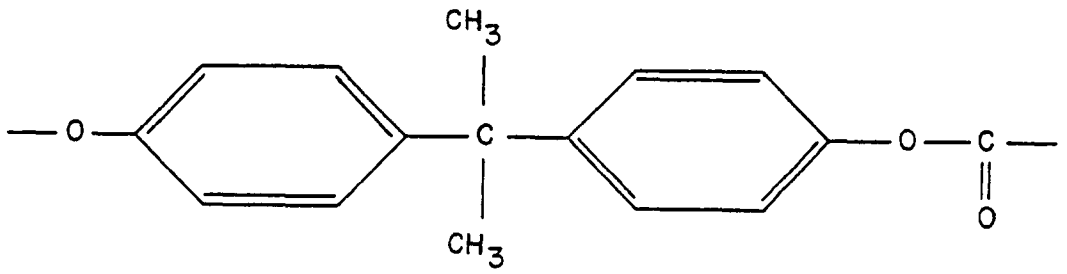


Figure 3.2 The structural formula for polycarbonates

is polymerized at temperatures (ranging from 50°-70°C) using a few percent of di-isopropyl peroxydicarbonate (IPP), as the catalytic agent.

All polycarbonate polymers are crystalline thermoplastics of good mechanical properties. They have unusually high impact strength, even at low temperatures, ascribed in part to a combination of relatively high ordering in the amorphous regions and considerable disordering in the crystalline regions[64]. They have low moisture absorption, good heat resistance (useful to 240°C), and good thermal and oxidative stability in the melt. Makrofol polycarbonate is free of plasticizers. Some of the physical properties of polycarbonate plastics are listed in Table 3.3.

3.2.2 Effects of Radiation on Polymers

The interaction of radiation with a polymer and the subsequent events that can occur can be divided into three distinct periods of time[68]. The first period, lasting less than 10^{-15} seconds, is that of energy dissipation by the incident radiation and the absorption of this energy by matter. There are three ways to absorb energy in a solid[68]:

(a) electron displacement (both ionization and excitation are included under this heading),

(b) atomic displacement, and

(c) generation of an impurty atom as a result of a nuclear reaction.

The second period, lasting anywhere from 10^{-12} to 10^{-19} seconds, involves the transport and disposition of absorbed

TABLE 3.3

MECHANICAL, PHYSICAL AND ELECTRICAL PROPERTIES OF POLYCARBONATE FILMS

Specific gravity	1.2
Refractive index	1.5
Electrical resistivity at 30°C	2×10^{17} ohm-cm
Effect of heat	Decomposition at > 240°C
Burning rate	Self-exting.
Dielectric constant at 800 C/sec	2.8
Clarity	Transparent
Tensile strength	8000 - 9000 psi

TABLE 3.4

SOME EFFECTS OF HIGH ENERGY RADIATION ON POLYMERS

1. Excitation
2. Production of unsaturation and bond rupture
3. Ionization
4. Scission of polymeric chains
5. Production of free radicals

energy by the molecular motion as the thermal equilibrium within the solid is established. Again there are three alternatives:

(a) energy can be emitted as luminescence,

(b) it can be dissipated as heat,

or (c) energy can be stored as potential energy in the form of chemically reactive species.

The path followed depends strongly on the structure of the molecule and the environmental conditions.

The third and final period is that of the establishment of chemical equilibrium. Here, the potential energy stored in the form of chemically reactive species is dissipated. Diffusion processes and reaction rates extend the duration from a minimum of about 10^{-8} seconds up to months or years.

To recapitulate, it is convenient to think of three distinct phases:

(a) energy absorption,

(b) establishment of a thermal equilibrium,

and (c) the establishment of a chemical equilibrium.

The primary mechanism for the absorption of energy deposited by charged particles is electronic and atomic displacements or nuclear reactions. Except at very low velocities of the incident particle, the predominant mechanism of energy absorption is through electron displacement, i.e. through ionization and excitation of electrons of the absorbing medium. Since polymers do not readily luminesce, the bulk of absorbed energy goes either into heat or is stored as potential energy of reactive species. The manner

in which the energy is divided between ionization and excitation depends upon the type of particle, its velocity and the state of absorbing medium. Very little is known of the number, types, or distribution of the chemically reactive species that are formed. Even less is known of the manner in which these species react with each other or with substances present in the matrix of the bulk material (such as oxygen or water).

In general, the irradiation of polymers produces either cross linkage or scission[69,70]. Cellulose nitrate undergoes scission at a rate which is considerably higher than other polymers, about 13.5 scissions per 100 eV of dose[71]. The scission reaction breaks the molecule into smaller fragments, decreasing the molecular weight, increasing the solubility, and lowering the softening point. Scission is often accompanied by gas evolution. This is particularly so for cellulose nitrate, where over 95% of evolved gas is hydrogen. The mechanical properties of polymers are also changed by scission. The shortened chains and the large number of chain ends lead to a weakening and embrittlement. Free oxygen present in matrix of the polymers is thought to play an important role in the process of scission. Instead of recombining with each other or some other portion of the polymer chain, the broken chain's ends now combine with oxygen to produce scission. Some of the known effects of radiation on polymers are summarised in Table 3.4.

Polymers containing a high percentage of aromatic rings have been found to be resistant to radiation, those

with highly aliphatic structure are the least resistant[71]. There is also a general trend for polymers with the largest molecular size to be more susceptible to radiation damage. This arises from the fact that a small number of chain scissions or cross-links can change a large percentage of the molecules. In agreement with these observations, cellulose nitrate is found to be one of the most sensitive of all polymers to high energy radiation.

3.2.3 Alkaline Etching of Polymers

It is important to understand the alkaline degradation of cellulose nitrate and polycarbonate SSTRs in order to explain the phenomenon of preferential track etching.

(i) Alkaline etching of cellulose nitrate (CA80-15 SSTR)

The nitrate groups of cellulose nitrate cannot be removed by sponification with alkali, which is the normally used procedure to remove ester groups. Instead, during alkaline treatment an oxidative degradation occurs; the nitrate groups are reduced to nitrite, and alkali soluble substances are formed[72].

Alkali acts on the sugar nitrates to convert primary and secondary nitrate groups to aldehyde and ketone groups respectively[72]:

$$RCH_2ONO_2 + KOH \longrightarrow RCHO + KNO_2 + H_2O \qquad (3.2)$$

$$R_2CHONO_2 + KOH \longrightarrow R_2CO + KNO_2 + H_2O \qquad (3.3)$$

Such reactions also occur with cellulose nitrate, and the corresponding oxycelluloses formed (RCHO and R_2CO) are

rapidly degraded by alkali[73], being extremely sensitive to alkaline cleavage of the glucosidic (ether) bonds linking them to the cellulose chain[17]. This reduces the DP rapidly and the small molecules are readily dissolved.

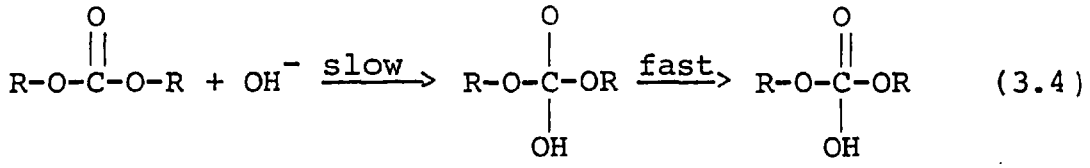
Note that it is high concentration of OH^- ions which derives the reactions (3.2) and (3.3) to completion, therefore a high pH is necessary for significant alkaline etching. Plasticizers reduce the bulk etching rate substantially[74], probably by reducing the access of the OH^- ions to the cellulose nitrate chains. However, the ability of alkalis to swell the structure aids the penetration and etching rate.

Preferential track etching is due to the much more rapid alkaline attack along the damage trail than in the bulk material. This may be understood in terms of the oxidative degradation of cellulose nitrate which occurs during the process of radiation damage. The oxycellulose along the damage trail is rapidly cleaved and dissolved by the alkali; accessibility is also considerably greater due to the broken chains in the latent track. By contrast the bulk material has first to undergo the relatively slow reactions (3.2) and (3.3) before the process of dissolution begins. Penetration of the alkali along the damage trail is also aided by the presence of acidic groups, via the process of base-exchange[75].

(ii) Alkaline etching of polycarbonates (Makrofol and CR-39 SSTRs)

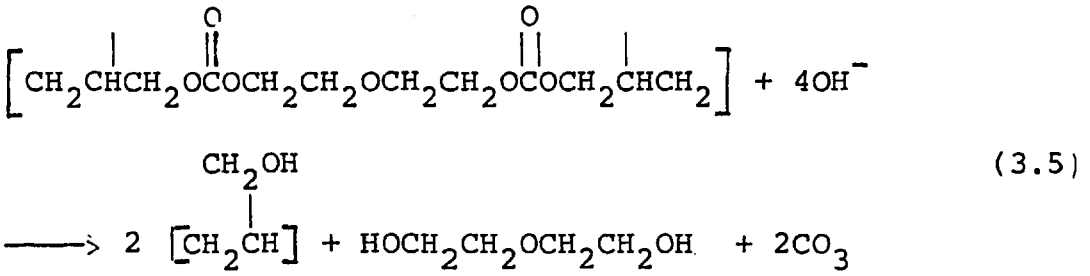
The rate at which polycarbonates are degraded by alkali is equal to the rate of cleavage of the carbonate linkages.

The rate determining step for the cleavage of the carbon ester bond is the addition of OH^- ions to the carbonyl carbon[76]:



(3.4)

The attack by OH^- results in the hydrolysis of the carbonate ester bonds in CR-39 polycarbonate and can be represented as follows:



(3.5)

The lines extending from the CH groups in the uncleaved polymer indicate where crosslinking to other chains can occur[77], thus giving CR-39 its network structure. The organic etch products are poly-allylalcohol (PAA) and 2,2' oxidiethanol. Additional etch products can arise from incomplete conversion of the double bonds in the monomer and from the catalyst used for polymerisation[77].

The alkaline etching of a bisphenol A polycarbonate such as Makrofol, where phenol is a common etch product, is inherently simpler than CR-39, since cleavage of one or two carbonate linkages can release the bisphenol A anion from a chain of the polymer, whereas, for a fragment of PAA to be released, all the carbonate linkages binding the fragment to the CR-39 network must be hydrolysed.

3.3 CHEMICAL ETCHING OF LATENT TRACKS

The method consists of immersing the irradiated SSTRs in a suitable chemical reagent. The reagent must be capable of slightly etching the bulk material, while at the same time preferentially attacking the particle damage trails. In the case of cellulose nitrate and polycarbonates, a strong hydroxide such as sodium hydroxode is normally used. Bulk etching enlarges the track region to the point, where it becomes visible under an ordinary light microscope.

The etching process can be affected in a complex way by a large number of variables including the exact composition and history of the SSTR and the type, concentration and the temperature of the etchant. Orientation of the surface, agitation of the etchant, as well as the presence of impurities may alter the etching behaviour.

Development of charged particle tracks by means of chemical etching is, in principle, similar to that of the chemical etching of dislocations in crystals[78]. Tracks are linear imperfections with a diameter less than about $100^{o}A$[79]. For track development the rate of chemical attack of the particle damage trail, V_T must be greater than that of the bulk material, V_B i.e. V_T/V_B (etch rate ratio) > 1. It is an important parameter which is used to denote the degree of preferential etching.

Under ideal conditions (absence of diffusion effects, homogeneous track recording material) the etched tracks are conical in shape, with sharp terminal ends. The quantity θ, one half of the cone angle, is given by[79]

$$\theta = \sin^{-1} V_B/V_T \qquad (3.6)$$

As etching proceeds, the vertex of the cone remains sharp until it reaches the point, where the particle came to rest, further etching causes the apex to become rounded (see Fig.3.3).

Not all of the particle damage trails (latent tracks) which intersect the surface of the recorder can be developed through the chemical etching technique. In order to produce a latent, etchable track, a charged particle must have a rate of energy loss above a certain critical value, characteristic of that material. The quantity V_T/V_B is a function of the rate of energy loss of the charged particle, increasing as the rate of energy loss increases. For lighter ionizing particles $V_T/V_B \longrightarrow 1$, and tracks are not observed. There is also a geometrical restriction, latent tracks making an angle less than $\theta_c = \sin^{-1} V_B/V_T$ with the surface will not be seen because the surface dissolves more rapidly than the tracks can deepen[11] (as discussed in the following section). Thus it is desirable to have the etch rate ratio as large as possible.

The bulk etch rate, V_B is sensitive to a large number of variables such as the exact composition of the recorder and the type of etchant and the etching conditions. At the same time, the track etch rate, V_T is also a function of the type and the velocity of the charged particle that produced the damaged trail. Thus the quantity, V_B provides information with regards to the chemistry of the sample and of the

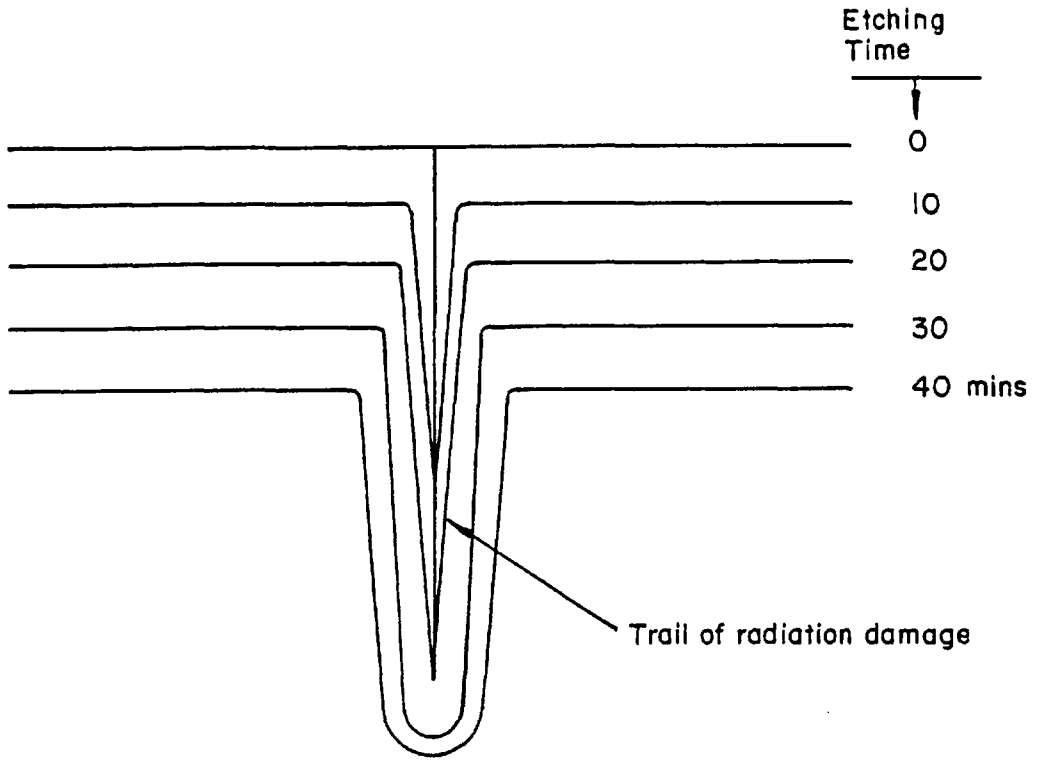


Figure 3.3 Cross-sectional view of a typical track after different etching times. The best etching time is 20 minutes. With longer etching, the track will no longer increase in length, but only in width

etching process, while V_T also provides information about the charged particle. In order to understand the track etching process, it becomes necessary to study the effects of various parameters on V_B and V_T individually as well as on V_T/V_B.

3.3.1 Critical Angle for Track Detection

The critical angle for track detection, θ_c is defined as the smallest angle of incidence of a particle to the surface of the SSTR, which will leave an observable track after etching.

Consider a track shown in Fig.3.4 , which is obtained after etching for time, t. V_T and V_B have the usual meanings and R' is the residual track length. Now

$$R = V_T\, t \tag{3.7}$$

$$\begin{aligned} L' &= L - V_B\, t \\ &= R \sin\theta - V_B\, t \\ &= R\,(\sin\theta - V_B/V_T) \end{aligned} \tag{3.8}$$

$$R' = L'/\sin\theta \text{ and } R'p = L'/\tan\theta$$

For small angles, $\tan\theta = \sin\theta$

$$\therefore\ R'p = L'/\sin\theta \tag{3.9}$$

Equation (3.8) must be positive if a track is to be observed. Therefore, the critical condition for track detection is

$$\sin\ \theta_c = V_B/V_T$$

For angles of incidence less than arc sin (V_B/V_T), the surface is removed at a greater rate than the normal component of V_T, and therefore no track is observed.

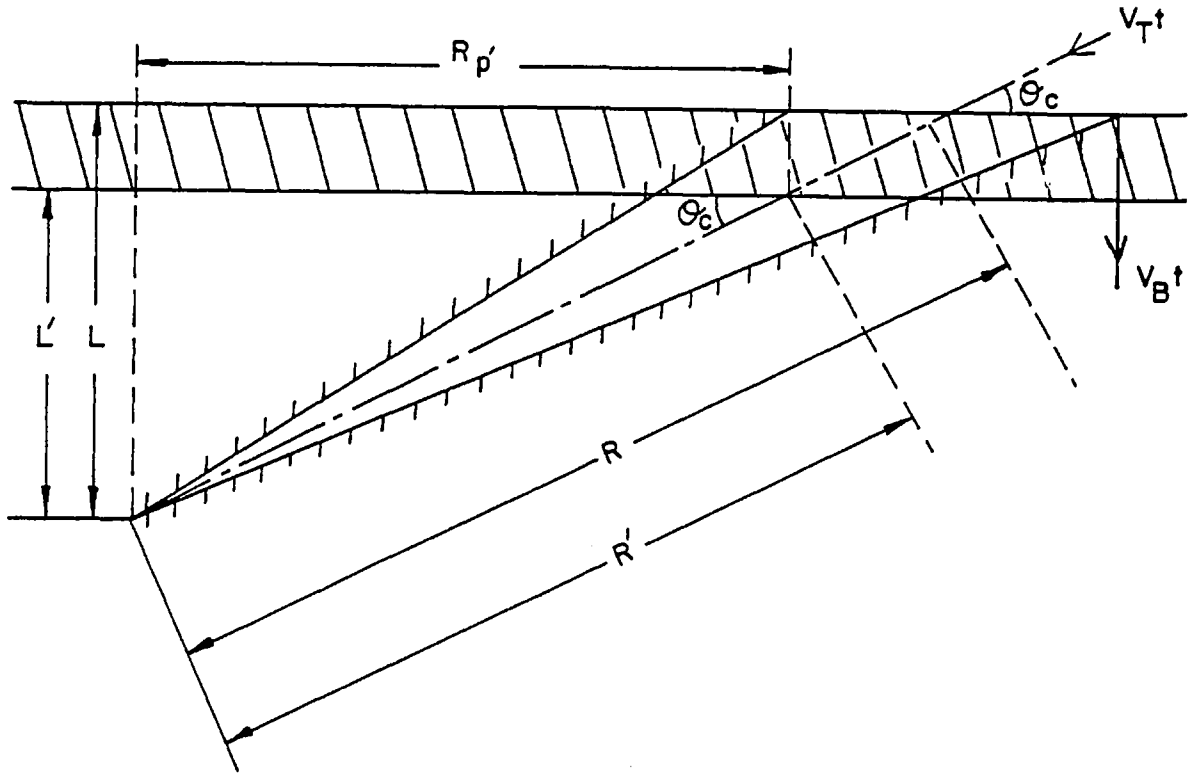


Figure 3.4 Diagrammatic representation of an etched track. The critical angle for track detection is given by the relation, $\theta_c = \sin^{-1} V_B/V_T$

3.3.2 Etching Efficiency

In the case of 'intrinsic' SSTRs, where particle tracks originate throughout the volume of the detector, tracks that may be revealed by etching originate at depths ranging from O to H (see Fig.3.5), where H is the maximum depth from which a particle may start and still produce an etchable track. Those from depth, H must all have travelled normal to the surface to have reached it, and those at a depth, δ can arrive at angles between arc sin (δ/H) and 90°. Because, in order to be etched at the surface, the angle to the surface must be greater than θ_c, all of the tracks from a given depth will be etched as they cross the surface provided $\delta > H \sin \theta$. For $\delta < H \sin \theta$, some of the tracks are inclined at less than θ_c, to the surface and are therefore not revealed by etching[11]. The situation is illustrated in Fig.3.5, in which the line, BD represents the fraction of the tracks in the upward hemisphere of solid angle that reach the surface and ACD (which bounds the shaded area) represents the fraction that is etchable. Simple geometry given in Fig.3.5, shows that the fraction of tracks reaching the surface but not revealed by etching is just the ratio of the two triangles ABC/OBD, which is $\sin^2 \theta$. Alternatively, the fraction revealed is $1 - \sin^2 \theta_c$ ($= \cos^2 \theta_c$).

3.3.3 Etching Experiments

(i) The etching apparatus

The etching apparatus consisted of glass test tubes containing the alkaline solutions with a rubber cork. It was chosen because it is resistant to attack by the etchant and

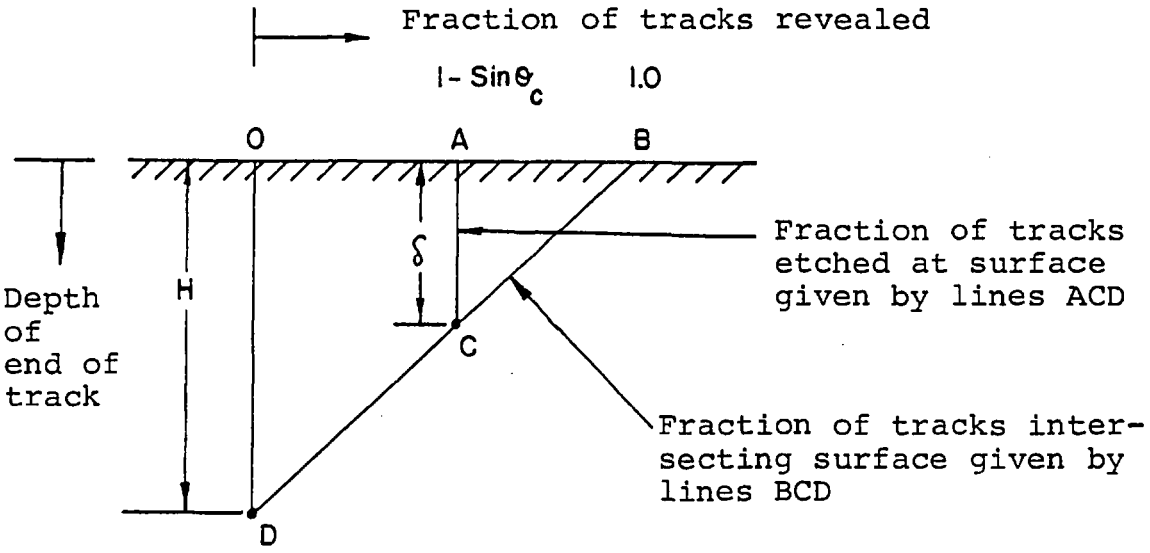


Figure 3.5 The fraction of a random distribution of tracks of length, L that is revealed by a short etch as a function of the depth of the lower end of the track. The fraction is constant at a depth, δ and then decreases linearly to zero at depth L. A fraction $\cos^2\theta$ of tracks that intersect the surface is revealed by etching

is readily available. The use of the cork is necessary because of the heat conduction and to keep the concentration of the solution unvaried during the etching process due to evaporation.

The test tubes were suspended in a water bath which was heated by an electric coil. The water level in the bath was kept at a constant height. The current of the coil and the subsequent heat could be adjusted by a variac. The temperature of the water bath was controlled by means of a thermostat. The accuracy of the regulator was so good that the temperature recorded did not vary more than $\pm$ 0.1°C.

(ii) The etching procedure

After placing the test tubes containing the etchant in the water bath, it was necessary to wait for about 15 minutes so that the solution acquires the specified temperature. The accuracy of the alkaline etchants was controlled by titration to within $\pm$ 0.05 N.

It was found that by floating the recorder on the surface of the solution, some bubbles accumulate under the irradiated side and cause some spots on the film surface, which in some cases, could not be easily distinguished from the tracks. Therefore, the films were kept vertically in the etching solution to allow the bubbles to come out and have no or less effect on the films. Stirring of the etchant was found to be not useful since it favours the bulk etch rate, V_B over the track etch rate, V_T.

When the films had been etched they were removed from the etchant and placed in a stop bath of diluted acetic acid (1%) for a few minutes to prevent further etching. Afterwards the films were washed in distilled water, dried in a dessicator and mounted on microscope glass slides (0.8 - 1.0 mm thickness) along with glass cover-slips ($\sim$ 0.1 mm thickness) with narrow sellotape for examination under optical microscope.

(iii) Measurement of bulk and track etch rates (V_B and V_T)

The bulk etch rate, V_B was measured in two ways:

(a) Thickness measurements of the SSTR before and after etching, i.e.

$$V_B = \frac{\Delta x}{\Delta t} \qquad (3.10)$$

where Δx = thickness dissolved and Δt = etching time interval.

The change in the film thickness was determined by two methods:

(i) by focussing the microscope on the two surfaces of the detector before and after etching, and

(ii) by a high resolution thickness measuring device, Universal S.I.P. 214 B (shown in Fig.3.6).

(b) Diameter measurements of vertically incident 0.60 MeV alpha particles. As $V_T >> V_B$, the diameter of alpha particles can be treated as

$$d_\alpha = 2\ V_B t \qquad (3.11)$$

for a given etching time 't'.

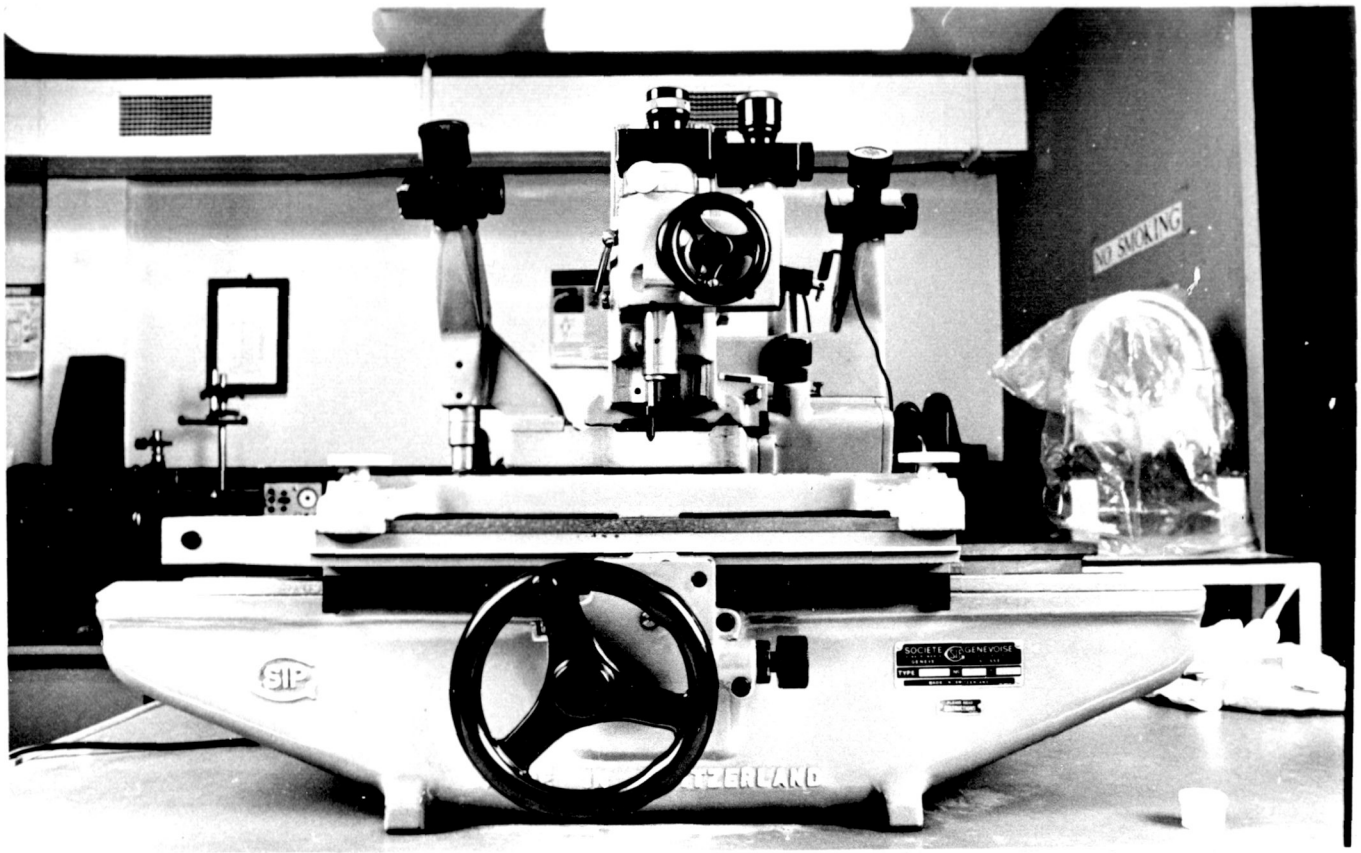


Figure 3.6 High resolution thickness measuring machine (Universal S.I.P.214B), used to measure the change in the SSTR thickness to determine the bulk etch rates, V_B of CA80-15, CR-39 and Makrofol K.G.

The confirmity of these two kinds of measurements was checked for CA80-15 in 2.5 N NaOH at (60 ± 0.1)°C and was found to be within the systematic errors. The thickness measurements are more convenient for high etching rates, while the diameter method is reliable only up to diameters of about 6 μm.

The track etch rate, V_T was measured by irradiating CA80-15 and CR-39 SSTRs with 6 MeV alpha particles with a low angle of incidence (10°) to the surface of the detector. The alpha particles were available from the Harwell Van de Graaf (see Chapter 4). V_T was then determined by measuring the projected length of the track at various etching times and a correction was made for the loss of bulk material during etching.

3.3.4 Results and Discussion (Effects of the Etchant Temperature and Concentration on V_B, V_T and V_T/V_B)

(i) Cellulose nitrate (CA80-15 SSTR)

The bulk etch rates of CA80-15 as a function of NaOH and KOH concentration at 19°C, 31°C and 60°C are shown in Fig. 3.7(a) and (b). All curves saturate at different concentrations for NaOH and KOH. The lower the temperature, the lower is the concentration where the curve starts levelling out.

The plateau bulk etch rates in NaOH for a given temperature are lower than those in KOH. This indicates that KOH etches better than NaOH for the same etchant concentration and temperature. The fast etch rates in KOH can be explained

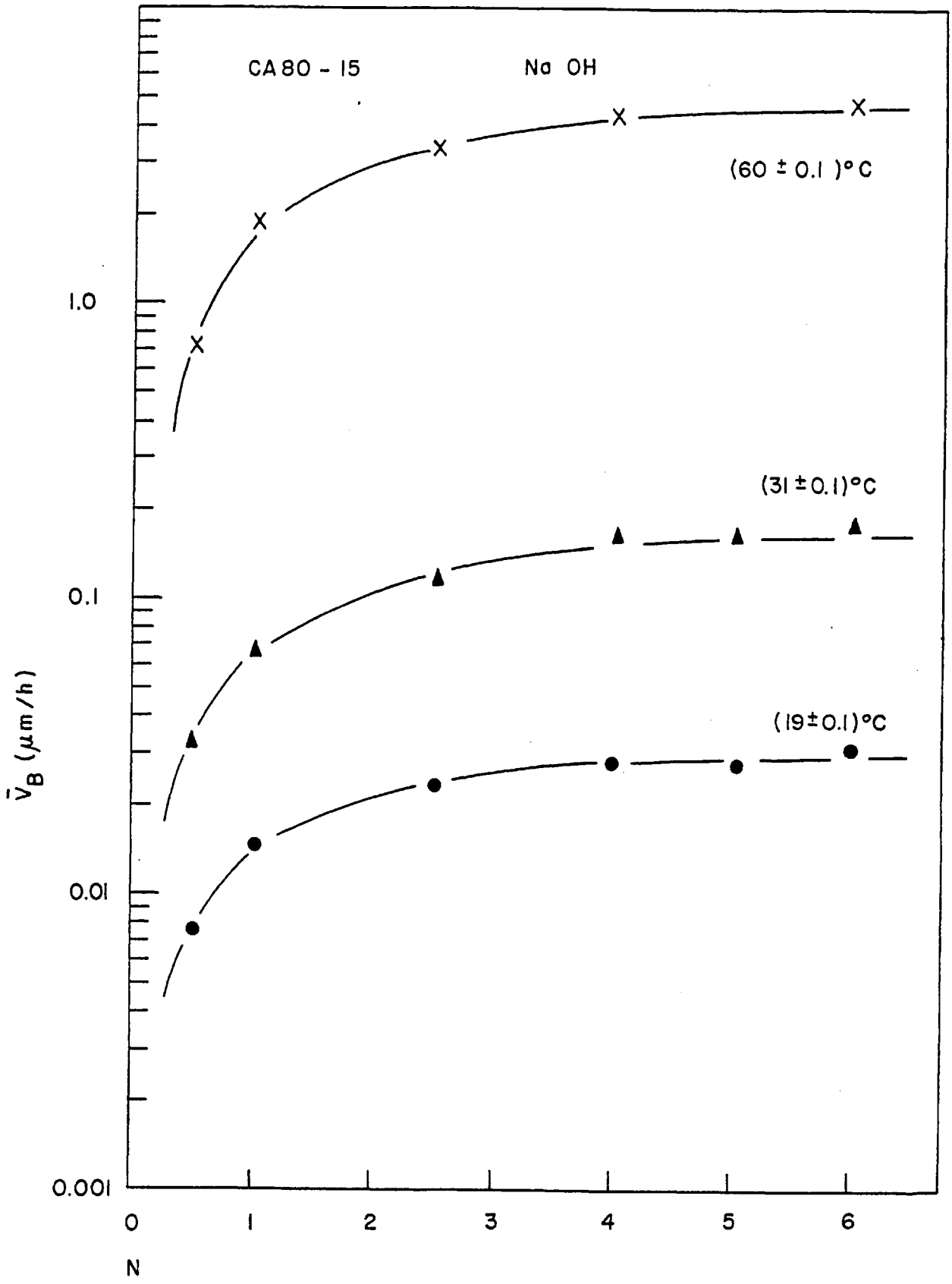


Figure 3.7(a) Average bulk etch rate, $\bar{V}_B$ of CA80-15 as a function of NaOH concentration, N (normals) at 19°C, 31°C and 60°C, without etchant stirring

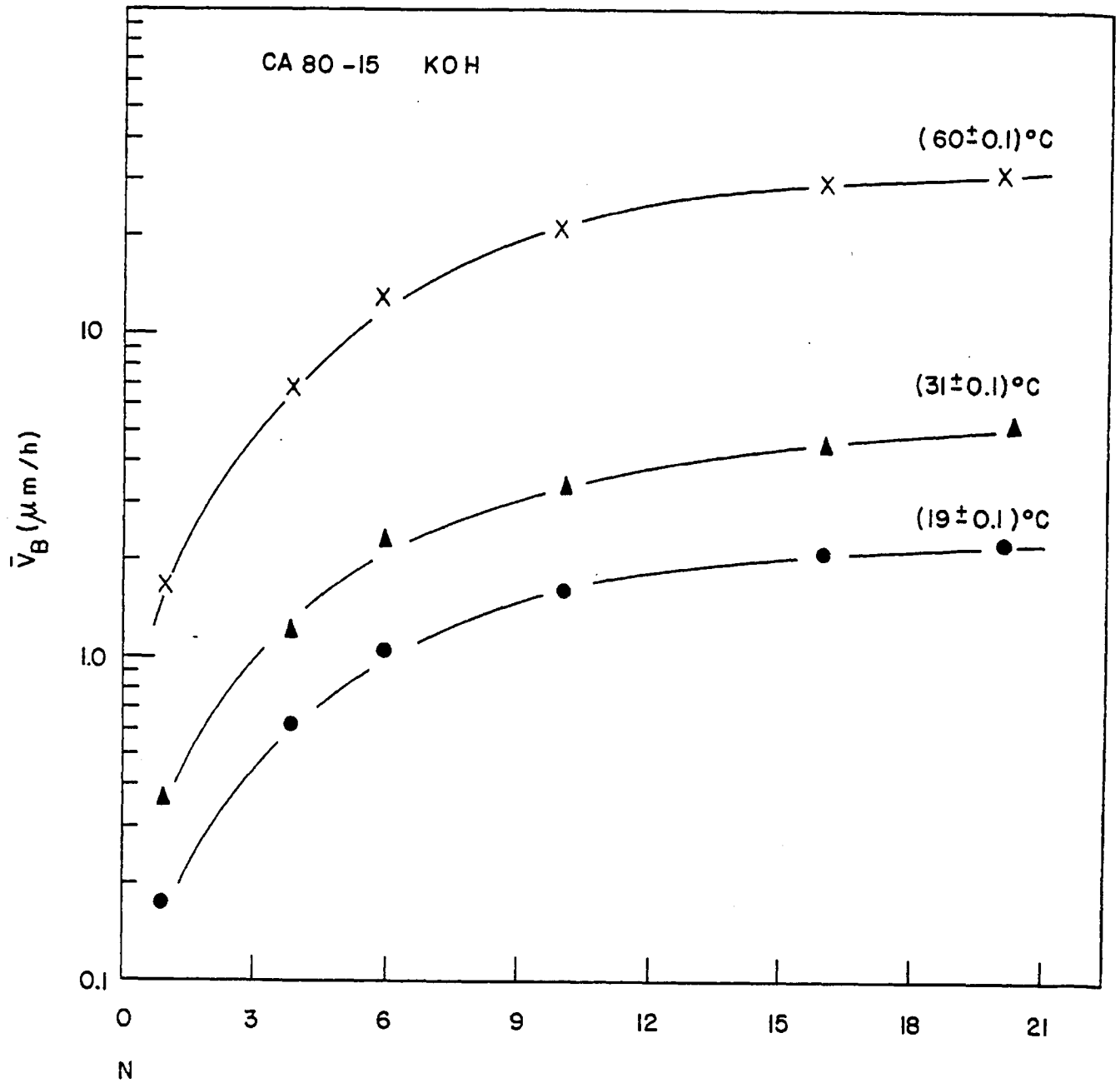


Figure 3.7(b) Average bulk etch rate, $\bar{V}_B$ of CA80-15 as a function of KOH concentration, N(normals) at 19°C, 31°C and 60°C; without etchant stirring

by considering the radii of K^+ and Na^+-ions in aqueous solutions (see Table 3.5). These radii lead to different hydration number (the number of water dipoles around these ions) and therefore to reactions of different strengths. The small K^+-ion with fewer water dipoles is more mobile than Na^+ ions and therefore reacts faster.

It was observed that during etching of cellulose nitrate, a thin colloidal layer of degraded cellulose nitrate molecules and plasticizer, together with the components of the etching solution is formed on the surface of the plastic[80]. This layer was found to dissolve in water when disturbed. The existence of this layer may affect the bulk etch rate of the plastic and contribute to the plateaus of Fig.3.7.

The effect of the plasticizer (camphor) in cellulose nitrate is quite important. Since camphor is neither attacked nor soluble in etchants, (as shown in Table 3.6) therefore, its buildup at the surface of the recorder would be expected to increase with increasing hydroxide concentration, now as the amount of camphor available at the surface per unit time would be greater, hence the less solubility. If the layer inhibits further etching, then one would expect a levelling-off tendency in the bulk etch rate as a function of the etchant concentration, as was observed in these experiments, Fig.3.7.

Diffusion of the etch products through the camphor layer must also be considered. If their diffusion is greatly retarded, they would also build up at the surface and this might also inhibit further etching. This means that the

TABLE 3.5

SOME PARAMETERS OF Na^+ AND K^+ IONS

Parameter	Ion	
	Na	K
Radius of the bare ion (^oA)	0.95	1.33
Radius of the ion + water dipoles (^oA)	2.76	2.32
Number of water dipoles per ion	3-4	2-3

TABLE 3.6

SOLUBILITY OF CAMPHOR AT 40^oC

Solvent	Solubility (g/ℓ)
Water	2.13
4.0N KSCN	2.01
3.0N KOH	0.16
6.25N NaOH	0.03

build up of the colloidal layer at the surface of the detector consists mainly of the plasticizer (camphor) and the rest is degraded cellulose nitrate. This is confirmed by the observed levelling-off behaviour of the bulk etch rate with increasing etchant concentration at a given temperature for both plasticized and un-plasticized cellulose nitrate[17].

It is evident from Fig.3.7 that the etchant temperature is by far the most influential parameter on the bulk etch rate of cellulose nitrate. An increase in the etchant temperature from 19°C to 31°C and up to 60°C (Figs.3.7(a) and (b)) results in about 6 and 25 fold increase in the etch rate, respectively at an etchant concentration of 2.5N NaOH. This reflects the importance of maintaining a constant temperature during etching if reproducibility and quantitative measurements are required.

Figs.3.8(a) and (b) show the bulk etch rate of CA80-15 as a function of $(\text{temperature})^{-1}$. The slope of the curve gives the activation free energy, $\Delta F_B^* = 1.03$ eV for bulk etching of CA80-15 (explained in the following section on V_T/V_B).

The rate of etchant attack on latent tracks was also found to vary with the etchant concentration. This is demonstrated in Fig.3.9, where the time in minutes needed to completely etch-out fission-fragment tracks in CA80-15 is given as a function of the concentration of NaOH. A temperature of 60°C was used. Tracks etched in solutions as dilute as 0.1N were observed; for lower etchant concentrations the etch times become prohibitively long (0.5×10^4 minutes).

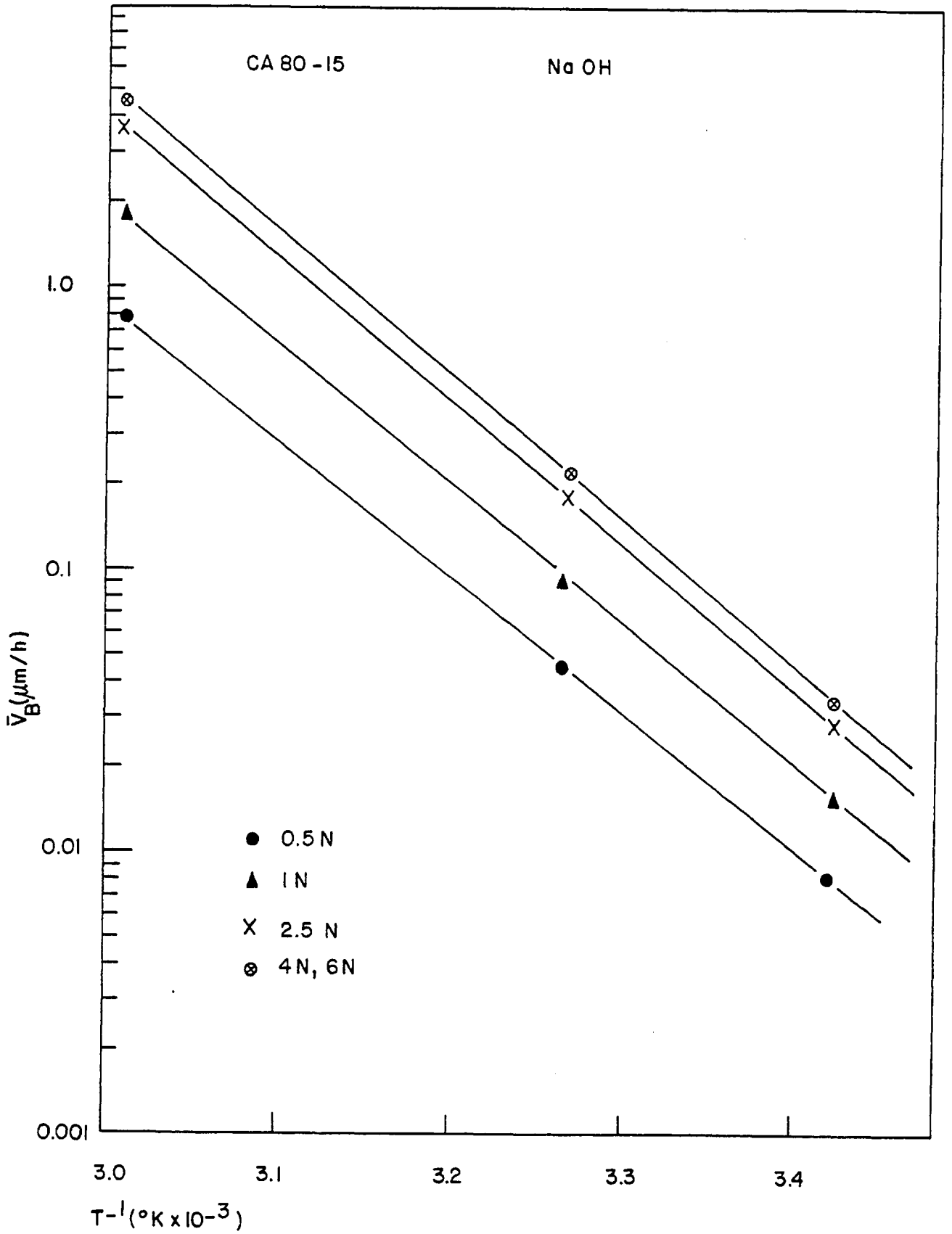


Figure 3.8(a) Dependence of the average bulk etch rate, $\bar{V}_B$ of CA80-15 on the etchant temperature, at different NaOH concentrations

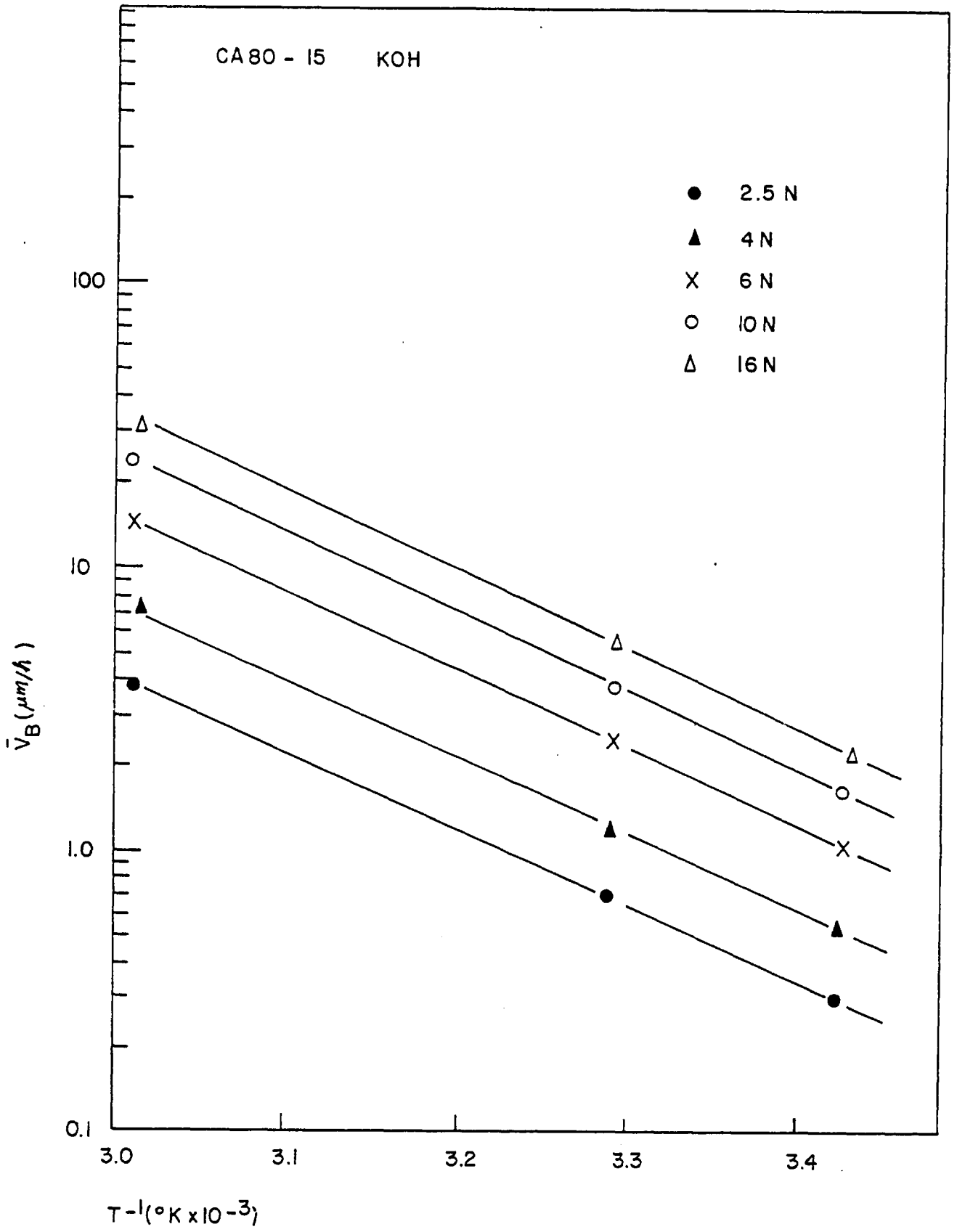


Figure 3.8(b) Dependence of the average bulk etch rate, $\bar{V}_B$ of CA80-15 on the etchant temperature, at different KOH concentrations

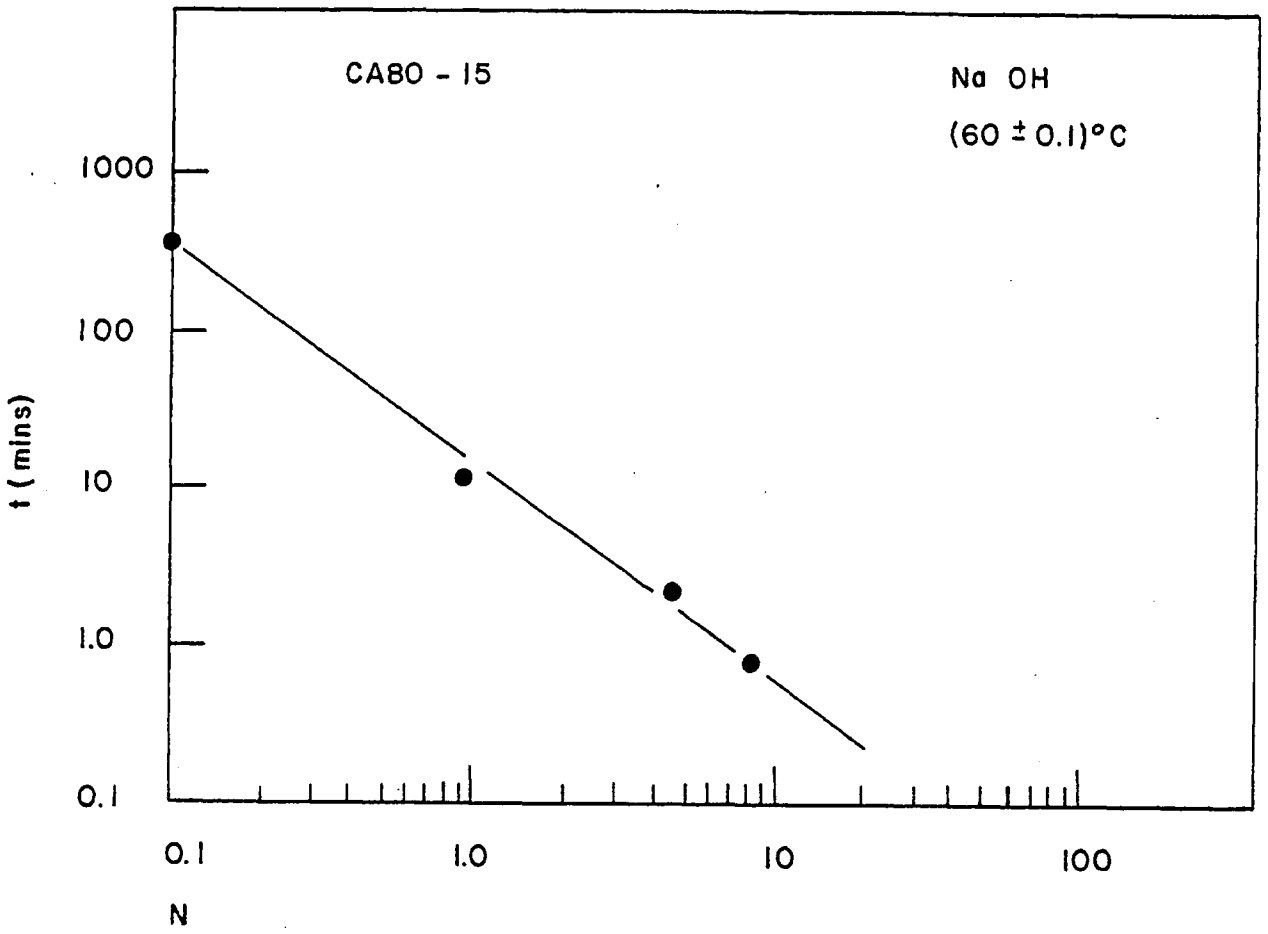


Figure 3.9 The time, t, required to etch out fission fragment tracks in CA80-15 as a function of NaOH concentration at 60°C

Considerable swelling of the recorders also occurred in the dilute solutions. Over the entire range of concentration, tracks of comparable appearance were observed.

The track etch rate, V_T and the etch rate ratio, V_T/V_B for CA80-15 as a function of NaOH concentration and temperature is plotted in Fig.3.10(a) and (b). The saturation in V_T, and the subsequent decrease in its value can be explained in terms of the rate of increase of the concentration of etch products and the swelling of the recorder at low etchant concentrations. The swelling of the plastic makes it possible for the basic solution to penetrate deeply and attack the radiation damaged area of the plastic, thus increasing the track etch rate.

(a) Dependence of the etch rate ratio (V_T/V_B) on temperature

It was noted as the etch temperature is decreased, the etch rate ratio, V_T/V_B is increased (Fig.3.10(b)). It is possible to predict this dependence by considering a simple model. Adopting a diagram similar to that used in the activation complex theory of chemical reaction rates, the free energies of the reactants and products are plotted in Fig. 3.11. Here, F_B is the free energy associated with the bulk material and the etchant, F_T is the free energy of the track region and the etchant, F_A is the free energy of the activated complex, and F_P is the free energy of the products. The quantity ΔF_T^* is the activation energy for track etching, ΔF_B^* is the activation energy for bulk etching, and ΔF is the reaction free energy. The free energy associated with the region of the recorder traversed by a highly ionizing

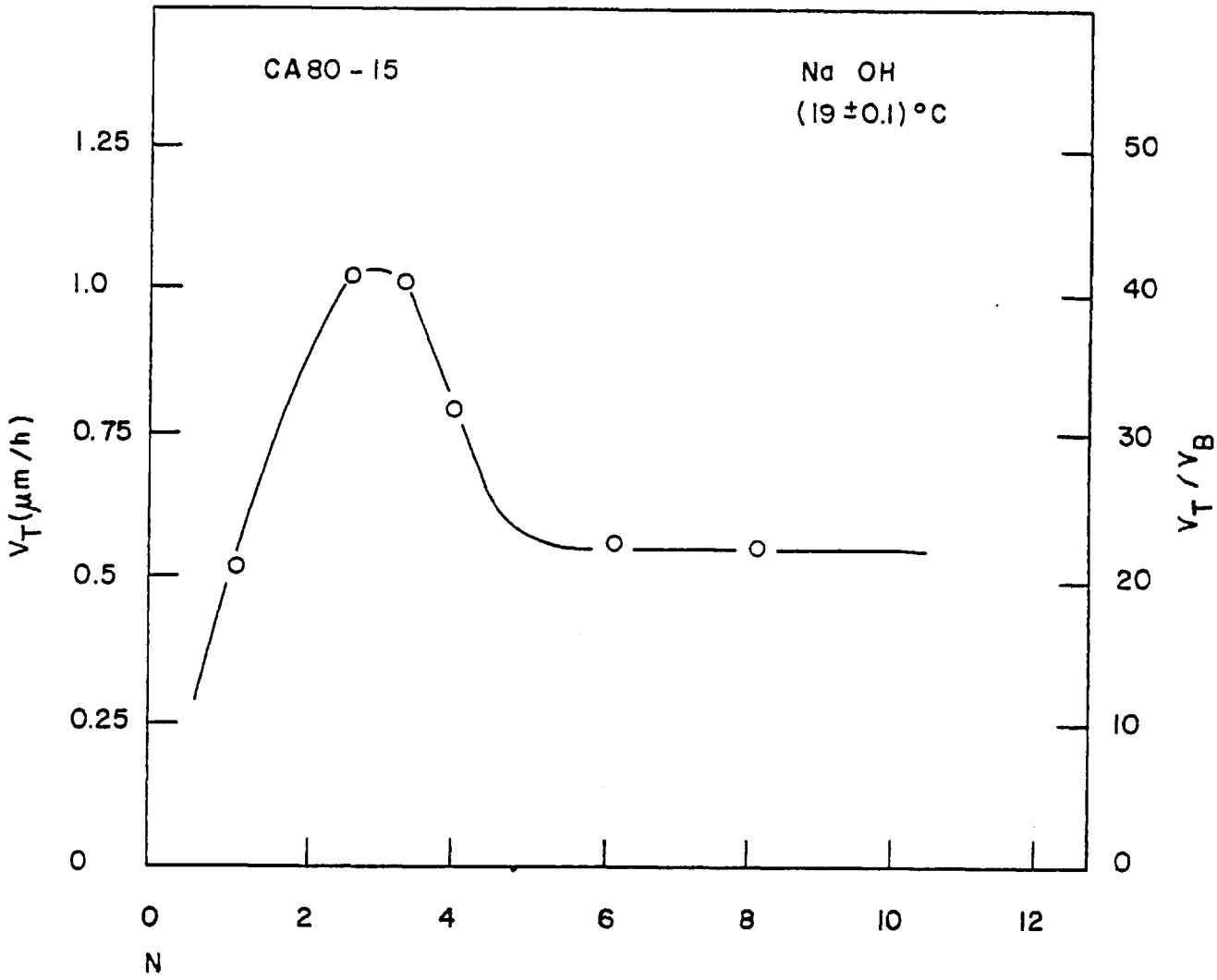


Figure 3.10(a) Dependence of the track etch rate, V_T and the etch rate ratio, V_T/V_B for 6 MeV alpha particles in CA80-15 on NaOH concentration, N(normals) at 19°C

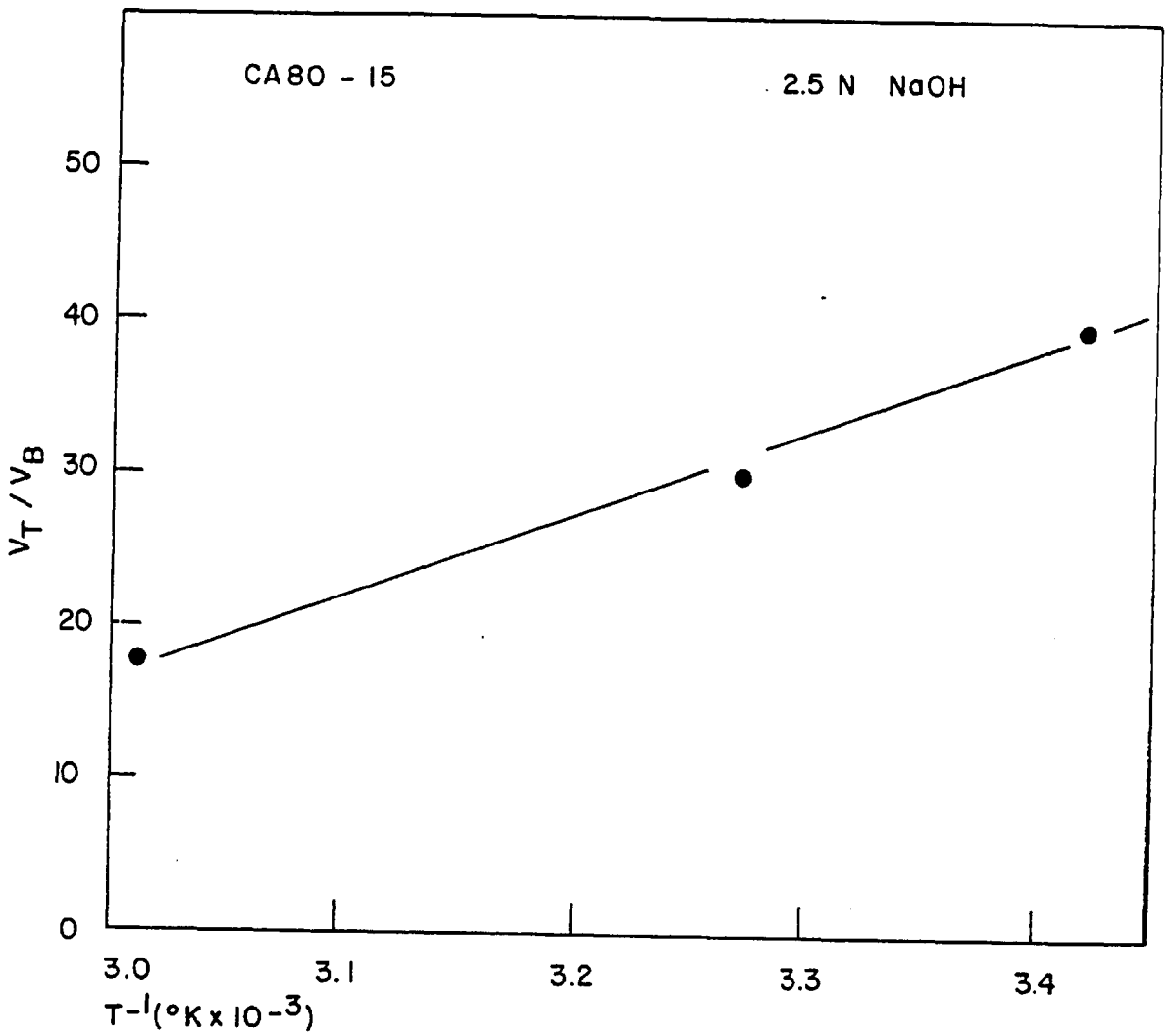


Figure 3.10(b) Dependence of the etch rate ratio, V_T/V_B for 6 MeV alpha particles in CA80-15 on the etchant (2.5N NaOH) temperature

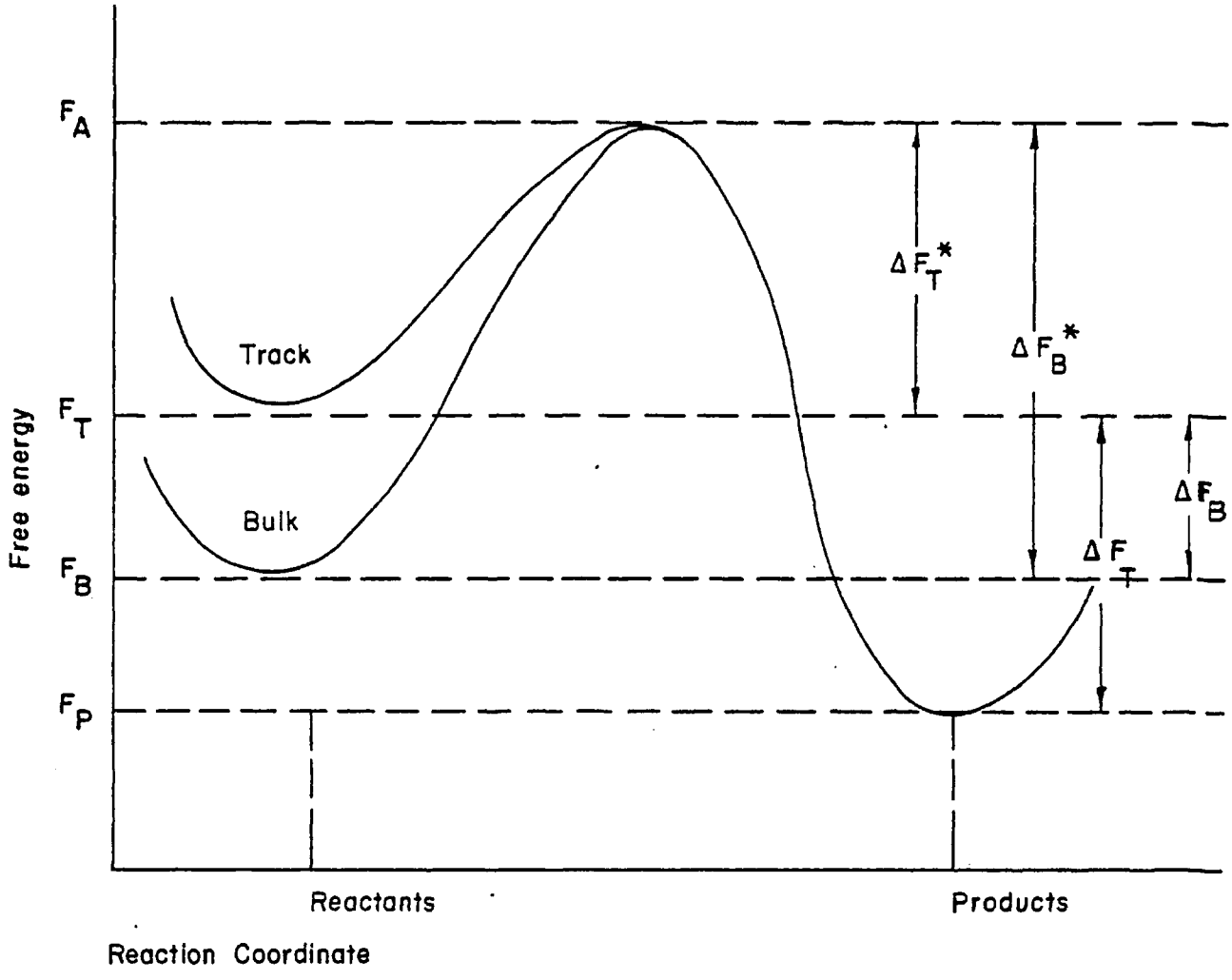


Figure 3.11 A free energy diagram of irradiated and unirradiated cellulose nitrate

particle is greater than that of the bulk material, $F_T > F_B$. From statistical mechanics we know that the probability that an atom undergoing thermal vibration will have a value of free energy equal to or greater than any value ΔF^* above its ground state is given by:

$$P = \exp(-\Delta F^*/kT) \tag{3.12}$$

If, in the chemical reaction in question, the rate controlling step has an activation free energy per atom of ΔF^*, the rate of this reaction will be proportional to $\exp(-\Delta F^*/kT)$. The overall rate of the reaction can simply be expressed as:

$$V = Be^{-\Delta F^*/kT} \tag{3.13}$$

where T = absolute temperature of the chemical

k = Boltzmanns constant (8.67×10^{-5} eV/^{o}K)

B = proportionality constant

Applying this relationship to the chemical etching of tracks, the etch rate along the particle trajectory is given by:

$$V_T = Ce^{-(F_A - F_T)/kT} \tag{3.14}$$

and the bulk etch rate is given by

$$V_B = De^{-(F_A - F_B)/kT} \tag{3.15}$$

Taking the ratio of equations (3.14) and (3.15):

$$V_T/V_B = C/D\ e^{(F_T - F_B)/kT} \tag{3.16}$$

Equation (3.16) predicts that as T is decreased V_T/V_B will increase, also as the difference between F_T and F_B is increased V_T/V_B will increase, and if $F_T = F_B$ and $C = D$, then

$V_T = V_B$. These predictions agree with experiment (Fig.3.10). By noting that $\sin\theta = V_B/V_T$ (equation 3.6), equation (3.16) can be written in the following form:

$$\ell n(1/\sin\theta) = (F_T - F_B)/kT + \ell n(C/D) \qquad (3.17)$$

The above equation shows a linear relationship between $\ell n(1/\sin\theta)$ and $1/T$, with a slope of $(F_T - F_B)/k$. This predicted linear dependence is observed in Fig.3.10(b). The slope shows that $(F_T - F_B) = 0.3$ eV. Measurement of the slope from Fig.3.10(b) gives $\Delta F_B^* = 1.03$ eV, hence the activation free energy of track etching, ΔF_T^* is found to equal 1.33 eV.

(ii) Polycarbonates (CR-39 and Makrofol K.G SSTRs)

The bulk etch rate of CR-39 in NaOH and KOH as a function of etchant temperature and concentration is shown in Fig.3.12(a) and (b). It is quite obvious that the bulk etch rate is much higher when etched in KOH than that obtained by etching it in NaOH (due to the reasons discussed in the preceding section). This difference becomes more and more significant with the increase in the etchant concentration. An appreciable increase in V_B is observed when the temperature of the NaOH etchant is increased from 70°C to 80°C at higher concentrations.

It was found that in the investigated concentration range between 2N and 12N and the temperature interval between 60°C and 90°C, the bulk etch rate of CR-39 can be well described by the relation:

$$V_B = G_B N^{n_B} \exp(- F_B/kT) \qquad (3.18)$$

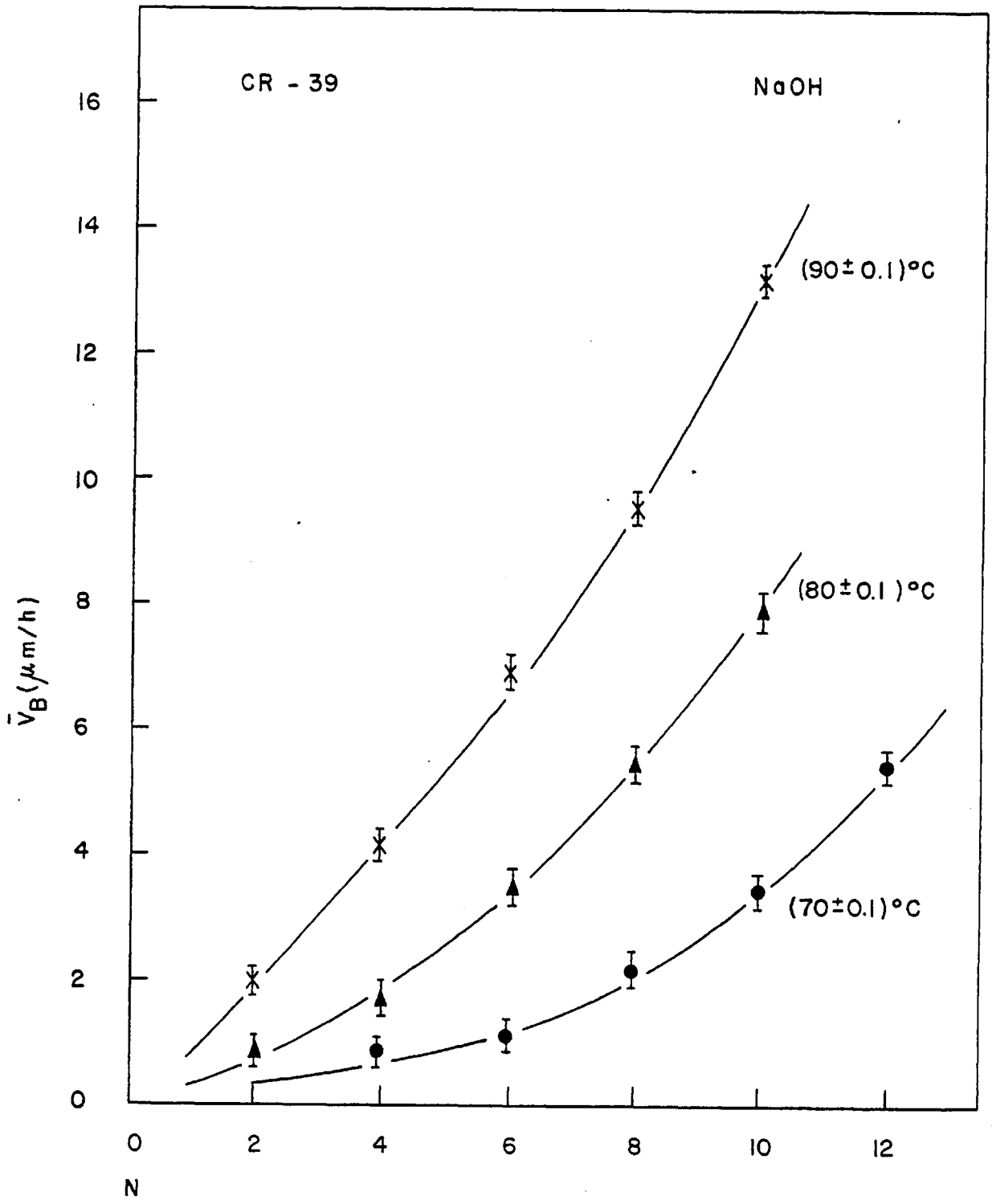


Figure 3.12(a) Average bulk etch rate, $\bar{V}_B$ of CR-39 as a function of NaOH concentration, N(normals) at different temperatures; without etchant stirring

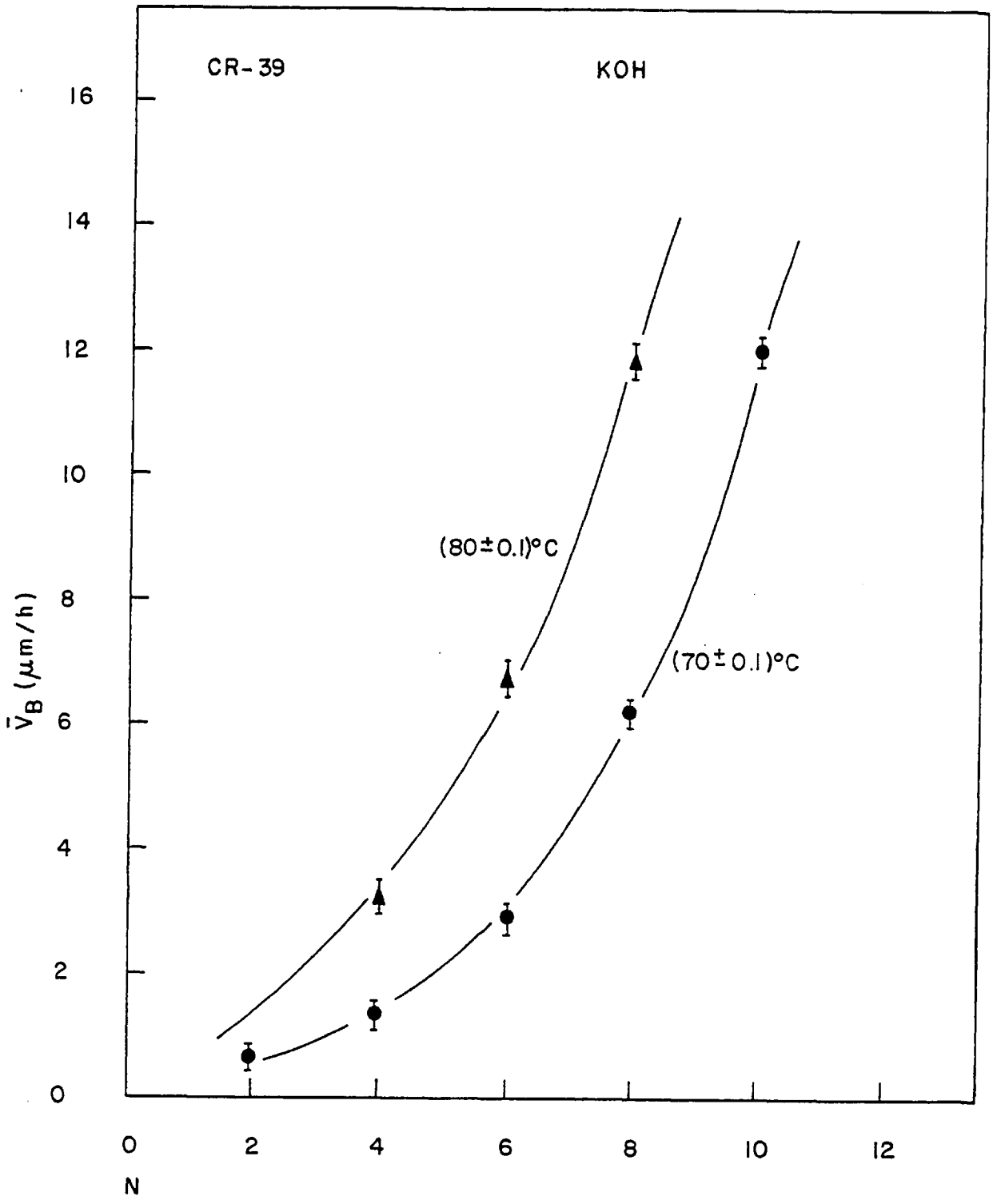


Figure 3.12(b) Average bulk etch rate, $\bar{V}_B$ of CR-39 as a function of KOH concentration, N (normals) at 70°C and 80°C; without etchant stirring

where T = absolute temperature of the etchant

N = concentration of the etchant in normals

k = Boltzmanns constant (8.67×10^{-5} eV/^{o}K)

The fitting procedure gave the values F_B = 0.88 eV, G_B = $(8.2 \pm 0.4) \times 10^{11}$ µm/h and n_B = 3/2 respectively.

Fig.3.13 shows the bulk etch rate of Makrofol K.G in NaOH and KOH at 60°C. The comparison of the two polycarbonates (CR-39 and Makrofol K.G) shows that CR-39 is one of the hardest plastic track recorder presently known.

The bulk etch rates of both above mentioned polycarbonate SSTRs do not saturate in the investigated etchant concentration range 2-12N. This can be explained on the basis of the chemical composition of polycarbonates. These polymers do not contain any plasticizers, therefore the effect of the colloidal layer which is formed during etching process and serves as a shield between the etchant and the plastic surface, is minimum.

The track etch rate, V_T for 6 MeV alpha tracks in CR-39 as a function of etchant temperature and concentration is shown in Fig.3.14. The dependence of V_T on etchant temperature and concentration can also be described by an empirical relation similar to the one used for V_B (equation 3.18), with $G_T = (9.5 \pm 0.5) \times 10^{11}$ µm/h, n_T = 7/4.

From the data given in Figs.3.14 and 3.15 for the etch rate ratio (V_T/V_B) the relation:

$$(V_T/V_B) \simeq (G_T/G_B)\, N^{n_T - n_B} = 1.4N^{1/4} \qquad (3.19)$$

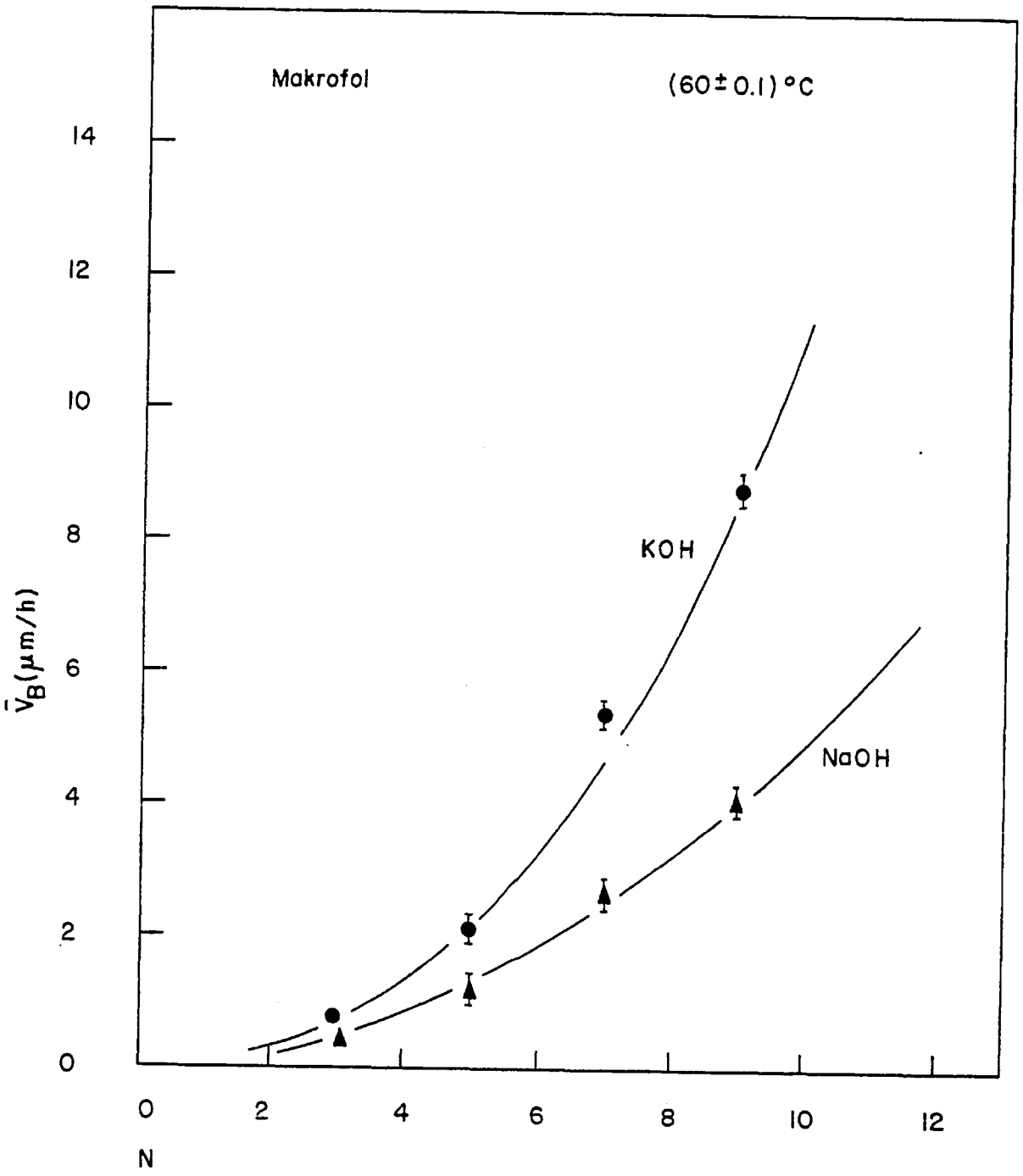


Figure 3.13 Average bulk etch rate, $\bar{V}_B$ of Makrofol K.G as a function of etchant concentration, N (normals) at 60°C; without etchant stirring

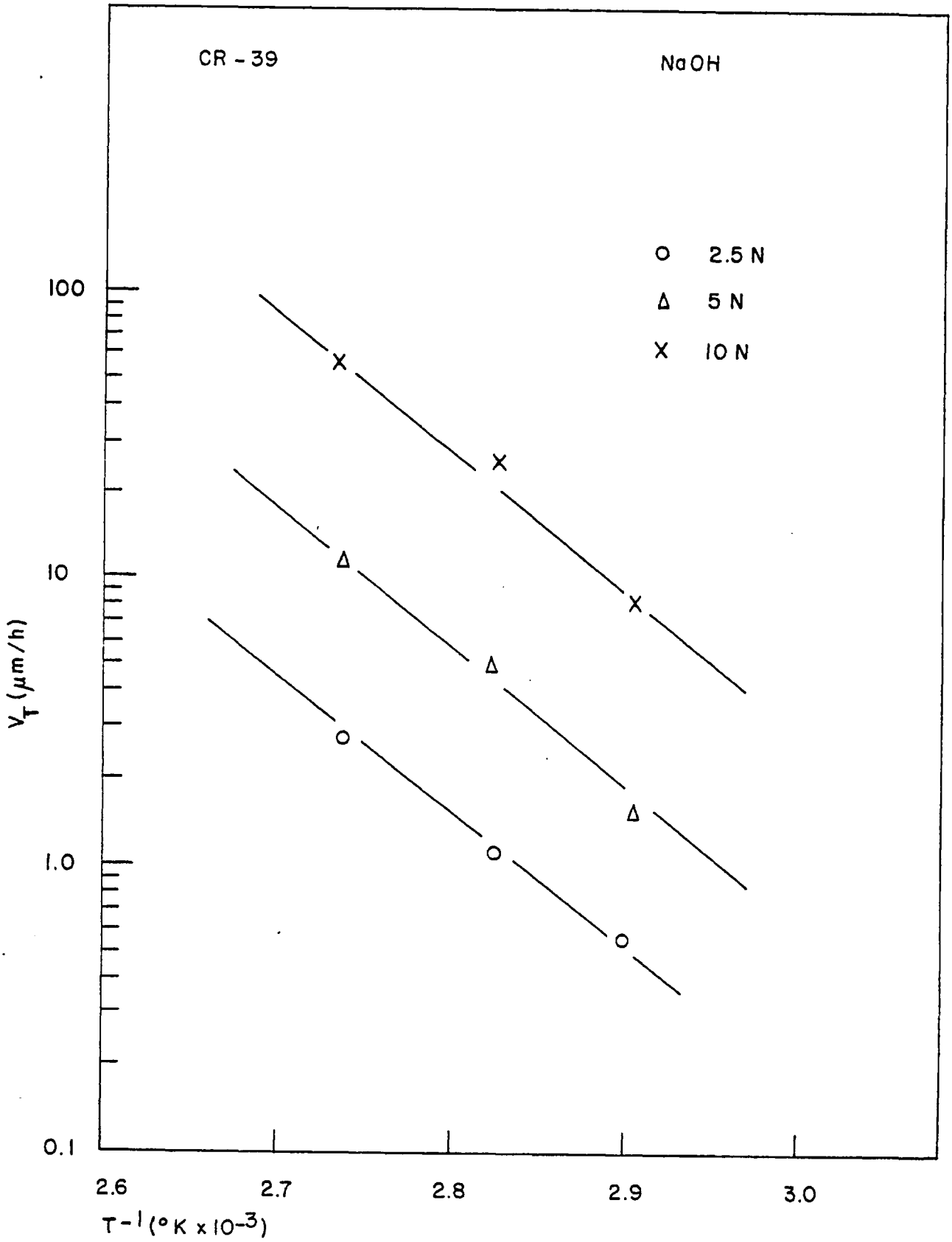


Figure 3.14 Dependence of the track etch rate, V_T for 6 MeV alpha particles in CR-39 on the etchant temperature, at different NaOH concentrations

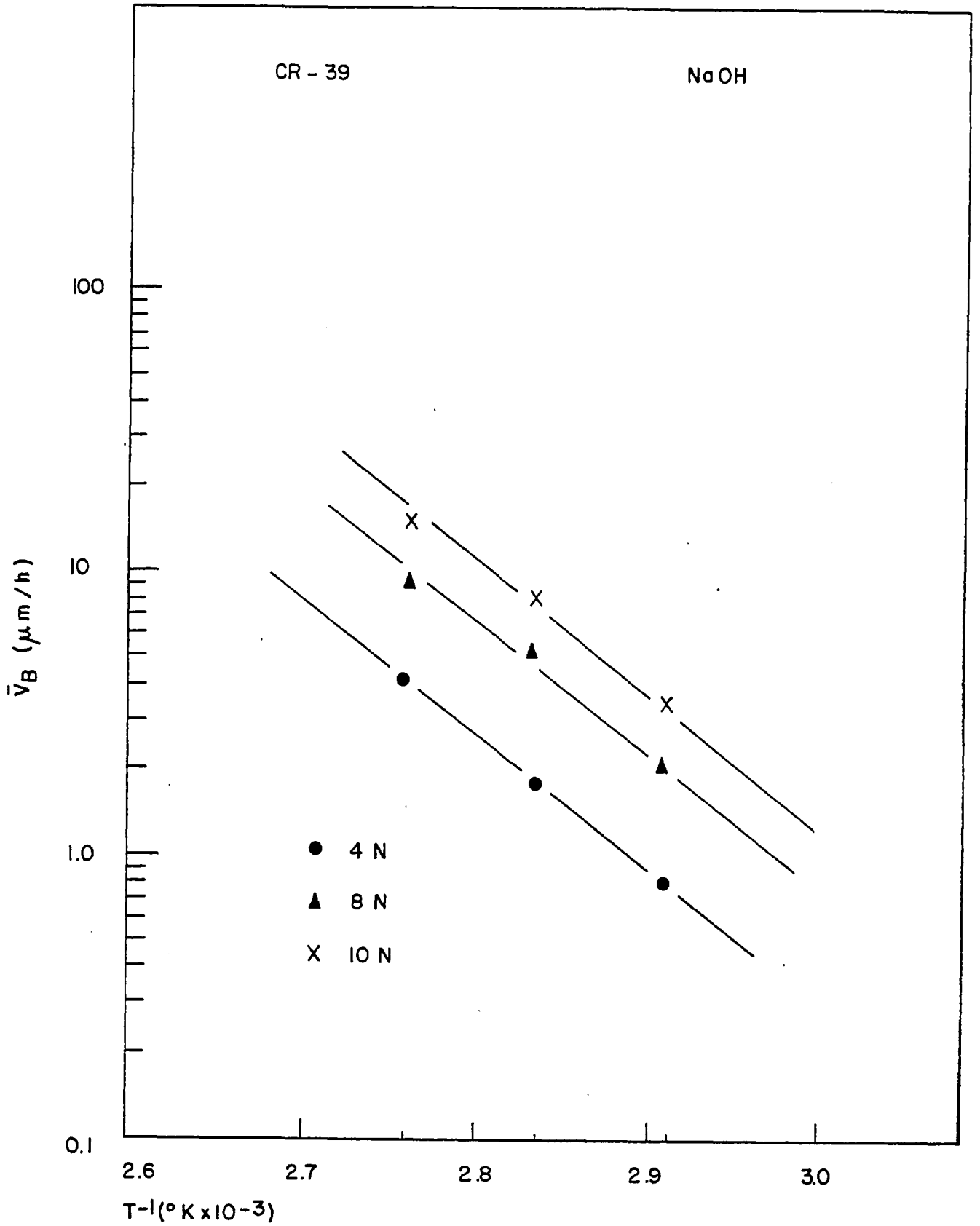


Figure 3.15 Dependence of the average bulk etch rate, $\overline{V}_B$ of CR-39 on the etchant temperature, at different NaOH concentrations

is obtained; the validity of which was repeatedly checked and proved for a range of NaOH concentrations between 1N and 10N. At concentrations more than 10N, a levelling-off tendency seems to appear, which is due to the build up of etch products on the surface of the detector.

3.4 TRACK OBSERVATION AND COUNTING

One of the most important parts of any work related to SSTRs is the observation and counting of tracks. It should be noted that the predominant factor with respect to the precision of counting is the track contrast against background and generally the clarity of tracks. These hold true in no matter what counting technique is employed. Therefore, in addition to the optimal etching conditions, it is essential to employ the right optical techniques to observe the tracks.

The counting in the present study was performed by eye and/or using the automatic track counting technique developed at Imperial College (see Chapter 7). Eye counting was found to be laborious and time-consuming. However, considering the eye to be the best possible detector, it was decided to use the eye-counts as bench-mark observations for the optimization of the automatic counting technique.

3.4.1 Optical Techniques for theObservation and Measurement of Tracks

The basic information needed for many track studies consists simply of measurements of track densities. The most direct, commonly used counting method is manual observation

through the microscope using an eye-piece with a calibrated grid and counting the number of tracks in a series of fields of view. However, sometimes it is necessary to measure the track parameters, such as track lengths, diameter or cone angles. The precision with which track parameters of interest may be measured depends upon the optical resolution attainable as well as the ability to perform the actual measurements.

The microscopy of etched tracks has a number of unusual aspects that are generally not encountered in ordinary microscopy. The problem centres on the fact that usually the etched tracks are in the form of transparent cavities rather than opaque objects such as silver grains in the processed nuclear photographic emulsions. Some of the major difficulties encountered are as follows:

(a) The difference in the index of refraction of the track cavity and the bulk material is small.

(b) Inhomogeneities and inclusions present in most commercial plastics cause a variation in the index of refraction of the bulk material.

(c) The often heavily pitted surfaces of the etched plastics degrade the optical image.

(d) Thick specimens may require objectives and condensers with larger working distances than usually available.

(e) Track cavities tend to fill up with liquids when immersion objectives are used, thus reducing track image contrast.

(f) Track dimensions may be small, requiring the use of high numerical aperture (N.A.) objective-condenser combinations.

Most of these difficulties, in general, can be overcome by the use of either one or a combination of the optical techniques that are described below.

(i) Bright-field, transmitted light illumination

(a) Dry objectives

For many measurements, track observations, and rapid scanning of the specimens at low magnifications, dry objectives are easy and convenient to use. A few dry lenses, even of moderate magnifying power, have long working distances. This permits the observation of steeply dipping, long tracks when tilting of the specimen is required. The Vickers, AEI 651035, x 40, N.A. = 0.57 objective having a working distance of 6mm is an excellent example of this type of lens. The main limitation of the dry objectives is the lack of high resolution. While dry objectives are available with N.A.'s of up to 0.95, most of the lenses with N.A.'s over about 0.60 require the use of an exact thickness coverglass. This requirement decreases considerably their utility.

(b) Immersion objectives

These are generally of two types, oil or water. The immersion objectives are characteristically of higher N.A. (up to about 1.40) than the dry lenses. Consequently, they are capable of higher resolution. The use of these objectives requires procedures that are considerably more exacting than those necessary with the dry lenses. To achieve the full resolution of the objectives with N.A.'s of over 1.0 requires the use of an oil immersion condenser. However, the use of

an oil immersion objective, without oiling the condenser will still give greater resolution than that possible with the dry lenses. It is possible to overcome the problem of oil seepage into track cavities by covering the SSTR with a transparent film such as glass cover-slip or a thin plastic film. However, it is essential to eliminate the air gap between the cover-slip and the SSTR. Otherwise, the numerical aperture greater than 1.0 cannot be achieved.

The depth of field of the high N.A. objectives is very small. This feature makes the oil immersion objectives less desirable for general scanning than the dry objectives. However, the immersion objectives are extremely valuable for precise measurements.

Table 3.7 shows some characteristics of optical objectives and the approximate limits of useful magnification and resolution which can be achieved on optical microscopes.

(ii) Dark-field illumination

A practical resolution of about 0.1 μm can be obtained with the use of oil immersion, dark-field illumination. Although this type of dark-field illumination requires a careful and a time consuming optical alignment, it is one of the few techniques available for the observation of very small tracks, such as low energy recoil particles.

The lower power, dry, dark field techniques are very useful in the general scanning work. The depth of field is considerably greater than with bright-field illumination, permitting the observation of large track segments. The

TABLE 3.7(a)

SOME CHARACTERISTICS OF OPTICAL MICROSCOPE OBJECTIVES

Objective Focal Length (mm)	N.A.	Objective Magnification	Working Distance (mm)	Diameter of Field (mm)	Depth of Field (μm)	Final Magnification		
						Eye-Piece		
						x8	x50	x20
25	0.15	x5	23	3.2	20	x40	x50	x100
16	0.28	x10	7	1.6	10	x80	x100	x200
4	0.74	x40	1	0.4	2	x320	x400	x800
2	1.30	x100	0.25	0.15	1	x800	x1000	x2000
0.16	1.40	x130	0.20	0.12	0.75	x1040	x1300	x2600
0.14	1.45	x160	0.18	0.10	0.50	x1280	x1600	x3200

TABLE 3.7(b)

THE APPROXIMATE LIMITS OF USEFUL MAGNIFICATION AND RESOLUTION OF OPTICAL MICROSCOPES

Objective Magnification	N.A.	Useful Final Magnification Limit	Optical Resolution (μm) 1.22 λ/2N.A.	
			λ ≃ 0.425 μm	λ ≃ 0.625 μm
x5	0.15	x100	1.73	2.54
x10	0.28	x200	0.93	1.36
x40	0.74	x740	0.35	0.52
x100	1.30	x1300	0.20	0.29
x130	1.40	x2400	0.19	0.27
x160	1.45	x3000	0.18	0.26

considerable image contrast of track to background is also quite helpful. For accurate track parameter measurements dark-field is not particularly useful since track dimensions tend to be somewhat exaggerated.

(iii) Phase contrast microscopy

For observation of small, low contrast tracks, such as recoil proton tracks, phase contrast microscopy can be effectively utilised. It is particularly useful for the observation of long narrow tracks, where the retention of liquids has rendered the terminal ends of tracks invisible under bright field illumination. However, if the track contrast is adequate for the standard bright-field optics, the phase contrast image is less satisfactory. For the larger tracks with appreciable dip angles, a 'halo' surrounds the image.

Phase contrast is available in the normal, or the positive, and the negative types. For track observations, the negative type is found to be more useful. In this case the track image is delineated by a sharp black border. This unique feature distinguishes the image obtained with the negative phase contrast techniques from that of the positive phase, or the standard dark-field illumination.

(iv) Incident light illumination (reflection)

For track observations in SSTRs which are very thick (> 2 mm), the use of incident light optics is found to be useful. The resolution of the surface-reflected light systems is somewhat inferior to the transmitted light systems. Because

of image degradation, observations are restricted to depths of less than about 30 μm into the volume of the specimen. With long working distances and dip cones available, incident light techniques can be used for observation of tracks in SSTRs that are still immersed in the etching solution contained in opaque etching tanks[81].

3.4.2 The Microscope Equipment (used in the present study)

The microscope used for most of the present work was a Reichert (model MEF2, transmitted light) with dry (x15, x50 or x70) or oil-immersed (x140 or x150) objectives together with x8, x10 or x12.5 oculars. The microscope stage and fine focus controls are equipped with dials so that the stage area can be scanned with precision for track counting and measurement purposes. In fact, track dimensions can be measured to an accuracy of $\pm$ 0.5 μm. One eye-piece is equipped with a Bausch and Lomb micrometer disc consisting of a square grid divided into 36 squares. The length of a side of the square was calibrated with a stage micrometer.

The microscope stage position is defined so that the same frame will not be counted more than once. At every frame position the tracks in the field of view bounded by the square are counted from the top row of squares to the bottom. If the tracks cross the left or top line they are not counted, whether they begin or end within the square. If they cross the right or bottom line they are counted, so that a proper statistical estimate of the track density can be obtained without deciding which is the beginning or end of the tracks. When the counting in one field is completed

the stage is moved so that a track or spot crossing one boundary is moved on to the opposite boundary and the counting process is repeated. When counting all tracks on the recorder, care is taken to move from one scanning path to another by displacing the scanning path one field of view after a given path is completed and the counting process is repeated. Overlapping correction (where appropriate) was performed by discriminating double, triple etc. by the size of the track.

3.4.3 Track Counting Conventions

This is particularly important in the case of 'intrinsic' SSTRs which have been exposed to neutrons, as the tracks produced have a wide range of dimensions. A convenient practical choice of $\sim$ 1 μm for $V_B t$ (where t is the etching time) can be made so that tracks are large enough to be visible in the microscope but such that few new tracks have been uncovered by removal of the material from the surface of the SSTR (i.e. prolonged etching effects, see Chapter 4). A second alternative is to make $V_B t$ large relative to the track dimensions and count only sharp-bottomed tracks having dimensions bigger than about 1 μm, while rejecting all shallow looking tracks. Since for long etching times the rate of display of new tracks will be balanced by the rounding out of old tracks after their full lengths have been dissolved away, the procedure will give a reproducible, steady-state value, as long as the track density is not so large that overlapping tracks are common. A more laborious but well-defined procedure[82], is to count all tracks as a function of etching time and extrapolate back to the track density at zero etching time.

In the present work, out of the three above mentioned procedures, the second was found to be the most reproducible and hence, employed in all track density measurements in SSTRs exposed to neutrons.

3.5 CONCLUSIONS

Three materials namely CA80-15, CR-39 and Makrofol K.G were selected on the basis of the results from the preliminary experiments, for detailed examination as the SSTRs for fast neutron measurements. Smooth surface of excellent optical quality after prolonged periods of etching, in the case of CR-39, makes it particularly suitable for fast neutron dosimetry using recoil proton tracks.

The choice of the etchant temperature and concentration depends on the final use of the SSTR. For reaction rate measurements etching at high temperatures ($60^{o}C$) will reveal tracks within a few minutes. The tracks are of acceptable quality for counting which can be done under lower magnification in order to scan over a wide area of the etched surface. The control of the etchant temperature to within $\pm$ $0.1^{o}C$ is necessary to prevent errors of greater than $\pm$ 1% in the track density.

However, if the shape of tracks is to be measured in order to determine particle energies, then very careful control over the etching process is required. It is not satisfactory to etch at high temperatures since the etching time must be accurately known, which is not possible as some etching continues to take place when the SSTR is removed from the etchant.

The SSTR is always washed in water to neutralize the etchant after etching is completed, if etching takes place at 60°C then a few seconds in transferring the SSTR to water is sufficient for etching to continue and cause significant error in analysing track dimensions.

Etching at low temperatures, although time consuming, does permit control over the etching process. A few seconds in transferring an SSTR into water at the end of etching will result in an insignificant effect on the track dimensions. Furthermore, the etching at low temperature ensures that the SSTR suffers very little damage and that the resulting tracks are of a high quality. A variation of $\pm$ 0.5°C at 19°C will result in a $\pm$ 1% change in V_T/V_B for a 2.5N etchant for CA80-15 while at 60°C a $\pm$ 0.5°C variation will result in a 4.0% change in V_T/V_B.

CHAPTER 4

EXPERIMENTS

4.1 INTRODUCTION

If a SSTR such as CA80-15 or CR-39 is irradiated in a fast neutron spectrum, tracks will be produced from a wide range of nuclear reactions resulting from neutron interactions with the constituent elements such as H, C, N and O. Since the cross-sections of these elements with respect to neutron interactions vary with energy over the energy range of interest in reactor physics, the track density will be dependent on the neutron spectrum. It is therefore necessary to investigate the sensitivity of CA80-15 and CR-39 for the various neutron reactions as a function of energy. These reactions are concerned with recoils from H, C, N and O and also from the products of threshold reactions, $^{14}N(n,\alpha)^{11}B$ and $^{14}N(n,p)^{14}C$ etc.

Also, one of the conclusions reached as a result of a recent intercomparison exercise on neutron dosimetry using SSTRs[83], was that it was desirable to find optimum procedures for processing, evaluation and calibration of these detectors.

This chapter deals with experimental details and results from a series of irradiations involving particle accelerators, reactor and other charged particle sources, which were performed to characterise the track density in CA80-15, CR-39 and Makrofol K.G , as a function of energy. The main characteristics of these irradiations are given in Table 4.1. The effect of chemical etching on neutron detection efficiency

TABLE 4.1

MAIN CHARACTERISTICS OF VARIOUS IRRADIATIONS PERFORMED (CA80-±5, Makrofol K.G. and CR-39)

Particle	Source	Energy (MeV)	Dip Angle
Protons	Van de Graaf, Harwell	0.45-4	90°
Alphas	Van de Graaf, Harwell,	0.6-5	90°
	Am-241	0.1-5.4	2π-geometry
	Cf-252	6.1	2π-geometry
Nitrogen-14	Van de Graaf, Harwell	3.5	90°
Thermal Neutrons	Reactor 'Consort'	0.25×10^{-7}	
Fast Neutrons	Cf-252	2.1	90°
	IBIS, Harwell	0.2-17.0	0°-90°

is also examined. Finally, some conclusions are drawn on neutron sensitivity of various SSTRs.

4.2 EXPERIMENTS ON THE Van de Graaf ACCELERATOR

These experiments consist of CA80-15 and CR-39 irradiations with protons, alpha particles and nitrogen ions of various energies, which were performed using the 6MV Van de Graaf accelerator at A.E.R.E., Harwell. The purpose of these experiments was to study the registration and detection properties of CA80-15 and CR-39 with reference to the particles of concern in the present work. The alpha particle detection efficiency of CA80-15 has been studied[84], but information on protons and heavy ions is limited. Therefore more emphasis was given on proton irradiations.

The two major objectives of the present experiments were:

(i) Examination of the counting efficiency within the particle limits (energy wise) for track detection. This is defined as the number of tracks counted over the number of detectable particles incident upon the SSTR. It should generally be expected that the counting efficiency is a constant close to 100%, depending primarily on the track size discrimination against background and overlapping corrections, if any. However, these problems can be minimised or even eliminated by the appropriate selection of the irradiation length, so that the overlapping is only statistical.

(ii) Examination of the detection efficiency, i.e. determination of the maximum and minimum particle energy limits for track detection, $_{X}E_{i}$ and $_{N}E_{i}$, respectively.

The above, make it clear that a detailed study of the detection properties of a given SSTR with regard to a specified particle requires a considerable amount of irradiations. Moreover, to assure that the information obtained will be within realistic terms, these experiments must comply with the following conditions:

(a) The particle beams must be well calibrated with respect to energy; their intensity should be well monitored and the particle dose must be known with confidence.

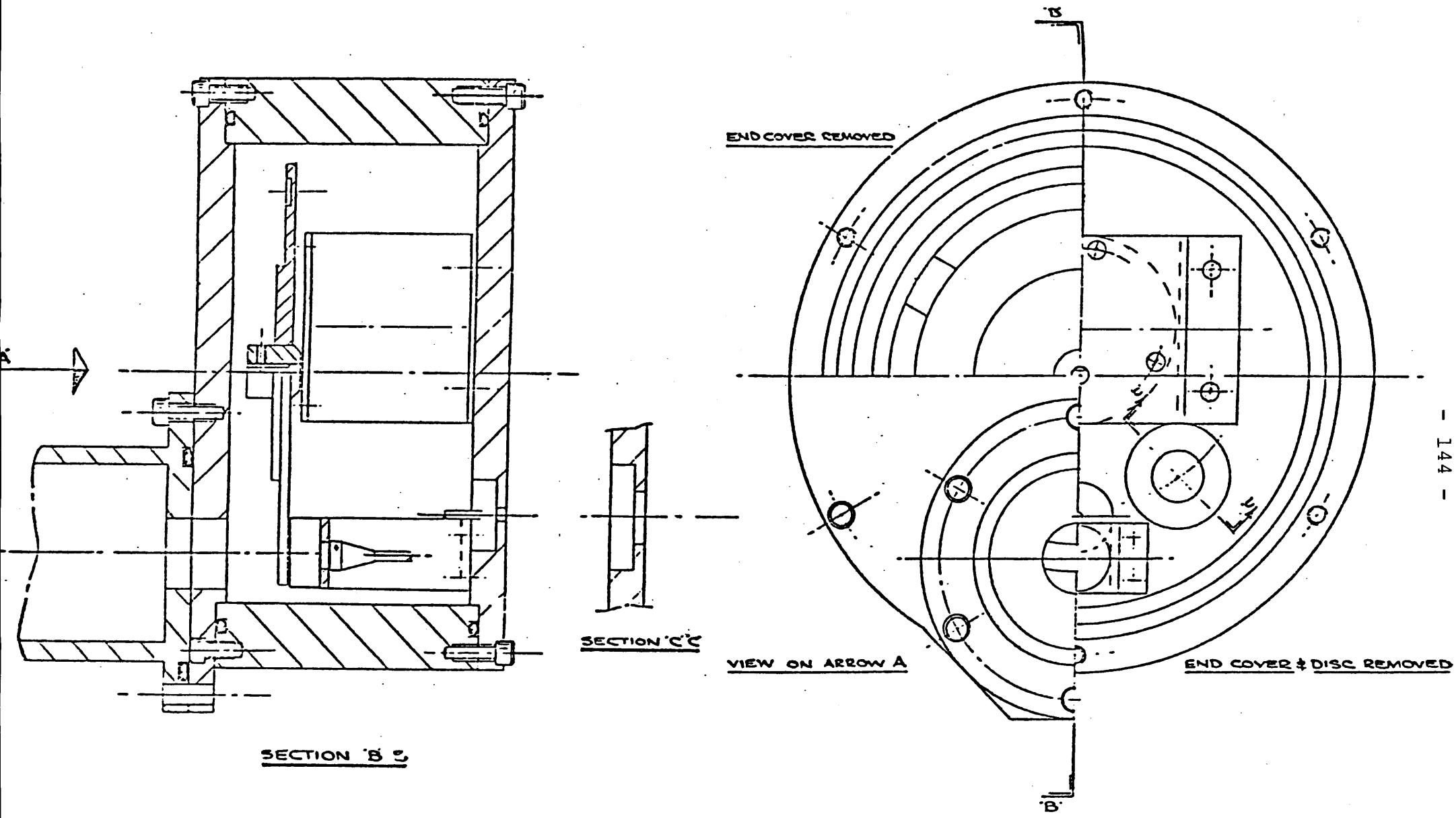
(b) The irradiation length should be controlled accurately and the particles should not undergo any energy losses before striking the surface of the film.

(c) The experimental set-up should provide a high energy resolution (narrow energy mesh) and preferably various angles of incidence.

4.2.1 Description of Experimental Set-Up on Van de Graaf

This is a vertical Van de Graaf capable of terminal energies of up to 6 MV and accelerating both gaseous and metal ions. Its two main target areas each contain a number of flight paths which are connected to the accelerator via a rotatable 90° analysing magnet.

As a result of collaboration with A.E.R.E., Harwell, an accelerator vacuum box, shown in Figs. 4.1(a) and (b), was



Scale: 1/1.93

Figure 4.1(a) Accelerator vacuum box

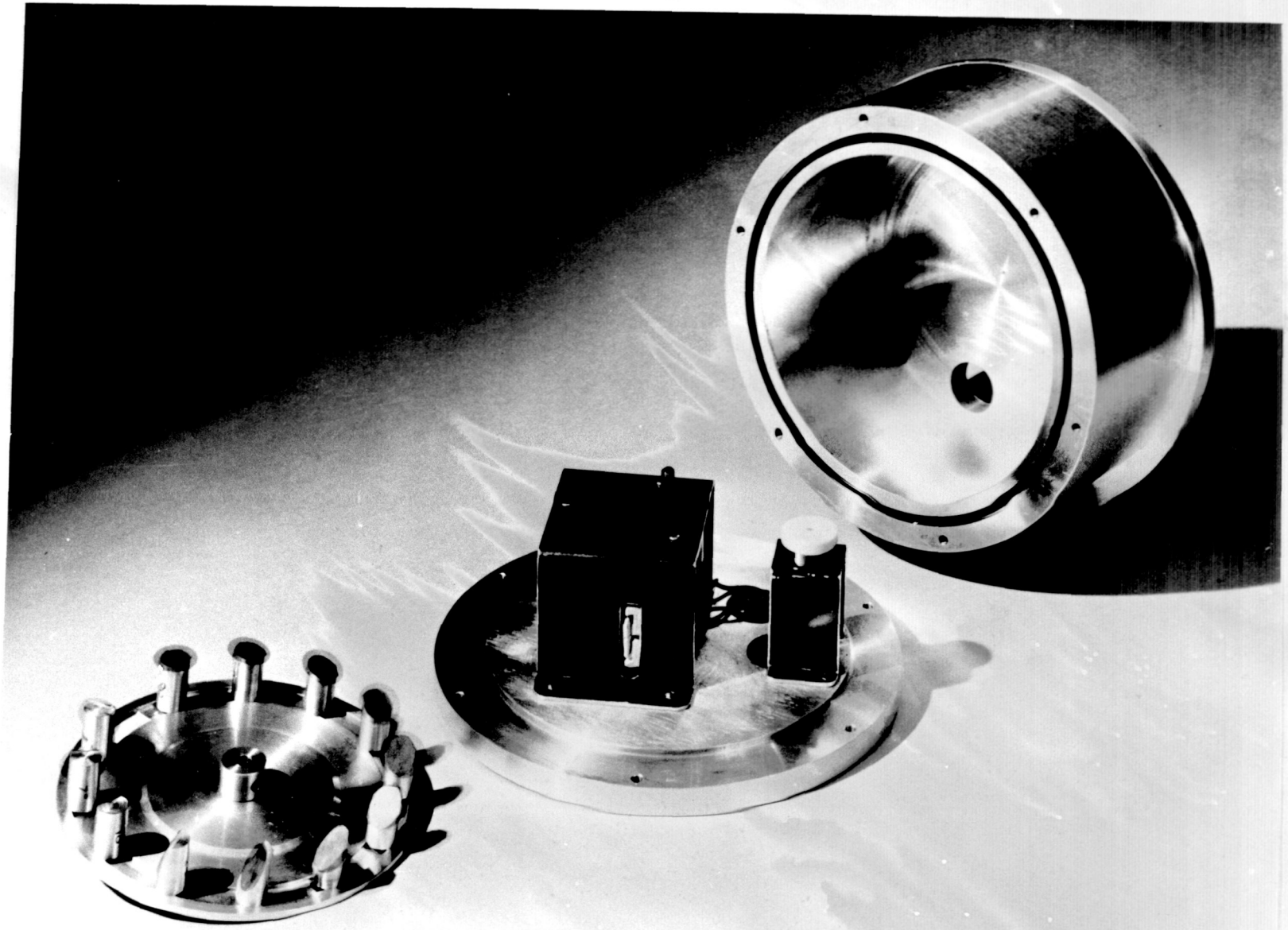


Figure 4.1(b) SSTR rotator system, showing rotator with 12 recorders, back-plate with motor and semi-conductor detector, and housing with beam hole

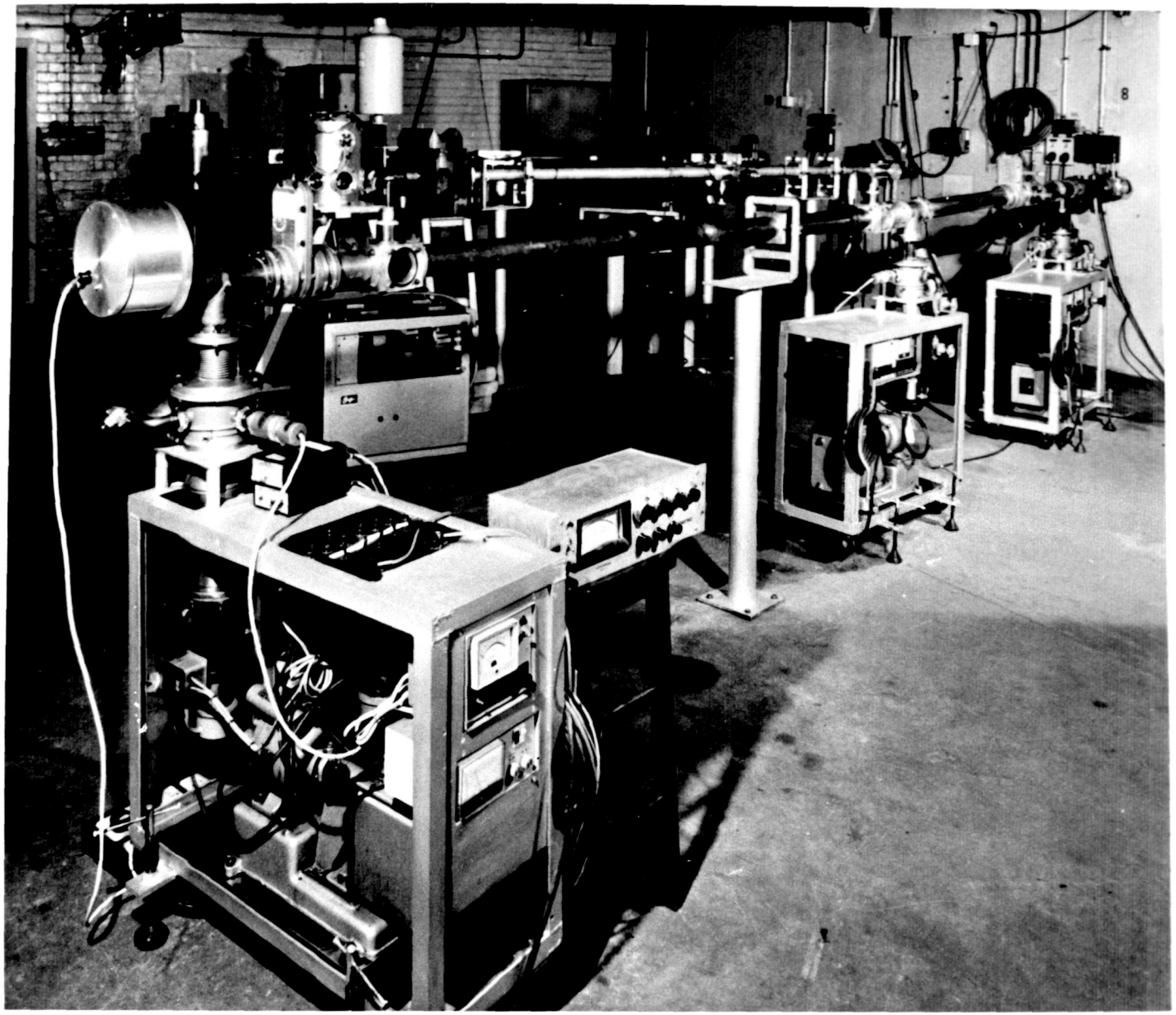


Figure 4.1(c) Beam tube assembly terminating in the rotator system containing SSTRs and semi-conductor particle detector

constructed[85]. This design was considered to most closely meet the conditions set out in the previous section and provides a rotating wheel, where for a certain particle energy, SSTRs can be irradiated at several angles at the same time.

The films are kept firm on the respective demountable pieces by the action of the double-sided sticky tape.

The end of the tube from the accelerator, on which the base is mounted before irradiation is seen in Fig.4.1(c). The monitor of the beam gives the absolute dose of particles received, while the particle dose per unit area can be found by normalising over the area of the monitor cover hole (see white plastic cover in Fig.4.1(b)).

The vacuum is sustained by the continuous action of a vacuum pump. The irradiation length can be controlled with high precision by the operator.

4.2.2 Experimental

The main reason for adopting the rotating wheel mode to perform irradiations was to overcome the problem arising from the instability of the particle beam. In other words, if the SSTR was stationary, it would be extremely difficult to control the particle dose due to fluctuations on the intensity of the beam and it would be almost impossible to assure repeatability of the experimental conditions. On the other hand, irradiating many films simultaneously has the advantage of reducing the experimental work.

(i) Protons

CA80-15 and CR-39 were bombarded with monoenergetic protons of 0.45-4 MeV, which had to be scattered at a gold foil of 100 $\mu g/cm^2$ thickness, to reduce the particle flux. The number of particles was measured by means of a semi-conductor detector. Protons were incident normal to the surface of the films and the irradiated sides on all films were marked.

The beam current was set together with the length of irradiation so that the track density for 90° incident protons was $\simeq 10^4$ tracks/cm^2, which is a convenient density for both automatic and manual counting, since track overlapping is less than 5%.

(ii) Alpha particles

CA80-15 films were bombarded with monoenergetic alpha particles of 0.6-5 MeV. This alpha particle energy-range is particularly important in the present work, as most of the alpha particles produced from the threshold reactions such as $^{14}N(n,\alpha)^{11}B$ in CA80-15 exposed to fast neutrons, lie in this energy range. Alpha particles were incident normal to the surface of the films.

Various reasons made it impossible to irradiate CR-39 films with well calibrated alpha particles from the accelerator. Therefore, a 0.2 μCi calibrated Am-241 source ($E_\alpha \simeq 5.4$ MeV) and a 1 μCi Cf-252 source ($E_\alpha \simeq 6.1$ MeV), were used. The two modes of alpha-decay from ^{241}Am have similar energies of 5.484 MeV ($\sim$85.2%) and 5.442 MeV ($\sim$ 12.5%). The energies of

the alpha particles were varied by passing them through aluminium sheets of various thicknesses.

(iii) Heavy ions

It became possible to irradiate CA80-15 films with 3.5 MeV nitrogen-14 ions only, and therefore the deduction from these experiments can be extrapolated to ^{12}C and ^{16}O ions (other two constituents of CA80-15 in 'heavy ions' category), as long as some sort of weighting factor can be introduced. The latter was done with regard to certain magnitudes of importance to the theoretical response calculations presented in Chapter 2.

(iv) Etchings

The irradiated films were stored at $\sim 4^{\circ}C$ until etching and evaluation could be carried out, typically within a few weeks of irradiation. CA80-15 films were etched in 2.5N NaOH aqueous solution at $19^{\circ}C$ for several time steps. Cold etching conditions were adopted as they permit precise control over the etching process (see also Chapter 3), thus making track dimension measurements more accurate. This is particularly important for proton tracks, as the low stopping power (dE/dx) places them close to the limit of detectability in CA80-15.

It was found from the CR-39 bulk etch rate measurements (Chapter 3), these films are highly resistant to the alkaline etchant attack. Therefore, it was necessary to etch CR-39 films at a high temperature to reveal tracks in a reasonable period of time; hence these films were etched in aqueous solution of 6N NaOH at $70^{\circ}C$.

As control, the same plastic sample but unirradiated was treated with the same etching agents under the same etching conditions. Tracks were counted under optical microscope with total magnification of x400 - x560.

4.2.3 Results and Discussion

(i) CA80-15

(a) Protons

Proton tracks were observed with energies from 0.45-0.70 MeV, with small amount of etching. The number of tracks was the same as the semiconductor count within 5% limits of error. No proton tracks were observed with energies greater than 1 MeV. Table 4.2 refers to results from counting tracks on CA80-15 films created by protons incident at 90°. It can be seen that the counting efficiency is with a good confidence of the order of 100%. This arises from the measurements below 0.7 MeV, where the difference from 100% can easily be explained by statistical errors and track overlapping correction inadequacies.

Fig.4.2(a) shows the track diameter plotted as a function of layer removed from the film surface for various proton energies. In the measurement of track diameters, a minimum of 40 tracks were sampled at each energy and the mean diameter determined. It can be seen from this figure that protons having an energy of less than 500 keV, cause the formation of track immediately from the start. For protons with energy greater than 500 keV, degradation within the detector to this value is necessary if tracks are to be revealed.

TABLE 4.2

TRACKS FROM PROTONS INCIDENT ON THE CA80-15 FILMS AT 90°

Energy (MeV)		0.45	0.5	0.6	0.7
Monitor* Dose	In Protons	3716	2900	2776	2534
	Integrated Current $\int Idt$	4.46×10^{-8}	4.54×10^{-8}	6.4×10^{-8}	8.4×10^{-8}
Expected Track Density ** (in tracks/cm^2)		1.35×10^{4}	1.05×10^{4}	1.09×10^{4}	0.92×10^{4}
Observed Track Density (in tracks/cm^2)		1.27×10^{4} $\pm$ 3.21%	0.98×10^{4} $\pm$ 4.68%	1.15×10^{4} $\pm$ 3.8%	0.87×10^{4} $\pm$ 5.6%
C_{eff} (counting efficiency)		94.09%	93.3%	105%	94.5%

* The monitor dose corresponds to the absolute dose of protons. The irradiation lengths were of the order of a few minutes.

** The area to find the track density (i.e. area of the monitor cover hole) is: $A = \pi r^2 = 0.275\ cm^2$

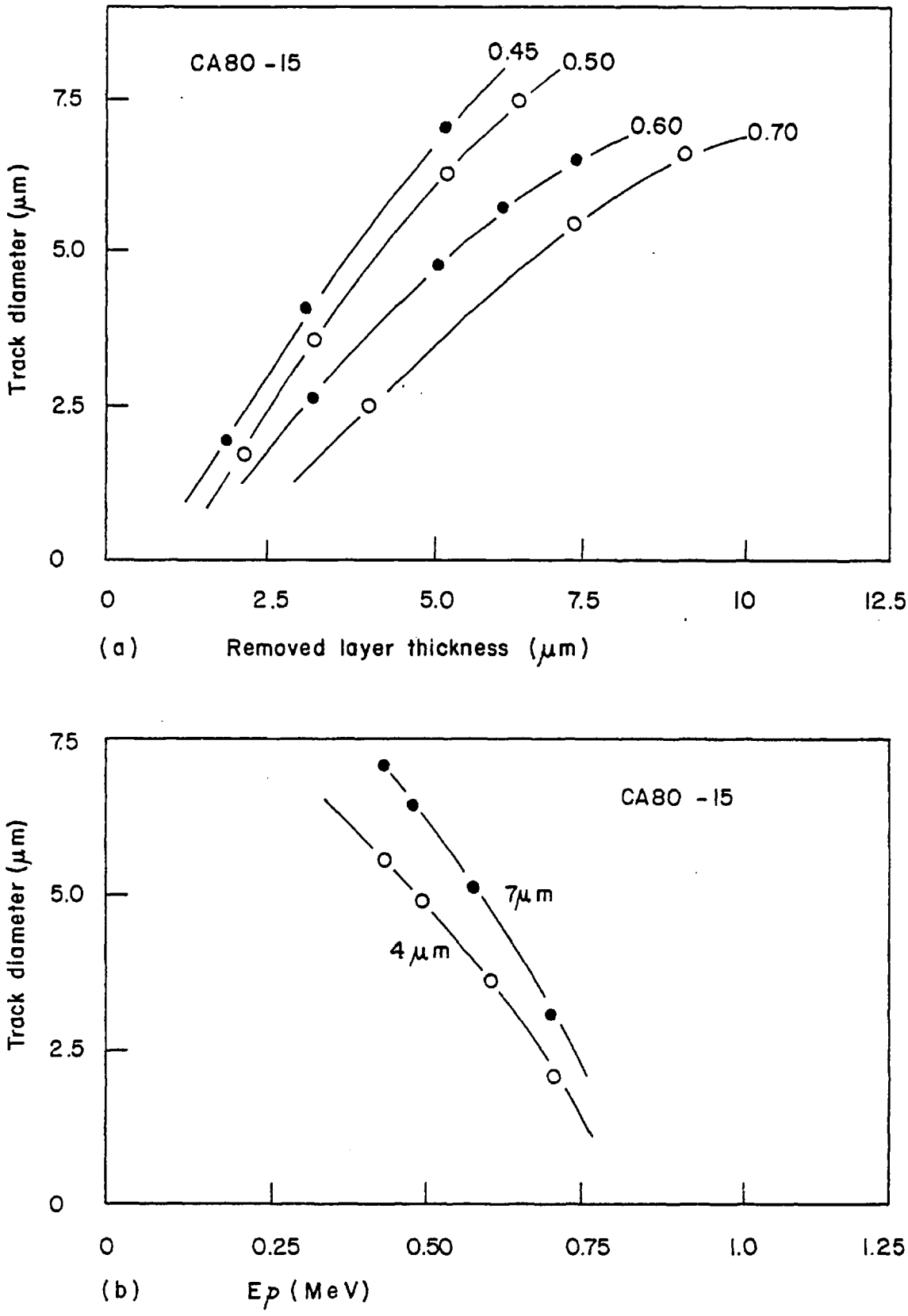


Figure 4.2 (a) Track diameter as a function of the layer removed from the film surface (by etching in 2.5N NaOH at 19°C) for various proton energies in MeV

(b) Track diameter as a function of proton incident energy at removed layer thicknesses of 4 μm and 7 μm

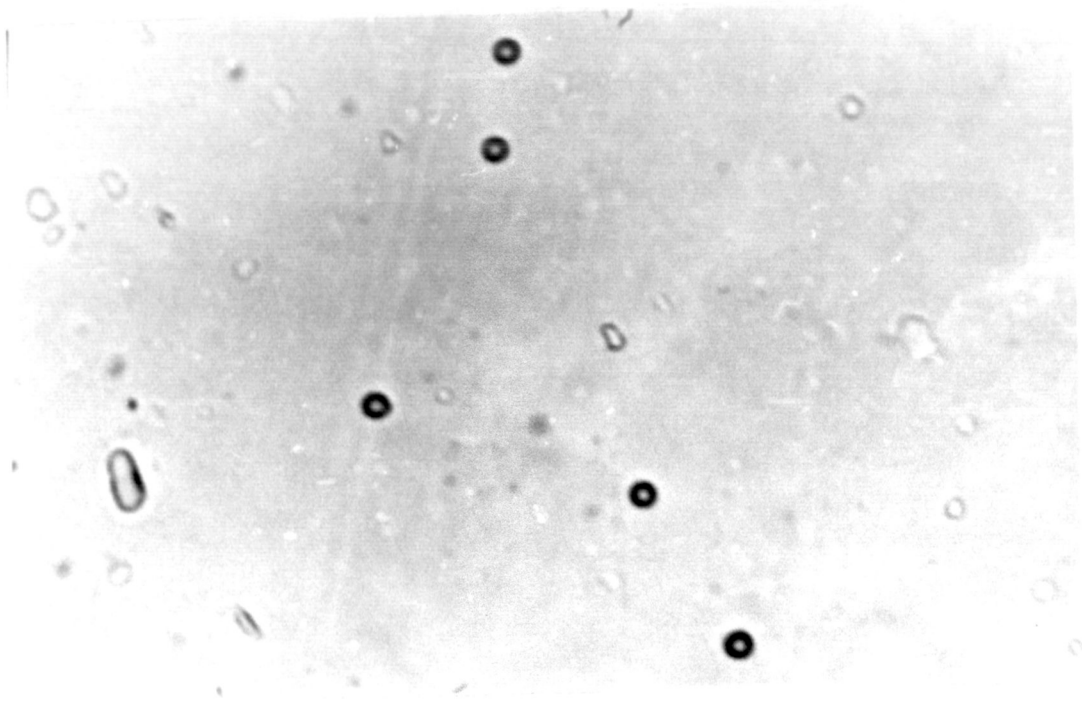
The relationship between the diameter of tracks and proton incident energy at a particular removed layer thicknesses is shown in Fig.4.2 (b). It can be seen, from the diameter of the tracks obtained at a particular thickness of the etched layer, it is possible to draw conclusions on the entrance energy of the protons. Figs.4.3(a) and (b) show microphotographs of 0.45 and 0.5 MeV proton tracks in CA80-15. The optical contrast increases with decreasing energy due to the rapid growth of the radiation damage density.

The histogram of diameter distributions of 0.6 and 0.7 MeV tracks at a removed layer thickness of 4 μm is shown in Figs.4.4(a) and (b).

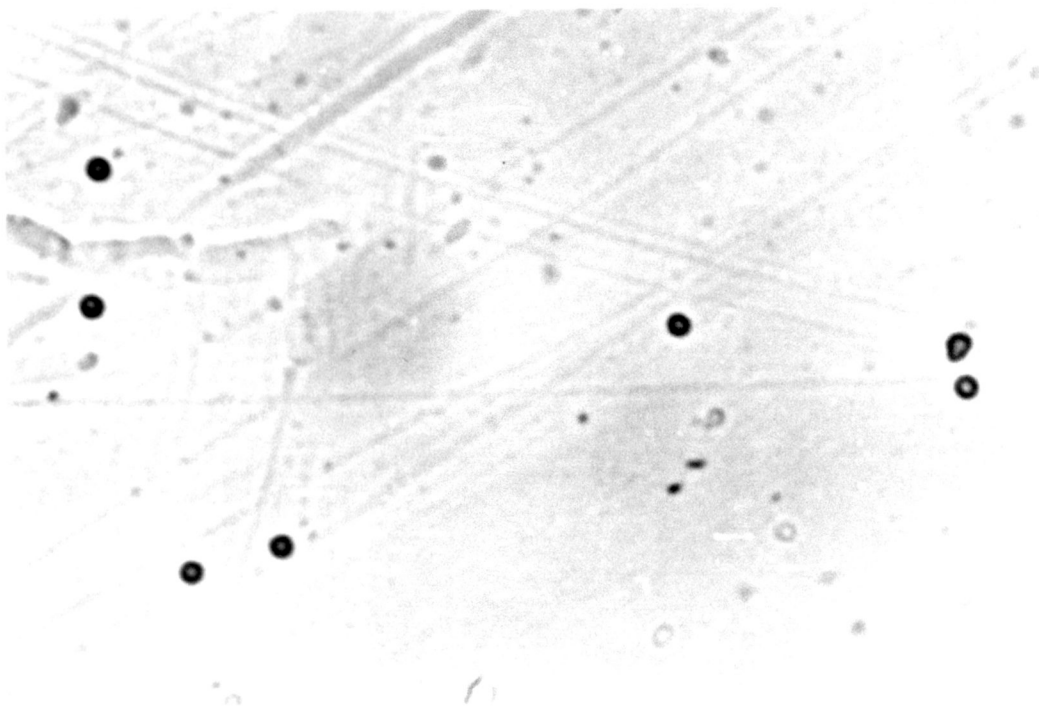
(b) Alpha-particles

Table 4.3 refers to results from counting tracks on CA80-15 films created by alpha particles incident at 90°. It can be seen that the counting efficiency again, is of the order of 100% within 5% limits of error.

Fig.4.5(a) shows the track diameter plotted as a function of film removed for various alpha particle energies. It can be seen that alpha particles must have an energy less than 2 MeV for tracks to be visible with small amounts of etching. The track diameter as a function of the alpha particle energy at a particular removed layer thickness is shown in Fig.4.5(b). A linear extrapolation of the curves in this figure shows that at $\sim$ 1 μm layer removal, alpha particles below $\sim$ 5 MeV would be visible. This value is a

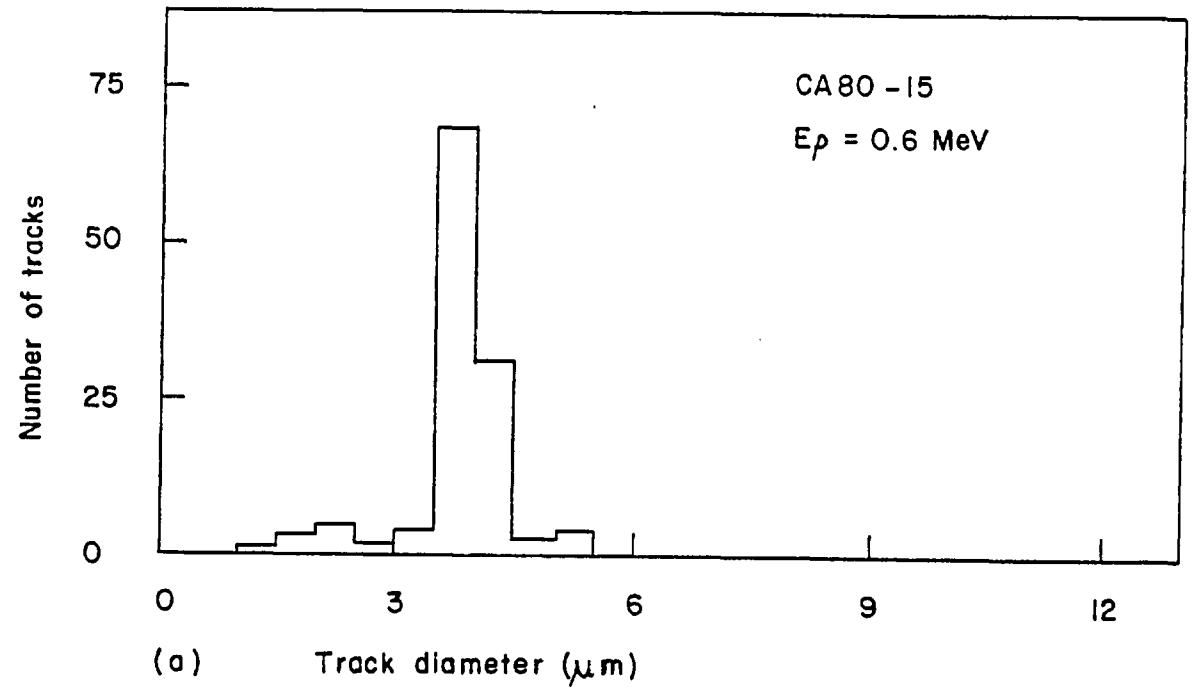


(a)



(b)

Figure 4.3 (a) and (b) 0.45 and 0.5 MeV proton tracks (respectively) in CA80-15 at 90° incidence, etched for 72 hours in 2.5N NaOH at 19°C and observed at a magnification of (x 50 x 10)



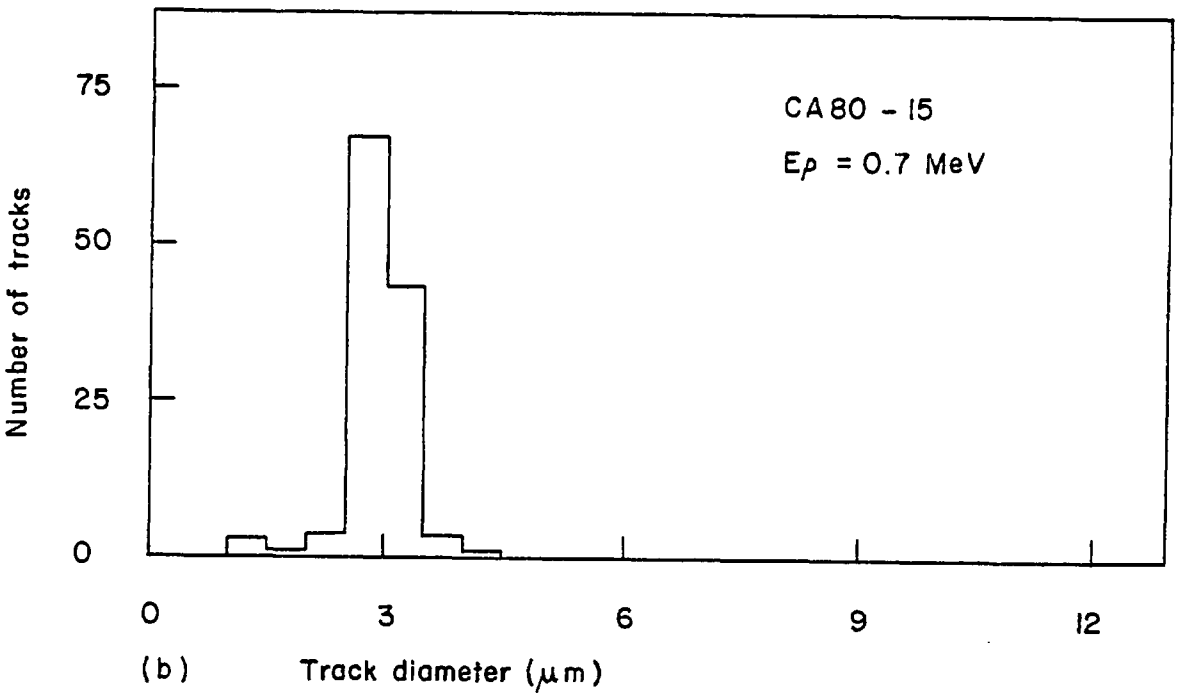


Figure 4.4(a) and (b) The histogram of diameter distributions of 0.60 and 0.70 MeV proton tracks in CA80-15 at a removed layer thickness of 4 μm in 2.5N NaOH at 19°C

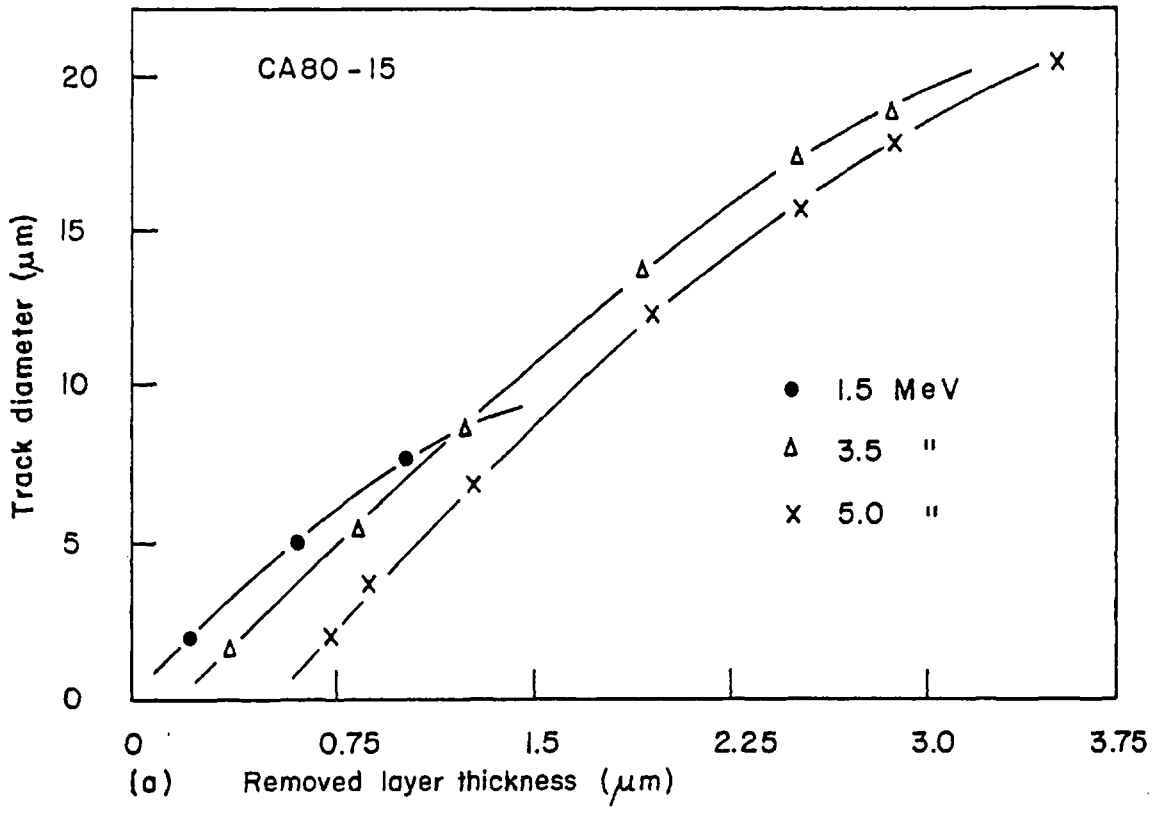
TABLE 4.3

TRACKS FROM α-PARTICLES INCIDENT ON THE CA80-15 FILMS AT 90°

Energy (MeV)		1	2	3	5
Monitor* Dose	In α-Particles	2698	2734	2716	2758
	Integrated Current $\int Idt$	2.58×10^{-7}	4.06×10^{-7}	9.31×10^{-7}	2.1×10^{-6}
Expected Track Density** (in tracks/cm^2)		0.98×10^4	0.99×10^4	0.98×10^4	1.0×10^4
Observed Track Density (in tracks/cm^2)		0.956×10^4 $\pm$ 2.18%	1.03×10^4 $\pm$ 1.95%	0.93×10^4 $\pm$ 2.35%	0.96×10^4 $\pm$ 2.88%
C_{eff} (counting efficiency)		97.55%	104%	94.8%	96%

* The monitor dose corresponds to the absolute dose of alpha-particles. The irradiation lengths were of the order of a few minutes.

** The area to find the track density (i.e. area of the monitor cover hole) is: $A = \pi r^2 = 0.275$ cm^2.



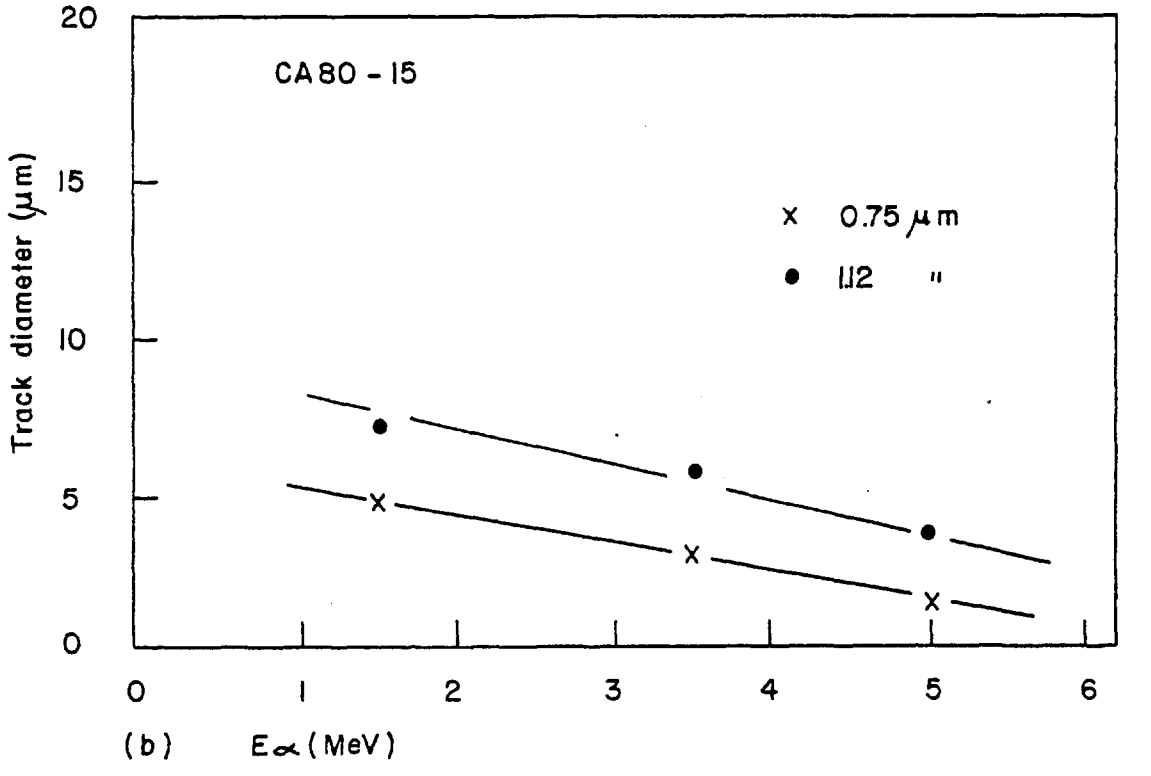


Figure 4.5 (a) Track diameter as a function of removed layer thickness in 2.5N NaOH at 19°C for various alpha particle energies
(b) Track diameter as a function of alpha particle energy at removed layer thickness of 0.75 μm and 1.12 μm

function of the removed layer thickness from the surface of the SSTR.

A microphotograph of 2 MeV alpha particle tracks, incident normal on the surface of CA80-15 and etched in 2.5N NaOH at 19°C and observed at a magnification of 500x is shown in Fig.4.6.

(c) Nitrogen-14 ions

Figs.4.7(a) and (b) show microphotogaphs of 3.5 MeV, Nitrogen-14 tracks in CA80-15 at 90° incidence, etched for 24 hours (corresponding to etched layer thickness of $\sim$ 1 μm) in 2.5N NaOH at 19°C. The optical magnifications are 500x and 560x, respectively. The track counting efficiency was of the order of 100% within limits of error.

(ii) CR-39

(a) Protons

Table 4.4 refers to results from counting tracks on CR-39 films created by protons of various energies incident at 90°. Figs.4.8(a), (b), (c) and (d) show microphotographs of 0.5-3 MeV proton tracks in CR-39. The etching conditions were 7.5 hours in aqueous solution of 6N NaOH at 70°C. It can be seen that the quality of the tracks is excellent and because the energy resolution of the detector is so good, it is possible to determine the energy of incident protons from measurements of track diameters at a particular etching condition. Proton tracks up to 4 MeV were revealed in CR-39. It was found that CR-39 retains its

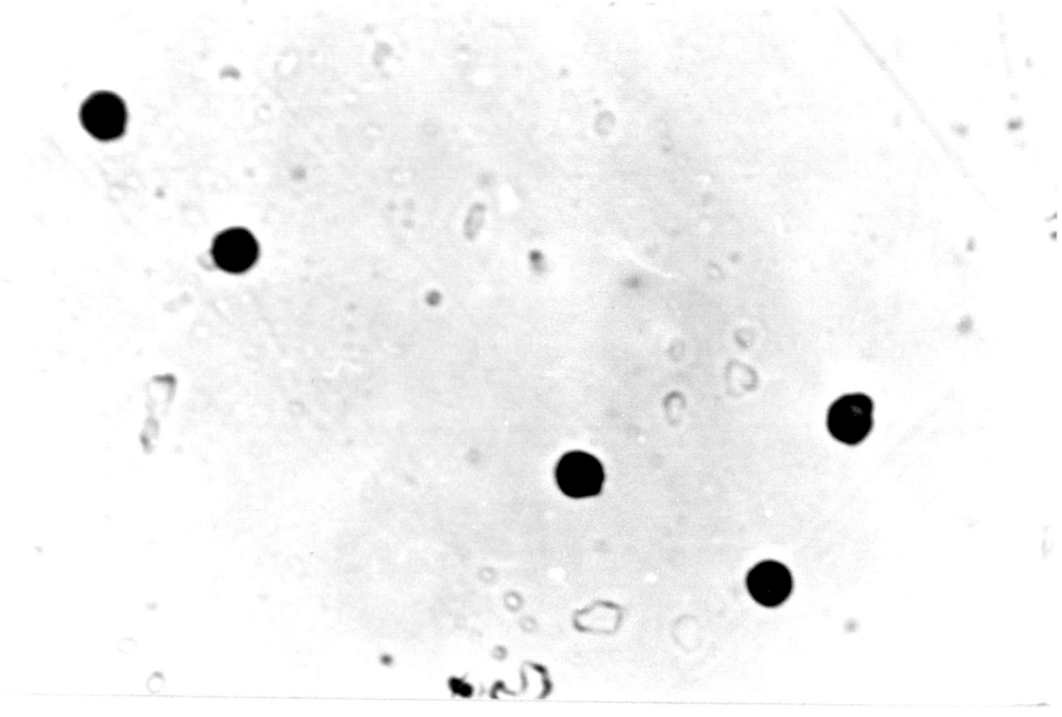
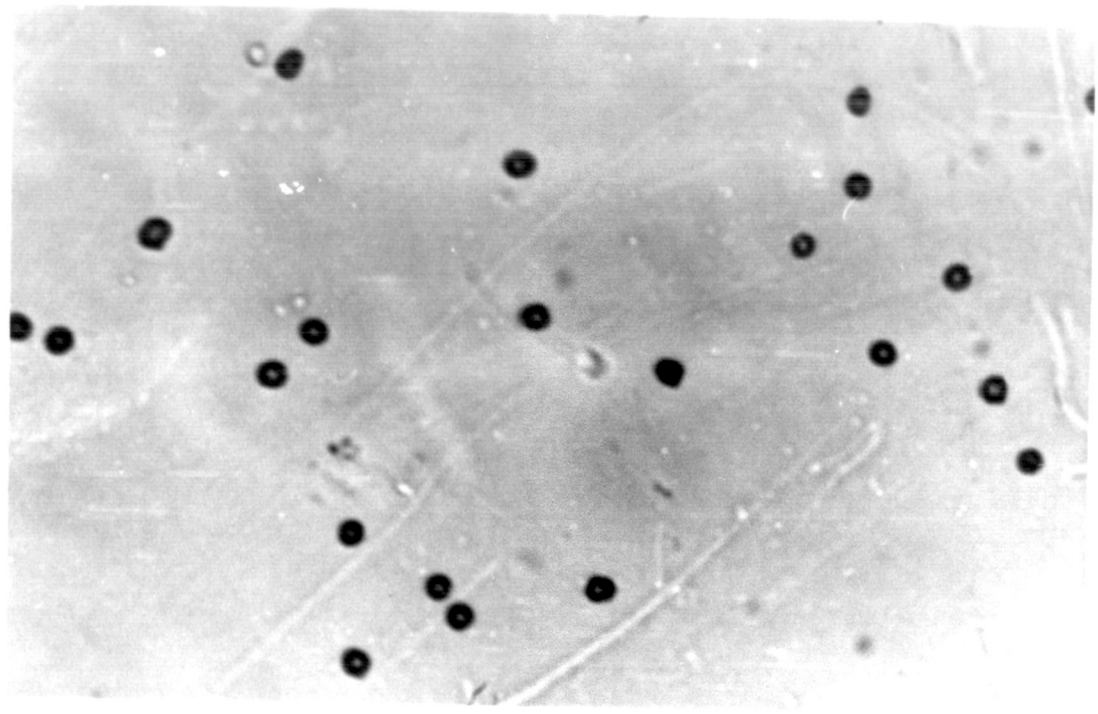
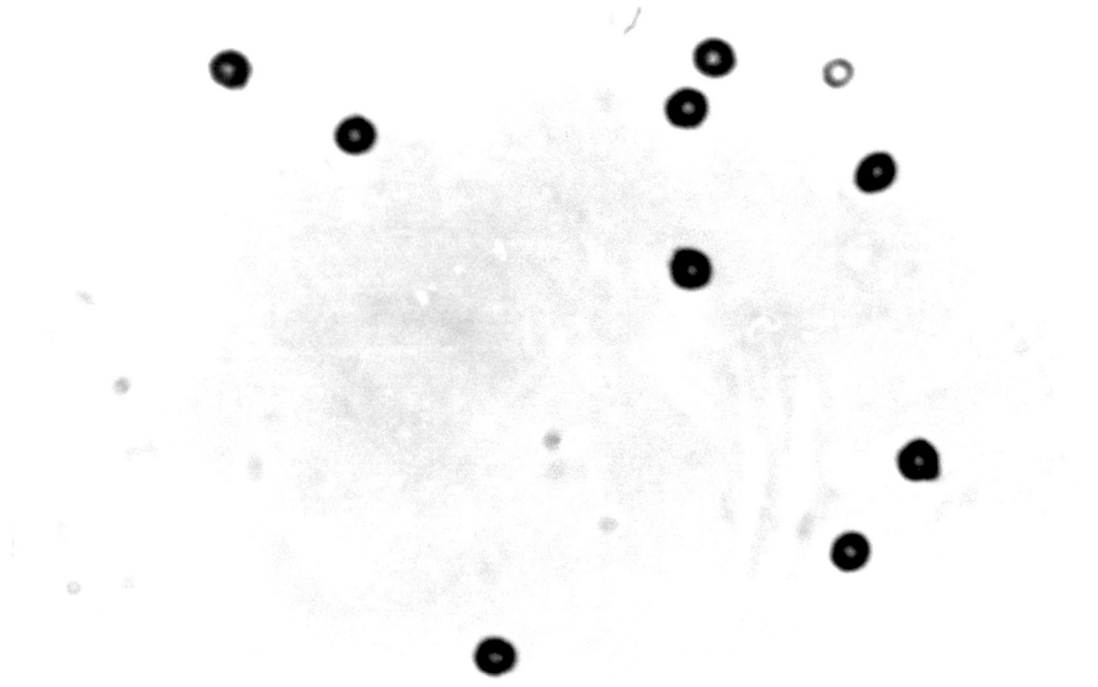


Figure 4.6 Tracks of 2 MeV normally incident alpha particles in CA80-15, etched for 40 hours in 2.5N NaOH at 19°C and observed at a magnification of (x 50 x 10)



(a)



(b)

Figure 4.7 (a) and (b) Tracks of 3.5 MeV normally incident N-14 ions in CA80-15, etched for 24 hours in 2.5N NaOH at 19°C and observed at magnifications of (a) (x 50 x 10), (b) (x 70 x 8)

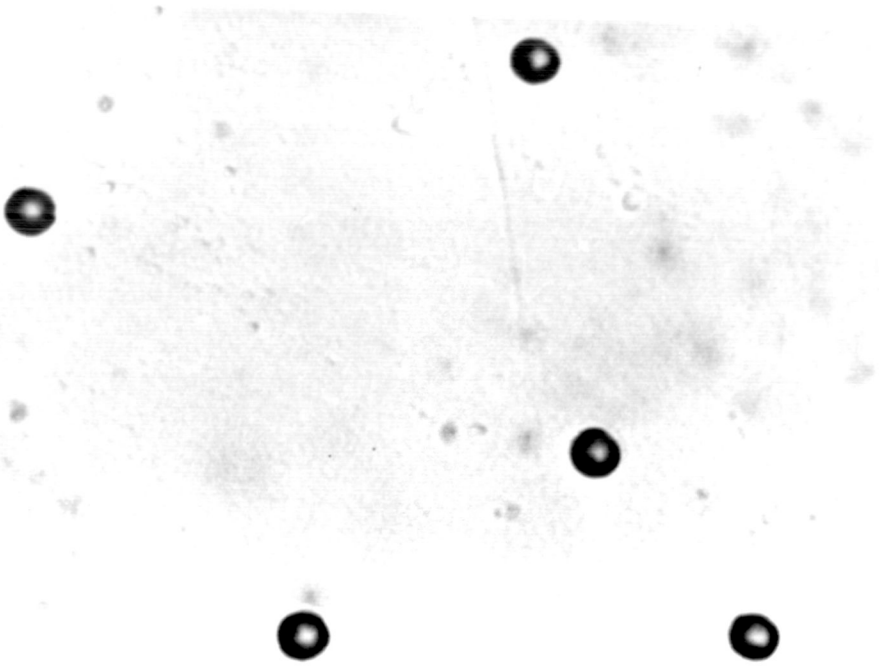
TABLE 4.4

TRACKS FROM PROTONS INCIDENT ON THE CR-39 FILMS AT 90°

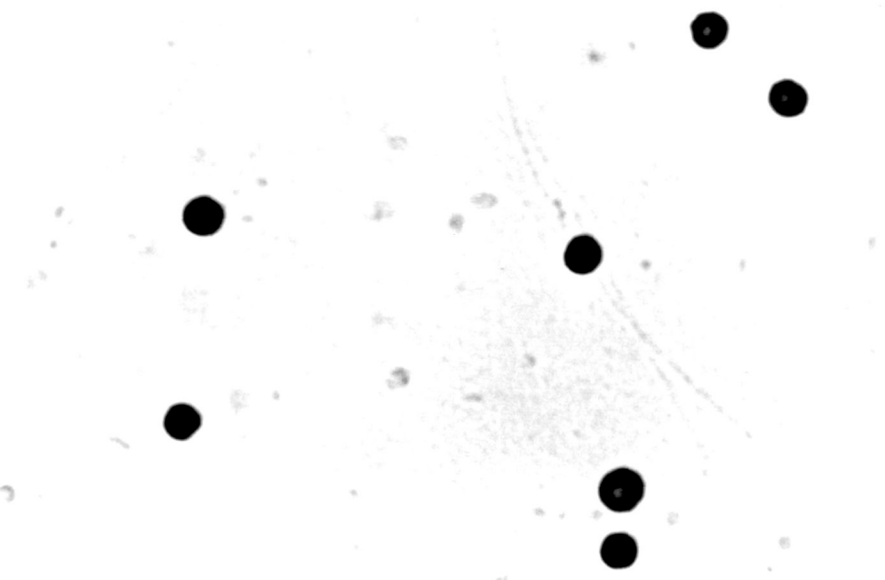
Energy (MeV)		0.50	1.0	2.0	3.0
Monitor* Dose	In Protons	2936	3194	2618	2588
	Integrated Current $\int Idt$	4.5×10^{-8}	2.4×10^{-7}	6.7×10^{-7}	1.6×10^{-6}
Expected Track Density** (in tracks/cm^2)		1.06×10^{4}	1.06×10^{4}	0.95×10^{4}	0.94×10^{4}
Observed Track Density (in tracks/cm^2)		1.02×10^{4} $\pm$ 2.61%	0.94×10^{4} $\pm$ 3.02%	0.92×10^{4} $\pm$ 2.4%	0.91×10^{4} $\pm$ 3.68%
C_{eff} (counting efficiency)		96.2%	88.2%	96%	96.8%

* The monitor dose corresponds to the absolute dose of protons. The irradiation lengths of the order of a few minutes.

** The area to find the track density (i.e. the area of the monitor cover hole) is: $A = \pi r^2 = 0.275\ cm^2$.

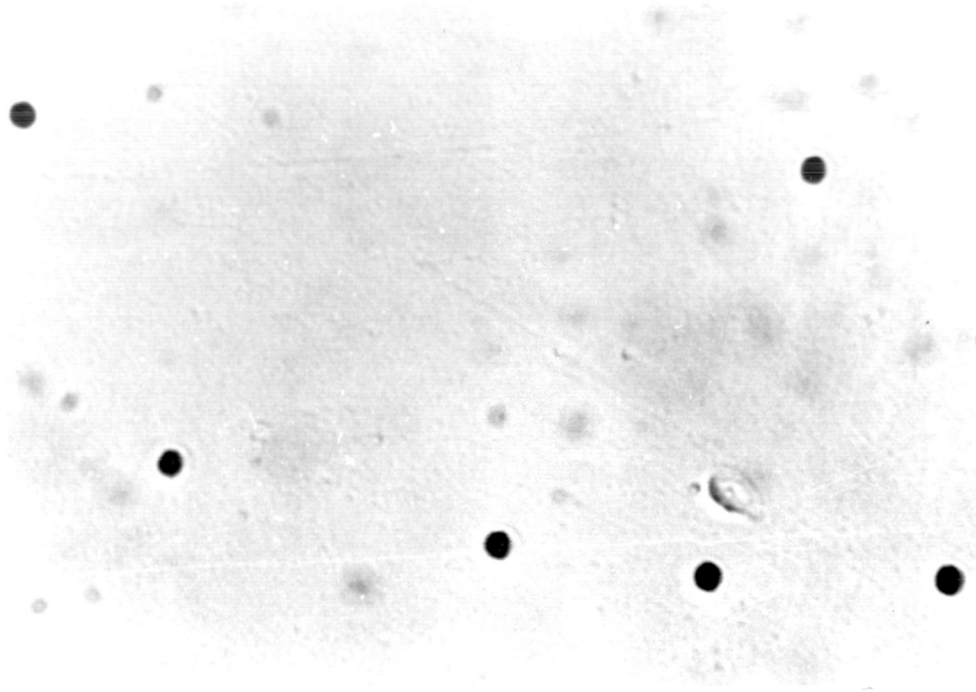


(a)

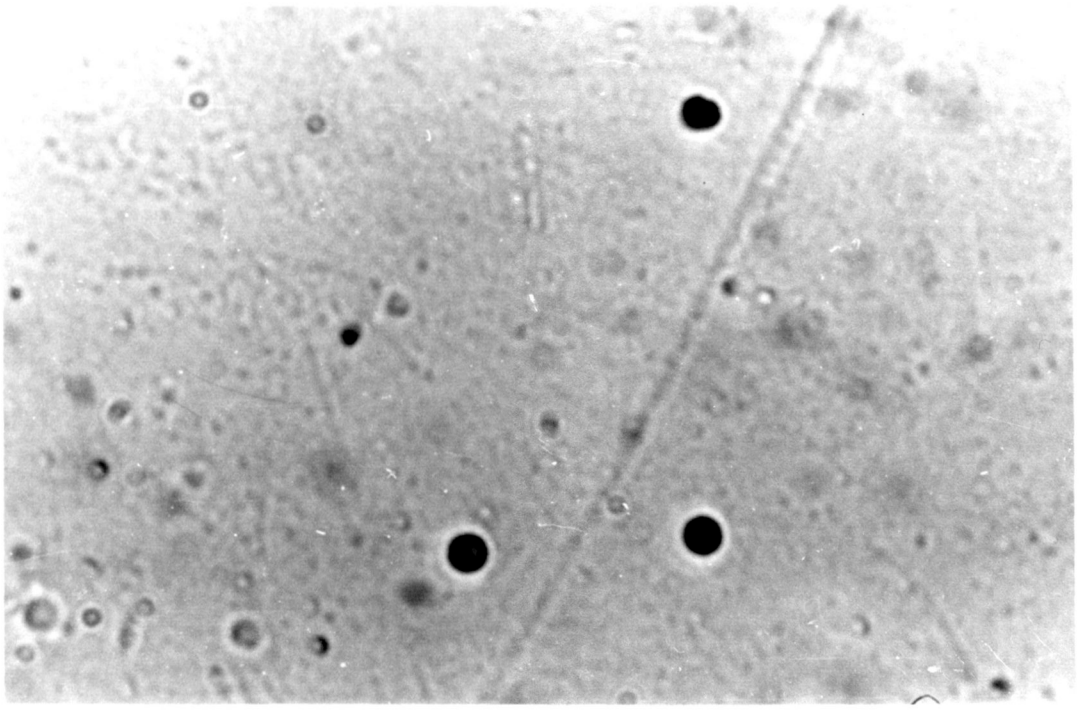


(b)

Figure 4.8 (a) & (b) Tracks of normally incident protons in CR-39, etched for 7.5 hours in 6N NaOH at 70°C.
(a) 0.5 MeV, observed at (x 50 x 8),
(b) 1 MeV, observed at (x 50 x 8)



(c)



(d)

Figure 4.8 (c) & (d) Tracks of normally incident protons in CR-39, etched for 7.5 hours in 6N NaOH at 70°C.
(c) 2 MeV, observed at (x 50 x 8),
(d) 3 MeV, observed at (x 50 x 10)

smooth surface of excellent optical quality even after long periods (24 hours) of etching in 6N NaOH at 70°C.

Figs.4.9(a) and (b) show the track diameter of proton tracks in CR-39 as a function of the removed layer thickness and the proton energy, respectively. A linear extrapolation of track diameter versus proton energy shows that at a removed layer thickness of $\sim$ 3 μm proton tracks below 3 MeV can be revealed. By increasing the length of etching, as shown in Fig.4.9(b), higher and higher energy limits of track revelation can be obtained.

The histograms of diameter distributions of 0.5, 1 and 2 MeV proton tracks at an etched depth of $\sim$ 5.3 μm is shown in Fig.4.10. It is observed that the distributions are quite narrow, indicating better energy-resolution and low background.

(b) Alpha-particles

Fig.4.11 shows the track diameter in CR-39 as a function of alpha particle energy, etched in aqueous solution of 6N NaOH at 70°C. It is observed that from about 2 to 4 MeV the track diameter varies rather rapidly and the curve becomes slightly flattened beyond that energy. Fig. 4.12 shows a microphotograph of alpha particles in CR-39, from ^{241}Am-source with 8 μm aluminium foil, (2π-geometry, $E_\alpha \simeq 3$ MeV), etched in aqueous solution of 6N NaOH at 70°C for 3 hours. Note the excellent optical quality and low background of the etched surface.

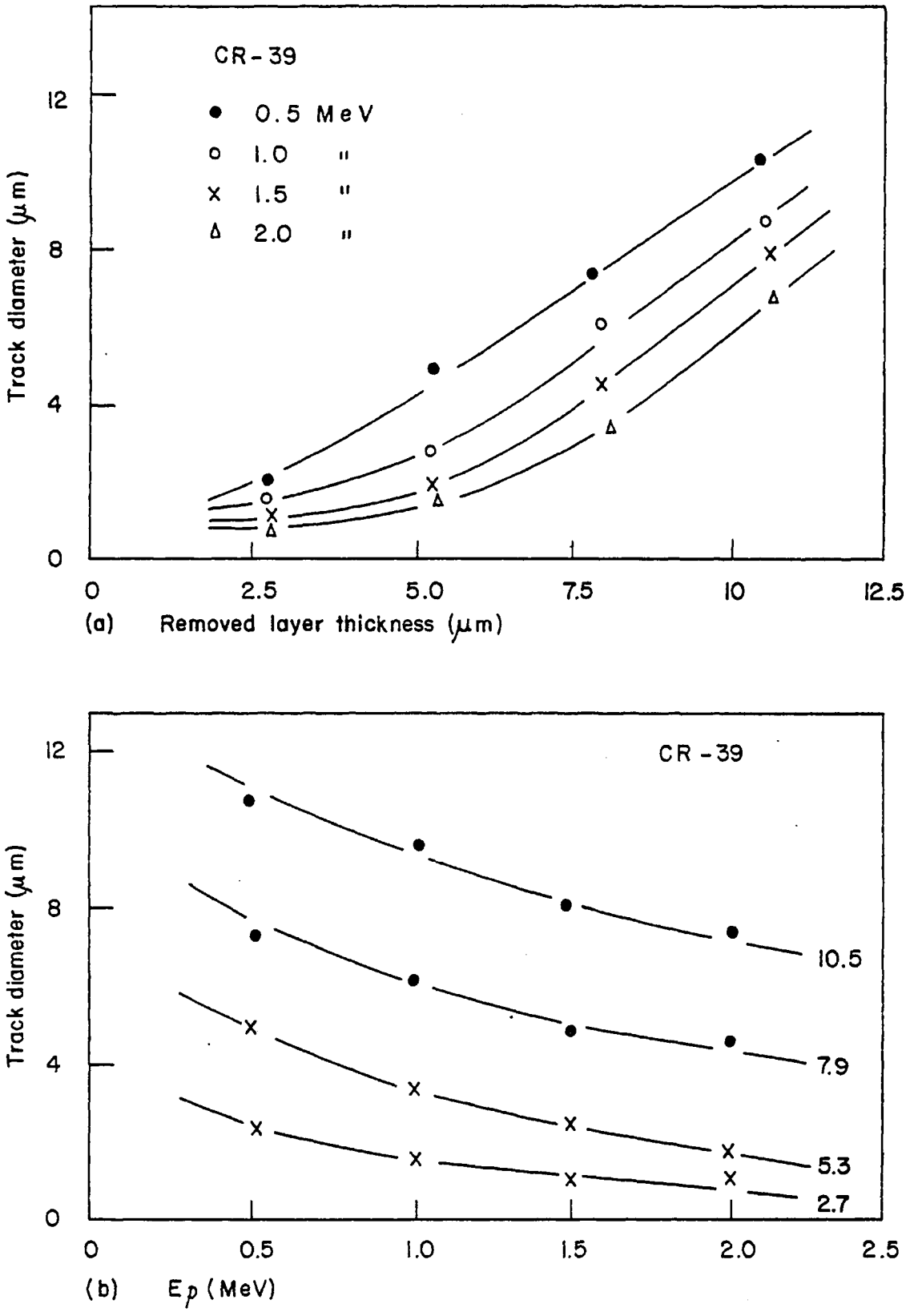


Figure 4.9 (a) Track diameter as a function of removed layer thickness in 6N NaOH at 70°C, for various proton energies

(b) Track diameter as a function of proton energy for various values of the removed layer thickness (in μm)

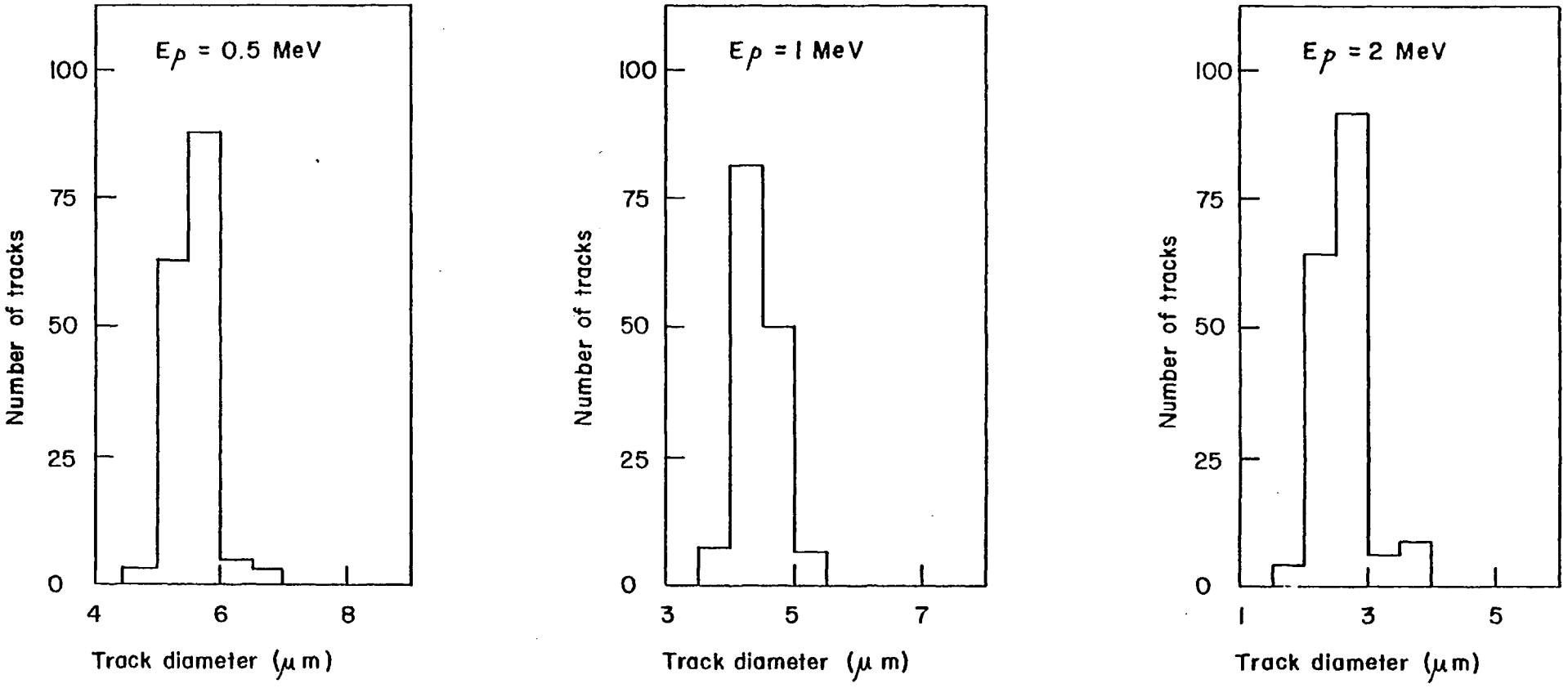


Figure 4.10 Diameter distributions of normally incident protons in CR-39 at an etched depth of 5.3 μm

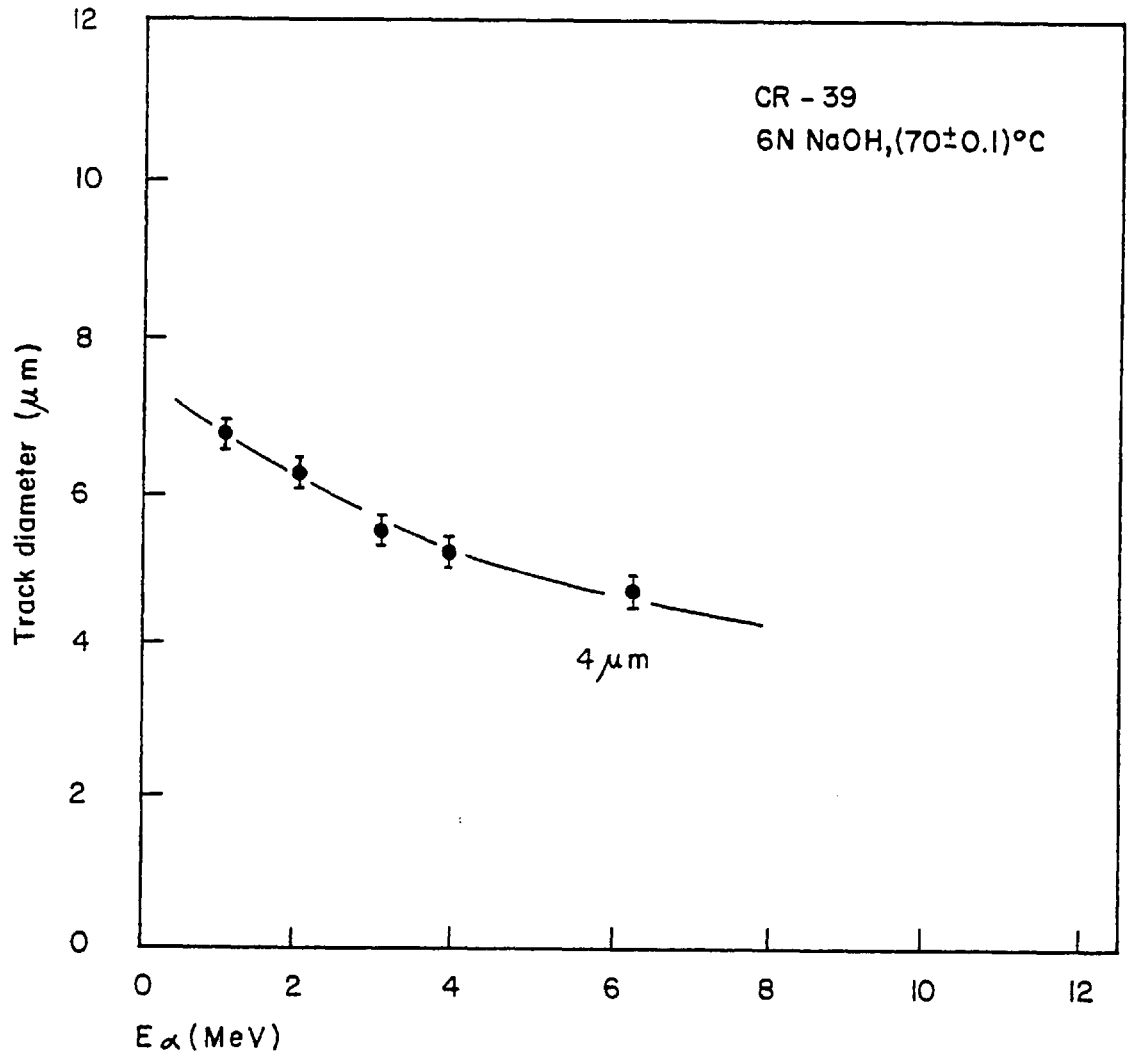


Figure 4.11 Track diameter in CR-39 as a function of alpha particle energy at a removed layer thickness of 4 μm in 6N NaOH at 70°C

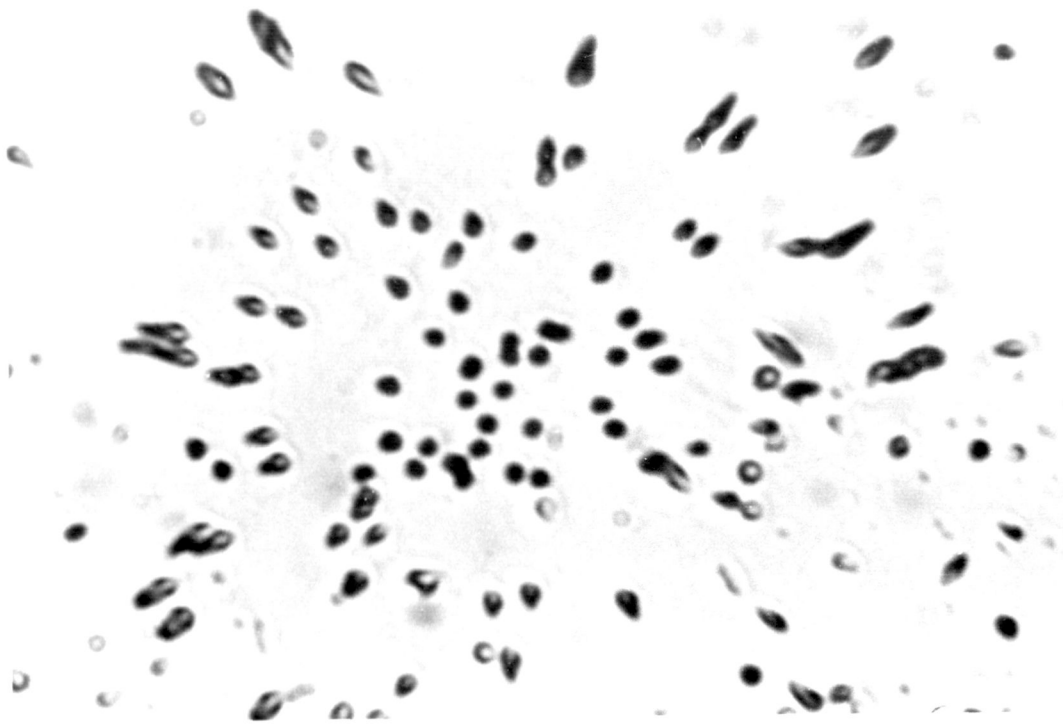


Figure 4.12 Tracks of 3 MeV alpha-particles in CR-39 etched for 3 hours in 6N NaOH at 70°C, and observed at a magnificantion of (x 50 x 10). CR-39 was irradiated in 2π-geometry with an ^{241}Am-source

CR-39 response to alpha particles in the energy range from 3 to 6 MeV (Fig.4.11) is such that differential alpha particle spectrometry would be difficult in this range. However, the response and sensitivity in this ionization region make CR-39 an excellent candidate for integral (n,α) reaction rate measurements.

4.3 EXPERIMENTS ON THE REACTOR 'CONSORT'

These experiments consist of CA80-15 irradiations in the vertical thermal column facility[86], of the University of London reactor 'Consort' at Silwood Park.

It was established in the previous section that CA80-15 is sensitive to low energy protons. Due to the high nitrogen content of CA80-15 (see Table 2.3), it was necessary to investigate its response to thermal neutrons, which produce 0.534 MeV protons from the $^{14}N(n,p)^{14}C$ reaction (Q-value = 0.626 MeV, σ = 1.7b)[87].

It was essential to find the sensitivity of CA80-15 to thermal neutrons with a good accuracy, since it was decided to use this SSTR for the selective detection of fast neutrons in the presence of low energy neutrons.

4.3.1 Description of the Vertical Thermal Column Facility

The vertical thermal column facility (VTC) consists of a stack of graphite blocks in a 5 x 5 array and 3 blocks in height. The cross-sectional side elevation on the thermal column extension is shown in Fig.4.13(a), while the arrangement of the facility is shown in Fig.4.13(b). Each block

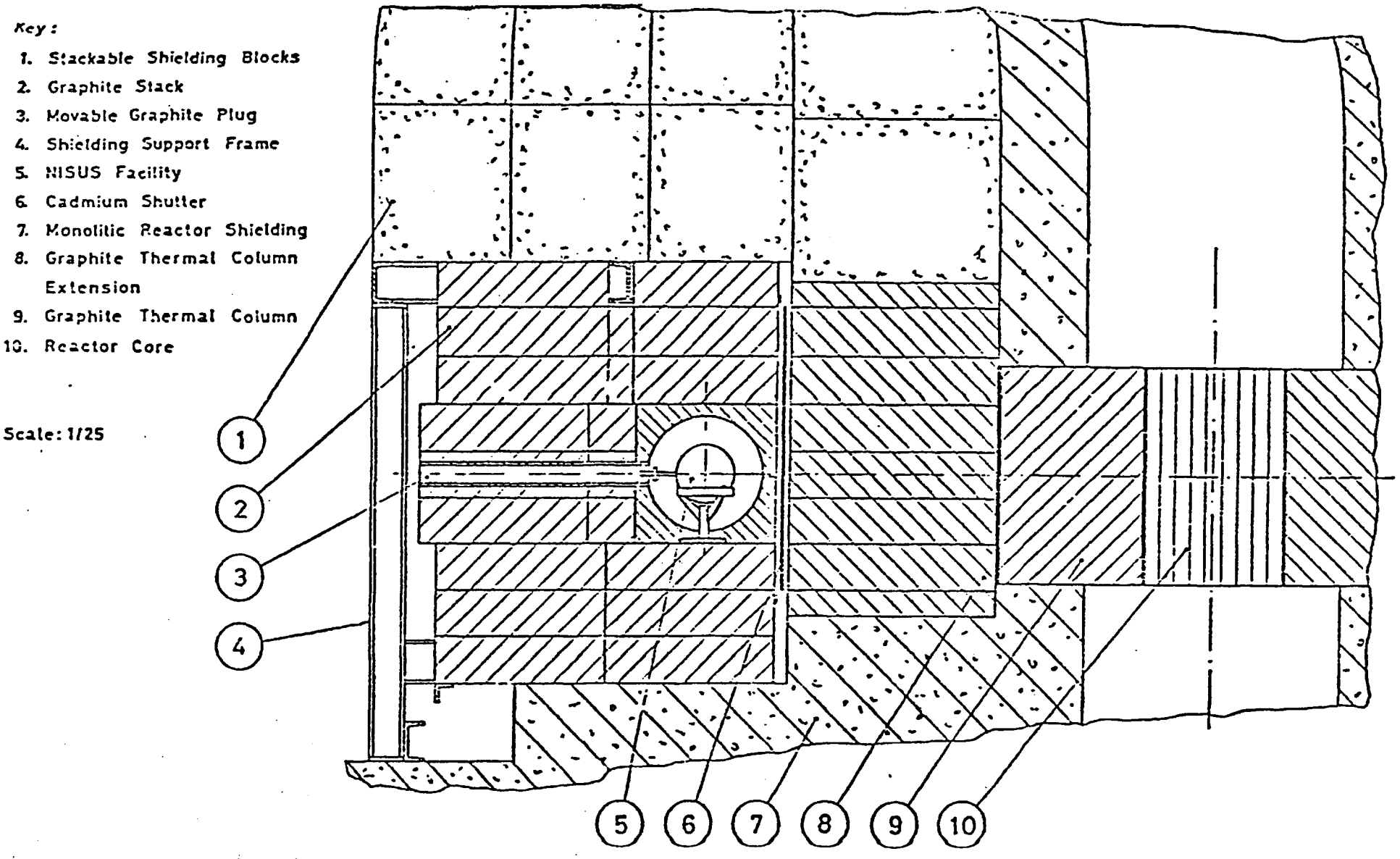


Figure 4.13(a) The cross-sectional side elevation on the thermal column extension

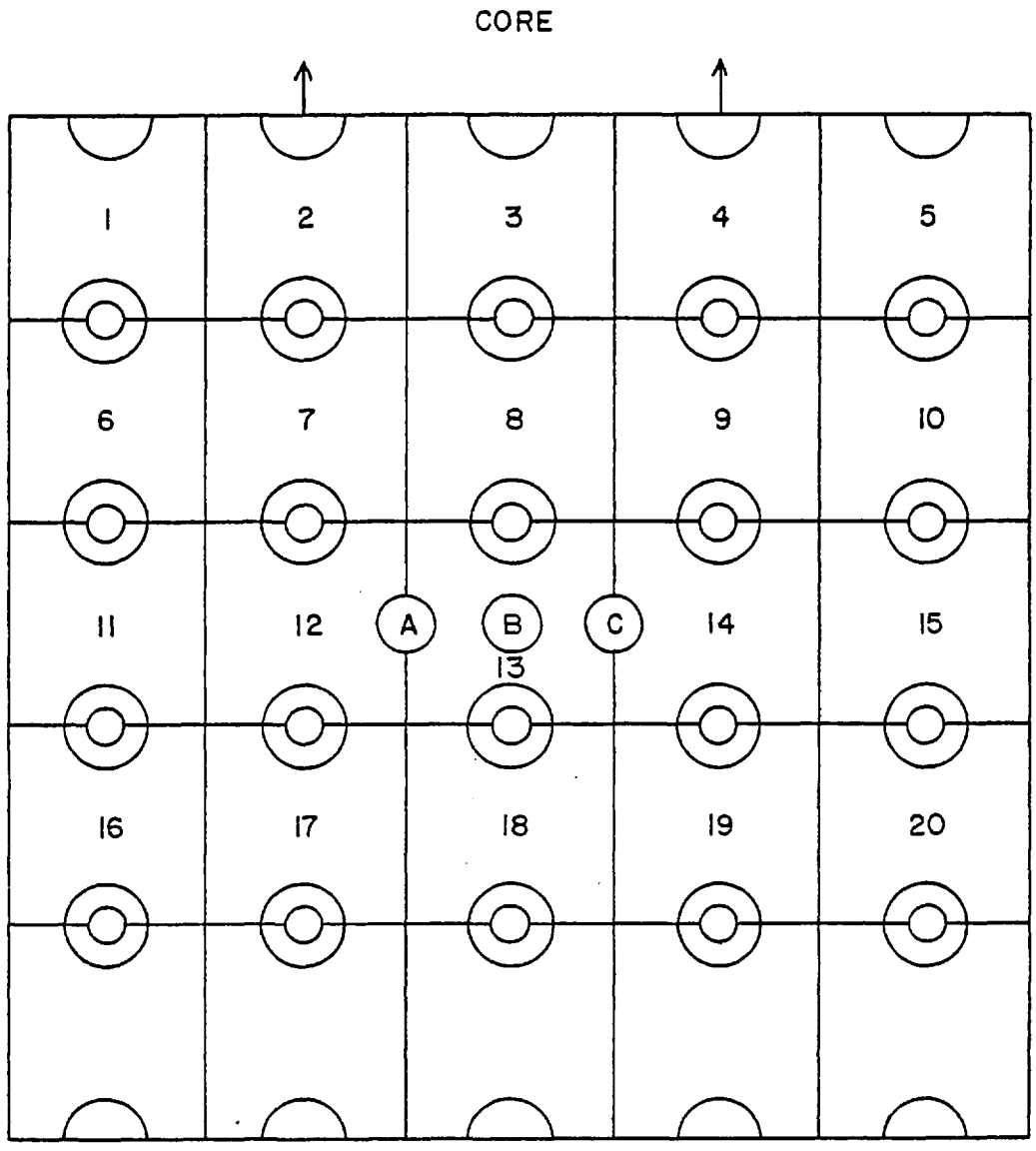


Figure 4.13(b) Arrangement of the vertical thermal column graphite stack

has semi-circular channels cut down two opposite sides and adjacent blocks make up circular channels which are filled with removable sleeves and channels.

The stack is supported on an aluminium cover plate resting on the vertical stub of the thermal column. The space between the stack and the cave walls is partially filled with small concrete blocks to improve the radiation shielding. The cave is closed in the vertical direction by concrete shielding blocks, one of which has conduits for electrical cables. The axial flux distributions have been measured[86], in positions B, 18 and 3 by removing the central plugs (Fig.4.14). The transverse flux distributions have been measured in each position at a constant height (61.5 cm) with the upper plug removed. Table 4.5 summarises the neutron fluxes in each position normalised to that at the centre (position B).

By making the assumption that the neutron flux distribution can be expressed in a form separable in the three Cartesian coordinates, i.e.

$$\phi(x,y,z) = X(x)Y(y)Z(z) \qquad (4.1)$$

and using the data from Table 4.5 and Fig.4.14, the flux at any accessible point in the stack may be estimated.

4.3.2 Experimental

In the case of thermal neutrons a sensitivity of 4.0×10^{-6} tracks per neutron for CA80-15 was calculated using the theoretical response equation 2.3 in Chapter 2.

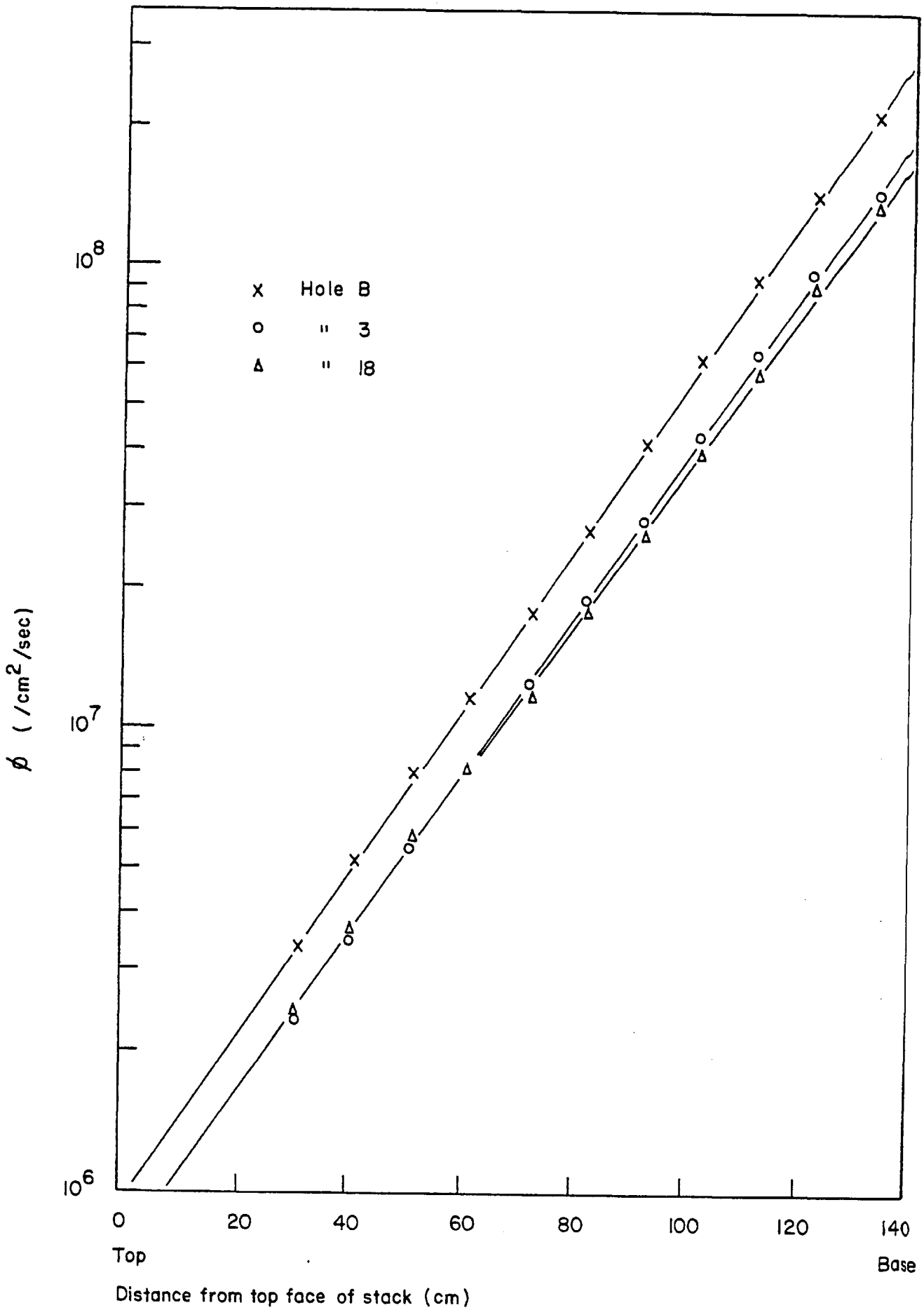


Figure 4.14 Flux distribution at 100 kW in the vertical thermal column facility

TABLE 4.5

RELATIVE TRANSVERSE FLUX DISTRIBUTION AT 61.5 cm FROM THE TOP FACE

Position	Relative Flux	Position	Relative Flux
1	0.36	13	0.99
2	0.63	14	0.85
3	0.72	15	0.49
4	0.63	16	0.40
5	0.35	17	0.64
6	0.49	18	0.75
7	0.86	19	0.66
8	0.99	20	0.40
9	0.85	A	1.00
10	0.47	B	1.00
11	0.50	C	0.99
12	0.85		

This value was used as a guide to decide the neutron fluence, which will result in a convenient track density for scanning purposes. From the neutron flux distributions given in Fig.4.14 and Table 4.5, it was decided to perform irradiation in hole 13 (see Fig.4.13(b)) at 35 cm below from top face.

CA80-15 samples (2 x 2 cm), along with two gold foils (weight 4.5 mg each), one each on either side of CA80-15 were contained in a standard aluminium container; which was lowered in the VTC and positioned at the desired height. One piece of CA80-15 was enclosed in a cadmium capsule (thickness 0.4 mm) which will absorb thermal neutrons. Gold foils were irradiated to check the accuracy of neutron flux data given in Fig.4.14. The samples were irradiated for 30 minutes at a full reactor power of 100 kW.

After the irradiation, the gold foil β-activity was measured on an absolute 4π β-γ coincidence counter. The neutron fluence calculated, $(7.10 \pm 0.35) \times 10^9$ n/cm^2 was in agreement to within 4% of the value given in Fig.4.14 for the position where the irradiation took place.

4.3.3 Results and Discussion

The thermal neutron irradiated CA80-15 films were etched in 2.5N NaOH aqueous solution at 19°C for several time steps. Cold etching conditions were adopted for reasons discussed earlier, in Section 4.2.2. As control the same plastic sample but unirradiated was treated with the same etching agent under the same etching conditions, and some background tracks were detected. Therefore, in order

to estimate the real number of proton tracks, produced from the threshold reaction $^{14}N(n,p)^{14}C$, it was necessary to subtract the number of background tracks from the total number of tracks per unit area detected in the irradiated CA80-15.

The track density as a function of the removed layer thickness (in 2.5N NaOH at 19°C) is shown in Fig.4.15(a). It was observed that the tracks grow in size and number during early period of etching, which can be explained as follows:

(i) very small features which were not originally perceptible are enlarged;

(ii) new tracks that begin and end beneath the original surface are encountered, and

(iii) the etching along a track having a low dip angle and damage that increases downwards reveals tracks partway along their lengths.

The track density reaches a plateau at an etched depth of $\sim$ 3.6 μm, because at long etch times some of the original tracks may be lost as their optical contrast is reduced.

Fig.4.15(b) shows the track diameter distributions at an etched depth of 3.68 μm in CA80-15 exposed to thermal neutrons. The wide range of diameter distribution is due to the basic property of 'intrinsic' SSTRs, that at any stage of etching the observation plane intersects tracks at all stages of production, ranging from the beginning of a track to the end of its range.

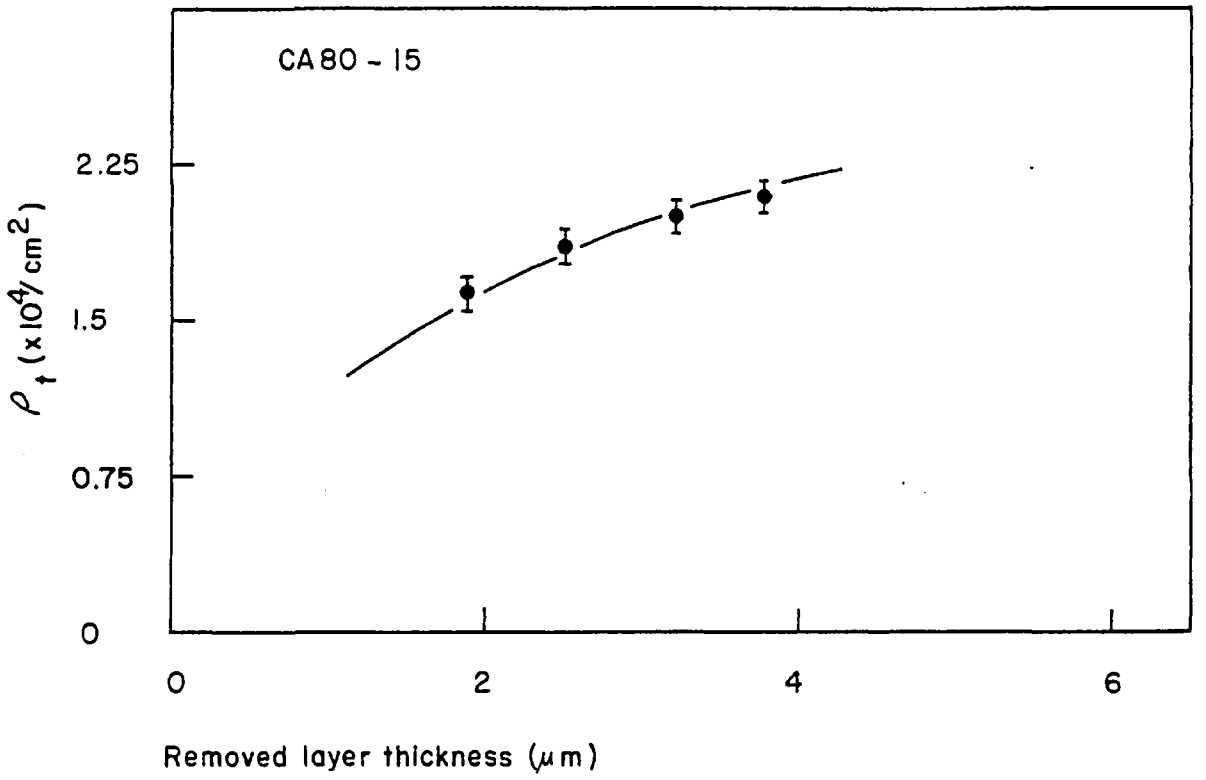


Figure 4.15(a) The track density, ρ_t as a function of the removed layer thickness, for CA80-15 exposed to thermal neutrons. Etching was carried out in 2.5N NaOH at 19°C

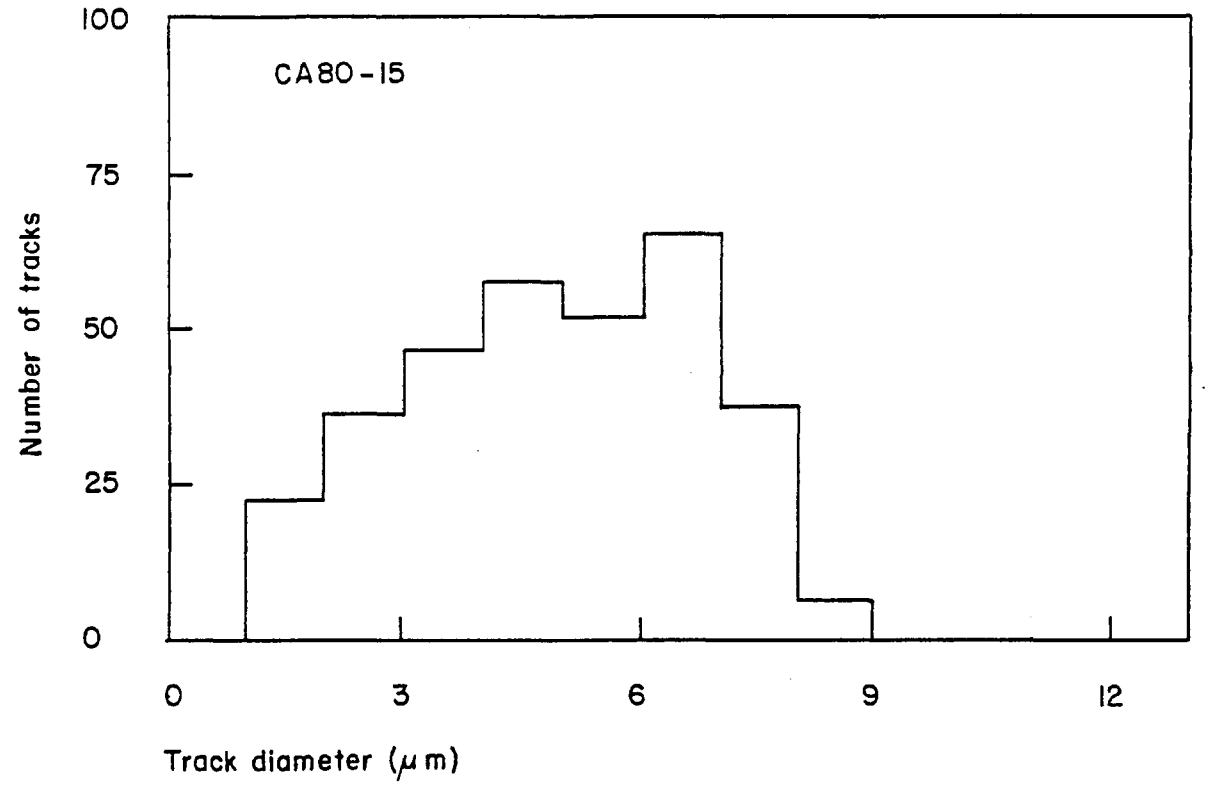


Figure 4.15(b) Track diameter distribution inCA80-15 exposed to thermal neutrons. Removed layer thickness is 3.68 μm

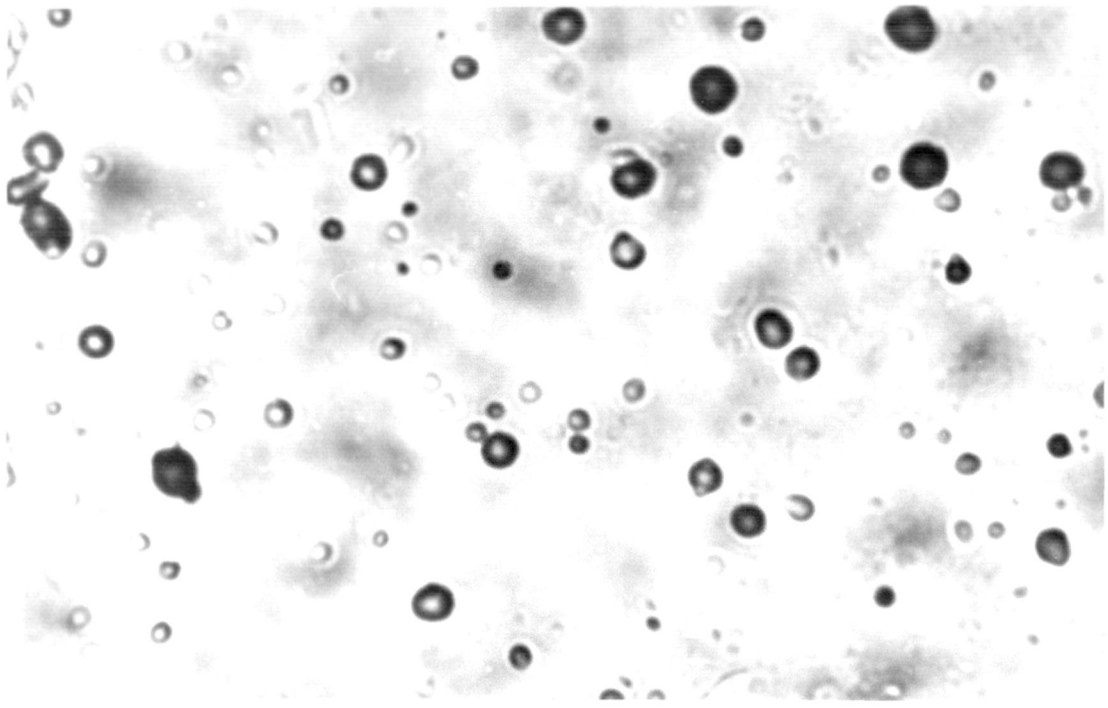


Figure 4.16 Proton tracks from $^{14}N(n,p)^{14}C$ reaction in CA80-15 exposed to thermal neutrons. Etched for 96 hours in 2.5N NaOH at 19°C and observed at a magnification of (x 70 x 8). Very large blobs are 'background' tracks

Fig.4.16 shows a microphotograph of proton tracks in CA80-15 exposed to thermal neutrons and etched in 2.5N NaOH at 19°C (removed layer thickness = 3.68 μm). Very large blobs are background tracks.

The sensitivity (η_{exp}) of CA80-15 to thermal neutrons is found to be $(3.40 \pm 0.22) \times 10^{-6}$ tracks per neutron, being visible after an etched depth of 4 μm. No tracks were observed in CA80-15 which was enclosed in cadmium capsule during the irradiation, but some background, which confirms that the observed tracks resulted from the $^{14}N(n,p)^{14}C$ reaction.

4.4 EXPERIMENTS ON THE 'IBIS' ACCELERATOR

These experiments consist of monoenergetic fast neutron irradiations performed using the IBIS accelerator at A.E.R.E. Harwell. The experiments were designed to give the sensitivity of CA80-15 and Makrofol K.G as a function of neutron energy. The two major objectives of the present experimental work were:

(i) Calibration of CA80-15 and Makrofol K.G as a function of neutron energy and the examination of the effect of chemical etching on the neutron detection efficiency of the SSTRs employed.

(ii) To examine the credibility of the theoretical model developed in Chapter 2 to calculate the neutron sensitivity of SSTRs as a function of energy.

4.4.1 Description of 'IBIS' Accelerator

IBIS (Intense Bunched Ion Source)[88], consists of a 3 MeV Van de Graaf machine equipped with a pulsed ion source. The machine consists of a high current radio-frequency ion source giving ∿ 1 mA of protons, deuterons, or helium ions, whose beam is chopped by sweeping it in an elliptical path across an aperture. Sweeping is accomplished by the two pairs of plates at right angles, connected through a suitable phasing network to a 1 Mc/sec oscillator.

After acceleration by the Van de Graaf, the beam enters a bunching system whose principal element is a wide aperture magnet between whose poles the charged particle beam can follow a path whose length depends on the point of entry. By sweeping the pulse of particles as they emerge from the machine across the entrance aperture to this magnet, different parts of the pulse follow different paths. When this sweep is suitably synchronised, the first path of the pulse is made to follow the longest path and the last part the shortest, so that all parts of the pulse arrive simultaneously.

The bombardment of targets like tritium, deuterium and lithium with protons, deuterons or helium ions produces neutrons. The energy of neutrons is a function of the angle of emergence from the target.

4.4.2 Experimental

The experimental set-up used for monoenergetic fast neutron irradiations at IBIS site, A.E.R.E, Harwell is shown in Fig.4.17. The fast neutrons emitted from the target have

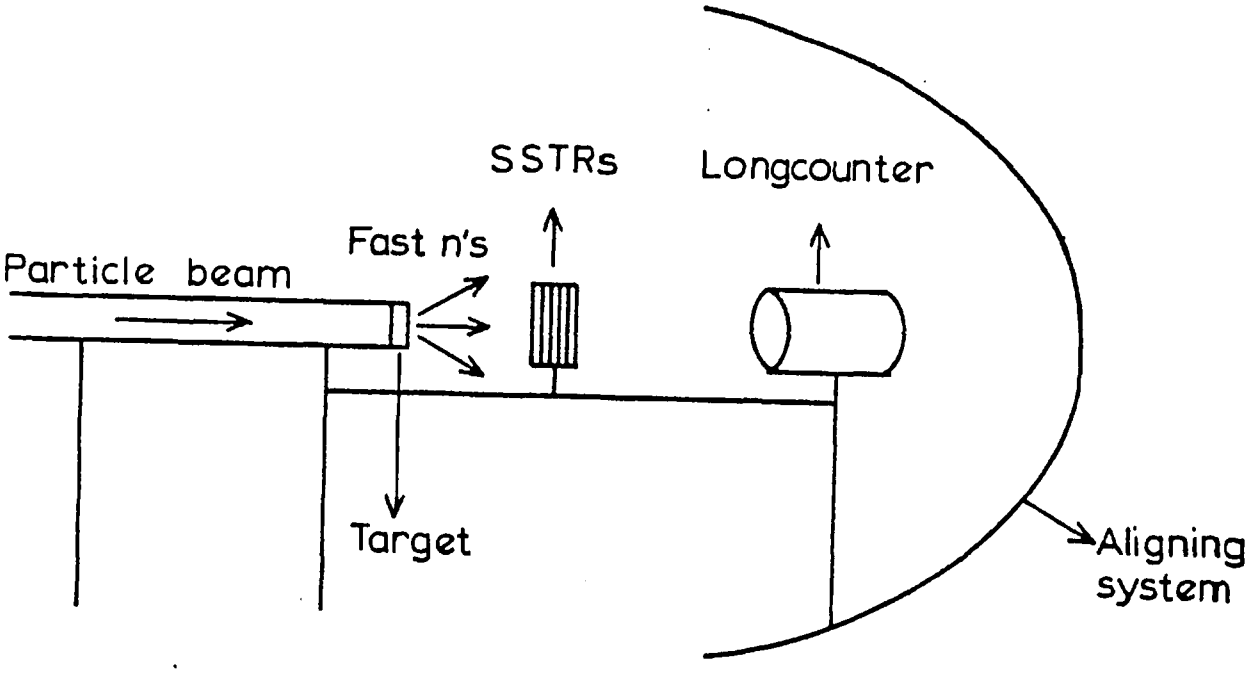


Figure 4.17 The experimental set-up used for monoenergetic fast neutron irradiations at the 'IBIS' site A.E.R.E., Harwell. Several energies and fluences of neutrons were obtained. Neutron fluences were monitored during irradiation by a BF_3 'long counter'

a wide energy range because the energy of the neutrons depends on thescattering angle. The neutrons are mono-energetic at a particular angle of emergence from the target. The target was located 15 feet above the floor. The floor constitutes a very large scatterer and it could constitute a serious background, if the apparatus were nearer to the floor.

Neutrons from 0.2 to 6 MeV were produced using D-D, P-T and P-Li reactions. This energy range is particularly relevant to reactor physics applications. However, to examine the sensitivity of CA80-15 at high neutron energies, particularly of the reaction $^{12}C(n,n')3\alpha$, 17 MeV neutrons were also produced from D-T reaction.

The neutron fluence was measured with a BF_3 'long counter' which was calibrated on a ^{252}Cf neutron source. The aligning system on the accelerator (see Fig.4.17) is such that the BF_3 counter 'sees' neutrons emitted from the target at a particular angle.

For a fission neutron source a sensitivity of 1.3×10^{-5} tracks per neutron for CA80-15 was calculated using the theoretical model developed in Chapter 2. This value was used as a guide to have a neutron fluence of about $10^9 n/cm^2$ in SSTRs, which will result in a convenient track density for counting purposes.

Makrofol K.G films were irradiated along with a 1.23 mg/cm^2 natural uranium foil to measure the neutron fluence by counting the tracks from the (n,f) reaction.

Neutrons were incident normal to the surface of the SSTRs (of area $\sim$ 4 cm^2) and the irradiated sides on all films were marked so as to compare the number of tracks on the 'front' and 'back' surfaces. To examine the angular dependence of the track density, irradiations at two neutron energies, namely 3 and 17 MeV were performed at 0°, 30° and 60° angles of incidence, in addition to at 90°. The main characteristics of these irradiations are summarised in Table 4.6. The neutron energies are accurate to within $\pm$ 4%.

The irradiated films were stored at $\sim$ 4^oC until etching and evaluation could be carried out, typically within a few weeks of irradiation. Etching was performed with aqueous solution of 6N KOH at 60^oC in several time steps up to a total of 60 minutes. All tracks having dimensions greater than $\sim$ 1 μm were counted under optical microscope with total magnification of up to x560. However, for triple track densities from $^{12}C(n,n')3\alpha$ reaction, higher magnifications of up to x1400 were used.

Fast etching conditions were selected in these experiments, as they let the tracks increase their size quickly for counting under lower magnification in order to scan over a wide area of the etched surface to get better statistics. Again, for control purposes, unirradiated samples were also etched and examined for background.

TABLE 4.6

MAIN CHARACTERISTICS OF THE MONOENERGETIC FAST NEUTRON IRRADIATIONS USING THE IBIS ACCELERATOR AT AERE, HARWELL

Reaction	Particle Energy (MeV)	Angle* (deg.)	Neutron Energy (MeV)	Neutron Fluence in SSTR's ($/cm^2$)
$^{7}Li(p,n)^{7}Be$	1.985	0	0.20	8.4×10^{8}
"	2.240	0	0.50	2.23×10^{9}
"	2.470	0	0.75	1.24×10^{9}
$^{3}H(p,n)^{3}He$	1.850	0	1.0	1.00×10^{9}
"	2.30	0	1.50	1.6×10^{9}
"	2.80	0	2.0	2.2×10^{9}
$^{2}H(d,n)^{3}He$	1.20	70	3.0	4.9×10^{8}
"	1.30	0	4.0	1.00×10^{9}
"	2.10	0	5.0	1.00×10^{9}
"	3.0	0	6.0	9.9×10^{8}
$^{3}H(d,n)^{4}He$	1.20	0	17.0	1.00×10^{9}

*Neutrons emitted from the target at these angles were received in SSTRs.

4.4.3 Results and Discussion

(i) CA80-15

Fig.4.18 shows the number of tracks of charged reaction products plotted as a function of etching time, for two neutron energies namely 3 and 17 MeV, neutrons were incident normal to the surface. The track density on the surface of the SSTR facing the neutron beam (the 'front' surface) as well as that on the 'back' surface (facing away from the beam) is shown.

Fig.4.19 shows the density of triple tracks from $^{12}C(n,n')3\alpha$ reaction as a function of etching time for 17 MeV neutrons. Again, data for front and back surface are given.

The most dramatic feature of both Figs.4.18 and 4.19 is the large difference in track density between the front and back surface of the films in the relatively early period of etching. In the case of all types of tracks counted at neutron energies of 3 and 17 MeV (Fig.4.18) the back surface shows a track density higher by a factor of $\sim$ 1.4 and 1.3 times, respectively at an etching time of 15 minutes, than that observed on the front surface. For the 3α events (Fig.4.19) the difference is more noticeable, the back surface density being 2.8 times higher. These differences presumably reflect the forward peaking of the angular distribution of the reaction products resulting from the high energy neutron interactions.

The track density in Fig.4.18 rises to a plateau value as the etch time is increased. As etching proceeds, the surface intersects new tracks and the track density increases.

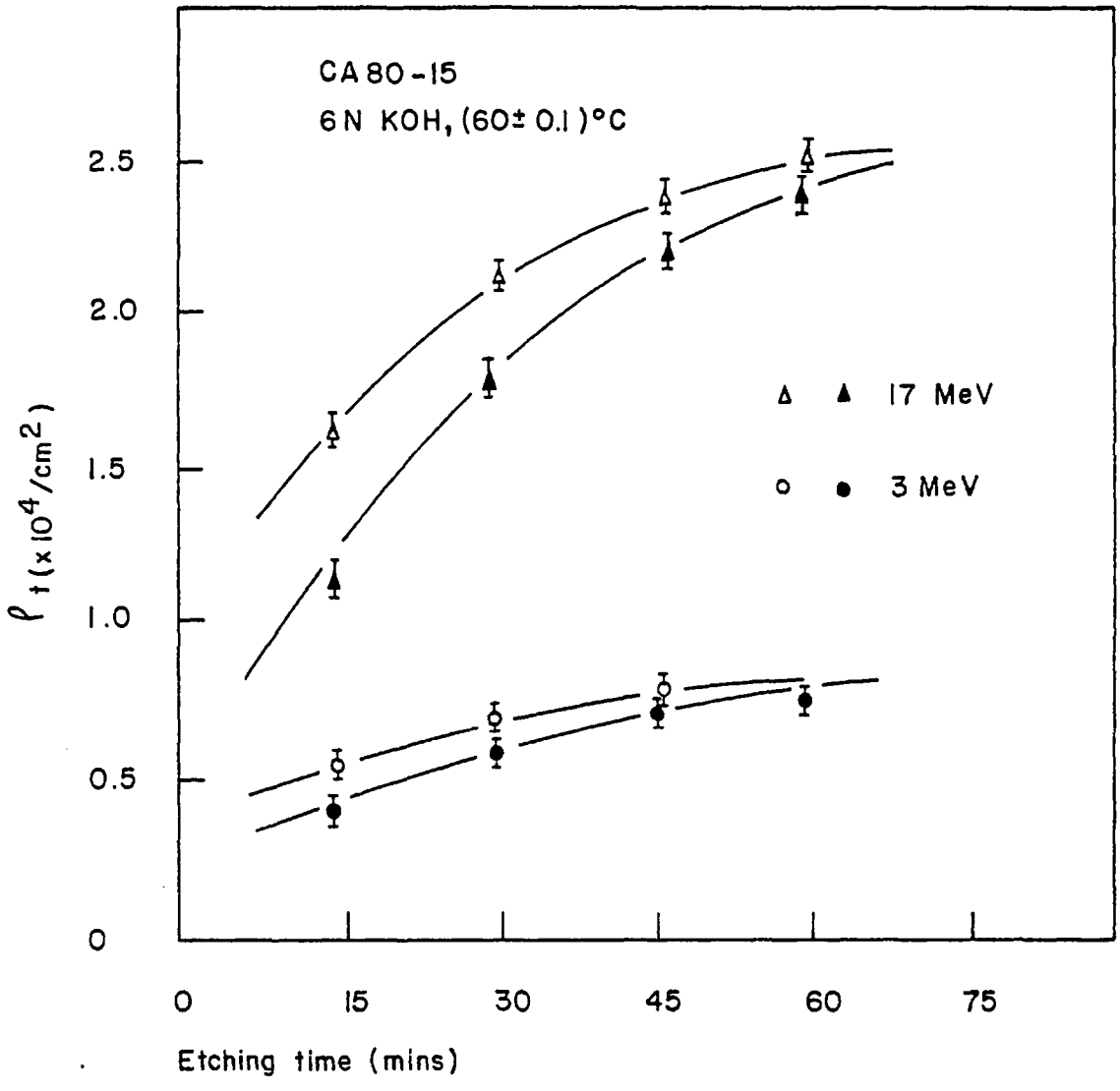


Figure 4.18 Track density, ρ_t as a function of etching time in 6N KOH at 60°C for two neutron energies. Track densities on the surface of the CA80-15 films facing the neutron beam and that on the back surface are represented by solid and open symbols, respectively

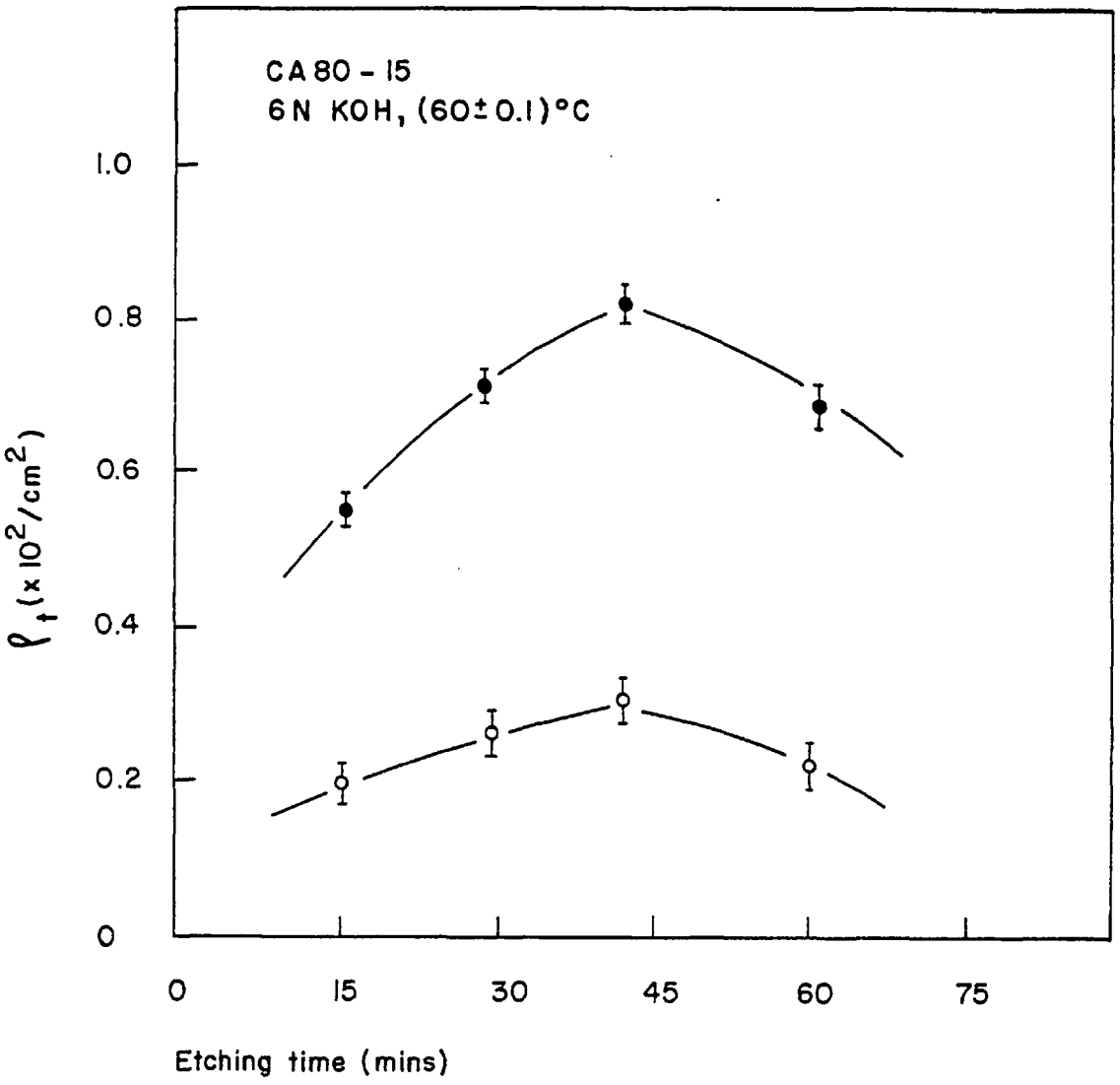


Figure 4.19 Density of triple tracks, ρ_t (from the reaction $^{12}C(n,n')3\alpha$) in CA80-15 as a function of etching time in 6N KOH at 60°C. Track densities on the 'front' and 'back' surfaces are represented by open and solid symbols, respectively

At long etch times some of the original tracks may be lost as their optical contrast is reduced. At higher neutron energies the tracks are generally longer and remain visible over much longer etch times. Therefore, the plateau track density is reached more slowly for the high energy neutrons. It was difficult to estimate the number of visible tracks due to each type of neutron interaction, since many recoils give rise to tracks similar to alpha particles.

The number of triple tracks as a function of etch time appears to pass through a maximum. This behaviour is probably the result of several factors.

Firstly, as the energy of the incident neutron increases so the energy available as kinetic energy for the three alpha particles also increases. For incident neutron energy of 17 MeV, it is possible for one of the alpha particles to have an energy of 6 MeV or more (the Q-value for the reaction $^{12}C(n,n')3\alpha$ is - 7.28 MeV) such an alpha particle will produce a track, which is very slowly etchable at the outset.. In such cases the event will not be identified as one of the 3α type until relatively long etchings have been reached. This event will become increasingly important at higher neutron energies.

The second factor governing the curves in Fig.4.19 is as follows. At high incident neutron energies, the spread in alpha particle energies becomes quite large. Therefore, at short etch times those 3α events which consist of entirely of low energy alpha tracks will be clearly etched out, whereas those consisting of higher energy alphas may

not be identifiable initially. At longer etch times these latter events will become visible, whereas the low energy events may by then be so overetched as to be difficult to identify. In case of lower neutron energies the above-mentioned overetching would account for the fall-off in the track density curve after long etch times (there being few high energy alpha events to compensate).

The experimental sensitivity, η_{exp} (in tracks/neutron) of CA80-15 is plotted as a function of neutron energy in Fig.4.20. The curve was obtained by counting all types of tracks on the 'front' surface at the optimum etching condition (6N KOH at 60°C, for 45 minuites). At a given neutron energy this etching condition corresponds to that at which the triple track density assumed its maximum value and at which the recoil and threshold reactions track density lay on the plateau,discussed earlier.

The sensitivity increases steeply with increasing neutron energy up to 3 MeV, after which this increase is not sharp; which can be explained as follows. The number of tracks per neutron is proportional to the aggregate of cross-sections for the elastic scattering of neutrons from H, C, N and O nuclei and for the threshold reactions such as $^{14}N(n,\alpha)^{11}B$, and also on the observable track length, L (see also Chapter 2) of these particles. The latter increases sharply with neutron energy in this energy range. Both of these factors contribute to an increase in the observed sensitivity of CA80-15 with increasing neutron energy. At neutron energies greater than 6 MeV, total neutron cross

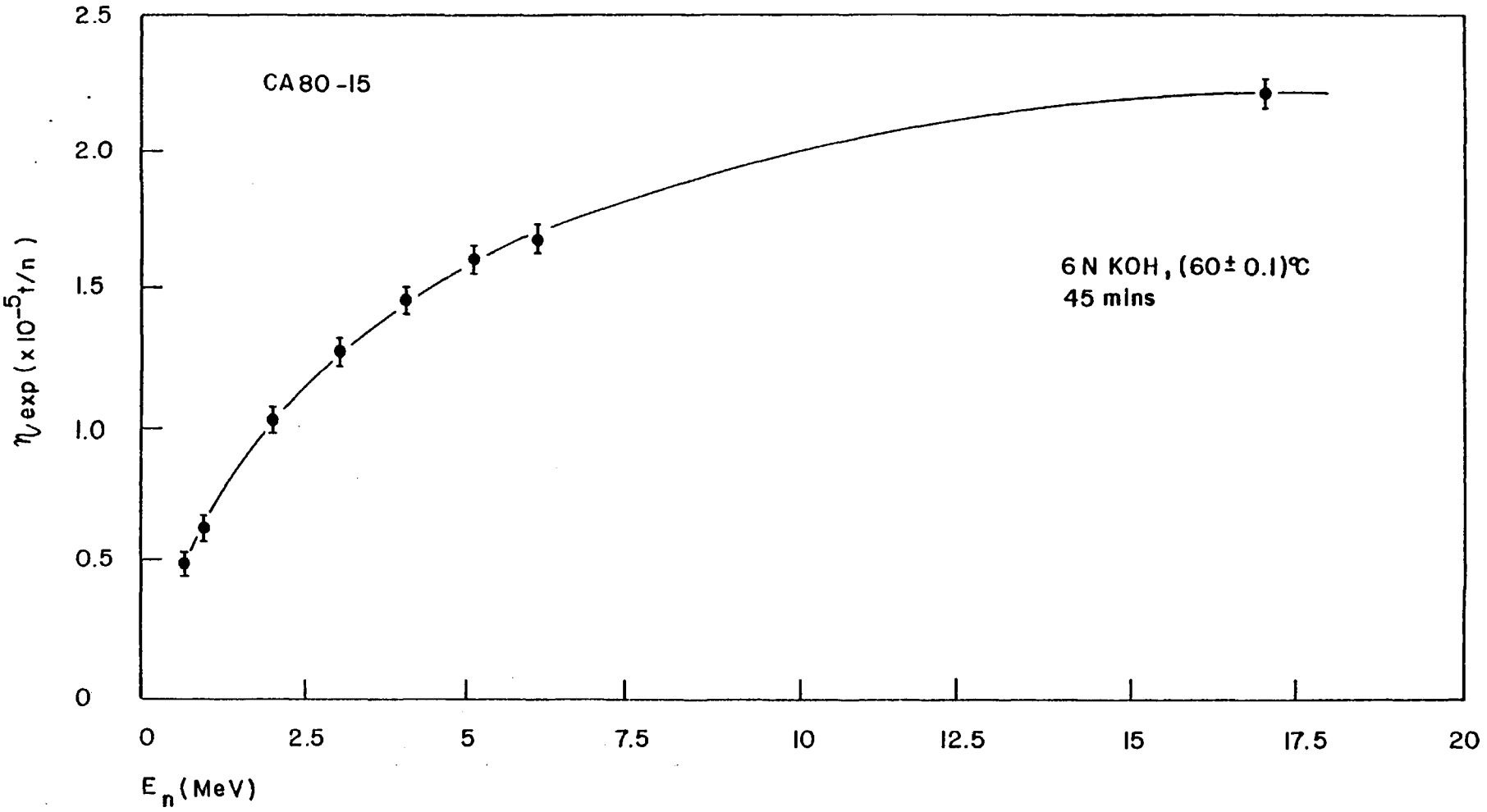


Figure 4.20 The neutron sensitivity, η_{exp} (in tracks per neutron) of CA80-15 as a function of neutron energy, E_n. Etching was carried out in 6N KOH at 60°C for 45 minutes

sections increase slowly with increasing energy and the observable track length, L also, remains constant, thus saturating the sensitivity at higher neutron energies.

A microphotograph of 3 MeV neutron induced tracks in CA80-15 etched for 45 minutes in 6N KOH at 60°C is shown in Fig.4.21. Most of the tracks observed at this energy are circular. This is due to the low range of C , N, O recoils and low energy alpha particles as well as due to the limited etchability of proton tracks i.e. they are visible only in the last few microns of their range in cellulose nitrate.

The number of triple tracks per neutron at the optimum etching condition (6N KOH at 60°C for 45 mins.) was found to be $\sim 8 \times 10^{-8}$ tracks per neutron; which is 20% greater than that obtained by Frank and Benton[47]. There are a number of possible reasons for this. First, it is obvious from the results described above (Fig.4.19) that the track densities are quite strongly dependent on the etching conditions. Secondly, it is clear that the number of 3α events, which are identified during scanning depends on the magnification and resolution of the microscope used. Frank and Benton[47], although they do not state the magnification under which tracks were counted, indicate that certain of their triple tracks "..... would not have been seen under the lower power, lower resolution microscope objective used in scanning and track counting", and conclude that their measured track densities do not include many of the $^{12}C(n,n')3\alpha$ events which occurred. Thirdly, there is some variation in the sensitivity of different types of cellulose nitrates, and therefore in

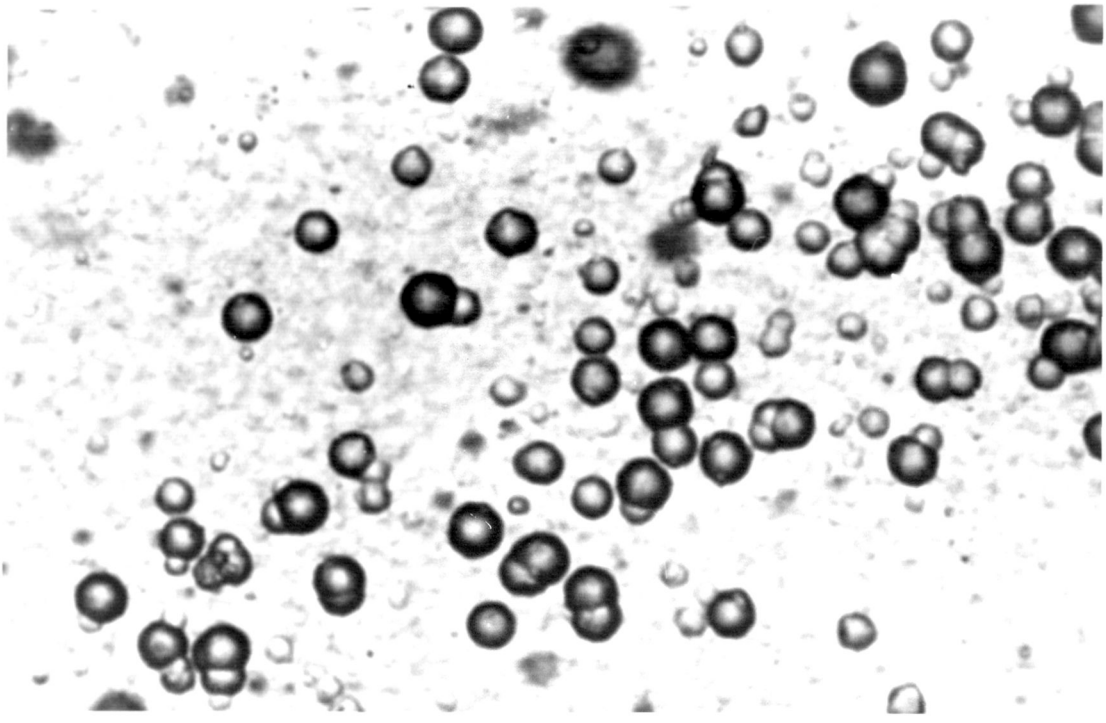


Figure 4.21 Tracks in CA80-15 exposed to 3 MeV neutrons from the 'IBIS' accelerator. Etching was carried out for 45 minutes in 6N KOH at 60°C and tracks were observed at a magnification of (x 50 x 10)

their ability to record different particles. This is clear from a compilation of etching behaviour of different cellulose nitrates, presented by Somogyi et al[89]. For example, the rate of energy loss at which the track etch rate equals twice the bulk etch rate varies from only 0.4 MeV cm^2/mg for the Kodak CA80-15 used here to 1.24 for uncoloured Daicel cellulose nitrate. Clearly, such differences must manifest themselves as considerable differences in neutron detection efficiency.

(ii) Makrofol K.G

The sensitivity of Makrofol K.G for neutron detection using the (n,f) reaction is given in Fig.4.22. This curve was obtained by irradiating Makrofol K.G in contact with a 1.23 mg/cm^2 natural uranium foil, using the IBIS accelerator. Etching was performed in 6N KOH aqueous solution at 60°C for 45 minutes. The sensitivity curve follows the ^{238}U-fission cross-section, which is to be expected.

A microphotograph of 5 MeV neutrons induced fission-fragment tracks is shown in Fig.4.23.

Angular dependences of CA80-15 and Makrofol K.G (with 1.23 mg/cm^2 natural uranium foil) i.e. the dependence of the counted track densities on the neutron angle of incidence on the surface of the films for two neutron energies namely 3 and 17 MeV is given in Fig.4.24. The fission-fragment detector (Makrofol K.G with U foil) shows the lowest variation of response as a function of the neutron incidence angle.

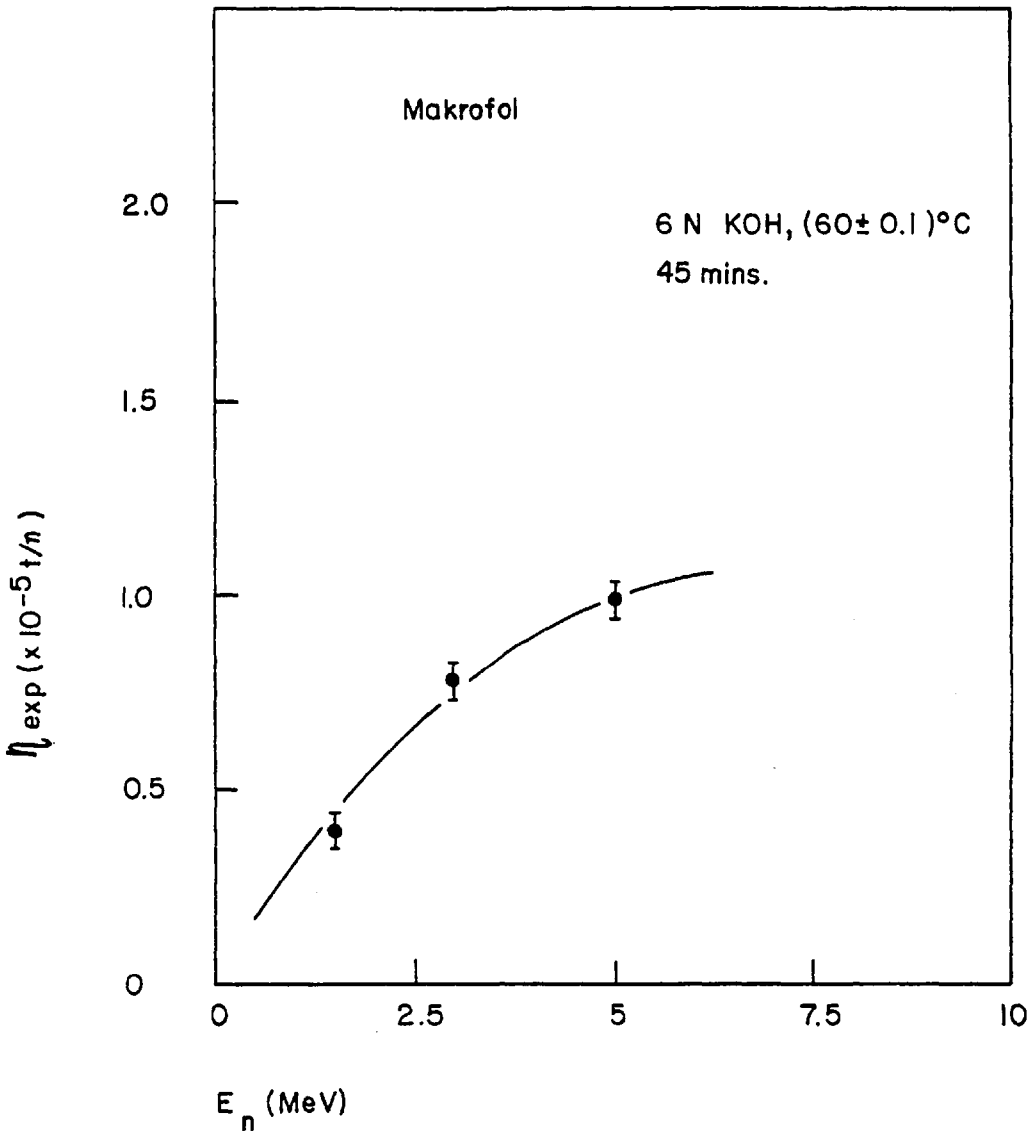


Figure 4.22 The neutron sensitivity, η_{exp} (in tracks per neutron) of Makrofol K.G in contact with a 1.23 mg/cm^2 natural uranium foil, as a function of neutron energy. The curve follows the ^{238}U fission cross section

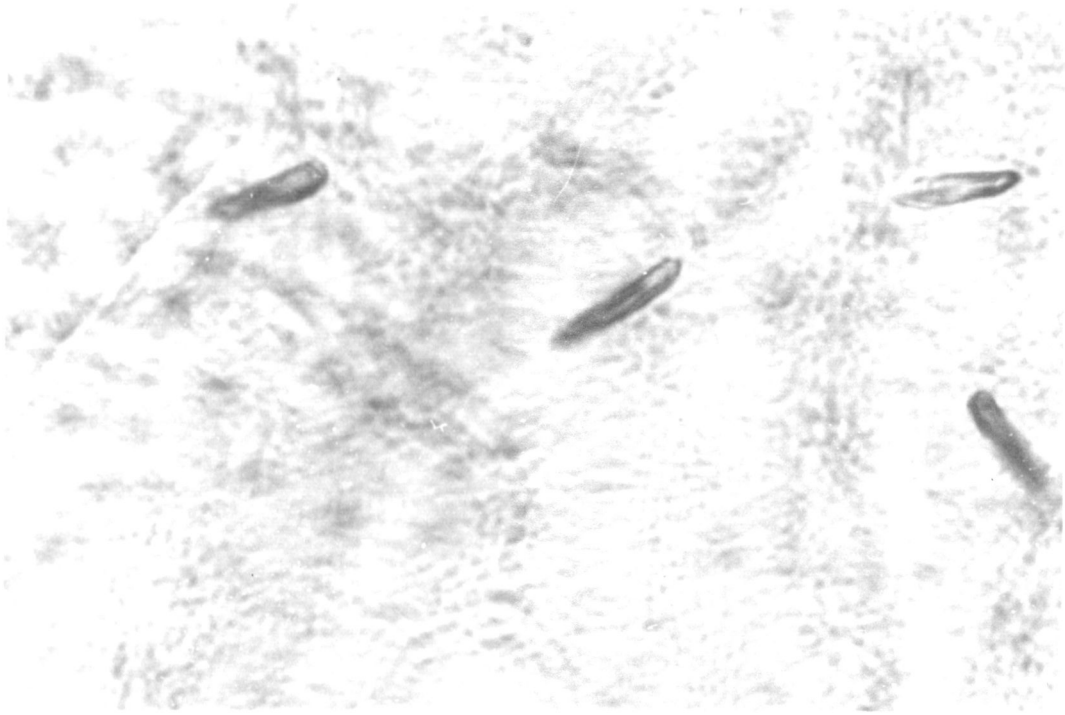


Figure 4.23 Fission-fragment tracks in Makrofol K.G. (in contact with a 1.23 mg/cm^2 natural uranium foil), exposed to 5 MeV neutrons from the 'IBIS' accelerator. Etched for 45 minutes in 6N KOH at 60°C and observed at a magnification of (x 50 x 8)

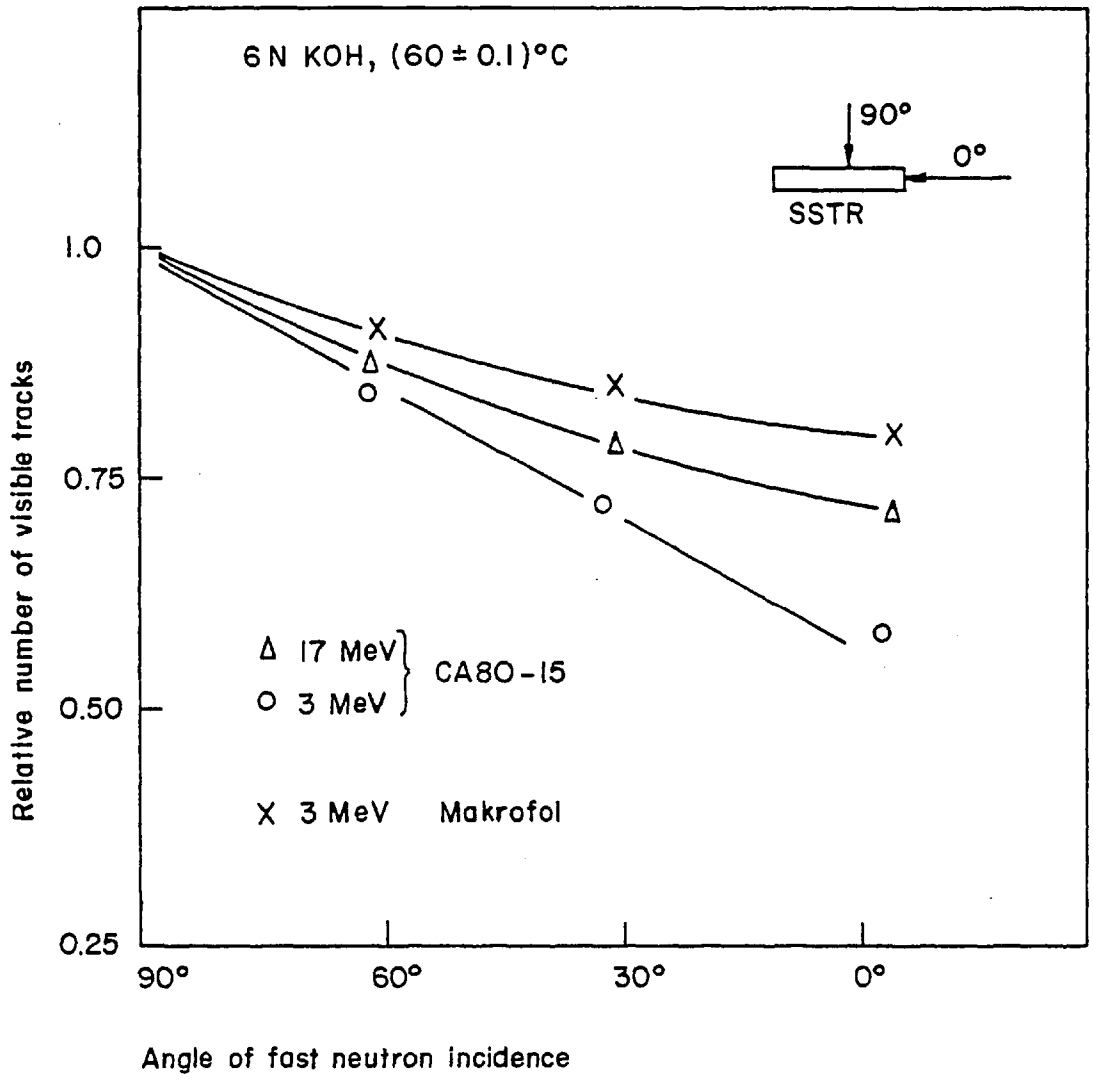


Figure 4.24 Angular dependence of track densities in CA80-15 and Makrofol K.G (in contact with a 1.23 mg/cm^2 natural uranium foil) for two neutron energies. The fission fragment detector shows the lowest variation of response as a function of the neutron incidence angle

The number of tracks is significantly low at lower angles of incidence in the case of CA80-15 at low neutron energy. This is due to the reduced etchability of those tracks (caused by 0° exposure) which are produced below the critical angle of track detection, θ_c in the material.

4.5 NEUTRONS IN CR-39

The large energy range for proton registration and low background count observed in the earlier experiments described in this chapter, make CR-39 an ideal SSTR for fast neutron dosimetry based on neutron-proton scattering. The sensitivity of CR-39 to recoil proton track registration was investigated in a variety of ways. In these experiments a calibrated ^{252}Cf-neutron source ($E_n = \overline{2.1}$ MeV) was used.

A piece of CR-39 was covered with 0.05 mm thick high density polyethylene on one side and with an (n,α) 'converter foil' (CA80-15 type B film which is coated with lithium tetraborate) on the other side. The middle portion of the CR-39 was not covered with any radiator material. The exposure was carried out so that CR-39 film received 2.1×10^{9} n/cm^{2}.

After the exposure, CR-39 was etched in 6N aqueous solution of NaOH at 70°C for varying time intervals. The track densities on the etched surfaces were determined by optical microscope. All tracks having dimensions greater than about 1 μm were included in the counting, while shallow looking etch pits were rejected.

4.5.1 Results and Discussion

The track densities and sensitivities (in tracks/neutron) as a function of the etching time, for three above mentioned neutron exposures are shown in Fig.4.25. The etching was carried out in 6N NaOH at 70°C. It is observed that the maximum track density for both bare and polyethylene covered CR-39 appears between ∿ 12 to 20 hours. For shorter etch times, tracks are simply too small to be effectively counted under the optical magnification used, while longer etch times tend to overetch some of the shallow tracks and thus also reduce track counting efficiency. The neutron sensitivity of polyethylene covered CR-39 at 12 hours etch, is ∿ 1.5 times higher than that for bare CR-39. This is due to additional recoil protons from the polyethylene, which also produce tracks.

The track density of CR-39 covered with lithium tetraborate film is much higher than the polyethylene covered and bare CR-39's. This can be explained as follows. The track density in this case includes both fast neutrons induced recoil tracks and tracks created by alpha particles from the $^{10}B(n,\alpha)^{7}Li$ reaction ($E_\alpha \simeq 1.5$ MeV, $\sigma_{thermal} = 3837b$) due to thermal and low energy neutrons present in the irradiation room. The track density, in this case increases rapidly in the early period of etching and after passing through the maximum, decreases sharply. This is due to etching out of alpha particle tracks which are present only at the surface of CR-39; this leaves only recoil tracks visible, which are distributed throughout the volume of CR-39.

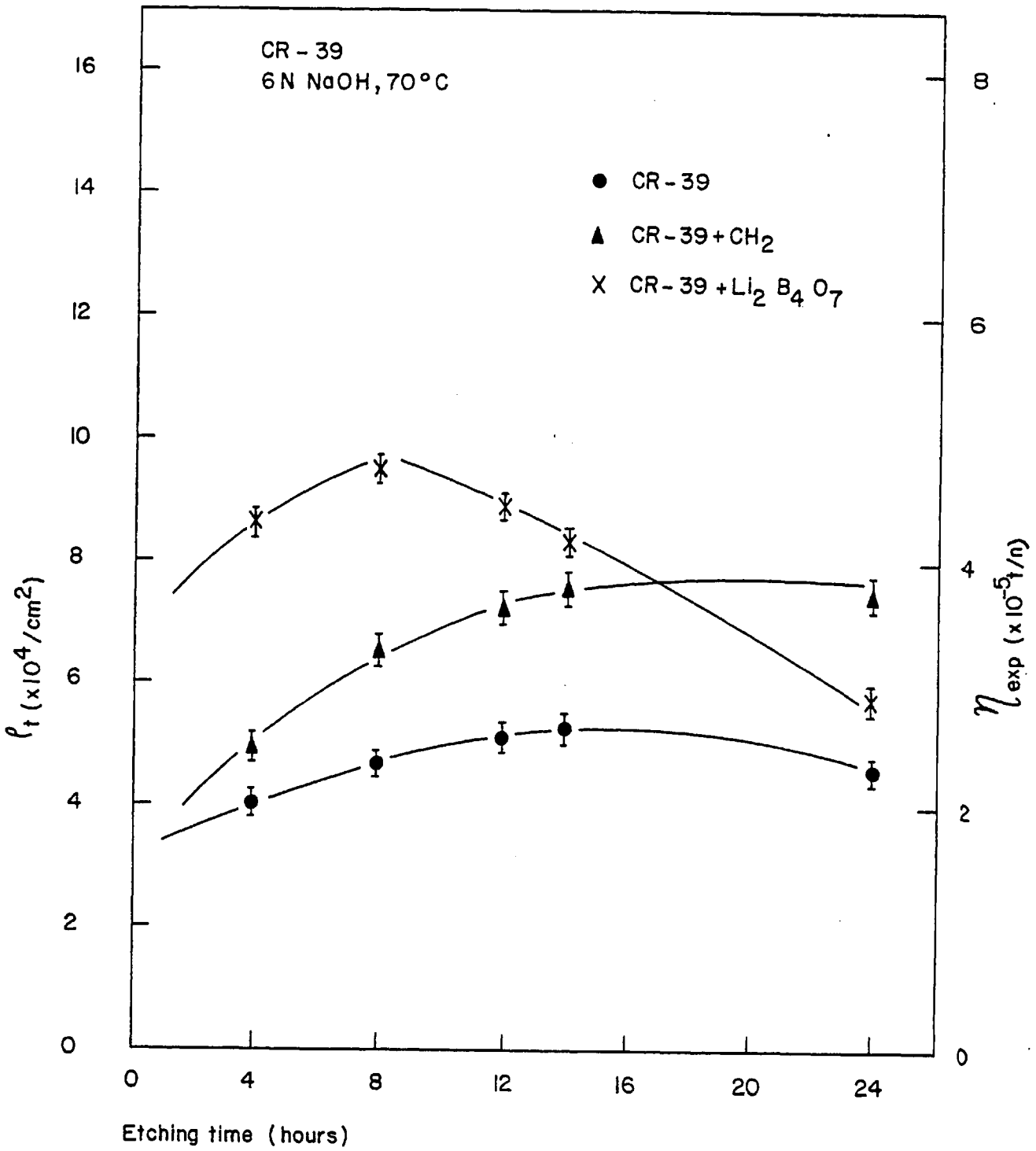
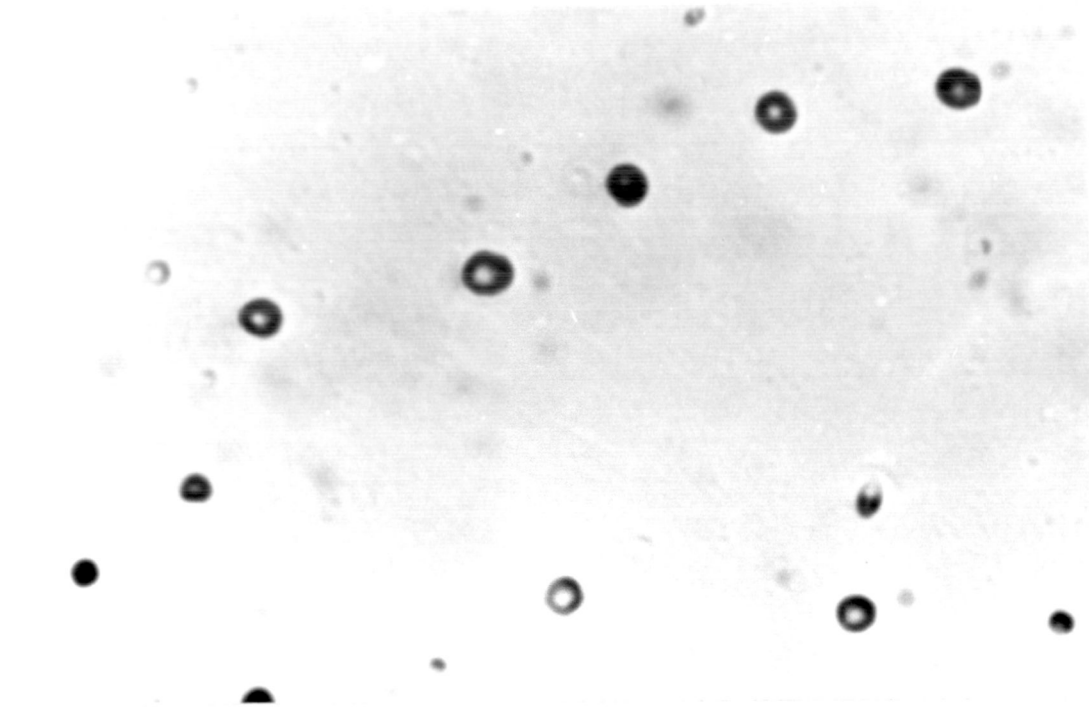
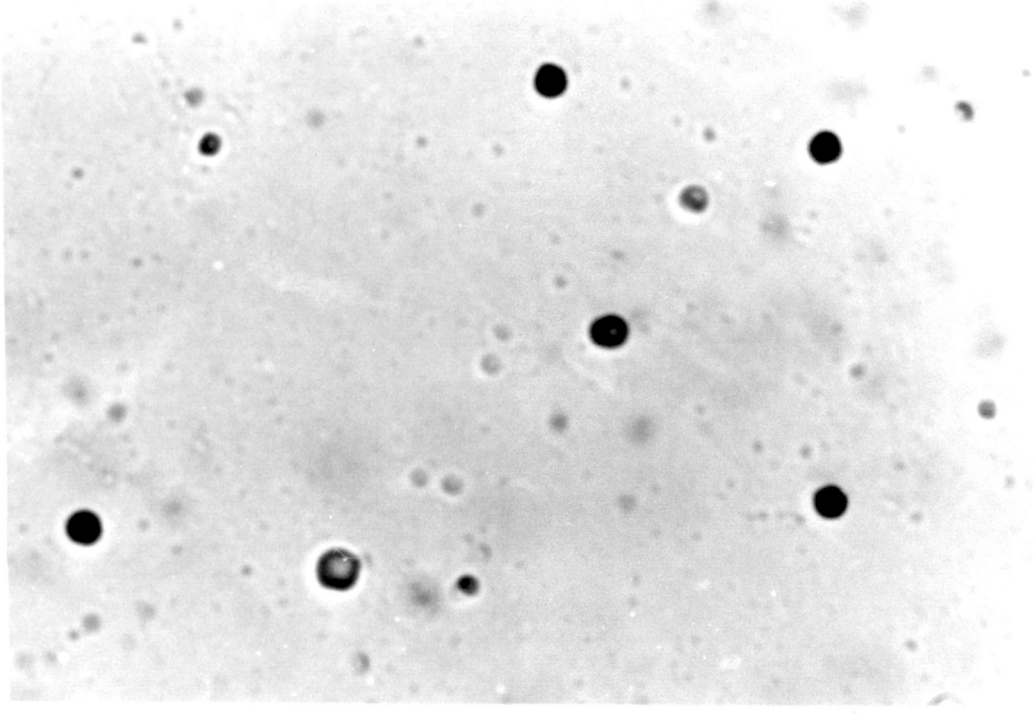


Figure 4.25 The track densities, ρ_t and neutron sensitivities, η_{exp} (in tracks per neutron) as a function of etching time in 6N NaOH at 70°C, for bare, polyethylene (CH_2) covered and lithium tetraborate covered CR-39's



(a)



(b)

Figure 4.26 (a) & (b) Recoil tracks in CR-39 exposed to fast neutrons from a ^{252}Cf-neutron source ($\overline{E_n}$ = 2.1 MeV. Etching was carried out for 7.5 hours in 6N NaOH at 70°C and tracks were observed at (x 50 x 8). (a) Polyethylene covered CR-39, (b) Bare CR-39

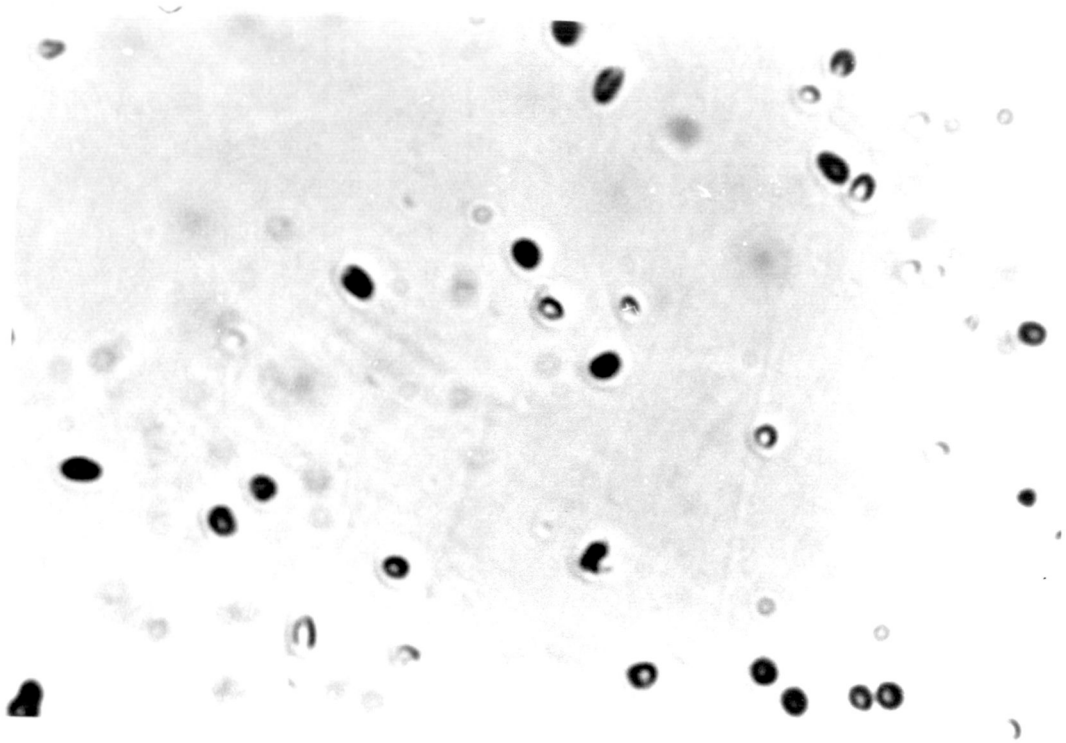


Figure 4.26 (c) Tracks in lithium tetraborate covered CR-39 exposed to fast neutrons from a ^{252}Cf-neutron source (E_n = 2.1 MeV). Etching was carried out for 3 hours in 6N NaOH at 70°C and tracks were observed at a magnification of (x 50 x 8)

Figs.4.26(a), (b) and (c) show microphotographs of etched surfaces of polyethylene covered, bare and lithium tetraborate covered CR-39's respectively.

It was found that the etched surface of CR-39 under proper etching conditions can have very low background track densities of the order of 2-3 tracks/mm^2. These results suggest the suitability of CR-39 together with a suitable polyethylene radiator and thermal (n,α) 'converter foil', as an effective neutron dosimeter having excellent sensitivity, where thermal neutrons can be measured by calculating the sensitivity ratio, from the track density in bare and (n,α) 'converter foil' covered CR-39 films.

4.6 CONCLUSIONS

The following summarised conclusions can be drawn from the present experiments:

(i) It was established that CA80-15 is sensitive to low energy protons and therefore have to be taken into account in addition to other particles when calculating the response to fast neutrons. Owing to the proton sensitivity and high nitrogen content of CA80-15 films, they must be wrapped in cadmium or some other neutron absorber for use in and around nuclear reactors, otherwise thermal neutron induced protons will interfere with recoil and other tracks produced by fast neutrons.

The sensitivity of CA80-15 is energy dependent, therefore a knowledge of neutron spectrum is necessary for reaction rate measurements in reactor physics

applications. For a fission neutron source, the sensitivity of CA80-15 after 45 minutes of etching in 6N KOH at 60°C is 1.2×10^{-5} tracks per neutron.

(ii) For a fission neutron source the sensitivity of Makrofol K.G in contact with a 1.23 mg/cm^2 natural uranium foil, after 45 minutes of etching in 6N KOH at 60°C is 0.6×10^{-5} tracks/neutron. The sensitivity follows the ^{238}U-fission cross-section.

(iii) The response of CR-39 to alpha particles from 3 to 6 MeV makes CR-39 an excellent candidate for integral (n,α) reaction rate measurements.

For a fission neutron source the sensitivity of CR-39 without any particle radiator, after 10 hours of etching in 6N NaOH at 70°C is 2.6×10^{-5} tracks per neutron. The sensitivity can be increased considerably by employing a suitable particle radiator, in which case etching time can also be decreased.

CHAPTER 5

SYSTEMATIC ERRORS AND SUMMARY OF THEORETICAL AND EXPERIMENTAL EVIDENCE

5.1 SOURCES OF SYSTEMATIC ERRORS

Repeated measurements of tracks belonging to the same SSTR or SSTRs of the same experimental series (i.e. irradiations in the same positions and the same neutron spectrum) are bound to give devious results due to statistical and systematic uncertainties due to the counting technique, the experimental conditions, the SSTR itself and the etching process.

Uncertainties in neutron measurements with SSTRs fall into four general categories:

(a) track etching;

(b) track scanning;

(c) time and position of irradiation exposure-

and (d) mass and uniformity of 'converter foils'.

Table 5.1 gives a summary of the actual uncertainties that were measured in the present experiments for these different categories. These categories do not include statistical uncertainty that arises in track scanning. It has been demonstrated that Poisson statistics are applicable for manual track scanning[58].

5.1.1 Chemical Etching

Care needs to be taken to control the chemical composition and the temperature of the etching bath. It was

TABLE 5.1

SOURCES OF SYSTEMATIC ERROR IN NEUTRON MEASUREMENTS USING SSTRs

Source	Error (%)
1. Chemical Etching	
(a) 'Intrinsic' SSTRs	± 1.0
(b) SSTRs with a (n,f) 'converter foil'	< ± 1.0
2. Manual Scanning	
(a) Area measurements	± 0.5
(b) Stage movements	< ± 0.5
(c) Track identification (isotropic incidence)	
(i) 'Intrinsic' SSTRs	± 1.0
(ii) SSTRs with a (n,f) 'converter foil'	± 0.5
3. Type and Position of Irradiation	
(a) Exposure to spontaneous fission sources	< ± 0.5
(b) Exposure to neutron fields	> ± 0.5, depending upon conditions
4. Quality of (n,f) 'converter foils'	± 1.0
Total Systematic Error	
(a) 'Intrinsic' SSTRs	± 3.5
(b) SSTRs with a (n,f) 'converter foil'	∿ ± 3.0

observed that the control of etching temperature to within $\pm$ 0.1°C at 60°C is necessary to prevent errors greater than $\pm$ 1% in the track density.

A variation of $\pm$ 0.5°C at 19°C results in a > 1% change in V_T/V_B (the etch rate ratio) for a 2.5N NaOH etchant, while at 60°C a $\pm$ 0.5°C variation results in a 4.0% change in V_T/V_B.

The 'background' in etched SSTRs can be divided into two categories: first type of background corresponds to a permanent background due to (unavoidable) imperfections of the surface of the SSTR, while the second type of background pertains to the permanent (constant) background plus etch pits produced in a particular experiment, and therefore varies with time (i.e. in different irradiations). The permanent background remains more or less constant within 'optimal' etching conditions, subject to reasonable statistical fluctuations, as long as the SSTR manufacturing procedure is standard.

Errors from etching uncertainties can be kept negligible if proper care is taken.

5.1.2 Manual Track Scanning

Scanning uncertainties are more complicated to measure because of the human element in track counting. Since the human element enters into how a scanner perceives tracks in relation to "unwanted features", it is difficult to quantify this problem except by experience. Experience shows that repeated measurements for isotropic tracks in 'intrinsic' SSTRs agree at the $\pm$ 1% level; while in the case of isotropic

fission tracks repeated measurements generally agree at $\pm$ 0.5% level.

In addition to the perception problem, the precision level in track scanning actually depends upon a number of factors which can produce uncertainty in the area scanned and hence in the overall measurements. These other factors are:

(i) measurement of the area of the grid used to define the counting area;

(ii) non-linearity in the dials used to measure the length of the scanning swaths;

(iii) uncertainty in the movement of the microscope stage from swath-to-swath;
and

(iv) decision of the scanner as to whether a track is touching a grid line defining the edge of the field.

The length of the grid defining the counting area in the present experiments was measured at the $\pm$ 0.5% level with a suitable stage micrometer. Ideally, the calibration of the stage area should be made every time before starting the scanning, since it depends upon the interocular spacing used on the microscope. Non-linearities in the dial gauges can be determined by comparison with the stage micrometer and these can be corrected for if significant.

Scanning errors can be reduced if the SSTR is pre-selected for superior quality. By proper selection (see Section 3.2, Chapter 3), uncertainties between tracks and 'background' can be kept at 1% level in 'intrinsic' SSTRs and below 1% level in SSTRs with (n,f) 'converter foils'.

5.1.3 Time and Position of Irradiation Exposure

If an exposure is made by placing the SSTR in direct contact with a 'converter foil', care must be taken to have good physical contact between the deposit and the SSTR. If this is done, errors from this cause should be negligible.

Uncertainties in exposure time can be made negligibly small if the total exposure time is made large relative to a few seconds. Errors of this type depend primarily upon exposure times to obtain desired track densities.

5.1.4 Quality of (n,f) 'Converter Foils'

If the (n,f) 'converter foils' used in measurements are not uniform in the radial direction then errors could be introduced in track counting should an insufficient area of the recorder be scanned. In most cases the mass and isotopic composition of 'converter foils' is known to be better than 1%. For most deposits that are vacuum evaporated, the uniformity is also within 1% uncertainty. For electroplated deposits the lack of uniformity is somewhat higher; when good precision is required it is often necessary to count all tracks over the entire area of the deposit.

In the present experiments with a natural uranium foil errors from this source are estimated to be less than 1%.

5.1.5 Summary

It can be seen from Table 5.1 that neutron measurements by 'intrinsic' SSTRs are subject to a total systematic error of $\pm$ 3.5%. In the case of SSTRs with a (n,f) 'converter

foil' the total systematic error is estimated to be 3.0%. These errors do not include the statistical variation in the number of tracks counted in an etched SSTR. Errors arising out of area and stage measurements of microscope can be eliminated by using a microscope having a good mechanical stage. Manual scanning errors due to track identification against 'background', and track counting can be reduced substantially by automation of track counting i.e. eliminating the subjective nature of human decisions (see end of the following section, 5.2.1 and Chapter 7).

5.2 COMPARISON BETWEEN THEORETICAL AND EXPERIMENTAL RESULTS

5.2.1 Response of CA80-15 to Thermal and Fast Neutrons

In the case of CA80-15 without any 'converter foil', the theoretical sensitivity to neutrons is compared with the experimental results in Figure 5.1 and Table 5.2. The predicted values were obtained by considering two boundary sets of "energy limits for the observable track length, L", for particles of interest (recall model developed in Chapter 2 to calculate the response of 'intrinsic' SSTRs to neutrons).

It can be seen that the theoretical values are higher ($\overline{11.6}$%) than the experimental ones in the neutron energy range 1.5-5 MeV; which can be explained as follows. In this neutron energy range the tracks in CA80-15 are mainly due to recoil protons which due to low ionization are difficult to visualize and distinguish from the 'background' present in CA80-15 (see Section 4.2.3, Chapter 4) which makes their manual counting particularly erratic; hence it is possible that some of the recoil proton tracks were not taken into

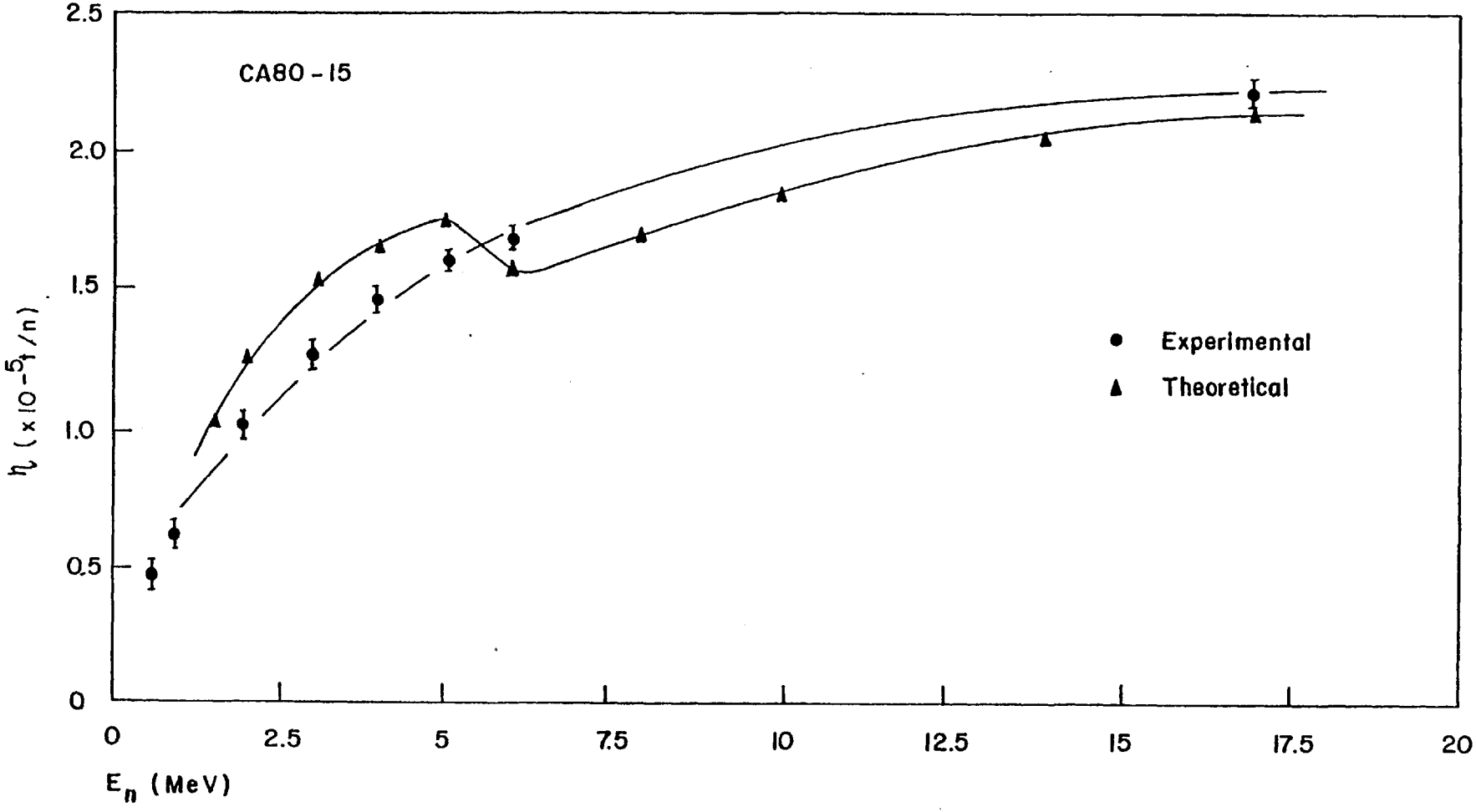


Figure 5.1 Theoretical and experimental neutron sensitivities, η_{th} and η_{exp} respectively (in tracks per neutron) of CA80-15. Experimental curve is for 45 minutes of etching in 6N KOH at 60°C (see Figure 4.20, Chapter 4)

TABLE 5.2

COMPARISON BETWEEN THEORETICAL AND EXPERIMENTAL SENSITIVITIES OF CA80-15 (η_{th} and η_{exp} RESPECTIVELY; IN TRACKS PER NEUTRON) AS A FUNCTION OF NEUTRON ENERGY, E_n

E_n (MeV)	η_{th} (x 10^{-5} t/n)	η_{exp} (x 10^{-5} t/n)	η_{exp}/η_{th}
Thermal	0.40	0.340 ± 0.022	0.85
1.5	1.11	0.95	0.86
2.0	1.33	1.090 ± 0.058	0.83
3.0	1.51	1.350 ± 0.073	0.90
4.0	1.61	1.450 ± 0.065	0.91
5.0	1.75	1.610 ± 0.055	0.92
6.0	1.62	1.650 ± 0.060	1.10
8.0	1.71	1.80	1.05
10.0	1.85	1.91	1.02
14.0	1.99	2.01	1.01
17.0	2.15	2.280 ± 0.055	1.06

TABLE 5.3

COMPARISON BETWEEN THEORETICAL AND EXPERIMENTAL SENSITIVITIES (η_{th} and η_{exp} RESPECTIVELY; IN TRACKS PER NEUTRON) OF MAKROFOL K.G IN CONTACT WITH A 1.23 mg/cm^2 NATURAL URANIUM FOIL

E_n (MeV)	η_{th} (x 10^{-5} t/n)	η_{exp} (x 10^{-5} t/n	η_{exp}/η_{th}
1.5	0.35	0.310 ± 0.024	0.88
2.0	0.78	0.64	0.82
3.0	0.80	0.680 ± 0.030	0.85
4.0	0.91	0.84	0.92
5.0	0.94	0.850 ± 0.040	0.91
6.0	0.95		
8.0	1.35		
10.0	1.61		

account, thus reducing the sensitivity. This argument is supported by the thermal neutron experiments which give a sensitivity of $(3.40 \pm 0.22) \times 10^{-6}$ tracks per neutron for CA80-15, which is 15% less than the predicted value. The tracks in CA80-15 exposed to thermal neutrons are also produced by protons (from $^{14}N(n,p)^{14}C$ reaction). The fluctuation in the theoretical response curve (Figure 5.1) at E_n = 6 MeV is due to the $^{16}O(n,\alpha)^{13}C$ resonance. The predicted values are $\overline{4.8}$% less than the experimental ones in the neutron energy range 6-17 MeV. However, shapes of both curves (η_{th} and η_{exp} as a function of E_n) within experimental errors predict a general tendency of increase in sensitivity with increase in neutron energy. The difference between the absolute number of tracks observed and predicted can be due to the following effects, which have not been included in the theoretical model;

(a) some etching effects, and

(b) effects due to the observer's subjective approach to track recognition.

The etching process in the case of 'intrinsic' SSTRs often results in tracks which appear as circles, rather than lines as was considered in theory. The circle has a diameter and "appearance", which is determined by the damage produced by the particle and the etching conditions. The diameter must be a certain minimum value to be registered as a count and should also have the same "appearance".

An observer chooses to register a track using his own criteria on the diameter and "appearance" which would not

necessarily coincide with those of a second observer. This aspect of track recognition can be parameterised by defining a counting efficiency parameter (ε) and a reproducibility parameter ($\Delta\varepsilon$).

These concepts are important because of the subjective nature of human decisions on the number of tracks and immediately point to the advantages of computer algorithms for track counting. A computer based track counting system can be expected to have a fixed value for ε and an almost zero value for $\Delta\varepsilon$.

5.2.2 Response of Makrofol (in Contact with 1.23 mg/cm^2 Natural Uranium Foil) to Neutrons

The theoretical sensitivity of Makrofol K.G in contact with a 1.23 mg/cm^2 natural uranium foil, to fast neutrons is compared with experimental results in Table 5.3 and Figure 5.2. The predicted values were calculated using the theoretical response equations derived in Section 2.3.1, Chapter 2.

It appears that the theoretical values are higher (8-18%) in the neutron energy range 1.5-5 MeV. It is quite understandable if one takes into account that the theoretical values are for a 'thick' (i.e. thicker than the range of fission fragments in the foil) fission foil. The mean range of fission fragments in uranium metal is 9.1 mg/cm^2 (see Figure 2.10); while the thickness of the fission foil used in the present experiments is 1.23 mg/cm^2 (natural uranium); which makes it a 'thin' foil. Therefore, all fragments produced i.e. from almost zero to the maximum energy do not reach the detector. However, the ratio of thicknesses of a

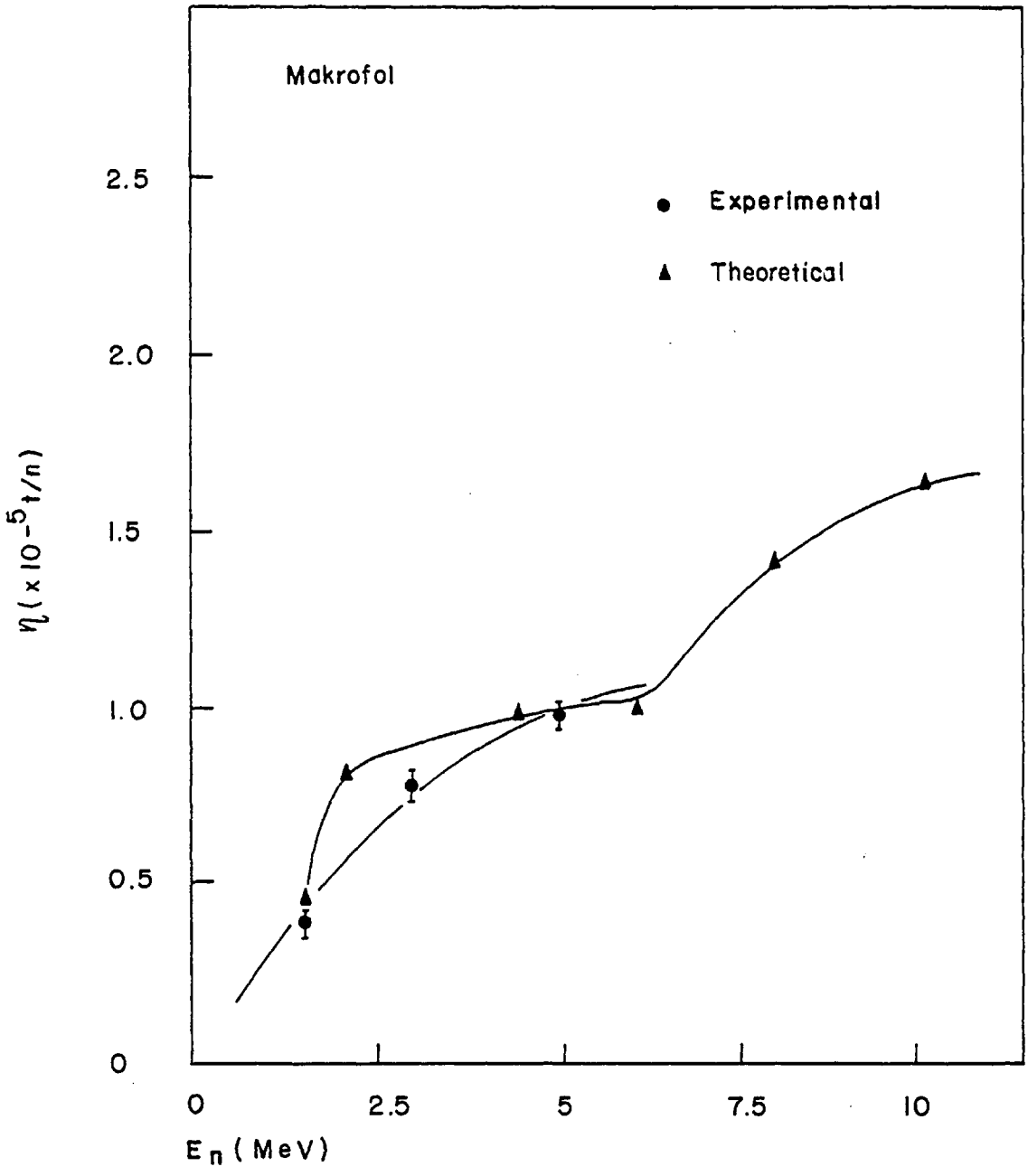


Figure 5.2 Theoretical and experimental neutron sensitivities, η_{th} and η_{exp} respectively (in trackes per neutron) of Makrofol K.G in contact with a 1.23 mg/cm^2 natural uranium foil. Experimental curve is for 45 minutes of etching in 6N KOH at 60°C (see Figure 4.22, Chapter 4)

'thick' foil and the foil used in the present experiments is not reflected in the ratio of theoretical and experimental sensitivities. This is due to the fact that the reduction of fission foil thickness by a certain factor, say five, reduces the neutron sensitivity by much less than this factor due to much reduced self-absorption of fission fragments in the foil[49].

Other factors contributing to rather high neutron sensitivity of 'thin' natural uranium foil is the contribution from other uranium isotope ^{235}U present in the foil.

CHAPTER 6

EFFECTS OF HIGH GAMMA DOSES ON SSTRs

6.1 INTRODUCTION

It is usually assumed that high doses of gamma-rays, such as are found in reactor physics and nuclear safeguards applications, do not affect the charged particle registration and revelation properties of SSTRs[84,90]. However, the validity of this assumption should be verified in the case of nuclear safeguards applications (it is planned to use SSTRs for the evaluation of tracks induced by fast neutrons emerging from transuranic nuclei accumulated in irradiated reactor fuel elements)[42], since it is known that gamma-rays and electrons cause significant radiation damage in all organic polymers and polycarbonates[91].

In order to determine the influence of gamma-rays on track registration and revelation properties of CA80-15 and Makrofol K.G SSTRs the following topics were investigated.

(1) The effect of high gamma-ray doses on track etching parameters: the track etching rate, V_T, the bulk etching rate, V_B, the threshold of track registration (the minimal value of energy loss, dE/dx) and the track registration efficiency.

(2) The limit of gamma-ray dose below which the basic properties of the SSTRs remain unchanged so that the effects of gamma-rays may be neglected.

(3) The etching conditions which minimise and maximise the influence of gamma-rays on the track registration and revelation properties of CA80-15 and Makrofol K.G SSTRs.

(4) The appropriate correction factors, depending on the gamma-ray dose, which must be introduced in interpreting the track measurements (number, length and diameter).

(5) If the bulk or track etching rates (V_B or V_T respectively) are affected by gamma-ray dose, whether their change can be used as an accurate measure of the gamma-ray dose.

6.2 EXPERIMENTS

6.2.1 Irradiations

In order to investigate the effects of gamma-ray dose on track registration and revelation properties of CA80-15 cellulose nitrate and Makrofol K.G polycarbonate SSTRs, six sets of detector films were exposed to varying doses of fission fragments, neutrons, alpha-particles and gamma-rays. Each set consisted of CA80-15 and Makrofol K.G detector films which were punched into strips of equal area (1 cm x 4 cm). These were individually weighed before gamma-ray irradiations on a microbalance capable of reading hundredths of a milligram. The fission-fragments were obtained from a 1 μCi spontaneous fission ^{252}Cf-source and alpha-particles from an ^{241}Am-source, which was covered with an aluminium foil of 20 μm thickness to reduce the energy of particles to ≃ 1 MeV. In both cases the films were in contact with the sources in 2 π-geometry. Monoenergetic fast neutrons were produced using the IBIS-accelerator at A.E.R.E. Harwell (see Chapter 4). The gamma-ray irradiations with a 10,000 Ci ^{60}Co-source were performed in the sterilization room of the Nuclear Technology Section, Department of

Chemical Engineering and Chemical Technology of Imperial College. The temperature of air was under $40^{o}C$ and the dose field was relieved from the ozone. The dose range from 1×10^{6} to 2.4×10^{7} Rads ($\pm$ 3%) was covered at dose rates of approximately 1×10^{6} rads/h.

The experiments were conducted in the following groups:

(A) : SSTRs were exposed to fission-fragments and subsequently to gamma-rays.

(B) : SSTRs were exposed to gamma-rays followed by fission-fragments.

(C) : SSTRs were exposed to fission-fragments only.

(D) : SSTRs were exposed to gamma-rays only.

(E) : SSTRs were exposed to monoenergetic fast neutrons and subsequently to gamma-rays.

(F) : SSTRs were exposed to gamma-rays followed by alpha-particles.

After gamma-ray exposures it was found that individual plastic strips tended to adhere to each other. However, upon separation, plastics retained their fine surfaces. A change in colour was noticeable in the case of CA80-15 for absorbed doses greater than 2×10^{6} Rads. All SSTRs were individually weighed once again before etching them.

6.2.2 Chemical Etching

After the gamma-ray exposures the six sets of SSTRs were stored at room temperature, away from light to avoid the UV-accumulation, which would give an effect similar to a gamma dose. The sets of SSTRs were etched simultaneously under eight different etching conditions, these being as follows:

E_1 : 2.5N NaOH at 19°C

E_2 : 6N NaOH at 19°C

E_3 : 2.5N NaOH at 60°C

E_4 : 6N NaOH at 60°C

E_5 : 2.5N KOH at 19°C

E_6 : 6N KOH at 19°C

E_7 : 2.5N KOH at 60°C

E_8 : 6N KOH at 60°C

The samples were etched in a controlled temperature bath whose accuracy is $\pm$ 0.1°C. Each SSTR was analysed and the following parameters measured: the track width, W for fission-fragments, the bulk etching rate, V_B and the number of tracks in the case of SSTRs exposed to fast neutrons followed by gamma-rays.

6.3 RESULTS AND DISCUSSION

Figs.6.1 and 6.2 show the variation of $\bar{W}_D/\bar{W}_o$ as a function of absorbed gamma-ray dose, D_γ in the case of CA80-15 SSTR for the eight etching conditions E_1-E_8. $\bar{W}$ denotes the average observed width of fission-fragment tracks with subscripts 'D' and 'o' referring to with and without gamma dose, respectively. It can be seen that there is a significant increase in the ratio, $\bar{W}_D/\bar{W}_o$ with increasing dose for the low temperature etching conditions, E_1, E_2, E_5 and E_6. Furthermore, the increase in the ratio is greater for the 'set A' detectors, which were exposed first to ^{252}Cf fission-fragments and then to gamma-rays, than the ones exposed in the reverse order (set B). On the other hand there is no

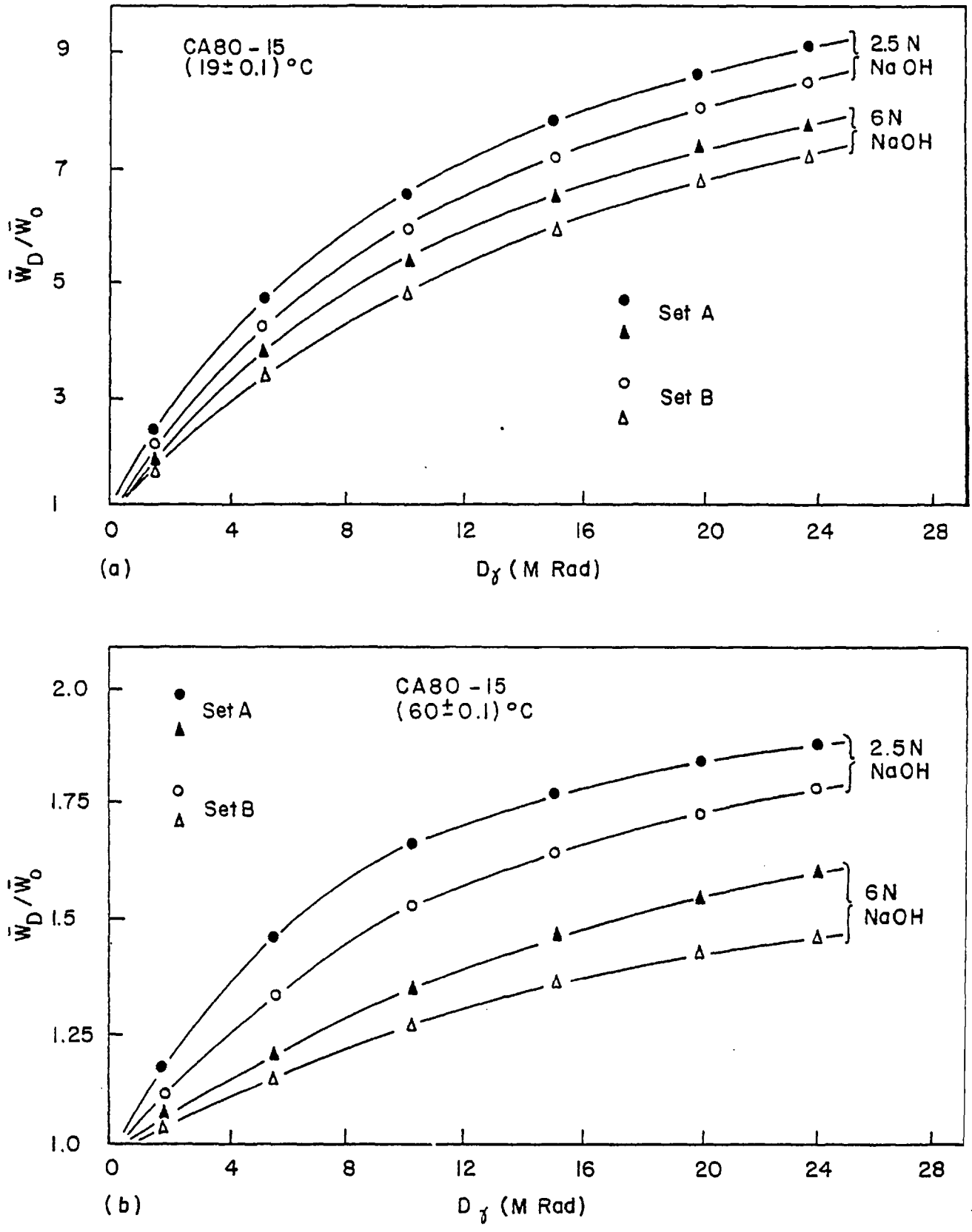


Figure 6.1 The ratio of average values of fission fragment track widths, $\bar{W}_D/\bar{W}_o$, in CA80-15 at gamma doses of 'D-megarads' and 'zero-megarads', as a function of absorbed gamma dose, D_γ. The etching was carried out for, (a) 10 hours, (b) 25 minutes, without interruption or stirring

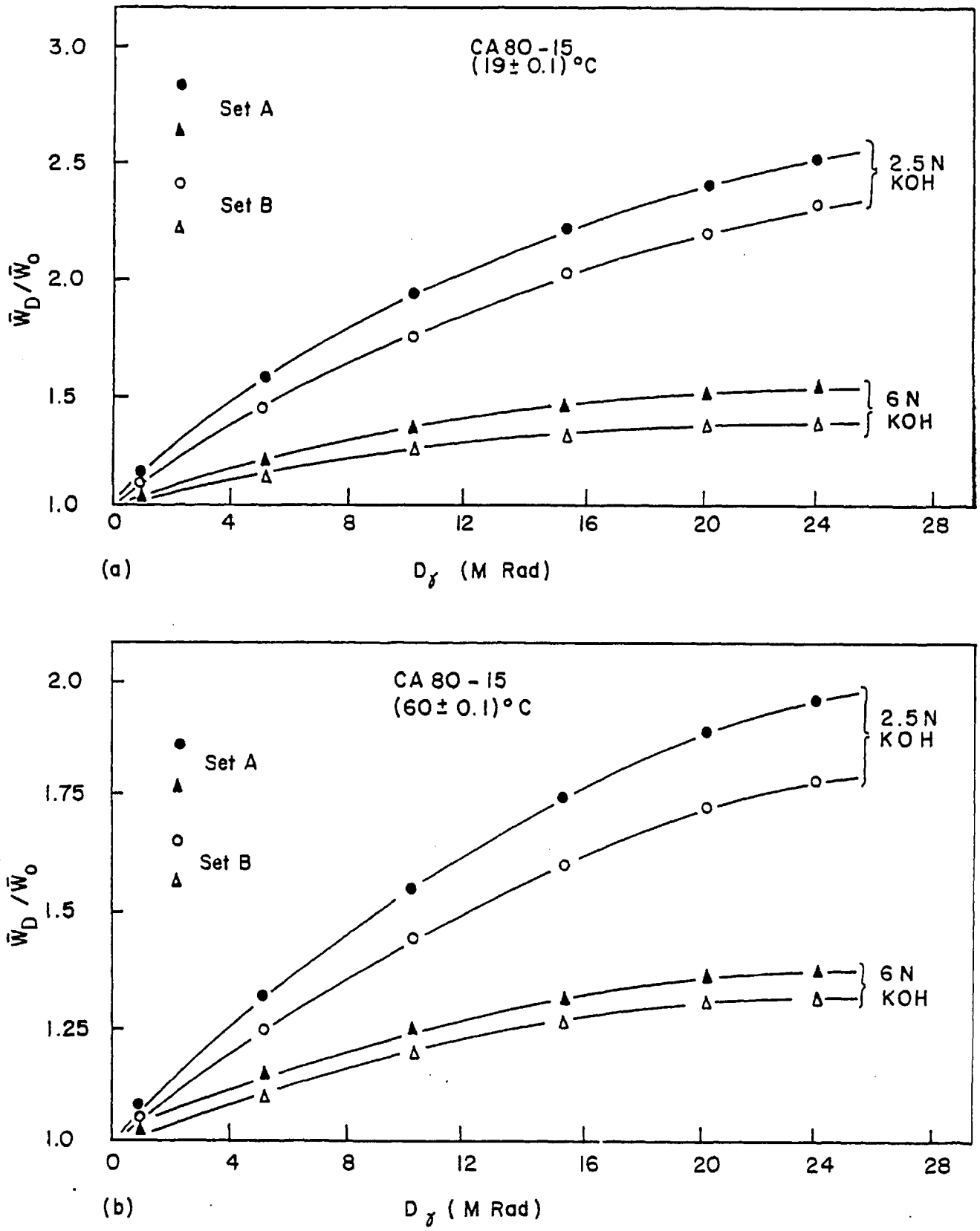


Figure 6.2 The ratio of average values of fission fragment track widths, $\bar{W}_D/\bar{W}_o$ in CA80-15 at gamma doses of 'D-megarads' and 'zero-megarads', as a function of absorbed gamma dose, D_γ. The etching was carried out for, (a) 2.5 hours, (b) 15 minutes, without interruptions or stirring

significant variation in the ratio, $\overline{W}_D/\overline{W}_o$ under fast etching conditions, E_3, E_4, E_7 and E_8, indicating that etching at high temperatures masks any effects due to gamma-rays up to some extent. One might conclude from these results that the gamma-ray doses in the megarad region cause significant enhancement in the damaged region, which increases with the increasing gamma dose. Thus, it appears that gamma-ray doses in the megarad region effectively increase the 'volume' and the 'density' of the damaged region. Also, the results from the 'set B' SSTRs indicate that even the general nature of the plastic is changed up to some extent by such high gamma-ray doses.

The bulk etch rates for CA80-15 SSTRs (set D) for various exposures at etching condition, E_8 are given in Table 6.1. In addition to the difference in the bulk etch rates, there is one other dose dependent effect present in the measurements. At doses above 10^7 rads there is a loss of mass from the plastic during the gamma-ray irradiation, as shown in Table 6.1. This is due to the escaping gases from the plastic. This effect was included in the bulk etching rate measurements.

Figs.6.3-6.7 show the variation of the average bulk etching rates, $\overline{V}_B$ and the ratio, $\overline{V}_{B,D}/\overline{V}_{B,O}$ as a function of absorbed gamma dose, D_γ in the case of CA80-15 and Makrofol K.G SSTRs for the eight etching conditions E_1-E_8. The bulk etching rate, $\overline{V}_{B,D}$ increases as a function of absorbed gamma dose, D_γ up to ≃ 8 M Rads according to the relation[92]:

$$V_{B,D}/V_{B,O} = \exp(k\ D) \qquad (6.1)$$

TABLE 6.1

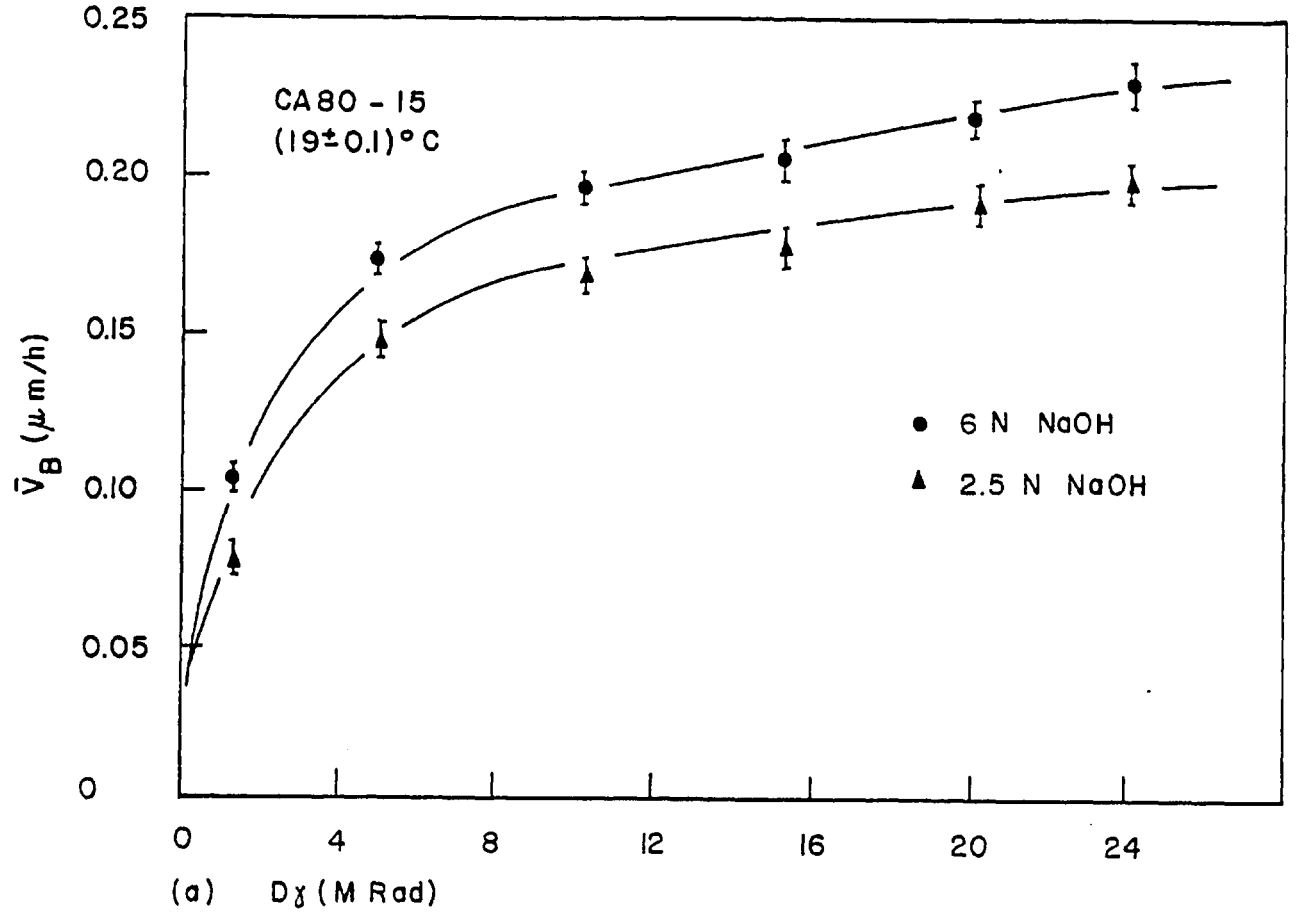
THE AVERAGE BULK ETCH RATES AND IRRADIATION MASS LOSSES FOR CA80-15. THE ETCHANT WAS 6N KOH AT (60 ± 0.1)°C

^{60}Co Absorbed γ-Dose (Rads)	Average Bulk Etch Rate ($\overline{V}_B$) (μm/h)	Equivalent Thickness of Mass Loss (μm)
0	13	0
5.0×10^6	16	0
1.0×10^7	18.5	0.08
1.5×10^7	20.5	0.14
2.0×10^7	22	0.28
2.4×10^7	23.5	0.37

TABLE 6.2

THE 'k-VALUES' FOR DIFFERENT ETCHING CONDITIONS IN CASE OF CA80-15

Etching Condition	'k-Value' (M Rad^{-1})
E_1 : 2.5N NaOH at 19°C	0.38
E_2 : 6N NaOH at 19°C	0.35
E_3 : 2.5N NaOH at 60°C	0.06
E_4 : 6N NaOH at 60°C	0.045
E_5 : 2.5N KOH at 19°C	0.18
E_6 : 6N KOH at 19°C	0.05
E_7 : 2.5N KOH at 60°C	0.10
E_8 : 6N KOH at 60°C	0.036



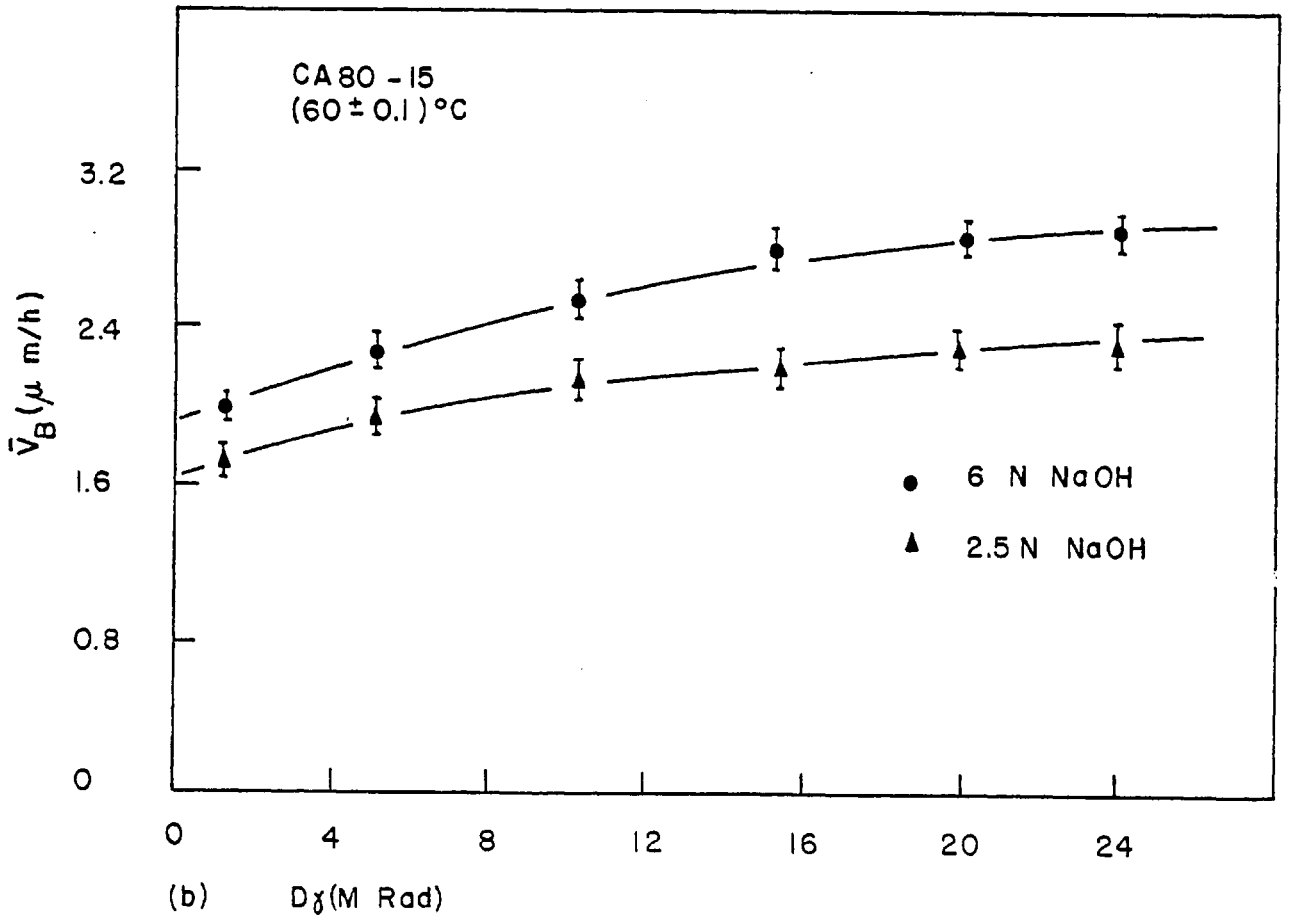


Figure 6.3 The average bulk etch rate, $\bar{V}_B$ of CA80-15 as a function of absorbed gamma dose, D_γ. Etched for, (a) 96 hours, (b) 5 hours, without interruptions or stirring

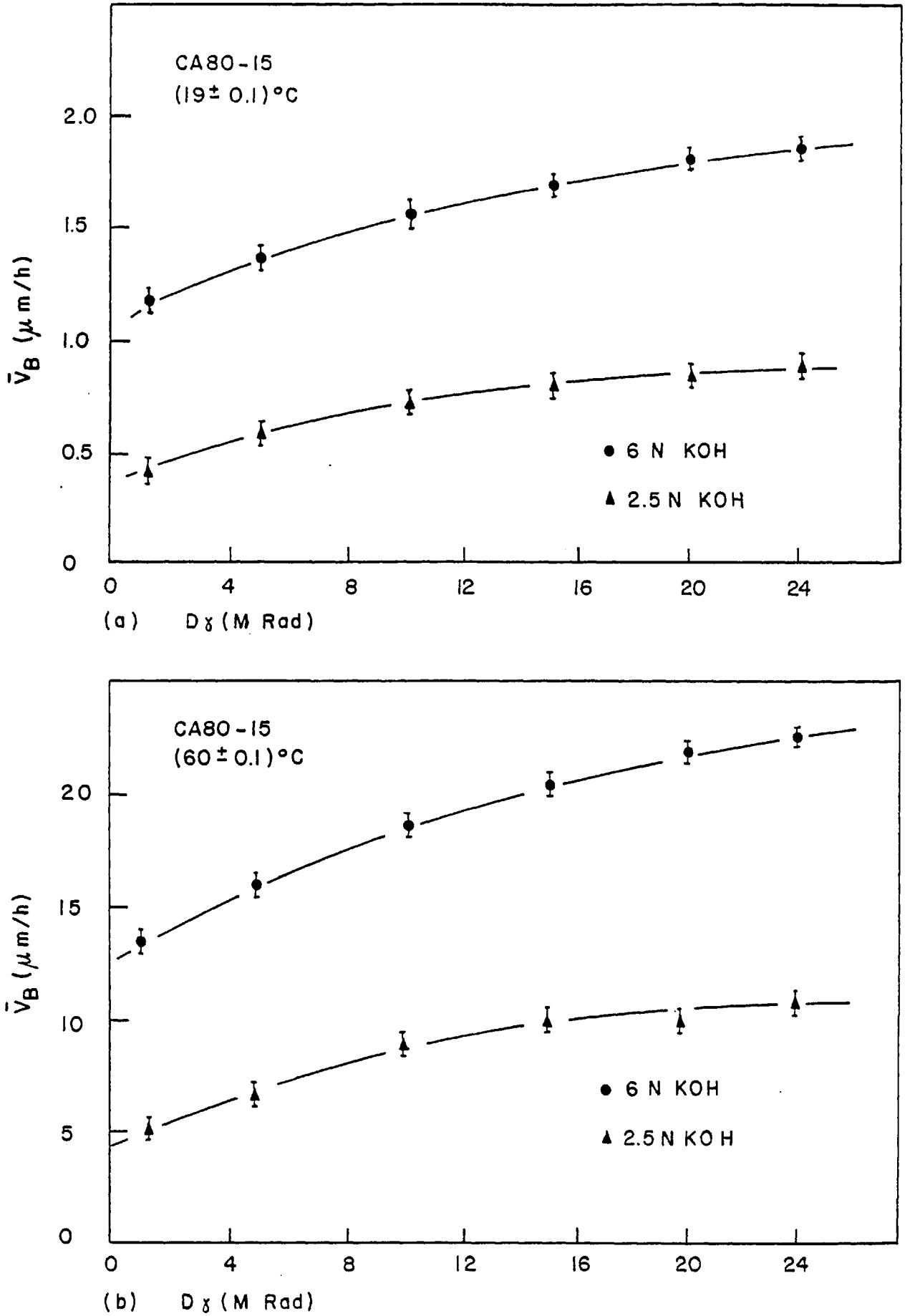


Figure 6.4 The average bulk etch rate, $\bar{V}_B$ of CA80-15 as a function of absorbed gamma dose, D_γ. Etched for (a) 25 hours, (b) 2.5 hours, without interruptions or stirring

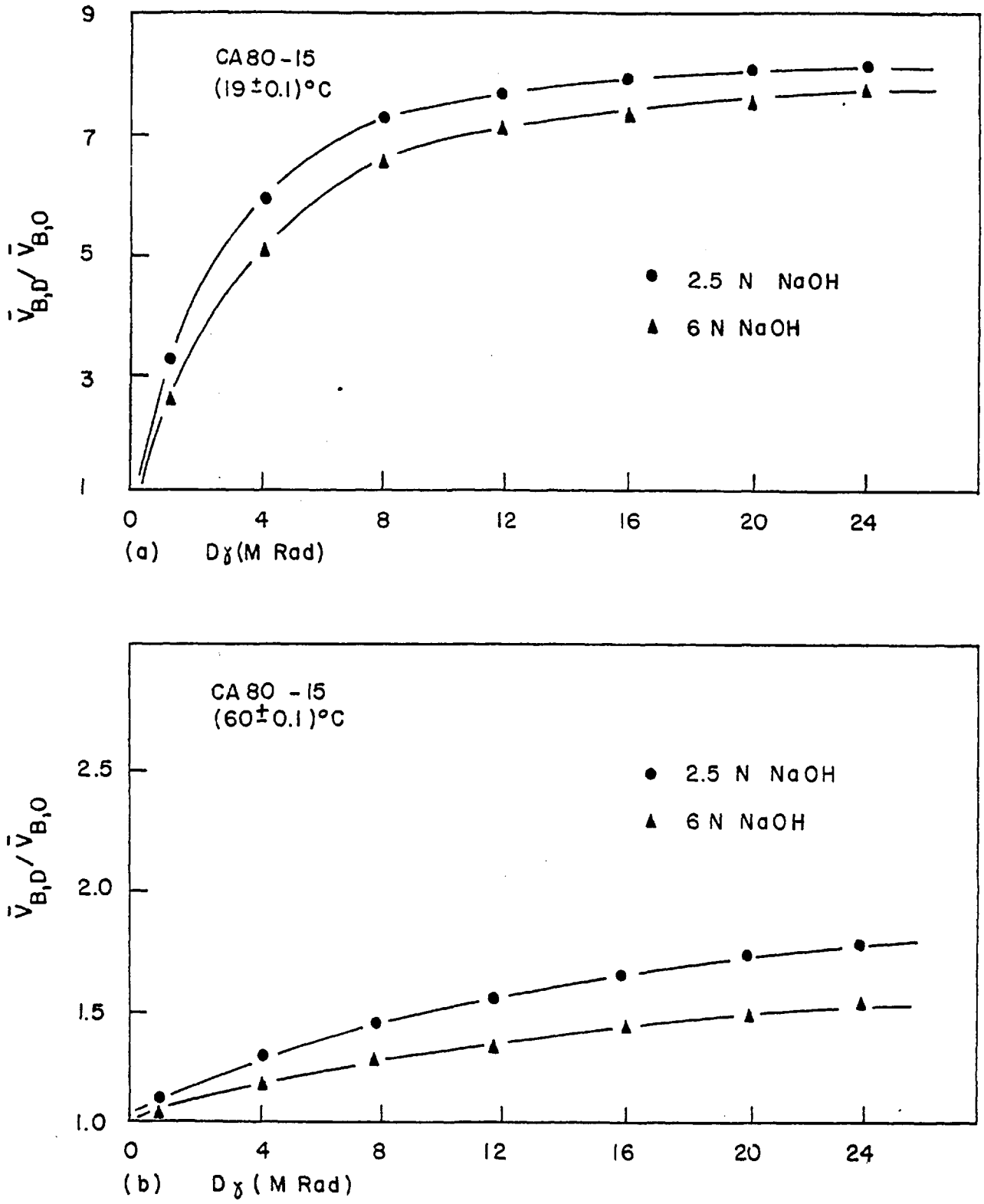


Figure 6.5 $\bar{V}_{B,D}/\bar{V}_{B,0}$, the ratio of average values of bulk etch rates of CA80-15 at gamma doses of 'D-megarads' and 'zero-megarads', as a function of absorbed gamma dose, D_γ, (a) averaged over an etching time of 96 hours, (b) averaged over an etching time of 5 hours

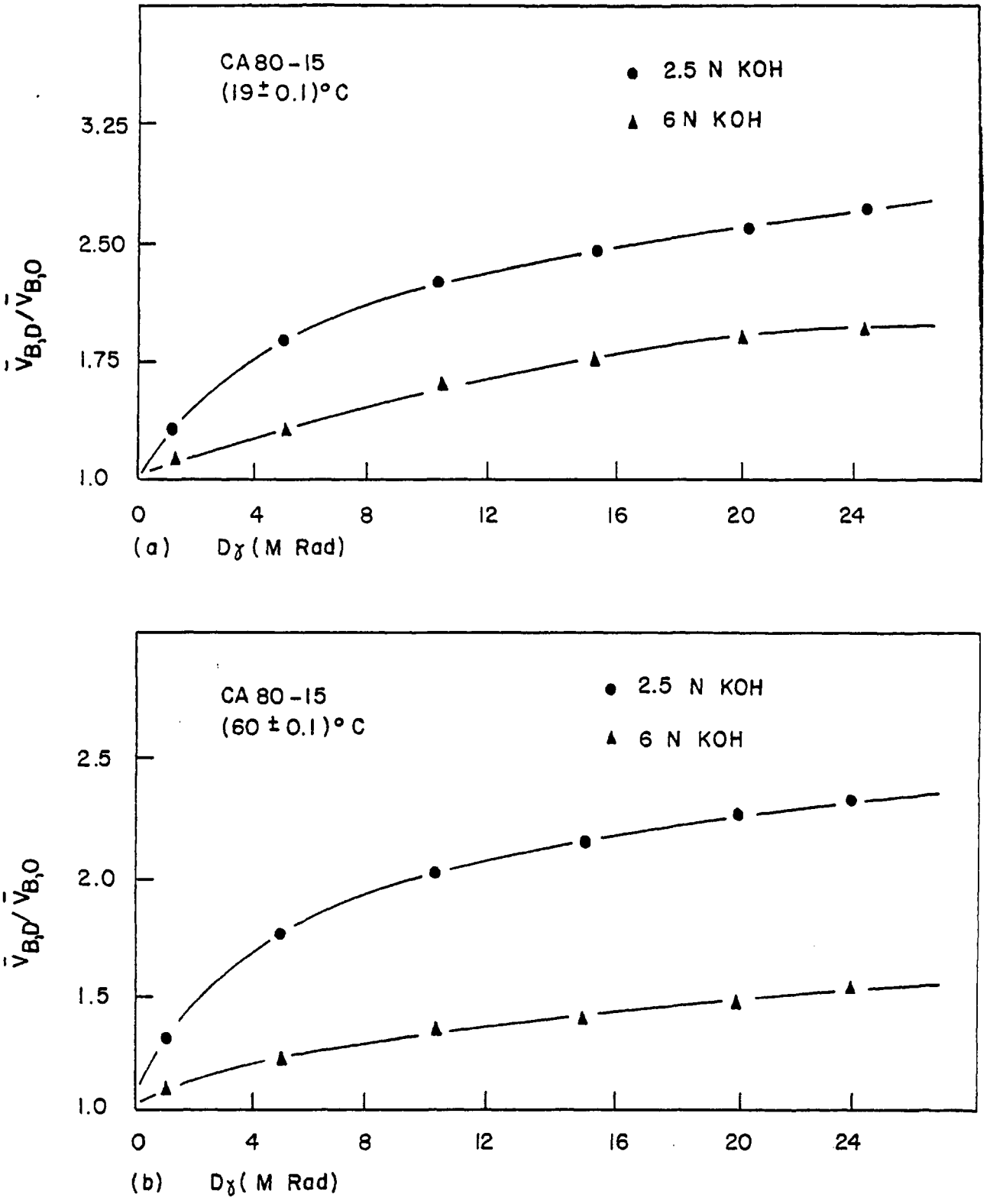


Figure 6.6 $\bar{V}_{B,D}/\bar{V}_{B,0}$ the ratio of average values of bulk etch rates of CA80-15 at gamma doses of 'D-megarads' and 'zero-megarads', as a function of absorbed gamma dose, D_γ, (a) averaged over an etching time of 25 hours, (b) averaged over an etching time of 2.5 hours

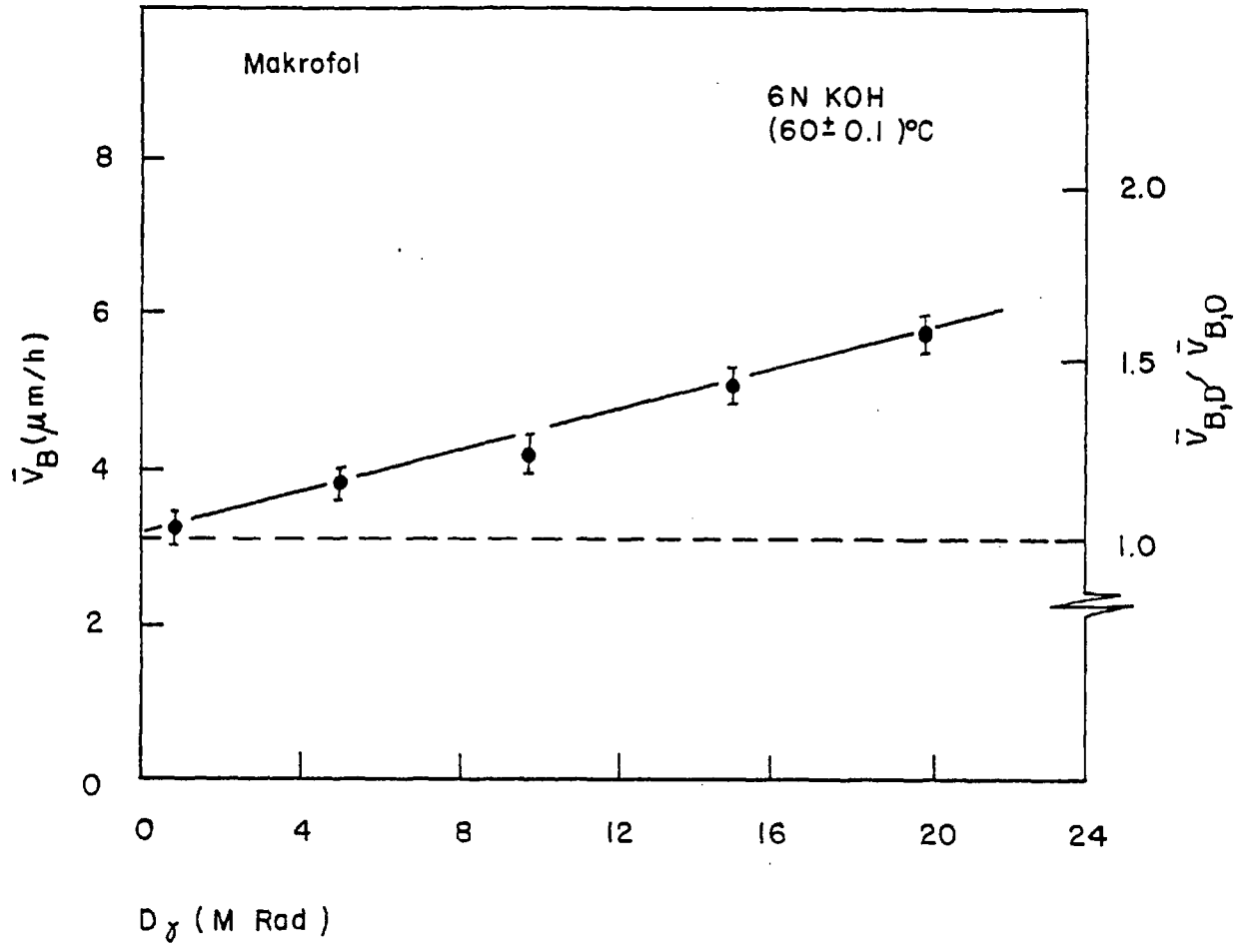


Figure 6.7 $\bar{V}_B$, the average bulk etch rate and $\bar{V}_{B,D}/\bar{V}_{B,O}$, the ratio of average values of bulk etch rates of Makrofol K.G at gamma doses of 'D-megarads' and 'zero-megarads', as a function of absorbed gamma dose, D_γ. The etching was carried out in 6N KOH at 60°C; without stirring

where $V_{B,D}$ and $V_{B,O}$ are the bulk etching rates at gamma doses of 'D-megarads' and 'zero-megarads' respectively, 'D' is the absorbed dose and 'k' is a constant. The 'k-values' for etching conditions E_1-E_8 (curves of Figs.6.5 and 6.6) are given in Table 6.2. Fig.6.7 shows that Makrofol K.G is less sensitive to gamma-rays than CA80-15.

The influence of different etching conditions on the ratio $\bar{V}_{B,D}/\bar{V}_{B,O}$ is similar to that shown for $\bar{W}_D/\bar{W}_o$ i.e. there is a significant increase for the low temperature etching conditions. A possible explanation of these results is the phenomenon of swelling[93] observed in cellulose and its derivatives in alkaline solutions at low temperatures (see Chapter 3). Swelling is known to be significant below 20°C[93] but negligible above 30°C. Furthermore, swelling is maximised at an ion concentration of 2.5N, which is the etching condition for E_1, E_3, E_5 and E_7. The swelling is related to the diffusion of ions into the cellulose nitrate due to ion exchange with acidic (carboxyl) groups. Since radiation damage involves the creation of such groups in cellulose nitrate, the swelling is considerably increased with radiation damage and consequently the bulk etching rate, V_B is also increased, since the more rapid penetration of the surface by ions will increase the rate of reaction and of dissolution of the surface.

Fig.6.8 shows the number of neutron induced tracks in CA80-15 exposed to 17 MeV neutrons followed by gamma-rays (set E) as a function of absorbed dose, D_γ. The track density starts decreasing at ≃ 8 M Rads, this is because of

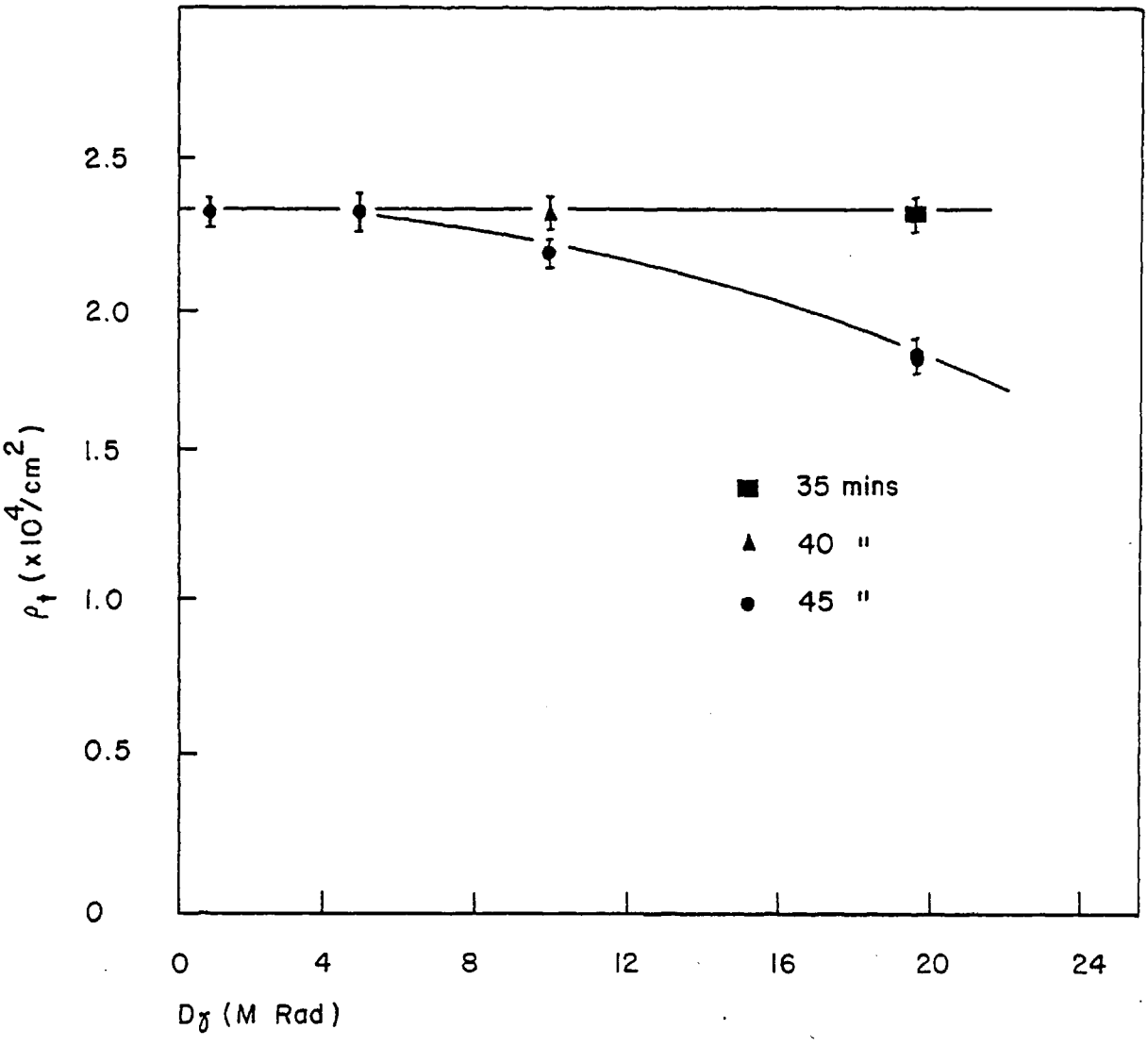


Figure 6.8 The track density, ρ_t in CA80-15 exposed to 17 MeV neutrons followed by gamma-rays, as a function of absorbed gamma dose, D_γ. Etched in 6N KOH at 60°C for various time intervals

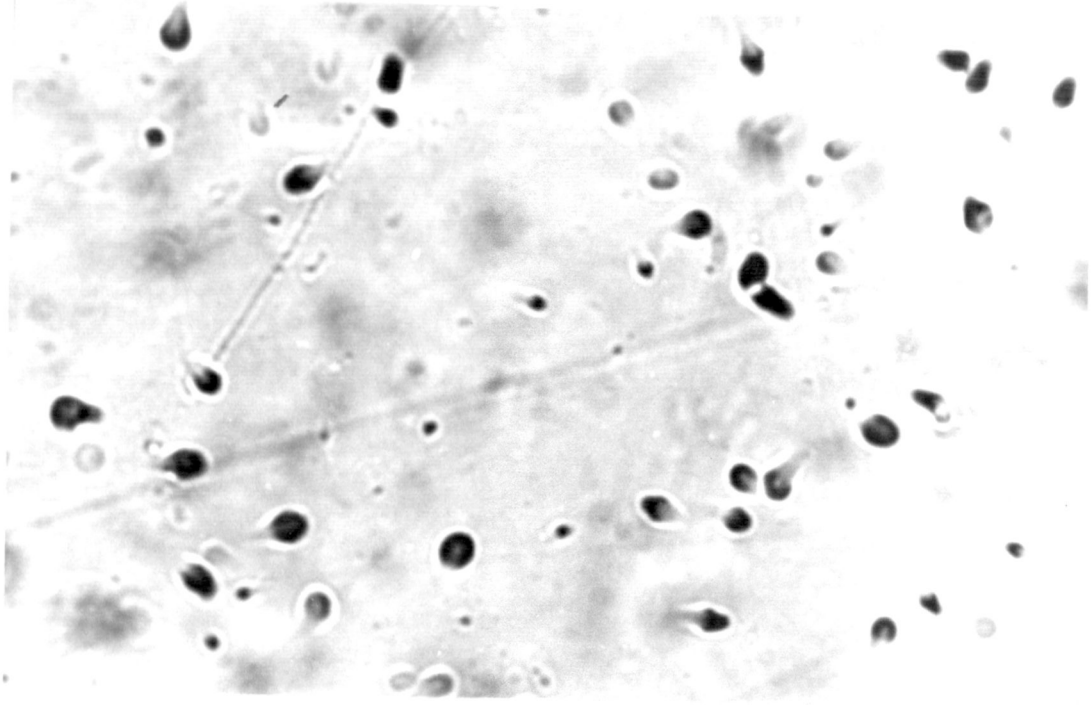


Figure 6.9 1 MeV alpha-particle tracks in CA80-15; subjected to a gamma-ray dose of 20 M rads and subsequently irradiated with alpha-particles. Etching was carried out in 6N KOH at 60°C for 10 minutes and the tracks were observed at a magnification of (x 50 x 8)

the increase in the bulk etching rate of CA80-15, which makes the background surface roughened thus making it difficult to avoid the counting loss. However, when etching times were reduced according to the increase in the bulk etching rate, the track density remained constant even at high gamma-ray doses as shown in the figure.

Fig.6.9 shows a microphotograph of alpha tracks in CA80-15 which was first subjected to a gamma-ray dose of 20 M Rads and subsequently irradiated with alpha particles from an ^{241}Am-source in 2 π-geometry (set F).

6.3.1 Errors

Errors in these measurements could be due to the calibration of the ^{60}Co-gamma-ray field, determination of the plastic thickness, the density of the different films and changes in the etchant strength and temperature. The dose calibrations are correct on an absolute basis to $\pm$ 3%. Within a single exposure the dose delivered to different films are equal to about 0.5%. Errors in the density of different films are quite small and probably negligible from strip to strip. The accuracy of the etching bath used is $\pm$ 0.1^{o}C, therefore resulting etch rate changes are < 2%.

6.4 CONCLUSIONS

The following summarised conclusions can be drawn from the results presented in this chapter.

(i) Gamma-ray doses in the region of a few megarads (and above) bring changes not only in the general structure

of the plastic SSTR, but also in the damaged region of the latent damage trail. Thus effectively increasing the 'volume' of the damaged region. The degree to which the damaged and undamaged regions are modified increases with increasing gamma-ray dose. Gamma-ray doses below the 'megarad region' do not alter the structure to any significant extent.

(ii) The influence of gamma-rays on the radiochemical changes in the bulk cellulose nitrate can be discriminated by varying the chemical etching conditions.

(iii) Gamma-ray doses up to 24 M Rads do not affect the track registration characteristics of CA80-15 and Makrofol K.G SSTRs.

(iv) The systematic increase in the bulk etching rate, V_B suggests the possibility of use of SSTRs for the measurement of large gamma-ray doses, while at the same time measuring neutrons. Some advantages of the technique are relative ease and simplicity of data read-out (measuring the thickness of plastic before and after etching, and comparing with a calibration curve) and high degree of reproducibility obtainable.

CHAPTER 7

AUTOMATIC COUNTING OF TRACKS IN SSTRs

7.1 INTRODUCTION

A problem associated with the use of SSTRs in the measurement of neutrons (determination of nuclear reaction rates), is the large number of tracks that must be counted for good statistics. If the tracks have to be counted by eye using a microscope, then the technique could be subject to errors due to the laborious nature of the work. This is particularly true in the case of 'intrinsic' SSTRs, where the resultant tracks have a wide range of dimensions and an observer chooses to count a track using his own criteria on the diameter and appearance, which would not necessarily coincide with those of a second observer. Thus making the technique subjective to human decisions on the number of tracks counted in an etched SSTR.

Various attempts have been made to automise the track counting in SSTRs. Ozalid method[94] and light scattering[95], are two of the earliest attempts in semi-automatic track counting. A spark counting method[96], applicable with plastic SSTRs has been successfully demonstrated. Recent investigations take advantage of digital computers in automatic scanners[97]. Three commercially available instruments, the Quantimet[98], the Classimat[99] and the Leitz T.A.S.[100], have been used in automatic track counting[101]. These instruments have a high capital cost, and often have peripheral equipment suited only to their prime task of analysing well-defined objects/images with sharp outlines.

A system has been developed at Imperial College[85], which permits the automatic counting of tracks using a TV camera and a mini-computer. The computer is now a common feature of nuclear physics laboratories and the addition of a TV camera together with a simple set of interfacing electronics, can result in a powerful system for automatic counting for a modest investment.

It is not sufficient just to count tracks, since more than one type of trakcs are visible in 'intrinsic' SSTRs and therefore it is necessary to discriminate against unwanted 'background'. Thus a variety of measurements must be performed on each track, such as area, length to breadth or some other specific parameter in order to determine if the track is valid.

Tracks appear under the surface of the recorder if they are at an angle to the surface and thus present an imperfect image for analysis. Focussing can therefore present problems.

The present system was developed so that a variety of form factors such as area to perimeter could be used to identify desired tracks. Focussing problems are overcome by using a range of grey levels (light intensity values), together with software discrimination, to reject out of focus images.

In this Chapter, the system hardware, software and its calibration for track counting are described and a typical analysis is presented, and compared with manual counting. Finally, some conclusions are drawn on the performance of the system.

7.2 SYSTEM HARDWARE

A block diagram of the system hardware is shown in Fig.7.1. The tracks in an etched SSTR are photographed from the optical microscope (Reichert model MEF2, described in Section 3.4, Chapter 3), on an Ilford PanF (35 mm) film. Developing for 3.5 minutes in Ilford contrast FF at 1:4 dilution produces negatives with adequate contrast which are used directly in the automatic counting system (see Fig.7.1).

Illumination of the negatives is by a 12V quartz iodine lamp with condenser lens and diffusing screen, using direct current to avoid loss of information during the TV scanning. A Sony AVC4600CE television camera with vidicon tube and 80 mm focal length lens, scans the negative. Its video signal is passed to a purpose built digitiser, which divides each of the 625 lines into 384 picture points, a number consistent with the resolution of the camera. The grid used in practice is restricted to 580 lines (y-coordinates, measured from top of frame) by 380 points (x-coordinates measured from left of frame). Each point is assigned a grey level on an equal interval scale from 0 to 7, enabling the level to be represented by three bits. The seven levels are contained within a 'window' which can be stretched or compressed relative to the video signal, either by altering the level 7 voltage or by adjusting the signal level (via the camera lens aperture or video gain).

The digitised information is transferred to a Digital Equipment Corporation (D.E.C.) PDP 11/45 mini-computer (24K,

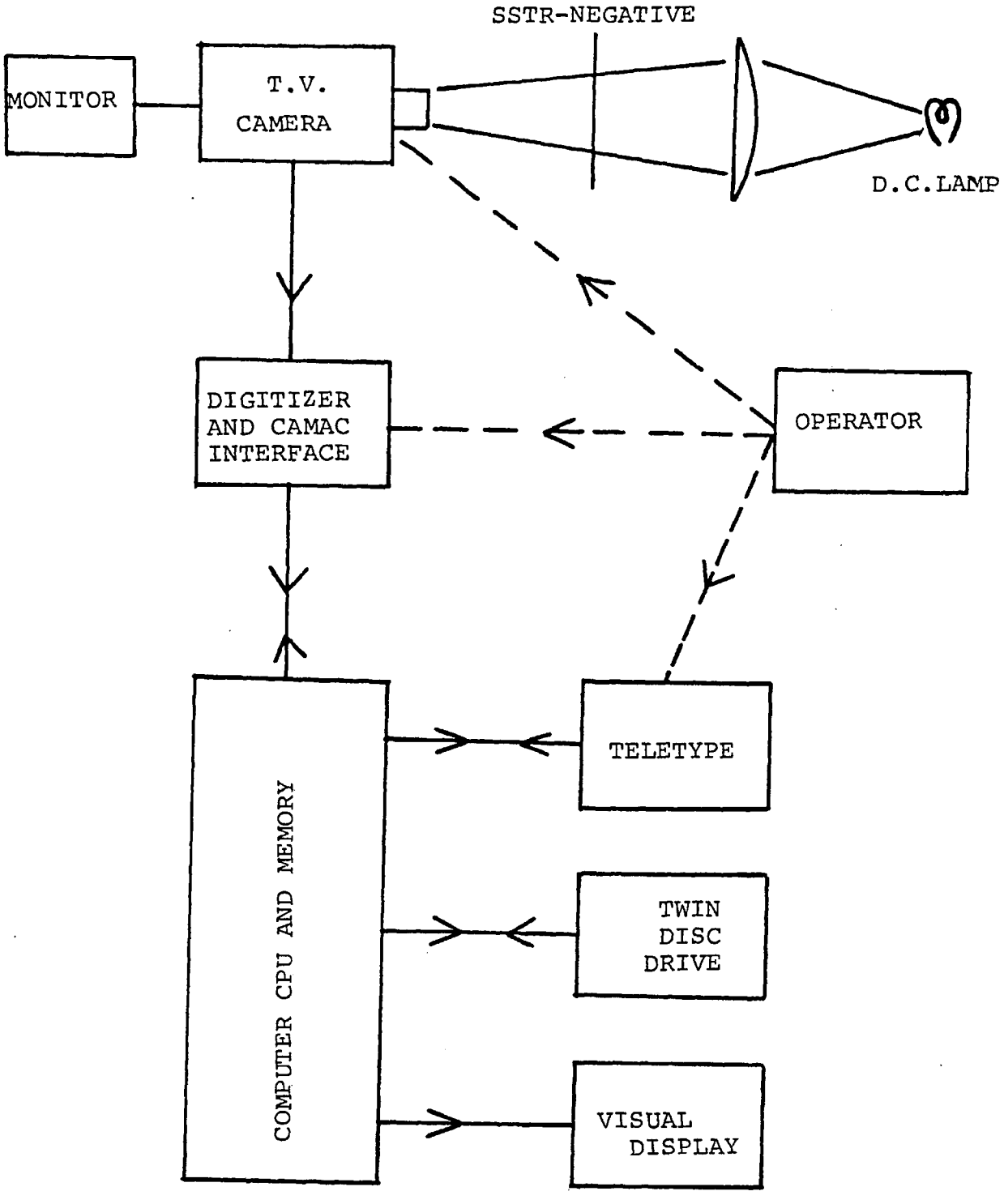


Figure 7.1 Block diagram of automatic track counting system hardware

16 bit words), the reading sequence of (x,y) coordinates, determined by the scanning speed and the interlaced scan pattern, is (1,1),(1,3), (1,5) ----,(1,570),(1,2),(1,4),(1,6)----,(1,580),(2,1),(2,3) etc. (The half line at the beginning of one of the two interlaced scans is masked out.) The grey levels are packed five to a word, gaps being left during the odd scans to be filled during the next even scan so that y-coordinates are stored consecutively. To overcome the apparent requirement for a buffer size of 44K for a complete frame, logic is incorporated to halt reading, when the x-coordinate reaches 128 or 256; software restarts reading after the 15K buffer, holding data from one third of the frame, has been emptied.

A D.E.C. RK-05 disc is used to hold the data from up to 24 frames for subsequent analysis (the area making up one photographic negative being determined by the overall magnificiation required to count with sufficient accuracy the smallest tracks of interest). The data can be recalled at any time to display on a video monitor (Tektronix 611) the detected images at or above any desired grey level, a useful facility in cases, where there is some doubt as to how the system will interpret certain features on the negative, such as areas of markedly different background intensity. The system set-up is pictured in Figs.7.2(a) and (b).

7.2.1 The Digitiser

A block diagram indicating important parts of the digitiser is shown in Fig.7.3. The basic function of this hardware is to divide each horizontal scan line (x-direction)

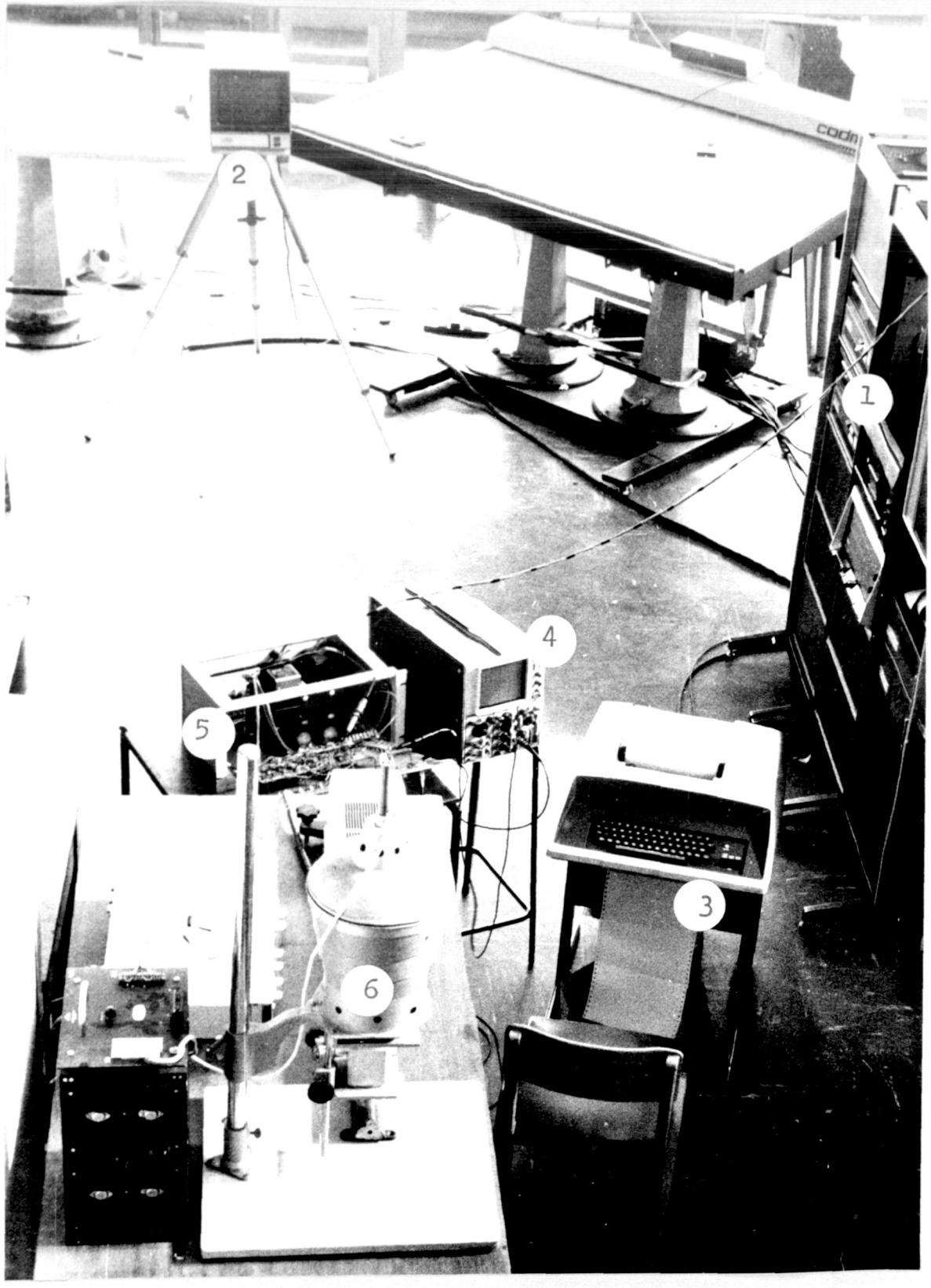


Figure 7.2 (a) Automatic track counting system set-up.
(1) PDP 11/45 computer, (2) Tektronix 611,
(3) Teletype, (4) Oscilloscope, (5) Digitiser,
(6) DC light source

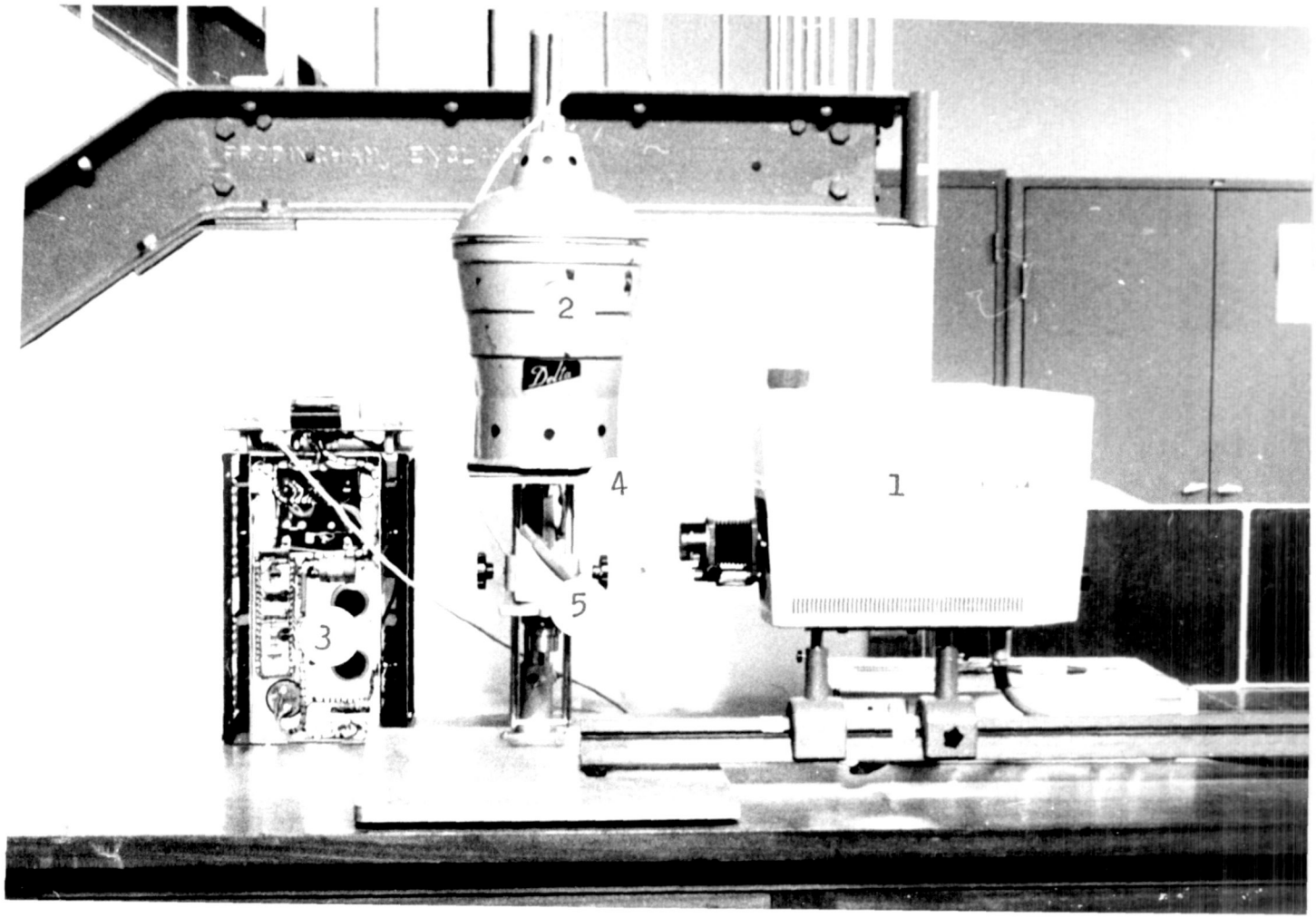


Figure 7.2 (b) Automatic track counting system set-up. (1) TV camera, (2) DC light source, (3) DC power supply, (4) SSTR negative, (5) Image reflector

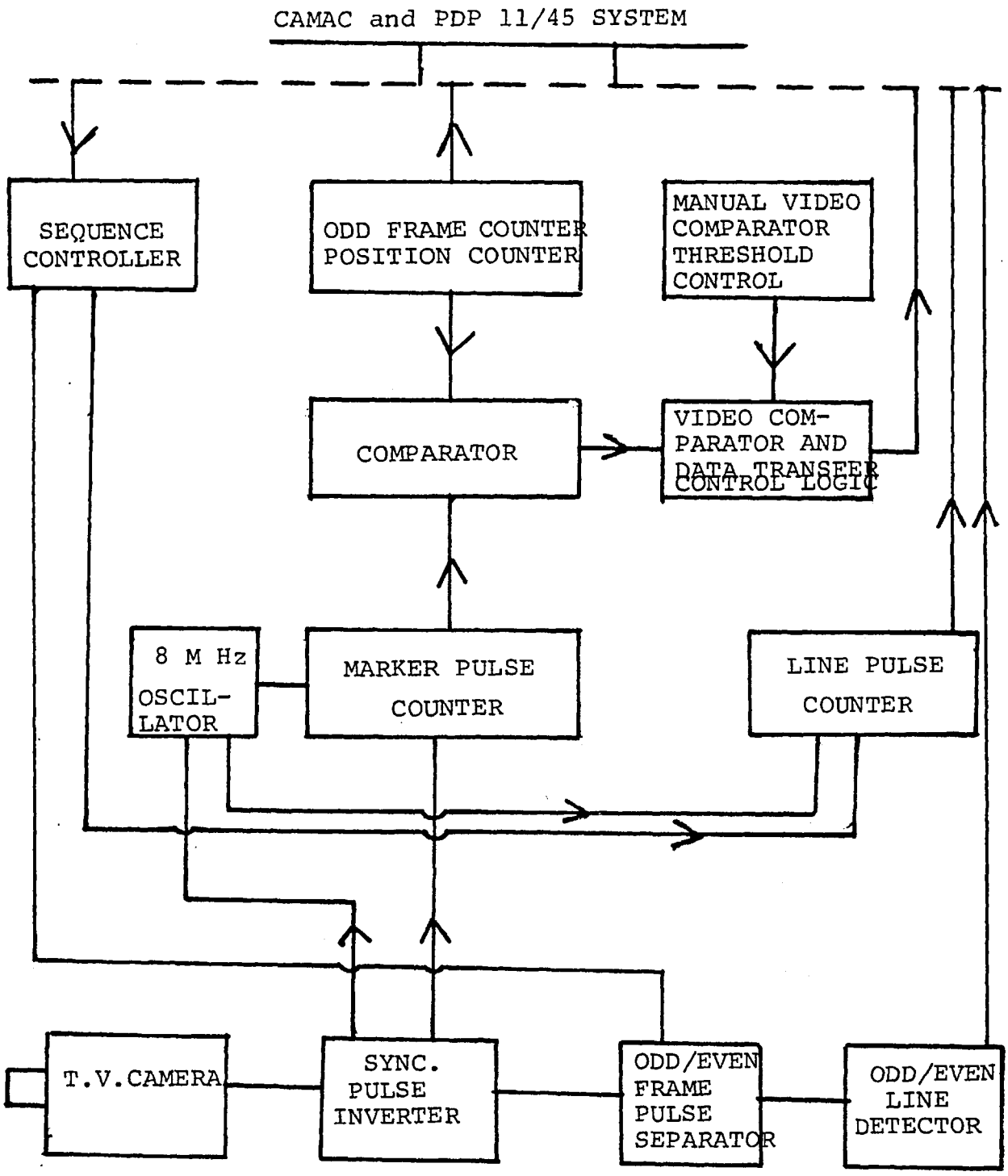


Figure 7.3 Block diagram of the digitiser

into 380 picture points. Since a minimum of 9 bits is needed to represent 625 or 380, outputs from the interface are designed to allow for 10 bits for y-coordinates and 10 bits for x-coordinates. An end of data flag, when all 380 x and 625 y coordinates are read, is set by switching on all 10 bits of x- or y-, thus representing a value so large (1023 in decimal) that software would register the end of information[102].

Output from the digitiser is fed to PDP-11/45 mini-computer, via the CAMAC interface modules. A complete picture array consists of 380 repeated interlaced scans, each repeat corresponding to a shift in the x-direction by one unit of x-coordinate. For each shift in the x-coordinate a vertical column of 625 y-coordinate grey levels is fed into the computer. Since interlaced scan is present, an initial set of odd y-coordinates is read into the buffer to be immediately followed by a set of even y-coordinates, with each shift in the x-direction. The CAMAC interface has up to 24 bits of parallel logic input. For the black and white system[85], only 22 bits are used, one bit to signify odd or even field scan and one for black or white, apart from the ten -x and ten -y bits, PDP-11 software for this early version therefore simply tests the black or white bit as well as the odd or even bit and sets up a black and white bit map in core making use of the x- and y-coordinate information. On a 24K memory machine with 16 bit word length, sixteen grey levels can be packed into each word, since in this early version only one bit signifies grey level. An array of 625 y- and 380 -x picture points

therefore needed a buffer size of approximately 15K which a 24K memory machine adequately accommodates.

7.2.2 Extensions to the Digitiser Hardware

Upon expanding to multi grey levels, software manipulation of incoming data was slow owing to the need for every (x,y) coordinate pair to be accompanied by 3 bits of grey level information. As a result, every other incoming data position was missed. Further, a new buffer size of 44K was needed to accommodate a single transfer of digitised 3-bit grey levels. (This corresponded to packing five 3-bit units of information into each PDP-11 word, the most significant bit (M.S.B.) left as a spare bit). In view of buffer size limitation on a 24K machine, it was decided to make three repeated transfers, each transfer embracing a third of the total number of 3-bit information units from a complete picture array of (x,y) coordinate pairs. To achieve this, additional logic was incorporated into the sequence control logic. When the x-coordinate position, indicated by the odd frame counter, reaches either 128 or 256, a pulse generated by the sequence control logic, is passed on to the data control line, which immediately stops the reading operation. PDP-11 software instruction later restarts the reading from where it left off, having first emptied the buffer for the earlier transfer.

A new criterion for software was also needed. It was decided to ignore, in the software, the available bits of x- and y-coordinates, but to test the odd or even bit for a repeated sequence. Since each shift in the x-coordinate

was accompanied by a set of consecutive odd and even y-coordinates, it was therefore possible to decode the relative positions of the 3-bits of grey level information by knowing the reading order.

Hardware modifications to the existing black and white system[85], therefore included the following:

(i) Introduction of seven grey levels (3 bits for grey level).

(ii) Masking out of first half line scans where they appeared.

(iii) Automatic stoppage to hardware, when data read in reached an x-value of either 128 or 256.

(iv) Addition of an adjustable seven grey level 'window' to allow for less contrast pictures to be meaningfully digitised and hence analysed.

In the block diagram of the digitiser (Fig.7.3) all above mentioned modifications are implemented.

7.3 SYSTEM SOFTWARE

A modular software system was devised for the digitiser in order to permit expansion into a variety of applications[102]. The flow of information through the system is indicated in Fig.7.4. The main aims of the software are:

(i) Identify individual detected image, linked images are regarded as one large image, which can be identified subsequently by a shape factor or area test.

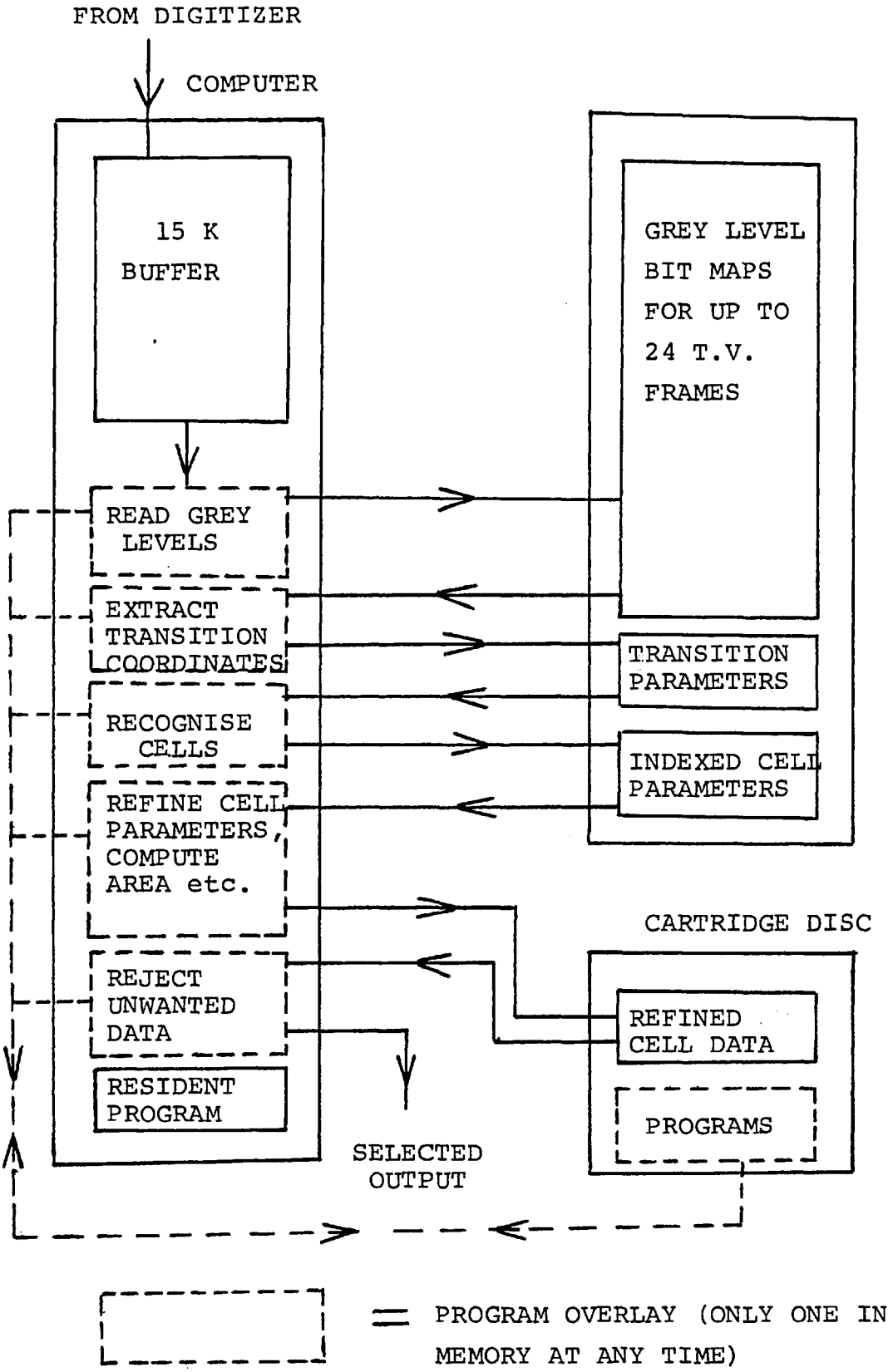


Figure 7.4 Flow of information through automatic track counting system

(ii) Assign a number to each image, hence 'counting' them.

(iii) Store up for each image, all digitised information on that image.

(iv) To repeat image identification at several grey levels.

(v) Compute area and perimeter of each image in picture point units (p.p.), from which a shape factor (S.F.), defined as $(\text{perimeter})^2/\text{area}$ is derived.

(vi) Discard 'background' from computation of area, based on an earlier calibration with standard track images of a given area.

7.3.1 Definitions

To understand the different routines described in the following pages, it is best to define some terminology used in the description:

(i) A 'picture point' is defined as an element of the 2-dimensional array which defines the entire picture. Its position in the array is determined by a (x,y) coordinate pair.

(ii) A 'picture function' is the digitised grey level value associated with a picture point. Mathematically, a picture function can be described as a real valued function of two real variables[103].

(iii) A 'cell' is made up of a set of physically adjacent picture points, whose picture functions

satisfy a given grey level criterion. The shape of each cell is determined by shape factor.

(iv) Each cell 'transition' is defined as that segment of a TV scan line along which consecutive picture functions, satisfy a grey level criterion.

(v) 'Voids' are regions in the 2-dimensional array, in which the picture functions fail to satisfy a set criterion.

7.3.2 Program and Data Structure on PDP-11

The main functions of the software together with the data organisation of each routine are now discussed.

(i) Routine CAMERA (Assembly language)

The routine CAMERA originally written for the black and white system (2 grey levels only) was expanded for use in the multi-grey level system. It used 10(x) and 10(y) bits to set up a binary map of grey levels.

A new version of this routine, coupled with hardware masking of the field scan is used to test the odd or even scan bit and to set-up a grey level binary map by shifting the x-coordinate after each complete picture scan. Main parameters describing the location of each transition in the digitised 2-D grey level bit map are the line number (y), start (x_{in}) and the end (x_{out}) of the transition.

(ii) Data Structure

On a 24K PDP-11, under DOS-BATCH operation with two fixed RK-05 disk derives (identified as disk 0 and disk 1), memory organisation plays a vital role in achieving speed and efficient use of available resources. Digitised information stored is thus confined to the first 432 sectors (corresponding to 24 files) of disk memory space. The remaining 360 sectors are assigned for dynamic data transfer between core and disk memory:

Total number of picture points used = 380(x) x 580(y)

Grey level bits = 3

Word length of PDP-11 = 16 bits

Allowing for 5 sets of grey levels into one word, buffer size required = 44K

Disk (5M Byte) storage: 60 sectors to each pass or 180 sectors for 1 frame (3 passes). At 256 words per sector, 180 sectors = 46,080 words

Maximum number of data files (contiguous) per disk = 24

Although 24 bits of parallel logic output were available from the digitiser, CAMERA only makes use of 4 bits of information to set-up the grey level binary map.

7.3.3 Routine LEVEL (Assembly language)

LEVEL accesses the binary grey level map on disk for a given set of arguments, namely x-, y-coordinates and n file, the data file number. It returns a value of grey level, LEV, for the (x,y,n file) set of arguments. During

compilation, LEVEL is used as a subroutine only and cannot be used on its own. Subroutine LEVEL can be linked, just before execution, with Fortran program CARIK (follows shortly) to determine coordinates of detected images.

7.3.4 Routine DIS2 (Fortran)

Simply displays bit map (on disk) on the Tektronix screen for any one of seven grey levels. Subroutines needed to feed this program are LEVEL and DOT2. DIS2 actually displays grey levels above a required level.

7.3.5 Routine DOT2 (Assembly language)

This routine returns a dot to the Tektronix display screen for a given (x,y) coordinate pair. Execution mode is CALL DOT2(X,Y). However, it is in turn fed by several other subroutines, which manipulate and display incoming information to the display screen.

7.3.6 Routine CARIK (Fortran)

CARIK creates a data file of considerably reduced information on disk, of (x,y) coordinate pairs at entry and exit from detected images at a required grey level. It searches the binary map along consecutive columns (i.e. in y-direction) and records the first entry (x,y)-coordinate pair to a detected image line or column, indicated by a sudden rise of the digitised video signal to or above the required grey level. The next (x,y)-coordinate pair to be recorded is at the position immediately before the video level next falls below the required grey level, and this

(x,y)-coordinate pair is the exit coordinate for that detected image line. When the video signal next rises above or to the required grey level, another set of entry coordinates is recorded and the pattern repeated for the rest of the scan lines. Where a detected image does not fall below the required grey level towards the end of a line scan, CARIK resets the video level to below the required grey level and records the end of line (x,y)-coordinate pair as exit coordinates for that image. Thus a solid row of detected picture points only has both end coordinates recorded irrespective of its real length. CARIK has been designed to search for x_{entry}, y_{entry} and x_{exit} from level 3 up to level 7. It has to be linked to subroutine LEVEL before execution.

Another important aspect of CARIK is in the search sequence on the binary map. Searching the bit map along x-direction (i.e. across each scan line) as opposed to y-direction (i.e. vertically downwards) would lead to an increase in computer time by a factor of x 380. A 580 x 380 array is scanned in 90 seconds in the y-direction.

7.3.7 Routine SORT (Fortran)

Software discrimination of in-focus from out-of-focus images is the main task of this routine. The data file created by the program CARIK is the input data to SORT. This routine is structured on a main program fed by other functional subroutines. Outputs from the main program are a set of individual detected images and their corresponding detected coordinates for one or more grey levels. Functional

subroutines which calculate area and/or perimeter in picture points, or shape factors or discriminate between in- and out-of-focus images using an area gradient method, can be added to execute immediately after the main program.

7.3.8 Routine SEARCH

SEARCH executes a coded chain search of all data from program CARIK and assigns an identity to each image thus determined. The grey level searched is the lowest level fed in to program CARIK.

7.3.9 Routine TENTU

This routine reads data from SEARCH, fills in voids and writes out cell data (number, shape factor, area) if needed. The images below a pre-calibrated value of cell area in picture points are not counted, thus rejecting some of the unwanted features.

7.4 CALIBRATION OF THE SYSTEM

The factors affecting the performance of the system can be divided into three groups, optical, electronic and statistical. The statistical accuracy is determined by the number of tracks per field of view, which depends on the overall magnification, which in turn depends on the physical size of the SSTR.

7.4.1 Grey-Level Setting

The most accurate and reproducible threshold setting is illustrated by plotting the number of tracks against different

grey levels. It is more accurate to consider the total number of tracks in several successive fields of view (i.e. several negatives), corresponding to one grey level, and counting the same field for another grey level and so on. Fig.7.5 shows the results of the two etched SSTRs (CA80-15) exposed to fast neutrons (2 MeV) and thermal neutrons. It can be seen from Fig.7.5 that levels 4 and 5 are the 'safe' working levels. At level 6, only few tracks with a high contrast are counted. Figs.7.6(a) and (b) show the digitised tracks displayed on Tektronix 611 screen at levels 4 and 5.

7.4.2 Size Setting

The size setting discriminates against features with an area (in picture points) less than a value chosen in discrete steps in the routine TENTU. A calibration was made to measure the track area (in p.p.) at the magnifications used in manual scanning ofSSTRs irradiated with 2 MeV neutrons (Chapter 4), and it was found that a track with 1 μm diameter has an area of 20 picture points in the digitiser. In manual scanning tracks with diameters less than 1 μm were not counted, therefore in the automatic counting,tracks with areas less than 20 picture points were rejected in the routine TENTU.

A typical frequency histogram of the number of tracks in CA80-15 exposed to 2 MeV neutrons, as a function of track area in picture points is given in Fig.7.7.

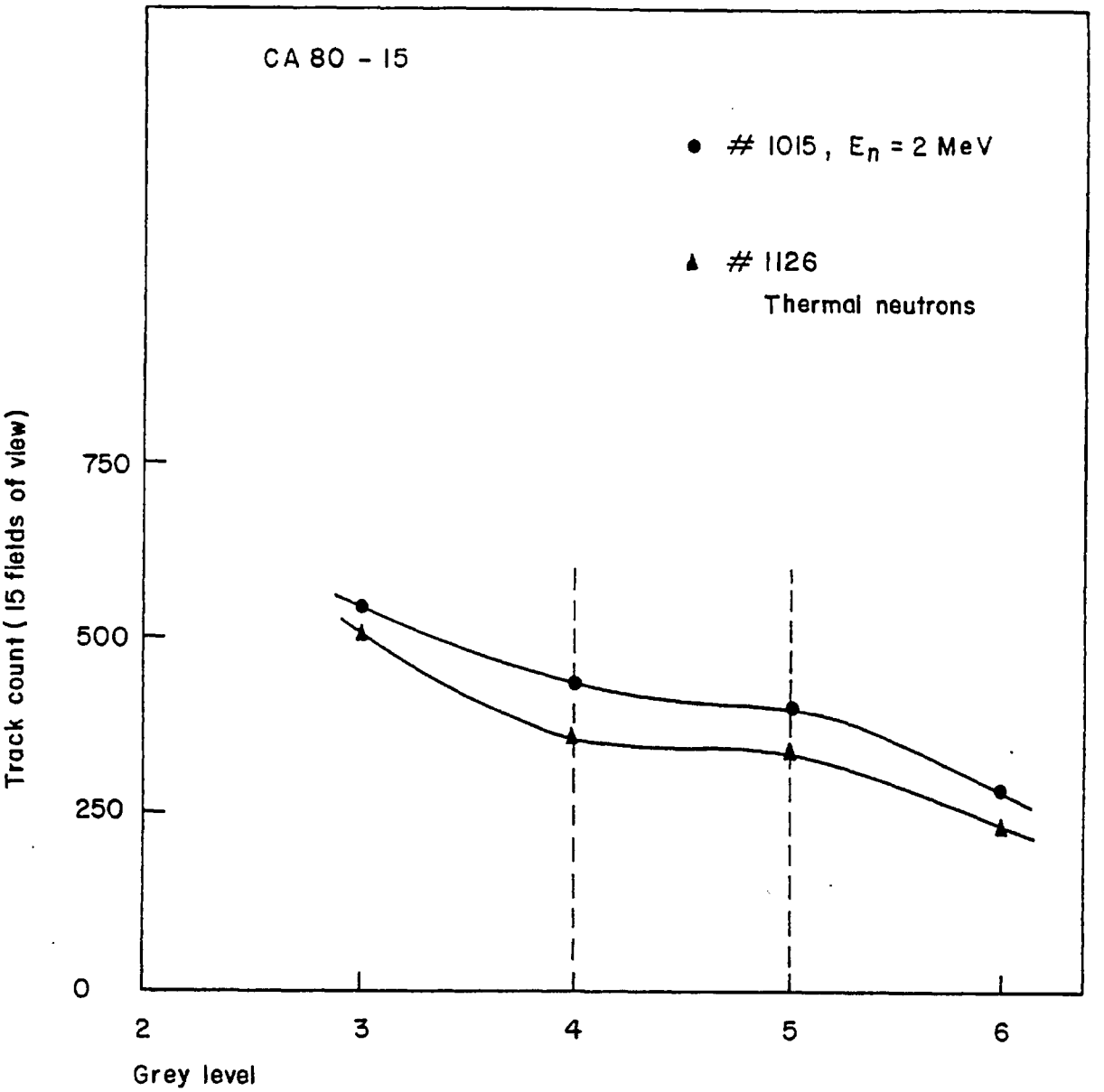
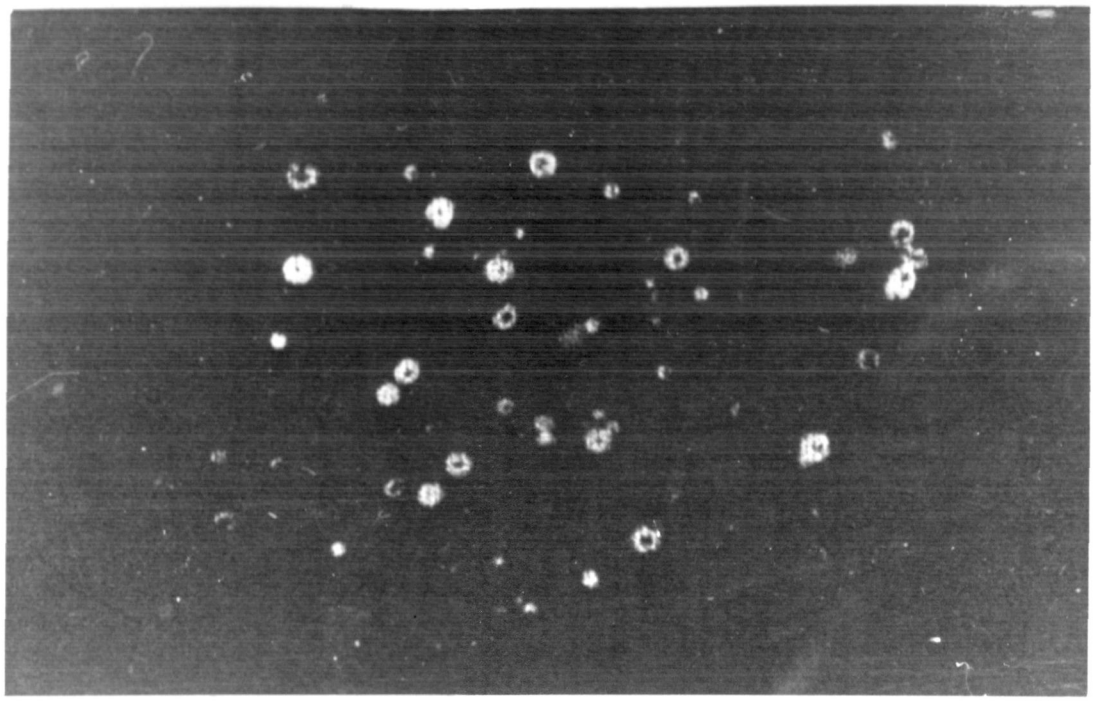
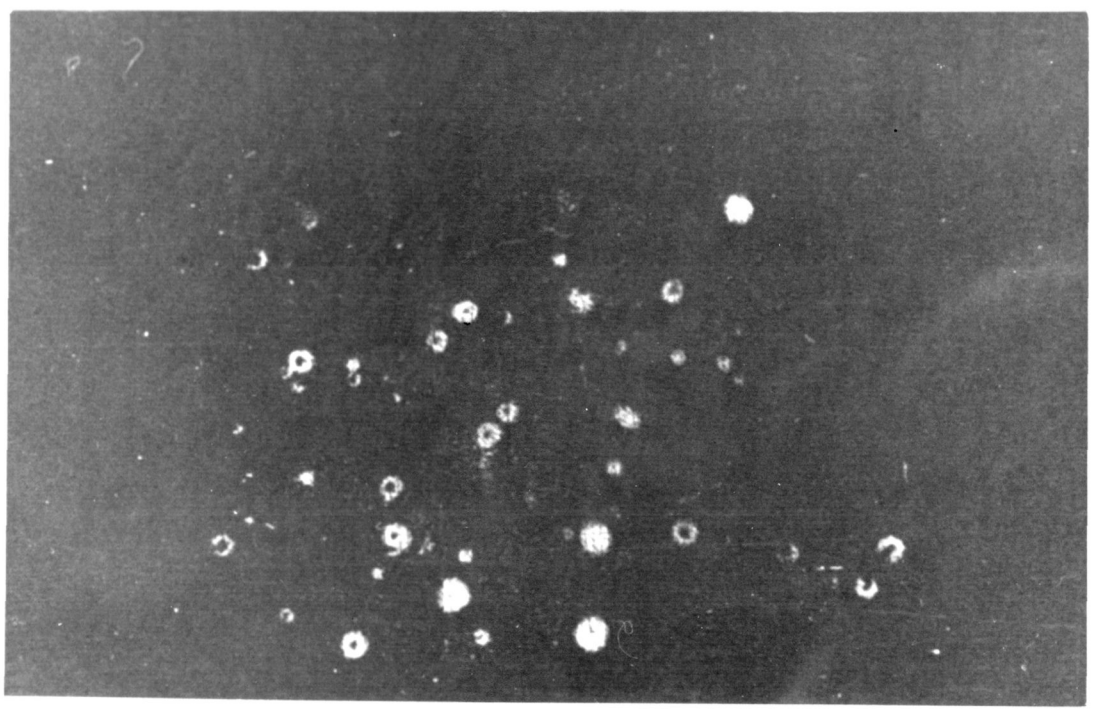


Figure 7.5 The track count in two CA80-15 films, exposed to 2 MeV neutrons and thermal neutrons, as a function of different grey levels. The track count is on plateau at levels 4 and 5



(a)



(b)

Figure 7.6 Digitised tracks displayed on Tektronix 611 screen.
(a) Grey level 4, (b) Grey level 5

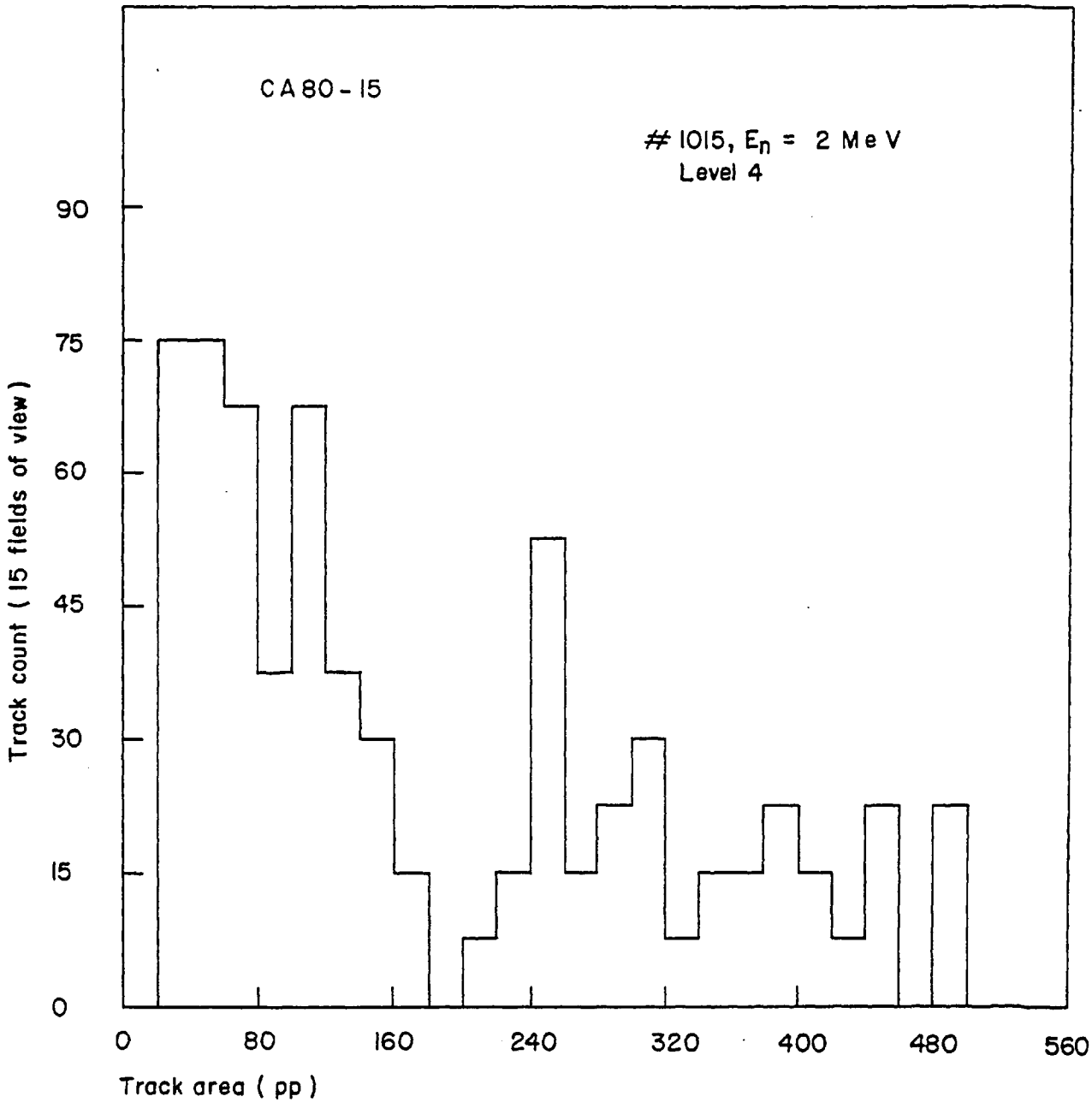


Figure 7.7 Typical frequency histogram of the number of tracks in CA80-15 exposed to 2 MeV neutrons, as a function of track area in picture points (pp)

7.4.3 Overlap Correction

If two tracks overlap the system counts them as one feature. Thus at high track densities, when the probability of overlap is high, it is necessary to make correction. In the present work, the overlapping correction was performed by setting two boundary numbers in the form separator, corresponding to the track area in picture points and separating the track area universe into three regions. Region 1 covered single tracks up to a track area of 250 p.p., region 2 covered double tracks up to an area of 400 p.p., and region 3 covered triple overlapping above an area of 400 p.p. Hence the number of tracks per frame was:

(number of singles) + 2 (number of doubles) + 3 (number of triples)

The region boundaries were determined experimentally by comparisons with eye-counting.

7.5 DATA ANALYSIS AND RESULTS

Experiments were made in order to test the reproducibility of counting on the system and to make comparisons between eye and automatic-counts, in the case of CA80-15 exposed to 2 MeV neutrons. The results for 15 fields of view in microscope (i.e. 15 negatives) are shown in Table 7.1. The quantities of interest in these comparisons are the reproducibility of each method of counting reflected in the ratios of counts of the two methods. The ratios are consistant with a constant value of counting ratio within $\pm$ 4% for track densities used in the present experiments.

TABLE 7.1

COMPARISON OF TRACK COUNTING BY EYE- AND BY THE 'DIGITISER', FOR CA80-15 EXPOSED TO 2 MeV NEUTRONS

Negative No. (1 Field of View)	Eye-Counts (Tracks/Field of View)	Auto.Counts (Tracks/Field of View)	Ratio Auto./Eye
3	39	41	1.05
4	44	45	1.02
5	45	43	0.96
6	43	45	1.04
7	39	43	1.10
8	41	42	1.02
9	46	44	0.96
10	44	46	1.04
11	38	39	1.02
12	41	40	0.98
13	40	44	1.10
14	40	43	1.07
15	41	42	1.02
16	41	43	1.04
17	44	46	1.04

Mean:

Eye-counts/field of view = 41.86

Auto-counts/field of view = 43.56

Track density (tracks/cm^2):

Eye - $= 2.093 \times 10^4$

Auto - $= 2.178 \times 10^4$

Ratio (Auto/Eye) = 1.04

For 15 fields of view, satisfactorily counted by both methods the mean ratio of the automatic-counts to eye-counts is 1.04.

7.5.1 Errors

There are two possible explanations for the difference of the ratio from unity:

(i) Repeated digitisation of a 'field of view' at intervals of 15 minutes, under the same lighting conditions often indicates, a given edge of the image does not remain in exactly the same position on the 580 x 380 grid of picture points covering the TV frame. A small shift of the order of one picture point, at this edge of an image is noticed in the present digitising system. The measurements of track image area in picture point units of several repeated scans of the same image show a change in area of the order of 1%; which can make a certain track image to be counted or rejected.

(ii) The other probable cause of discrepancy between the two methods is a systematic difference in the detection criteria of the human observer and the digitising system.

7.6 CONCLUSIONS

An off-line multi grey level automatic track counting system has been successfully used in the automatic counting of tracks in SSTR, produced by fast neutrons. Software developed for the present work can be expanded to determine the different parameters of nuclear tracks (for neutron

spectrometry), apart from its present capability to count them.

A part from the track overlap problem which can easily be overcome by choosing the right irradiation time and etching conditions, the main disadvantage of the system is the detection of some "unwanted features". It was found, this performance depends strongly on the focus, so that it is sometimes necessary to defocus a given field of view to get the right detection. Since tracks are normally darker than the background, slight de-focusing has no effect on the number of tracks per field of view. In order to get the best results, grey level threshold and in particular, size setting (track area distribution in routine TENTU) should be determined for any given sample. In practice, when dealing with tens of samples (such as reaction rate measurements), this procedure is time consuming. So it is assumed that the determination of track size setting for one or two specimens of a given set can be chosen as a typical setting for the rest of the samples.

The eye-counting speed depends on the number of tracks per field of view. The greater the number of tracks per frame, the larger the counting time. For a film with track density of the order of 3×10^4 tracks/cm^2, it takes about 3 hours to eye-count 30 fields of view for a typical 40 tracks per frame. On the present automatic counting system, minimum analysis time for one TV frame (one field of view with 40 tracks), is currently 6 minutes. Since eye-counting is not possible continuously for about 3 hours, counting by

the digitiser is about 6-8 times faster than eye. Development in three areas could make a substantial improvement:

(i) An improved track recognition algorithm to eliminate irrelevant features at an earlier stage of image processing.

(ii) A finer grid of picture points would allow larger areas of fields of view to be digitised in one frame without losing accuracy and resolution.

(iii) The use of cartridge discs for intermediate data storage has an adverse effect on running time, a computer with sufficient core or semi-conductor memory would solve this problem.

The experimental work involved in the present automatic counting system can be considerably reduced by mounting theTV camera on to the photo-tube of the microscope and counting the tracks direct from the SSTR, rather than from the negative. Stepping motors can be used to drive the SSTR across the field of view of the camera.

The most important advantage of the system is the reproducibility and the elimination of the subjective nature of human decisions on the number of tracks counted in an SSTR.

CHAPTER 8

APPLICATION OF SSTRs IN NUCLEAR FUEL SAFEGUARDS

8.1 INTRODUCTION

As spent fuel from nuclear power stations continues to accumulate, it becomes increasingly important to provide effective means for long-term disposal of this material. To this end, it is essential to assure:

(i) personnel safety during handling and transport;

(ii) long-term integrity of the storage medium,

and (iii) accurate accountability of the actinide content of the fuel.

The accomplishment of these objectives is dependent to a considerable degree upon development of means to characterize the radiation field associated with spent-fuel and to determine the elemental isotopic content of the spent-fuel[104],[42].

Direct radiochemical procedures can be used to determine the concentration of plutonium or other actinides in spent-fuel. However, procedures dealing directly with highly radioactive spent-fuel are complex and expensive. Hence, it is highly advantageous to either eliminate such procedures or reduce them to a bare minimum. A non-destructive method is therefore highly desirable.

Comprehensive measurement of spontaneous neutron generation from spent-fuel is also necessary for more accurate definition, prediction and control of personnel

radiation exposures and for assessment of the potential for damage to candidate geologic storage facility media[104].

Hence, neutron dosimetry measurements with spent-fuel can serve two broad purposes, namely to characterize the composition and the radiation environment. The first purpose includes the need to understand and quantify spent-fuel fissile isotopic compositions for reasons of economics, safeguards, or reactor physics. The second purpose encompasses health and safety requirements created by the spent-fuel radiation environment.

Neutron dosimetry measurements with spent-fuel can either be based upon spontaneously generated neutron emission from plutonium and higher actinide content of the fuel, or on neutron interrogation[105]. In the first method, neutrons emitted from spontaneous fission as well as from (α,n) reactions in irradiated fuel, are measured (a spent-fuel sample containing 200 kg of fuel emits $\sim 10^8$ n/sec[105]). The presence of the spontaneously-generated neutrons is strongly correlated with the higher actinide content. The second method makes use of a neutron interrogation source[105]. The interrogation source has an energy below the fission threshold of ^{238}U and Sb/Be or ^{252}Cf (with a moderator) are commonly used. The detectors measure neutrons from fissions induced in the fuel and must be able to contend with 'background' neutrons from the interrogation source and the fuel.

SSTRs have three important advantages over other neutron detectors in the neutron interrogation of spent-fuel:

(i) The detectors are so small that they can be quite easily mounted without upsetting the fuel storage arrangement and would therefore introduce a small experimental perturbation.

(ii) They are relatively insensitive to gamma radiation which is an important advantage,as a spent-fuel sample containing 200 kg of fuel also contains > 10^6 Ci of gamma activity(105).

(iii) They produce a permanent record of the experimental results.

A scoping experiment to study the feasibility of SSTRs (based upon calibrations reported in Section 4.4.3, Chapter 4) in fuel interrogation was performed at A.E.R.E., Harwell. In this experiment AGR fuel pins with different fuel enrichments were used.

8.2 EXPERIMENTAL ARRANGEMENT

The experimental set-up used in the present experiment is shown in Fig.8.1. AGR fuel pins (∿ 3 ft.long) containing 100 g of UO_2 enriched in ^{235}U at 0.4% (depleted U), 1.475% and 3.5% were arranged in a rectangular array (24 pins or 48 pins). Two ^{252}Cf spontaneous fission neutron sources were used to induce fission in fuel pins. ^{252}Cf neutron spectrum was moderated with polyethylene, so that the system was not particularly sensitive to ^{238}U content of the pins.

CA80-15 SSTRs enclosed in cadmium capsules were positioned to measure fast neutrons from the induced fission in ^{235}U of fuel pins; which depends on the fuel enrichment.

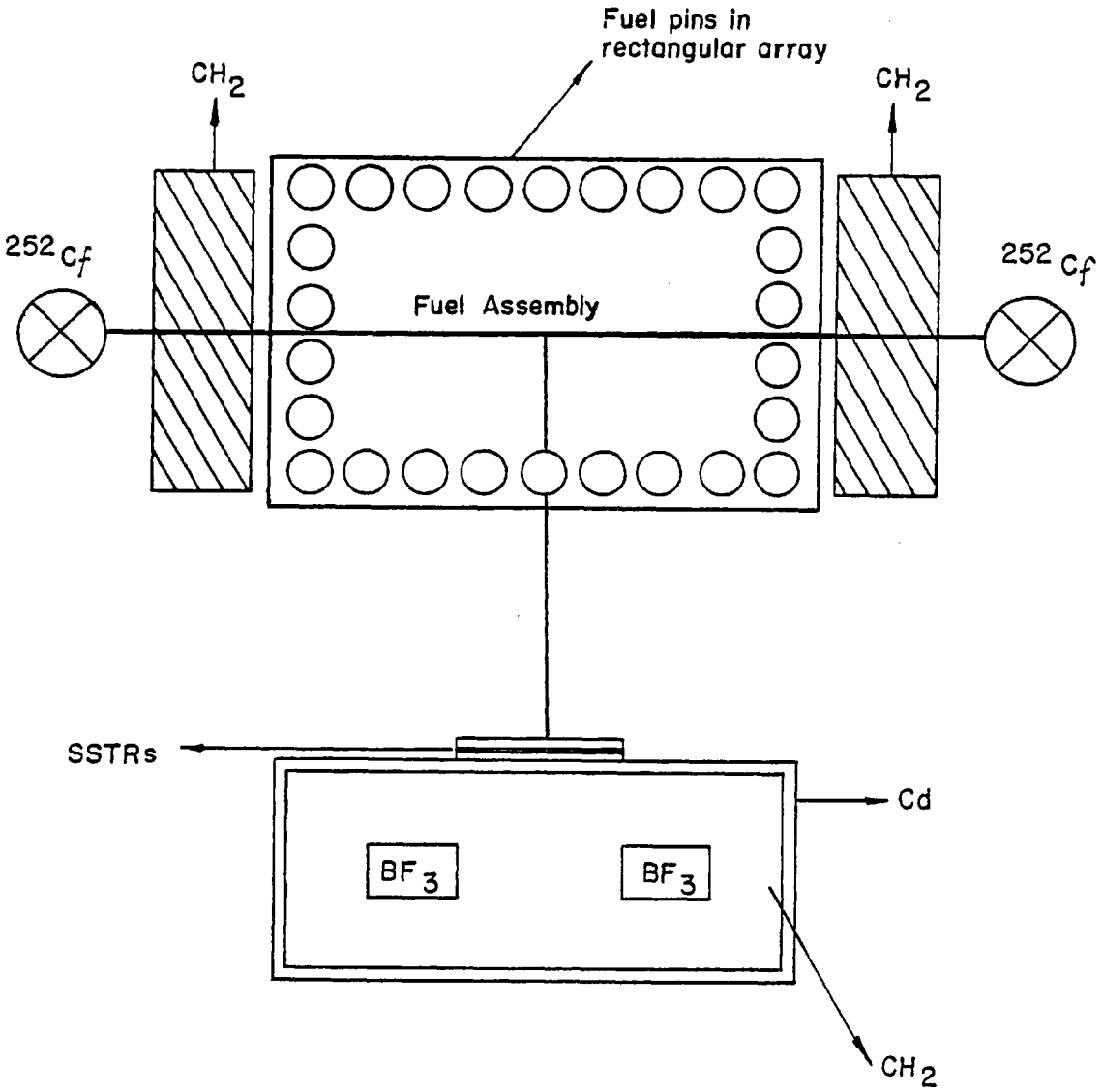


Figure 8.1 Experimental set-up used in the application of SSTRs in the neutron interrogation of reactor fuels at A.E.R.E., Harwell

Cd capsules were essential as CA80-15, because of its nitrogen content is sensitive to thermal neutrons (see Section 4.3.3, Chapter 4).

The tracks detected in SSTR arise from three sources, i.e.

$$T = B + S + I \qquad (8.1)$$

where:

T = total tracks detected in SSTR

B = background

S = scattered neutrons from ^{252}Cf interrogation source, and

I = neutrons from induced fission in fuel pins.

'B' and 'S' should be constant, if the number of pins is kept constant, while 'I' should vary with number of pins and enrichment i.e. the intensity of neutrons from induced fission should be proportional to the amount of fissile material present in the fuel pins.

Each SSTR exposure in the present experiment lasted for 16 hours so as to obtain acceptable track density for track scanning with good statistics.

8.3 RESULTS

The irradiated CA80-15 films were etched in 6N KOH at $60^{o}C$ for 45 minutes (these are the etching conditions for which CA80-15 was calibrated, see Section 4.4.3, Chapter 4). Results obtained are summarized in Table 8.1 and Fig.8.2. Note that the track density is quite acceptable for all the CA80-15 exposures.

TABLE 8.1

TRACK DENSITIES AND NEUTRON FLUXES
(MEASURED WITH A CA80-15 SSTR)
AS A FUNCTION OF NUMBER OF FUEL PINS AND FUEL ENRICHMENTS,
IN THE NEUTRON INTERROGATION OF FUEL EXPERIMENT

Number of Pins	Enrichment (%)	Track Density ($\times 10^4/cm^2$)	Flux ($\times 10^4$) n/(cm^2-sec)
24	0.40	0.51 $\pm$ 0.06	0.738
24	1.457	1.65 $\pm$ 0.12	2.387
24	3.50	3.68 $\pm$ 0.15	5.324
48	0.40	1.07 $\pm$ 0.10	1.548
48	1.457	3.41 $\pm$ 0.13	4.933
48	3.50	7.66 $\pm$ 0.30	11.082

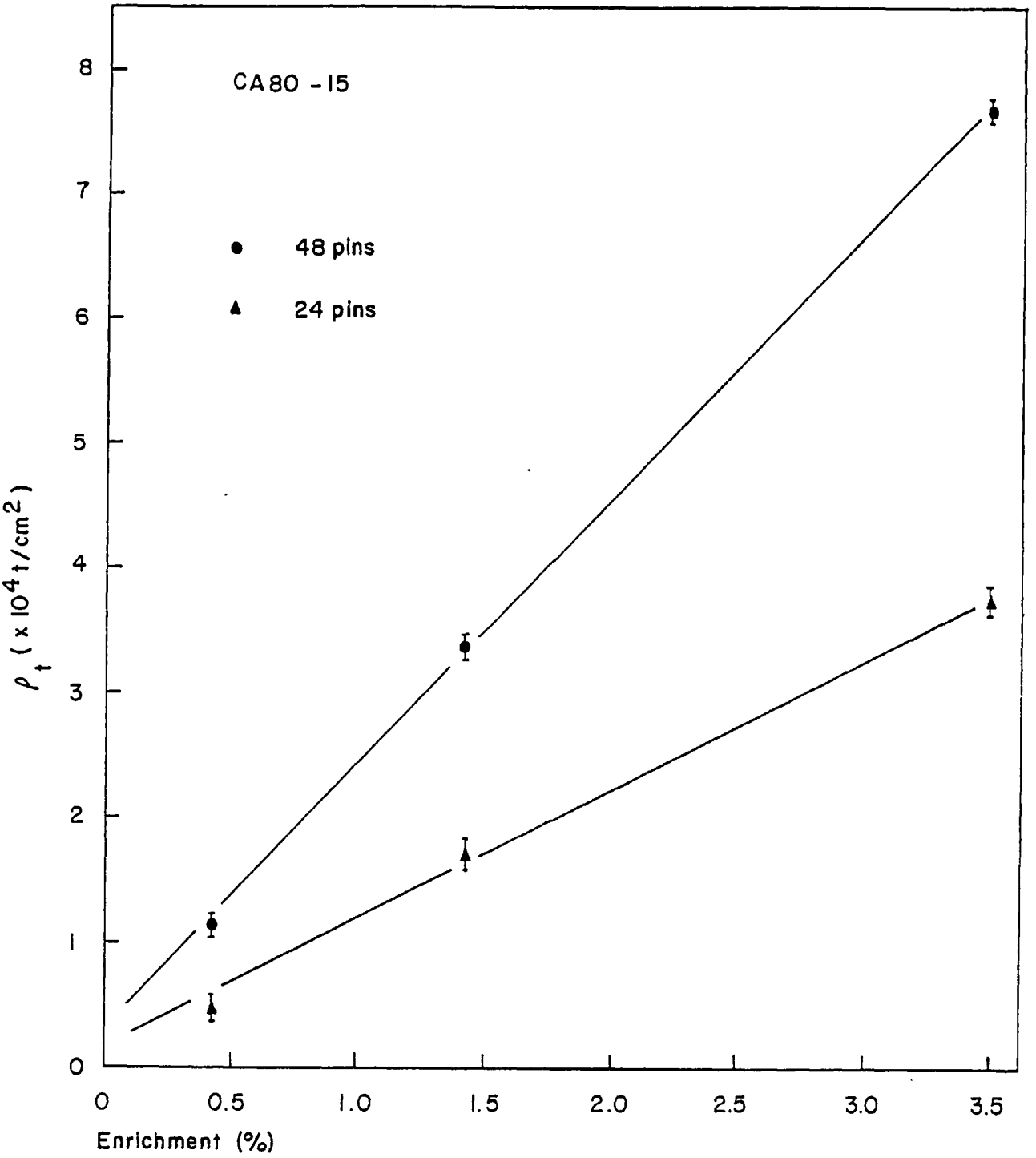


Figure 8.2 Track density, ρ_t in CA80-15 as a function of fuel pin enrichment and the number of pins. CA80-15 was etched in 6N KOH at 60°C for 45 minutes

Neutron fluxes in Table 8.1 were calculated from the track density using the neutron sensitivity calibration of CA80-15 to a fission neutron source (as reported in Section 4.4.3, Chapter 4). Flux perturbation effect due to the finite thickness of cadmium covers has been neglected in this treatment.

It can be seen from Table 8.1 and Fig.8.2 that the number of neutrons detected (within the limits of experimental errors) is proportional to enrichment of fuel in the pins in a particular arrangement (24 or 48 pins).

8.4 CONCLUSIONS

The results from the scoping experiment reported in the earlier sections of this chapter, suggest that, with suitable calibration SSTR neutron dosimetry can be successfully applied for non-destructive, fuel actinide or other fissile material assay and for characterization of the radiation environment associated with reactor fuel assemblies.

The rather large uncertainties in track density and hence in neutron flux given in Table 8.1 reflect the preliminary nature of this scoping experiment. While only 6.6% track scanning statistics were justified in these measurements, future track scanning could be performed to obtain an accuracy of 2-3%, using the automatic track counting system described in Chapter 7. Hence, considerable reduction in neutron flux uncertainties could be realised and used for actinide assay work with good accuracy.

As an off-line method, the SSTR technique has the disadvantage that the detector must be processed. However, there are several advantages over other systems, such as

- simple installation,
- permanent recording for documentation,
- absence of sophisticated instrumentation at the site.

Therefore, the SSTR technique seems to be a promising back-up system for an additional and independent assessment of fuel assemblies. As the SSTR method integrates over the exposure period, the total number of tracks in a given time interval can be evaluated and documented. With respect to the above mentioned advantages this method could be especially attractive to be applied by the national and international agencies to achieve a balanced safeguards system and to reduce field inspection efforts.

CHAPTER 9

SUMMARY OF CONCLUSIONS AND PROPOSALS FOR FUTURE WORK

9.1 SUMMARY OF CONCLUSIONS

In this thesis several conclusions were made concerning the application of Solid State Track Recorders to fast neutron measurements. The significant features are summarized below.

In Chapter 2 a theoretical model was developed to calculate the sensitivity of SSTRs to neutrons as a function of neutron energy. The main conclusions were the following:

(i) The response function for 'intrinsic' SSTRs was found to be due to a large number of different neutron interactions. The presence of hydrogen in the detector is important, since recoil protons make a significant contribution to the total response even at high neutron energy. Since the response of SSTRs is energy dependent, some knowledge of neutron spectrum to be measured would be required.

(ii) The energetical dependence of SSTRs with (n,f) 'converter' foils is determined by the fission cross section.

(iii) For a fission neutron source the sensitivities of CA80-15 without any 'converter' foil and of

Makrofol K.G with a thick ^{238}U-fission foil were calculated to be 1.30×10^{-5} and 0.80×10^{-5} tracks per neutron, respectively.

In Chapter 3 regarding the SSTR materials for neutron detection and the chemical etch development of tracks in SSTRs, the main conclusions were the following:

(i) The track etch rate ratio, V_T/V_B can be substantially increased either, through the reduction of the bulk etch rate or by etching at lower temperatures. Simple theoretical arguments were presented to explain this behaviour.

(ii) CR-39 was found to retain its smooth surface of excellent optical quality after prolonged periods of etching.

In Chapter 4 results from charged particle and neutron irradiations were presented. The more important features follow:

(i) CA80-15 is sensitive to low energy protons and hence to thermal neutrons due to its high nitrogen content (through the $^{14}N(n,p)^{14}C$ reaction).

(ii) For a fission neutron source the sensitivity of CA80-15 is 1.2×10^{-5} tracks per neutron, after 45 minutes of etching in 6N KOH at $60^{o}C$.

(iii) For a fission neutron source the sensitivity of Makrofol K.G in good contact with a 1.23 mg/cm^2

natural uranium foil is 0.60×10^{-5} tracks per neutron, after 45 minutes of etching in 6N KOH at $60^{\circ}C$. The sensitivity follows the fission cross section.

(iv) The response of CR-39 to alpha-particles from 3 to 6 MeV makes it suitable for integral (n,α) reaction rate measurements.

(v) Large energy range for proton registration and low 'background' count in CR-39 suggest its suitability for personnel fast neutron dosimetry using recoil tracks. For a fission neutron source the sensitivity of CR-39 without any particle radiator is 2.60×10^{-5} tracks per neutron, after 10 hours of etching in 6N NaOH at $70^{\circ}C$.

The main conclusions from investigation of possible systematic errors and comparison between experimental and theoretical results (Chapter 5) were as follows:

(i) Fast neutrons can be measured by 'intrinsic' SSTRs with an accuracy of $\pm$ 3.5%; while in the case of SSTRs with an (n,f) 'converter' foil an accuracy of $\pm$ 3.0% can be achieved. These figures do not include statistical uncertainty that arises in track scanning.

(ii) Experimental neutron sensitivities of CA80-15 and Makrofol K.G were found to be in agreement to within $\pm$ 15% of the theoretical results.

Results from the work carried out to study the effects of high gamma doses on SSTRs (Chapter 6) underline the importance of proper etching conditions for fast neutron dosimetry in presence of a high flux of gamma rays.

Automatic track counting technique described in Chapter 7 was found to be absolutely feasible to neutron induced track measurements and should help to overcome the subjective nature of human decisions on the number of tracks seen in an etched SSTR.

The results from the reactor fuel interrogation scoping experiment (Chapter 8), suggest that with suitable calibration SSTR neutron dosimetry can be reliably applied to non-destructive assay of spent fuels. The technique can be based on the automatic track counting system described in Chapter 7, so that a large number of SSTRs can be processed in a similar way to gamma counting of foils. The technique has been developed to a stage of yielding an absolute reaction rate including an investigation of possible systematic errors and sensitivity measurements.

9.2 PROPOSALS FOR FUTURE WORK

In view of an SSTR technique more or less similar to that already described, the following domains are recommended for further study.

9.2.1 Nature of Tracks in SSTRs

From the review of previous work on SSTRs presented in Chapter 1, it is clear that understanding the nature of

tracks in SSTRs has had far less attention in the past than have the applications of SSTRs. This gap provides an opportunity for productive future study.

9.2.2 Non-Destructive Assay of Spent Fuel Assemblies

Adaptation of the SSTR technique to fingerprint spent reactor fuel assemblies stored in water ponds seems absolutely feasible. SSTR may consist of a small aluminium button, 3.5 cm diameter and 1.25 cm depth, containing a 97% enriched and a highly depleted ^{238}U (^{235}U 10 ppm) foil in contact with a Makrofol K.G film. The button can be placed on or adjacent to a spent fuel assembly stored under water. Preliminary results show a correlation of track density to burn-up and further development of this technique is warranted as a possible verification measure, where preferred techniques such as sealing, optical surveillance or non-destructive gamma assay of spent fuel assemblies have for some reason been excluded.

9.2.3 Applications of CR-39

The response of CR-39 to alpha-particles in the energy range from 3 to 6 MeV makes it an excellent candidate for integral (n,α) reaction rate measurements. The present work indicated that the capabilities of CR-39 for proton spectrometry looked very promising. Excellent energy resolution coupled with unexpectedly large energy range for proton registration opens up new realms of SSTR activity, namely passive differential methods for proton spectrometry. In situ, proton recoil fast neutron spectrometry for

reactors and differential techniques for passive fast neutron personnel dosimetry are important examples that are singled out for special emphasis.

9.2.4 Applications of SSTRs in Nuclear Fusion

In recent years important advances have been made in controlled fusion experiments. Energy break-even experiments are now being proposed and designed in laboratories around the world. In order to document the power balance in these types of experiments, new and elaborate diagnostic techniques will have to be developed. In this regard, high sensitivity SSTRs capable of recording hydrogenic ion tracks can be of great interest in diagnosing high density implosions in laser fusion experiments. The two areas of application are, (i) neutron radiography of the Li target which is used as an intense source of high energy neutrons for the systematic study, evaluation and development of fusion reactor materials and (ii) passive spectrometry.

Throughout the neutron energy range that exists in fusion experiments i.e. up to 50 MeV only hydrogen (n,p) scattering cross section is accurately known. Using appropriate neutron collimators, hydrogenous radiators and vacuum scattering chambers, the entire fusion neutron spectrum can be measured with SSTRs placed at suitable (n,p) scattering angles. The proton energy sensitivity of CR-39 which extends up to at least 10 MeV can furnish unique passive neutron spectrometry in fusion experiments on both, an absolute and time-integrated basis.

REFERENCES

1. Becker, K. "Topics in Radiation Dosimetry". Suppl.1, p.79, ed. F.H. Attix, Academic Press, New York (1972).
2. Hassib, G.M., Medveckzky, L. Nuclear Instruments and Methods, 123, (1975), 395.
3. Pretre, S.B. "Neut.Monit.Rad.Prot.Purp.", Vol.III, p.99, I.A.E.A., Vienna, (1973).
4. Rago, P., Goldstein, N., Tochilin, E. Nucl.Applic., 8, (1970), 302.
5. Tymons, B.J., Tuyn, J.W.B., Baarli, J. "Neut.Monit.Rad. Prot.Purp.", Vol.III, p.63, I.A.E.A., Vienna, (1973).
6. Young, D.A. Nature, 182, (1958), 375.
7. Silk, E., Barnes, R. Phil.Mag., 4, (1959), 970.
8. Price, P.B., Walker, R.M. J.Appl.Phys., 33, (1962), 3407.
9. Fleischer, R., Price, P.B. J.Appl.Phys., 34, (1963), 2903.
10. Fleischer, R., Price., P.B. Science, 140, (1963), 1221.
11. Fleischer, R., Price, P.B., Walker, R.M. "Nuclear Tracks in Solids, Principles and Applications". University of California Press, Berkeley, (1975).
12. Fleischer, R., Price, P.B., Walker, R.M., Hubbard, E.L. Phys.Rev., 133, (1964), A1443.
13. Fleischer, R., Price, P.B., Walker, R.M. Phys.Rev., 156, (1967), 353.
14. Rossi, B. "High Energy Particles". Prentice Hall, New York, (1961).
15. Bovey, F.A. "The Effects of Ionizing Radiations on Natural and Synthetic Polymers". Interscience Pubs.Inc., New York, (1958).
16. Barkas, W.H. "Nuclear Research Emulsions". Acadmic Press, New York, (1963).

17. Benton, E.V. "A Study of Charged Particle Tracks in Cellulose Nitrate". NRDL-TR-68-14, (1968).

18. Monnin, M. Report PNCF-68-R19, (1968).

19. Katz, R., Kobetich, E.J. Phys.Rev., 170, (1968), 401.

20. Besant, C.B. Proc.7th Int.Colloq.Corpuscular Photography and Visual Detectors , Barcelona, (1970).

21. Childs, C.B., Slifkin, L. Phys.Rev.Let., 9, (1962), 354.

22. Schopper, E. Proc.8th Inter.Conf.Nuclear Photography and Solid State Detectors, Bucharest, (1972).

23. Boyett, R., Johnson, D., Becker, K. Rad.Res., 42, (1970), 1.

24. Somogyi, G. et al. "Solid State Nuclear Track Detectors". ed. H. Francois et al, Pergamon Press, Oxford, (1980).

25. Dixon, G. University of London Reactor Centre, private communication (1979).

26. Price, P.B. Phys.Rev., 164, (1967), 1618.

27. Tommasino, L., Amellini, C. Rad.Eff., 20, (1973), 253.

28. Tommasino, L. "Solid State Nuclear Track Detectors" ed. H. Francois et al., Pargamon Press, Oxford, (1980).

29. Somogyi, G. Rad.Eff., 34, (1977), 51.

30. Köhler, W. Rad.Eff., 3, (1970), 231.

31. Roberts, J.H. et al. Rad.Eff., 3, (1970), 283.

32. Frank, A.L., Benton, E.V. Proc.7th Int.Colloq.Corpuscular Photography and Visual Detectors, Barcelona, (1970).

33. Khan, H.A. et al. "Solid State Nuclear Track Detectors" ed. H. Francois, et al, Pergamon Press, Oxford, (1980).

34. Tuyn, J.W.B. Nucl.Applic., 3, (1967), 372.

35. Roberts, J.H. et al. Nucl.Applic., 5, (1968), 247.

36. Tuyn, J.W.B. Rad.Eff., 5, (1970), 75.

37. Besant, C.B., Ipson, S.S. J.Nucl.Energy, 24, (1970), 59.

38. Böck, H. "Solid State Nuclear Track Detectors", ed. H. Francois et al, Pergamon Press, Oxford (1980).

39. Iyer, R.H. et al. Nuclear Instruments and Methods, 109, (1973), 453.

40. Benton, E.V., Henke, R., Tobias, C. Science, 182, (1973), 474.

41. Qaqish, A.Y., Besant, C.B., Haque, A.U. Int.J.Nucl.Med. and Biol., 5, (1978), 261.

42. "Measurement of Fast Neutrons from Irradiated Fuel Elements". A.E.R.E., Harwell Contract with Imperial College, London, H4B 3134 EMR (1977).

43. BNL 400, Third Edition. Angular Distributions in Neutron-Induced Reactions, Vol.1, Z=1 to 20, (1970).

44. Evans, R.D. "The Atomic Nucleus". McGraw Hill, (1967).

45. Segre, E. "Experimental Nuclear Physics", Vol.II, John Wiley & Sons.

46. Baldin, A.M. et al. "Kinematics of Nuclear Reactions", Pergamon Press, Oxford, (1961).

47. Frank, A.L., Benton, E.V. Rad.Eff., 3, (1970), 33.

48. Becker, K. Heal.Phys., 12, (1966), 769.

49. Pretre, S. et al. Proc.1st Int.Congr.IRPA, Part I, p.491, Pergamon Press, (1966).

50. Niday, T. Phys.Rev., 121, (1961), 1471.

51. Hyde, E.K. "A Revised Version of a Review of Nuclear Fission", UCRL-9036, (1962).

52. Baumgartner, W.V. et al. Symp. on "Neutron Monitoring", p.433, I.A.E.A. Vienna, (1967).

53. Rago, P.G., Goldstein, N. Heal.Phys., 13, (1967), 654.

54. Heinzelmann, M. Atompraxis, Direct Informat, 14, (1968).

55. Stolz, W., Dörschel, B. Kernenergie, 12, (1969), 244.

56. Spurny, F. et al. Jaderna Energie, 22, (1976), 94.

57. BNL 325, 3rd Edition, "Neutron Cross-Sections", Vol.II, (1976).

58. Lycos, T. Ph.D. Thesis, Imperial College, University of London, (1976).

59. Lycos, T., Besant, C.B. Microscope, 24, (1976), 199.

60. Instructions for the use of CA80-15 films. Ref.JB/NP/V471, Kodak-Pathé, Paris.

61. Instructions for the use of CN-85 films, Kodak-Pathé, Paris.

62. Makrofol Polycarbonate Film, Properties and Applic., Bayer, (U.K.)Ltd.

63. Cartwright, B.G. et al. Nuclear Instruments and Methods, 153, (1978), 457.

64. Billmeyer, F.W. "Text Book of Polymer Science". Second Edition, John Wiley & Sons, (1971).

65. Bolker, H.I. "Natural and Synthetic Polymers". Dekker, New York, (1974).

66. Miles, F.D. "Cellulose Nitrate". Oliver and Boyd, London, (1955).

67. Spurlin, H. "Cellulose and Cellulose Derivatives", Part III, ed. E. Ott et al, Interscience, New York (1955).

68. Alger, R.S. "Physics and Chemistry of the Organic Solid State". ed. D. Fox, Interscience, New York, (1965).

69. Charlesby, A. "Atomic Radiation and Polymers". Pergamon Press, Oxford, (1960).

70. Burton, M. "Effects of Radiation on Materials". ed. J. Harwood et al, Reinhold, New York, (1963).

71. Carrol, J.G., Bolt, R.O. "Radiation Effects on Organic Materials". Academic Press, New York, (1963).

72. Honeyman, J. Advances in Carbohydrate Chemistry, 12 (1957), 130.

73. McBurney, L.F. "Cellulose and Cellulose Derivatives", Part II, ed. E. Ott et al, Interscience, New York, (1954).

74. Varga, B.B. "Nuclear Tracks in Cellulose Nitrate". M.Sc.Thesis, Imperial College, University of London, (1977).

75. Cooper, G.D., Williams, B. J.Organic Chemistry, 27, (1962), 3717.

76. Dial, W.R. Ind.Eng.Chem., 47(12), (1955), 2447.

77. Starkweather, H.W., Eirich, F.R. Ind.Eng.Chem., 47(12) (1955), 2452.

78. Amelinckx, S. "The Direct Observation of Dislocations". p.15, Academic Press, New York, (1964).

79. Fleischer, R.L., Price, P.B., Walker, R.M. Ann.Rev.Nucl. Sci., 15, (1965), 1.

80. Khan, H.A. Nuclear Instruments and Methods, 109, (1973), 515.

81. Maurya, A.L. "Solid State Nuclear Track Detectors". ed. H. Francois et al, Pergamon Press, Oxford, (1980).

82. Khan, H.A., Durrani, S.A. Rad.Eff., 13, (1972), 257.

83. Schrauke, H., Paretzke, H.G. Nuclear Instruments and Methods, 147, (1977), 169.

84. Qaqish, A.Y., Besant, C.B. Nuclear Instruments and Methods, 138, (1976), 493.

85. Qaqish, A.Y. Ph.D.Thesis, Imperial College, University of London, (1977).

86. "Neutron Flux Measurements in the Vertical Thermal Column Calibration Facility". Reactor Operations Note:9, (1974), University of London Reactor Centre, Silwood Park.

87. BNL 325. "Neutron Cross Sections", Vol.1, (1976).

88. Ferguson, A.T.G. Contemporary Physics, 5, (1964), 270.

89. Somogyi, G. et al. Nuclear Instruments and Methods, 134, (1976), 129.

90. Besant, C.B., Ipson, S.S. Rep.No.AEEW-M.881, Atomic Energy Establishment, Winfrith.

91. Varnagy, M., Csikai, J., Szegedi, S. Nuclear Instruments and Methods, 119, (1974), 261.

92. Price, P.B., Fleischer, R.L. Ann.Rev.Nucl.Sci., 21, (1971), 295.

93. Besant, C.B. et al. Rad.Eff., 34, (1977), 67.

94. Block, J. et al. Rev.Sci.Instruments, 40, (1969), 509.

95. Schultz, W.W. Nucl.Sci.Abs., 22, (1968), 37990.

96. Becker, K. et al. Nuclear Instruments and Methods, 124, (1975), 557.

97. Cohn, C.E. Rev.Sci.Instruments, 43, (1972), 12.

98. Jowit, D. Nuclear Instruments and Methods, 92, (1971), 37.

99. Gunther, G. Leitz.Sci. & Tech.Inf., Suppl.1,2, Wetzlar, (1972).

100. Muller, W. Leitz Sci. & Tech.Infor., Suppl.1,4, Wetzlar, (1974).

101. Azimi-Garakani, D., Williams, J.G. Nuclear Instruments and Methods, 147, (1977), 69.

102. Ow, C.S. Report TP/C/7904, Dept.Mech.Eng., Imperial College, London, (1979).

103. Rosenfeld, A. "Picture Processing by Computer". Academic Press, New York, (1960).

104. Gold, R., Ruddy, F.H., Roberts, J.H. "Solid State Nuclear Track Detectors". ed. H. Francois et al, Pergamon Press, Oxford, (1980).

105. Hooton, B.W. Proc. "European Nuclear Conference", Hamburg. Trans.Am.Nucl.Soc., Vol.31, p.510, (1979).

106. Jarmie, N., Seagrave, J.D. "Charged Particle Cross Sections". Report LA-2014, Los Alamos Scientific Lab., (1957).

107. Janni, J.F. Report AFWL-TR-65-150, Air Force Weapons Lab., Albuquerque, New Mexico, (1966).

108. Yuan, L.C., Wu, C.S. "Methods of Experimental Physics", 5, Pt.A,1, Academic Press, New York, (1955).

109. Barkas, W.H., Berger, M.J. National Research Council Publication, 1133, (1964), U.S. National Academy of Sciences.

110. Whaling, W. "Encyclopedia of Physics". ed. S. Flugge, 34, p.193, Springer-Verlag, Berlin, (1958).

111. Henke, R.P., Benton, E.V. Phys.Rev., 139, (1965), A2017.

112. Heckman, H.H. et al. Phys.Rev., 117, (1960), 544.

APPENDIX A

KINEMATICS OF NUCLEAR REACTIONS AND SCATTERING

Some of the important non-relativistic and relativistic equations used to calculate the energies of the reaction products are given in the following pages. The material is adopted from the Los Alamos report edited by Jarmie and Seagrave[106]. More complete accounts of nuclear reaction kinematics are available[46].

A1 NUCLEAR REACTIONS

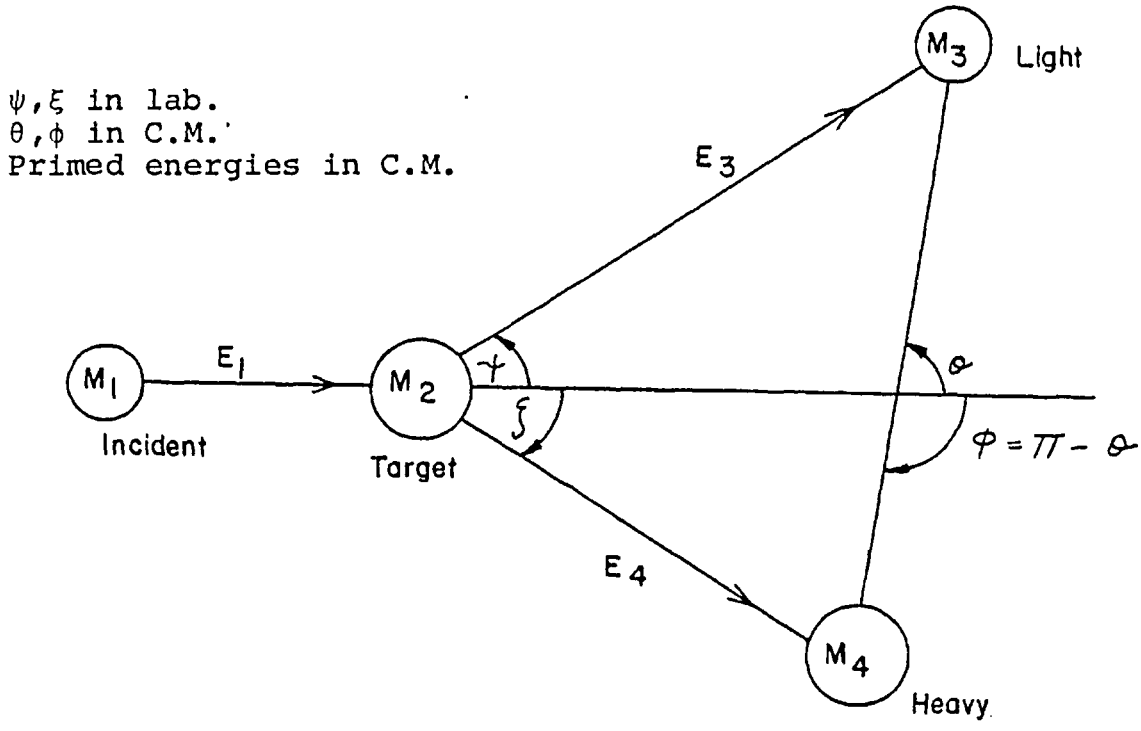
The kinematics of nuclear reactions are illustrated in Fig.A.1. The non-relativistic expressions for the energetics and solid-angle relations for nuclear reactions are listed in Table A.1. Some of the important non-relativistic and relativistic equations are given below. (The notation is explained in Fig.A.1.)

A1.1 Non-relativistic Kinematics

$$\sqrt{E}_3 = \frac{\sqrt{M_1 M_3 E_1}}{M_3 + M_4} \cos\psi \left[1 \pm \left\{ 1 + \frac{1 + M_4/M_3}{\cos^2\psi} \left[\frac{M_4}{M_1} \left(1 + \frac{Q}{E_1} \right) - 1 \right] \right\}^{\frac{1}{2}} \right] \tag{A.1}$$

$$E_3 = \frac{M_1 M_3 E_1}{(M_3 + M_4)^2} \left\{ 2\cos^2\psi + \frac{M_4 (M_3 + M_4)}{M_1 M_3} \left(\frac{Q}{E_1} - \frac{M_1}{M_4} + 1 \right) \right.$$

$$\left. \pm 2\cos\psi \left[\cos^2\psi + \frac{M_4 (M_3 + M_4)}{M_1 M_3} \left(\frac{Q}{E_1} - \frac{M_1}{M_4} + 1 \right) \right]^{\frac{1}{2}} \right\} \tag{A.2}$$



$$Q(\text{MeV}) = 931.16(M_1 + M_2 - M_3 - M_4) \quad \text{(a.m.u.)}$$

$$E_T = E_1 + Q = E_3 + E_4$$

$$E_3 = B\left[\cos\psi + (D/B - \sin^2\psi)^{\frac{1}{2}}\right]^2 E_T$$

$$E_4 = A\left[\cos\xi + (C/A - \sin^2\xi)^{\frac{1}{2}}\right]^2 E_T$$

where

$$\sin\xi = (M_3E_3/M_4E_4)^{\frac{1}{2}} \sin\psi$$

$$A = \frac{M_1M_4(E_1/E_T)}{(M_1+M_2)(M_3+M_4)} \quad ; \quad B = \frac{M_1M_3(E_1/E_T)}{(M_1+M_2)(M_3+M_4)}$$

$$C = \frac{M_2M_3}{(M_1+M_2)(M_3+M_4)}\left(1 + \frac{M_1Q}{M_2E_T}\right) = \frac{E_4'}{E_T}$$

$$D = \frac{M_2M_4}{(M_1+M_2)(M_3+M_4)}\left(1 + \frac{M_1Q}{M_2E_T}\right) = \frac{E_3'}{E_T}$$

Figure A.1 Kinematics of nuclear reactions

TABLE A.1

NON-RELATIVISTIC EXPRESSIONS FOR THE ENERGETICS AND SOLID-ANGLE RELATIONS FOR NUCLEAR REACTIONS

Lab energy of light product	$\frac{E_3}{E_T} = B + D + 2(AC)^{\frac{1}{2}}\cos\theta = B\left[\cos\psi + (D/B - \sin^2\psi)^{\frac{1}{2}}\right]^2$
Lab energy of heavy product	$\frac{E_4}{E_T} = A + C + 2(AC)^{\frac{1}{2}}\cos\phi = A\left[\cos\xi + (C/A - \sin^2\xi)^{\frac{1}{2}}\right]^2$
Lab angle of heavy product	$\sin\xi = \left(\frac{M_3E_3}{M_4E_4}\right)^{\frac{1}{2}} \sin\psi$
C.M. angle of light product	$\sin\theta = \left(\frac{E_3/E_T}{D}\right) \sin\psi$
Intensity or solid angle ratio for light product	$\frac{\sigma(\theta)}{\sigma(\psi)} = \frac{I(\theta)}{I(\psi)} = \frac{\sin\psi}{\sin\theta}\frac{d\psi}{d\theta} = \frac{\sin^2\psi}{\sin^2\theta}\cos(\theta-\psi) = \frac{(AC)^{\frac{1}{2}}(D/B - \sin^2\psi)^{\frac{1}{2}}}{E_3/E_T}$
Intensity or solid angle ratio for heavy product	$\frac{\sigma(\theta)}{\sigma(\xi)} = \frac{I(\theta)}{I(\xi)} = \frac{\sin\xi}{\sin\phi}\frac{d\xi}{d\phi} = \frac{\sin^2\xi}{\sin^2\phi}\cos(\phi-\xi) = (AC)^{\frac{1}{2}}\frac{(C/A - \sin^2\xi)^{\frac{1}{2}}}{E_4/E_T}$
Intensity or solid angle ratio for associated particles in the lab system	$\frac{\sigma(\xi)}{\sigma(\psi)} = \frac{I(\xi)}{I(\psi)} = \frac{\sin\psi}{\sin\xi}\frac{d\psi}{d\xi} = \frac{\sin^2\psi}{\sin^2\xi}\frac{\cos(\theta-\psi)}{\cos(\phi-\xi)}$

$$Q = \frac{M_3 + M_4}{M_4} E_3 - \frac{M_4 - M_1}{M_4} E_1 - \frac{2\sqrt{M_1 M_3 E_1 E_3}}{M_4} \cos\psi \qquad (A.3)$$

If a particle x with mass M_1 produces a(x,n) reaction on a stationary target nucleus of atomic mass M_2, the non-relativistic expression connecting the threshold energy E_{th} and the Q-value Q_o is

$$|Q_o| = \frac{M_2}{M_1 + M_2} E_{th} \qquad (A.4)$$

where

$$Q_o < 0$$

A1.2 Relativistic Kinematics

The particles are labelled 1,2,3,4 as in the Fig.A.1. Now defining

M = rest mass in MeV (i.e. C = 1)

T = kinetic energy

$E = T + M$ = total energy

P = relativistic momentum $= \sqrt{E^2 - M^2} = \sqrt{T^2 + 2MT}$

$E_T = T_1 + M_1 + M_2$

$A = 2M_2T_1 + 2M_1M_3 + 2M_2M_3 + 2Q(M_1 + M_2 - M_3) - Q^2$

$B = E_T^2 - P_1^2 \cos^2\psi$

$\frac{\partial B}{\partial \psi} = 2 P_1^2 \sin\psi \cos\psi$

$$T_3 = E_3 - M_3 = \frac{1}{2B}\left[E_T A \pm P_1 \cos\psi \sqrt{A^2 - 4M_3^2 B} \right] - M_3$$

(A.5)

$$T_4 = E_4 - M_4 = E_T - E_3 - (M_1 + M_2 - M_3 - Q) \qquad (A.6)$$

$$Q = M_1 + M_2 - M_3 - \left[M_1^2 + M_2^2 + M_3^2 + 2M_2E_1 - 2E_3(E_1 + M_2) + 2P_1P_3 \cos\psi \right]^{\frac{1}{2}} \quad (A.7)$$

$$\xi = \sin^{-1} \left(\frac{P_3}{P_4} \sin \psi\right) \quad (A.8)$$

$$\frac{\partial T_3}{\partial \psi} = - \frac{E_3}{B} \frac{\partial B}{\partial \psi} \pm \frac{P_1}{2B} \frac{A^2 + 4M_3^2 (E_T^2 - 2B)}{\sqrt{A^2 - 4M_3^2 B}} \quad (A.9)$$

The relativistic expression for the threshold energy in terms of Q is

$$E_{th} = |Q| \left(\frac{M_1 + M_2}{M_2} + \frac{|Q|}{2M_2}\right) \quad (A.10)$$

so that in terms of Q_o, the non-relativistic value (see Equation (A.4)), the true Q-value is

$$|Q| \simeq |Q_o| - \frac{|Q_o|^2}{2(M_1 + M_2)} \quad (A.11)$$

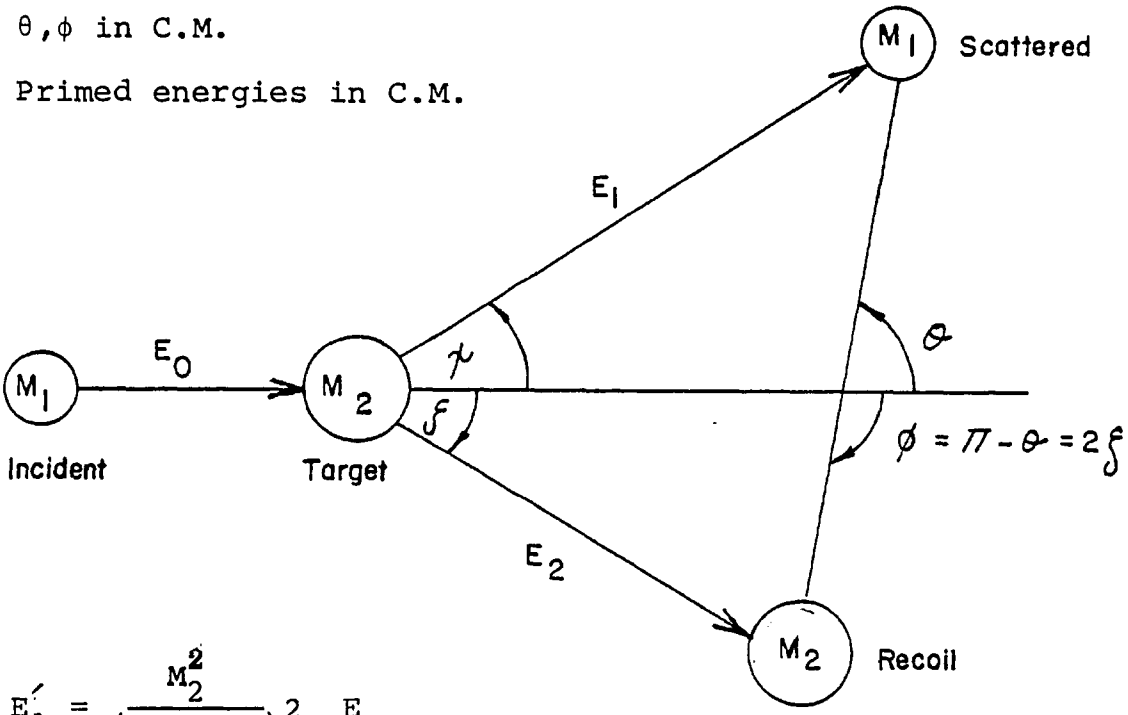
A.2 ELASTIC SCATTERING

The kinematics of elastic scattering are illustrated in Fig,A.2. The non-relativistic expressions for the energetics and solid-angle relations for elastic scattering, which are independent of energy are listed in Table A.2.

ψ, ξ in lab.

θ, ϕ in C.M.

Primed energies in C.M.



$$E_1' = \frac{M_2^2}{(M_1 + M_2)^2} E_o$$

$$E_2' = \frac{M_1 M_2}{(M_1 + M_2)^2} E_o$$

Figure A.2 Kinematics of elastic scattering

TABLE A.2

NON-RELATIVISTIC EXPRESSIONS FOR THE ENERGETICS AND SOLID-ANGLE RELATIONS FOR ELASTIC SCATTERING

Lab energy of the scattered particle	$\frac{E_1}{E_o} = 1 - \frac{2M_1M_2}{(M_1+M_2)^2}(1-\cos\theta)$ $= \frac{M_1^2}{(M_1+M_2)^2}\{\cos\psi + [(M_2/M_1)^2 - \sin^2\psi]^{\frac{1}{2}}\}^2$
Lab energy of the recoil nucleus	$\frac{E_2}{E_o} = 1 - E_1/E_o = \frac{4M_1M_2}{(M_1+M_2)^2}\cos^2\xi$ $\xi \leq \frac{1}{2}\pi$
Lab angle of the recoil nucleus	$\sin\xi = \left(\frac{M_1E_1}{M_2E_2}\right)^{\frac{1}{2}}\sin\psi$, $\xi = \frac{1}{2}(\pi-\phi)$ $\tan\psi = \frac{\sin 2\xi}{M_1/M_2 - \cos^2\xi}$
C.M. angle of scattered particle	$\theta = \psi + \sin^{-1}\left(\frac{M_1}{M_2}\sin\psi\right) = \pi - 2\xi$ $\cos\theta = 1-2\cos^2\xi$
Intensity or solid angle ratio for scattered particle	$\frac{\sigma(\theta)}{\sigma(\psi)} = \frac{I(\theta)}{I(\psi)} = \frac{\sin\psi}{\sin\theta}\frac{d\psi}{d\theta} = \frac{\sin^2\psi}{\sin^2\theta}\cos(\theta-\psi)$ $= \frac{M_1M_2\left[(M_2/M_1)^2 - \sin^2\psi\right]^{\frac{1}{2}}}{(M_1+M_2)^2(E_1/E_o)}$
Intensity or solid angle ratio for recoil nucleus	$\frac{\sigma(\phi)}{\sigma(\xi)} = \frac{I(\phi)}{I(\xi)} = \frac{\sin\xi}{\sin\phi}\frac{d\xi}{d\phi} = \frac{1}{4\cos\xi}$

APPENDIX B

RANGE-ENERGY AND ENERGY LOSS RELATIONS

B.1 INTRODUCTION

The knowledge of accurate range-energy and energy loss relations for charged particles is an essential requirement in the development and use of any charged particle detector. In the following pages, a general method for the calculation of range-energy and energy loss relations is described. The numerical values in the case of a cellulose nitrate SSTR are given in Table B.2 and in the form of graphs in Chapter 2. The accuracy of the relations is discussed.

In these calculations the energy loss experienced by a charged particle traversing matter is assumed to result strictly from the interactions with electrons of the stopping medium; inelastic collisions are neglected. This is a good approximation for energies below 500 MeV/nucleon; for energies above this value the probability for nuclear interaction becomes significant and the full range, given by this calculation, may not be achieved[107]. The distinction between the path length and range is also not made. Strictly speaking, this calculation gives the total path length of a charged particle, rather than its range; however for heavy ions this difference is small. Also, the density effect correction, δ is neglected as it becomes important only at velocities of about $\beta(=\frac{v}{c}) \simeq 0.87$ ($\sim$ 1.0 GeV/nucleon)[107,108].

B.2 METHOD OF CALCULATION

B.2.1 General Expressions

In order to achieve a broad coverage of the spectrum of particles, energies and stopping materials, the methods of Barkas and Berger have been employed in these calculations[109]. Their empirical representations of range-energy data have been modified and extended to lower energies.

The range of a charged particle in matter can be expressed by the general formula

$$R(\beta) = \frac{M}{Z^2}\left[\lambda(\beta) + B_Z(\beta)\right] \qquad (B.1)$$

where

M = mass of the particle in units of the proton

Z = charge of the particle in units of the proton

$\lambda(\beta)$ = range of an 'ideal' proton with velocity βC,

$B_Z(\beta)$ = the range extension in the same material

The units of $\lambda(\beta)$ and $B_Z(\beta)$ are moles of electrons per cm^2, and the units of $R(\beta)$ are g/cm^2.

An 'ideal' proton is a particle of protonic mass and charge which does not capture electrons or interact strongly with nuclei. The range extension, $B_Z(\beta)$ is the extension of the range caused by the neutralisation of the moving ion's charge by charge pick-up near the stopping end of the trajectory. The subscript, Z in $B_Z(\beta)$ indicates that the range extension is dependent upon the atomic number of the moving ion.

Equation (B.1) permits the calculation of ranges in g/cm^2 as a function of five parameters: A/Z, I_{adj}, Z, M and E[109]. The ratio A/Z is the atomic mass per electron of the stopping material in amu/electron; I_{adj} is the mean value of the ionisation potential in electron volts for the stopping material adjusted by assuming that the shell correction for relativistic particles is zero[109], Z, M and E are the atomic number, mass and energy of the incident ion, respectively.

The rate of energy loss, (dE/dx), is defined as

$$(dE/dx) = + (dE/dR)$$

and is obtained by differentiating the equation (B.1)

$$\frac{dR}{dE} = \frac{M}{Z^2}\left[\lambda'(\beta) + B_Z'(\beta)\right]\frac{d\beta}{dE} \qquad (B.2)$$

where R is the residual range of the particle. It is convenient to express λ as a function of the proton kinetic energy τ, then $\lambda(\beta) \rightarrow \lambda(\tau)$, and

$$\frac{dR}{dE} = \frac{M}{Z^2}\left[\lambda'(\tau)\frac{d\tau}{dE} + B_Z'(\beta)\ \frac{d\beta}{dE}\right] \qquad (B.3)$$

The quantity τ is the energy of a proton with the same β as that of the particle, so that

$$E = \tau\ M \qquad (B.4)$$

and

$$\frac{d\tau}{dE} = \frac{1}{M} \qquad (B.5)$$

Since the kinetic energy of the particle is given by

$$E = \left[\frac{Mm_pC^2}{(1-\beta^2)^{\frac{1}{2}}} - Mm_pC^2\right] \qquad (B.6)$$

then

$$\frac{dE}{d\beta} = \frac{Mm_pc^2}{(1 - \beta^2)^{3/2}} = \frac{1}{d\beta/dE} \qquad (B.7)$$

where 'm_p' is the rest mass of the proton.

Using Equations (B.3), (B.5) and (B.7)

$$\frac{dE}{dx} = \frac{1}{dR/dE} = \frac{Z^2}{\left[\lambda'(\tau) + \frac{B_Z'(\beta)(1 - \beta^2)^{3/2}}{Mm_pc^2\beta} \right]} \qquad (B.8)$$

The velocity β is given by the following relativistic expression,

$$\beta = \left[\frac{E}{Mm_pc^2} \left(2 + \frac{E}{Mm_pc^2}\right) \right]^{\frac{1}{2}} \Bigg/ \left[1 + \frac{E}{Mm_pc^2} \right] \qquad (B.9)$$

where

$$M = A/1.008 \text{ and } Mm_pc^2 = 931.141\ A(MeV)$$

The quantity A is atomic weight of the ion, and E is the kinetic energy of the ion.

Equations (B.1) and (B.8) express the range, and the rate of energy loss, (dE/dx) of a charged particle as a function of $\lambda(\tau)$, $\lambda'(\tau)$, $B_Z(\beta)$, $B_Z'(\beta)$ and β.

B.2.2 The Adjusted Mean Ionisation Potential, I_{adj}

Assuming Bragg's rule of the additivity of the stopping power effects of the various components, the value of I_{adj} for a given stopping material is computed from the I_{adj}'s of the individual constituents. For the ith constituent[109],

$$(I_{adj})_i = 12\ Z_i + 7 \text{ eV} \qquad Z \leqslant 13$$
$$(I_{adj})_i = 9.76\ Z_i + \frac{58.8}{Z_i^{0.19}} \text{ eV for } Z \geqslant 13 \qquad (B.10)$$

These empirical expressions of the experimental results are only approximate for values of $Z \lesssim 13$.

From the individual $(I_{adj})_i$ the I_{adj} for a compound is given by[109]

$$\ell n\ I_{adj} = < A/Z > \sum_i \frac{f_i Z_i}{A_i} \ell n(I_{adj}) \qquad (B.11)$$

where

f_i = fraction by weight of the ith component of the stopping material

A_i = atomic weight of the ith component,

and Z_i = atomic number of the ith component.

For a molecular material,

$$f_i = \frac{\mu_i A_i}{\sum \mu_j A_j} \qquad (B.12)$$

where μ_j is the formula number of the ith component. It is assumed that

$$<A/Z> = \frac{1}{<Z/A>} \qquad (B.13)$$

where the quantity

$$<Z/A> = \sum f_i \frac{Z_i}{A_i} \qquad (B.14)$$

B2.3 The Ideal Proton Range and its Derivative

The ideal proton range, $\lambda(\beta)$, and the actual proton range, $\lambda(\beta) + B_1$, are in practice hardly distinguishable[109]. Using the available range-energy data for protons, Barkas and Berger summarise the entire body of range data by a formula of the type

$$\ell n\ \lambda = \ell n\ <A/Z> + \sum_{n=0}^{N} \sum_{m=0}^{M} a_{mn} \ (\ell n I_{adj})_1^m (\ell n \tau)_1^n \qquad (B.15)$$

where a_{mn} are the coefficients used to fit λ. In this fashion, λ is a smooth function of I_{adj}. The quantity <A/Z> is the total number of nucleons per electron in the stopping material and can be calculated from Equation (B.14).

The quantity $\lambda'(\tau)$ is obtained by differentiation of Equation (B.15)

$$\lambda'(\tau) = \frac{\lambda}{10\tau} \sum_{n=0}^{N} \sum_{m=0}^{M} n a_{mn} (\ell n I_{adj})_1^m (\ell n \tau)_1^{n-1} \qquad (B.16)$$

where

$$(\ell n I_{adj})_1 = \frac{\ell n I_{adj}}{10}$$

and

$$(\ell n \tau)_1 = \ell n \frac{\tau}{10}$$

Three different sets of coefficients, a_{mn} are to be used to fit λ in three different energy regions.

Low energy region: up to about 1.0 MeV/nucleon

Medium energy region: 1-9 MeV/nucleon

High energy region: 7-1200 MeV/nucleon

For the low energy region, a least square fit of the form in Equation (B.15) was made to all of the low energy experimental range-energy data given by Whaling[110] up to 0.95 MeV/nucleon. The ideal proton's range was calculated by subtracting the range extension from the real range. The coefficients of Equations (B.15) and (B.16) for the low energy region are listed in Table B.1.

B2.4 The Range Extension and its Derivative

The range extension, $B_z(\beta)$, was calculated using the range extension for emulsion[109], $C_z \frac{(137\beta)}{z}$, scaled to an

TABLE B.1

COEFFICIENTS FOR $\lambda(\tau)$ IN THE LOW ENERGY REGION

N = 3 M = 3

m	n = 0	1	2	3
0	- 8.725	18.797	74.192	752.005
1	8.309	11.139	- 528.805	- 5558.937
2	- 13.396	- 64.808	1264.232	12843.119
3	12.625	54.043	- 934.142	- 9306.336

arbitrary material. The scaling is such that $B_z(\beta)$ has the same asymptotic value given by Barkas and Berger[109],

$$(7.0 + 0.85\ I_{adj}^{5/8}) < A/Z > 10^{-6}\ z^{8/3} \qquad (B.17)$$

Thus, the range extension, $B_z(\beta)$, is given by

$$B_z(\beta) = (31.8 + 3.86\ I_{adj}^{5/8}) < A/Z > 10^{-6}\ z^{8/3} C_z\ \frac{(137\beta)}{z} \qquad (B.18)$$

where $C_z(137\beta/z) \rightarrow C_z(\chi)$ is given in the regions

$$\begin{aligned} C_z(\chi) &= -0.00006 + 0.05252\chi + 0.12857\chi^2 && \chi \leq 0.2 \\ C_z(\chi) &= -0.00185 + 0.07355\chi + 0.07172\chi^2 - 0.02723\chi^3 && 0.2 \leq \chi \leq 2 \\ C_z(\chi) &= -0.0793 + 0.3323\chi - 0.1234\chi^2 + 0.015\chi^3 && 2 \leq \chi \leq 3 \\ C_z(\chi) &= 0.220 && \chi \leq 3 \end{aligned} \qquad (B.19)$$

For $\chi \leq 0.2$, $C_z(\chi)$ is obtained from the measurements of Henke et al[111] (see Fig.B.1(a)). For $\chi > 0.2$, the data given by Heckman et al is used[112] (see Fig.B.1(b)).

The derivative of the range extension, $B_z'(\beta)$ is obtained by taking the derivative of Equation (B.18) with respect to β,

$$B_z'(\beta) = (4.357 + 0.5288\ I_{adj}^{5/8}) < A/Z > z^{5/3} 10^{-3} C_z' \frac{(137\beta)}{z} \qquad (B.20)$$

with corresponding $C_z'(\beta)$

$$\begin{aligned} C_z'(\chi) &= 0.05252 + 0.25714\,\chi && \chi \leq 0.2 \\ C_z'(\chi) &= 0.07355 + 0.14344\,\chi - 0.08169\chi^2 && 0.2 \leq \chi \leq 2 \\ C_z'(\chi) &= 0.3323 - 0.2468\chi + 0.0459\chi^2 && 2 \leq \chi \leq 3 \\ C_z'(\chi) &= 0 && \chi \geq 3 \end{aligned} \qquad (B.21)$$

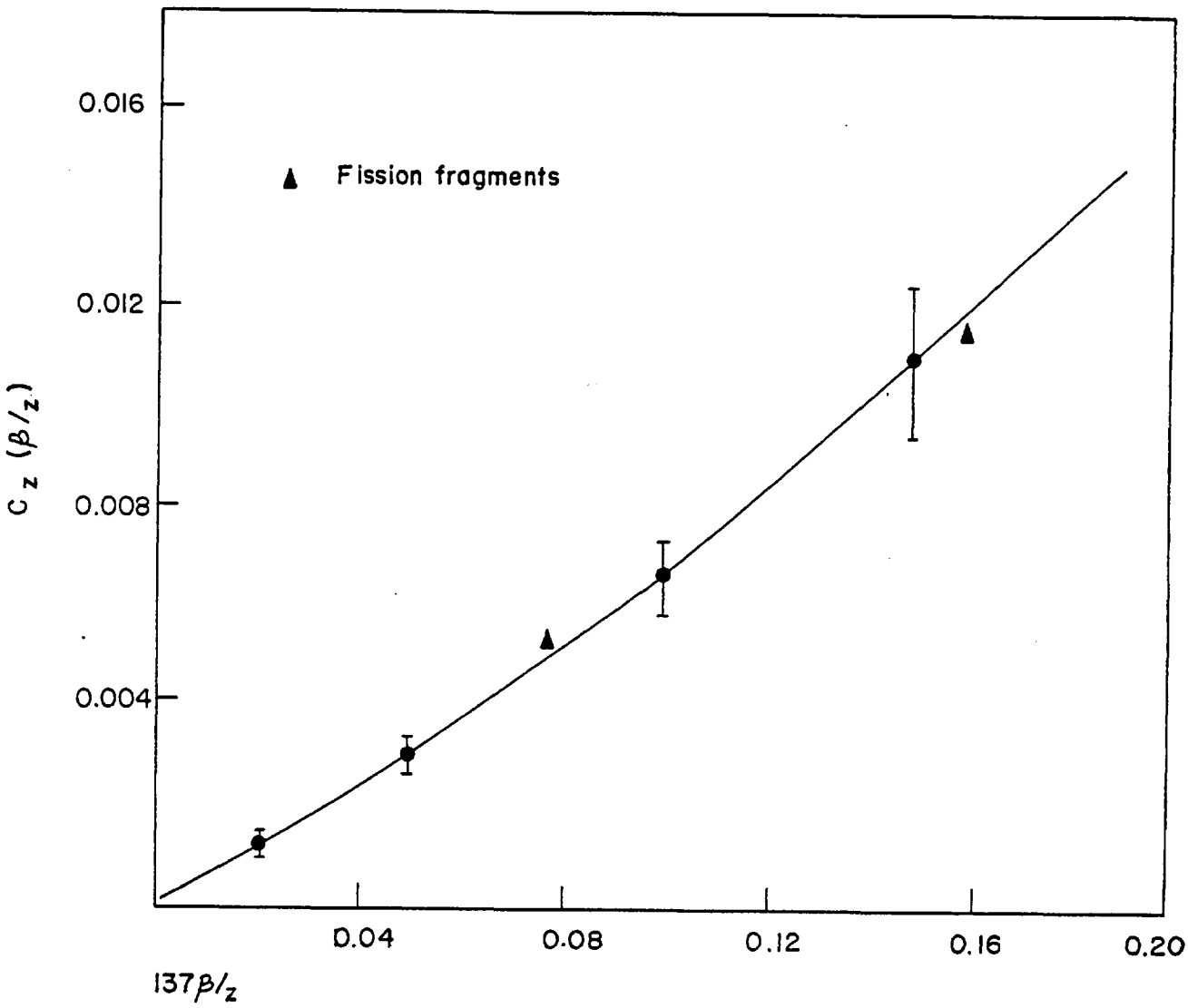


Figure B.1(a) Empirically derived curve relating the range-extension term to the velocity of the ion in units of the K-electron velocity (111)

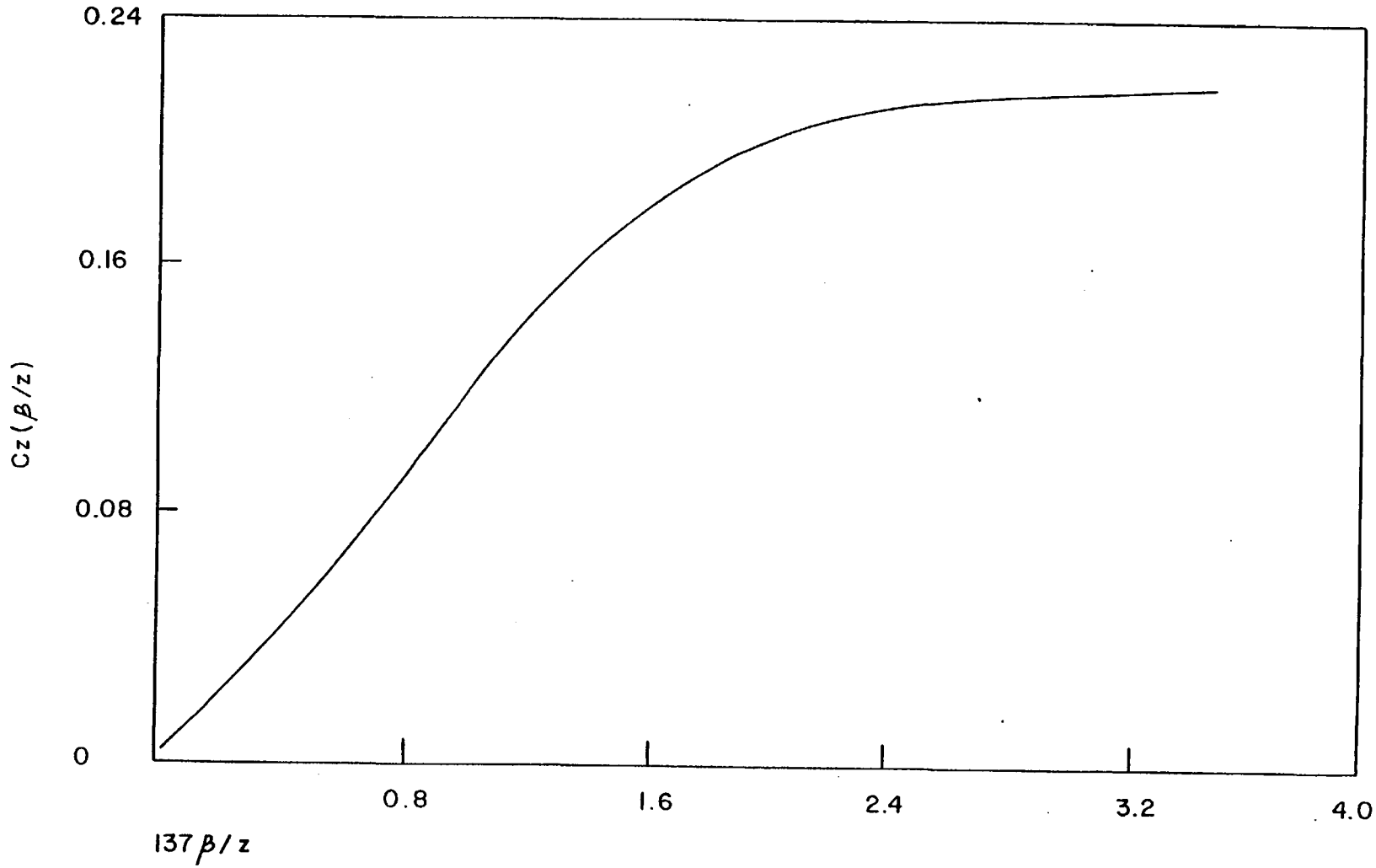


Figure B.1(b) Empirically derived curve relating the quantity $C_z(\beta/z)$ to the velocity of the ion in units of K-electron velocity[112]

The range, R, and the energy loss rate, (dE/dx), can now be evaluated from the fits to quantities $\lambda(\tau)$, $B_z(\beta)$ and their derivatives $\lambda'(\tau)$ and $B_z'(\beta)$.

B.3 DISCUSSION OF THE METHOD

The range extension, $B_z(\beta)$ is functionally related to the effective charge of the ion by[112]

$$B_z(\beta) = \int_0^{\beta} \left[(z/z^*)^2 - 1 \right] \frac{d\lambda}{d\beta'} \, d\beta' \qquad (B.22)$$

where z^* is the effective charge of the moving ion with atomic number z,

$$z^* = z\left[1 - \exp(-125\beta/z^{2/3}) \right] \qquad (B.23)$$

Although strictly true only for nuclear emulsions, Equation (B.23) can be used for other solids, except for very heavy ions at low incident velocities. Fig.B.2 shows z^*/z as a function of $\beta/z^{2/3}$.

The quantity $B_z(\beta)$ in Equation (B.22) is obtained by scaling the corresponding experimental expression for emulsion to other materials. It can be seen from Equation (B.22) that this procedure relies on two assumptions

(i) the effective charge, z^* is only a function of β and z, not a function of the stopping materials,

(ii) the proton range expression, $\lambda(\beta)$, can be scaled for different stopping materials.

The validity of the first assumption that, z^*/z is independent of the stopping material, seems to be demonstrated experimentally except for very heavy ions at low incident particle energy and very low stopping material density[109].

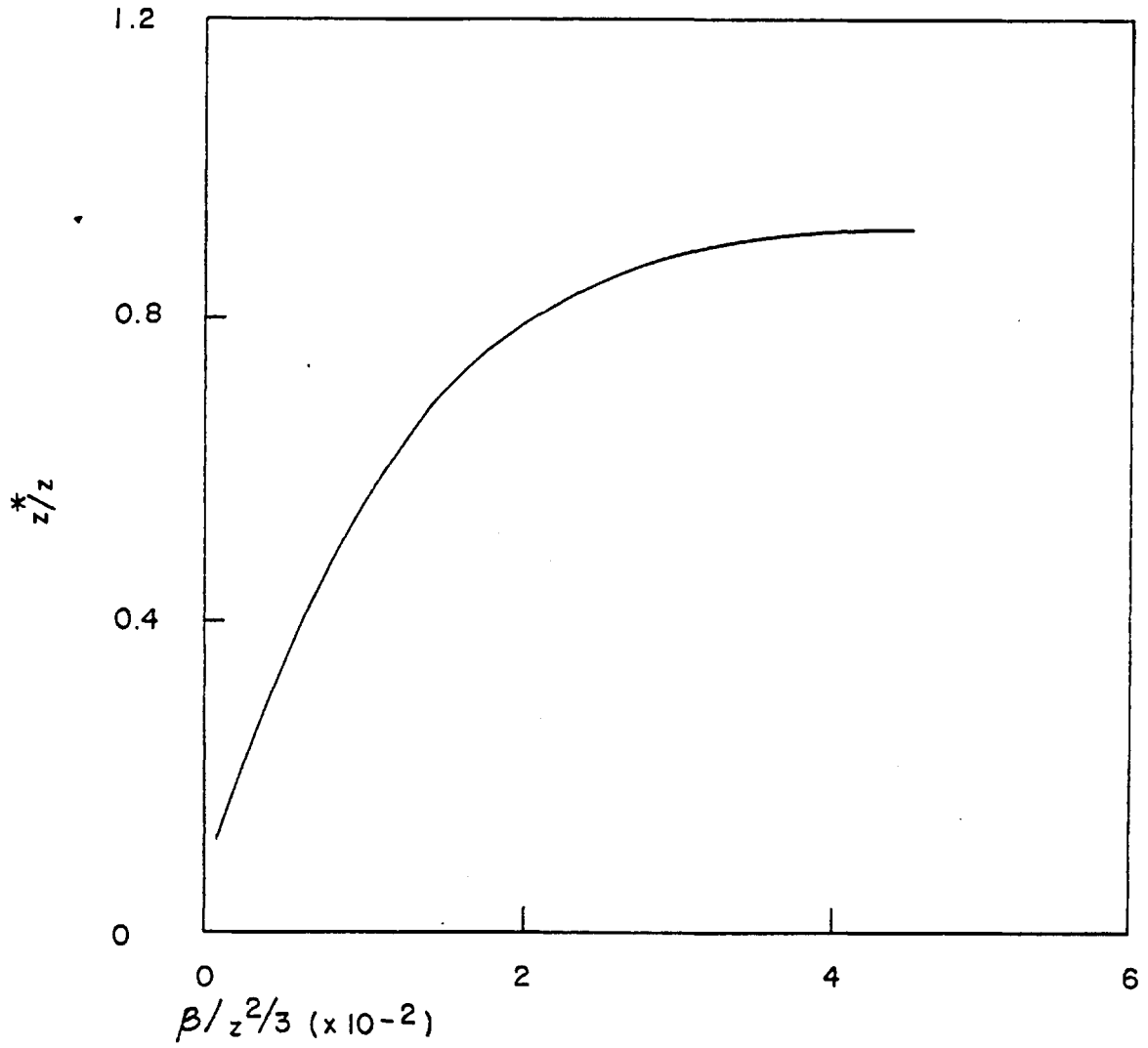


Figure B.2 The fractional effective charge, z^*/z as a function of the reduced velocity, $\beta/z^{2/3}$ of the ion

The second assumption is approximately true for small values of β. Barkas and Berger have used the expression

$$\lambda = (11.1 + 1.34\ I_{adj}^{5/8}) < A/Z > \beta^{10/3}\ g/cm^2 \qquad (B.24)$$

The $(1 + 0.121\ I_{adj}^{5/8})$ dependence of the range-energy relation and hence of B_z has been retained, but the experimental results for emulsion have been used to obtain the universal function that is to be scaled. Deriving B_z in this fashion is an imporvement over the use of the simplified analytic expression obtained from Equations (B.22) and (B.24), but still does not take into account the slight dependence of the shape of the curve $\lambda(\beta)$ upon the stopping material. Thus, an error will be introduced when I_{adj} of the material deviates significantly from I_{adj} for emulsion if $B_z(\beta)/\lambda(\beta)$ is not small. This situation is encountered when β is small and z is large.

In Fig.B.3 is shown a comparison of C_z used in the present calculation, (a), with the equivalent function used by Barkas and Berger, (b). While the two functions closely approximate each other in absolute values their slopes differ. Function (b) has a discontinuity at $(\beta/z) = 14.6$, thus resulting in a discontinuity in the (dE/dx). Also, while the function (b) can safely be used for calculating R and (dE/dx) of particles with E > 1 MeV/nucleon, it leads to serious errors at lower energies.

The calculated energy loss and range-energy data for ^{1}H, ^{4}He, ^{12}C, ^{14}N and ^{16}O in cellulose nitrate are given in Tables B.2(a) and (b).

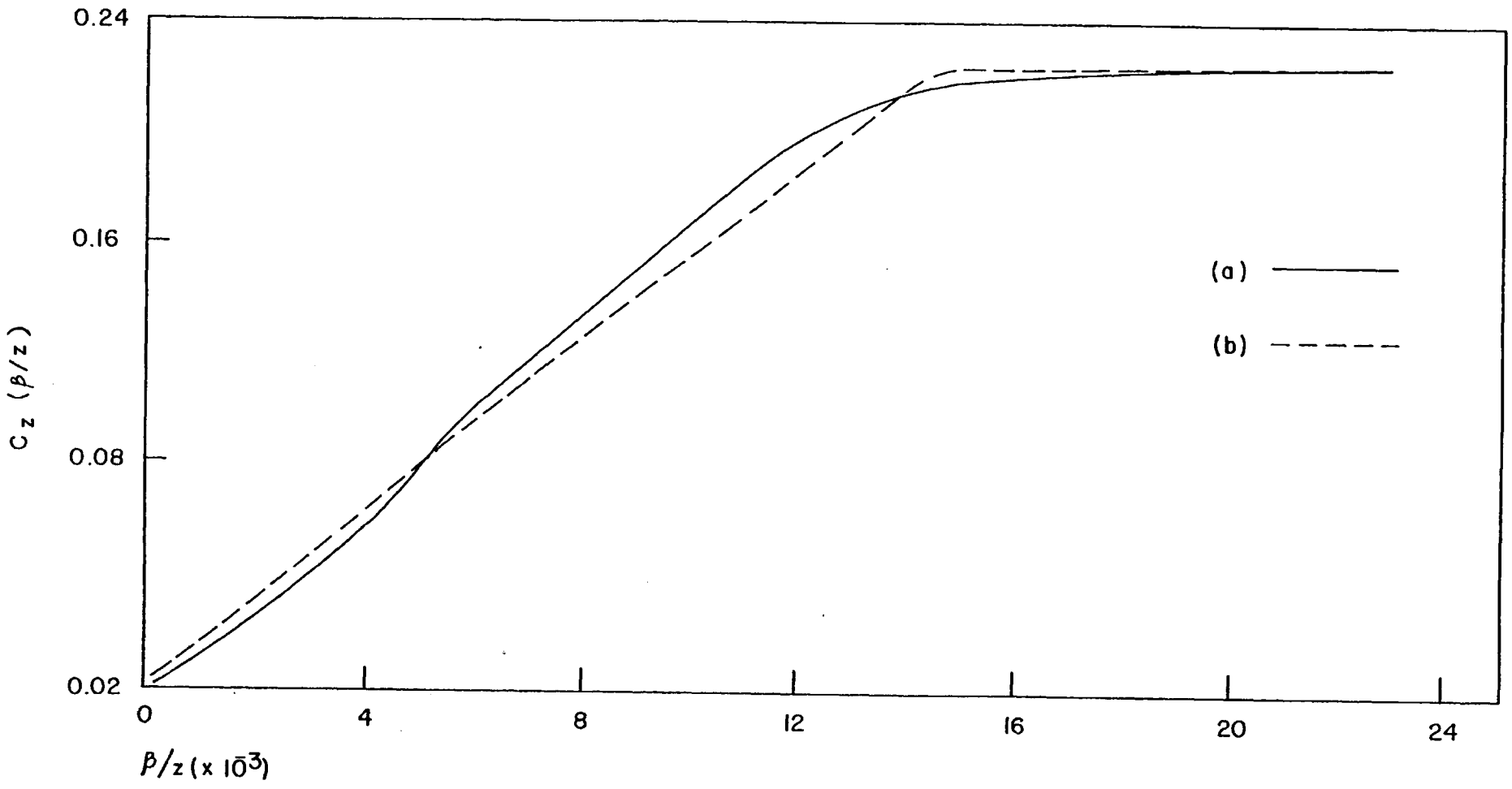


Figure B.3 The range-extension functions, $C_z(\beta/z)$ as a function of (β/z). Function (a) was used in the present calculations, function (b) is of the form used by Barkas and Berger

TABLE B.2(a)

ENERGY LOSS RATE IN CELLULOSE NITRATE

E/nucleon (MeV/amu)	(dE/dx) MeV/(mg/cm^2)				
	$^{1}_{H}$	$^{4}_{He}$	$^{12}_{C}$	$^{14}_{N}$	$^{16}_{O}$
0.04	0.76	1.94	5.69	6.07	7.07
0.06	0.80	2.01	6.35	7.03	7.69
0.08	0.78	2.03	6.79	7.89	8.65
0.10	0.77	2.03	7.11	8.62	9.16
0.15	0.68	1.98	7.57	8.93	10.00
0.20	0.60	1.92	7.79	8.99	10.05
0.25	0.54	1.84	7.88	9.10	10.06
0.30	0.49	1.77	7.89	9.56	10.07
0.40	0.42	1.65	7.79	9.92	11.10
0.50	0.37	1.48	7.60	9.68	10.09
0.60	0.36	1.34	7.38	9.21	10.08
0.70	0.34	1.22	7.15	9.01	10.06
0.80	0.29	1.12	6.90	8.62	10.03
0.90	0.26	1.05	6.55	8.45	10.01
1.00	0.24	0.97	6.47	7.88	9.46
1.50	0.18	0.74	5.58	7.43	9.39
2.00	0.15	0.60	4.87	6.89	8.75
2.50	0.12	0.51	4.32	6.01	7.81
3.00	0.11	0.45	3.48	5.89	7.02
4.00	0.08	0.35	3.21	5.32	6.01
5.00	0.07	0.29	2.68	3.98	4.80
6.00	0.06	0.25	2.32	3.64	4.04
8.00	0.05	0.20	1.84	2.98	3.27
10.00	0.04	0.14	1.54	2.02	2.74

TABLE B.2(b)

RANGE IN CELLULOSE NITRATE

E/nucleon (MeV/amu)	R (g/cm^2)				
	^{1}H	^{4}He	^{12}C	^{14}N	^{16}O
0.04	5.8×10^{-5}	1.0×10^{-4}	1.2×10^{-4}	1.26×10^{-4}	1.3×10^{-4}
0.06	8.4	1.4	1.6	1.66	1.7
0.08	1.0×10^{-4}	1.8	2.0	2.05	2.1
0.10	1.3	2.2	2.3	2.4	2.5
0.15	2.0	3.2	3.1	3.2	3.3
0.20	2.8	4.1	3.9	4.0	4.1
0.25	3.6	5.3	4.7	4.75	4.8
0.30	4.6	6.4	5.4	5.5	5.6
0.40	6.8	8.7	6.9	6.95	7.0
0.50	9.3	1.1×10^{-3}	7.5	8.0	8.5
0.6o	1.2×10^{-3}	1.4	1.0×10^{-3}	9.5	9.9
0.70	1.5	1.7	1.1	1.1×10^{-3}	1.1×10^{-3}
0.80	1.8	2.0	1.3	1.3	1.3
0.90	1.9	2.3	1.5	1.5	1.5
1.00	2.6	2.8	1.7	1.65	1.6
1.50	5.0	5.2	2.7	2.5	2.4
2.00	8.0	8.2	3.8	3.6	3.4
2.50	1.1×10^{-2}	1.1×10^{-2}	5.2	4.9	4.5
3.00	1.5	1.6	6.6	6.2	5.7
4.00	2.5	2.0	1.0×10^{-2}	8.8	8.4
5.00	3.8	2.6	1.4	1.4×10^{-2}	1.1×10^{-2}
6.00	5.2	5.2	1.9	1.6	1.5
8.00	8.8	8.8	3.0	2.8	2.4
10.00	1.3×10^{-1}	1.3×10^{-1}	4.5	3.8	3.5

APPENDIX C

NEUTRON CROSS SECTIONS

Neutron cross sections for various reactions, used to calculate the response of cellulose nitrate and Makrofol K.G SSTRs are given in the following pages. All data and curves are taken from BNL-325, Vol.I and II (1976).

Some thermal cross sections are listed below:

Reaction	σ(barns)
$^{6}Li(n,\alpha)^{3}H$	940 ± 4
$^{10}B(n,\alpha)^{7}Li$	3837 ± 9
$^{14}N(n,p)^{14}C$	1.81 ± 0.05

TABLE C.1

ELASTIC SCATTERING AND (n,α) REACTION CROSS-SECTIONS FOR ^{1}H, ^{12}C, ^{14}N AND ^{16}O AS A FUNCTION OF NEUTRON ENERGY

E_n (MeV)	^{1}H σ_{el}(b)	^{12}C		^{14}N		^{16}O	
		σ_{el}(b)	σ_{α}(b)	σ_{el}(b)	σ_{α}(b)	σ_{el}(b)	σ_{α}(b)
0.25	8.0	4.2					
0.5	6.0	4.0					
0.75	4.5	2.50					
1.0	4.0	3.50			0.001		
1.5	3.2	2.0			0.02		
2.0	3.0	1.80			0.05		1.50
2.5	2.5	1.6			0.10		0.60
3.0	2.2	2.30		1.3	0.20		1.10
3.5	2.0	1.6		1.2	0.40		3.0
4.0	1.95	2.30		1.50	0.35	0.05	1.20
4.5	1.90	2.2		1.25	0.34	0.05	1.30
5.0	1.8	1.5		0.65	0.30	0.20	1.50
5.5	1.75	0.95		1.25	0.08	0.01	1.10
6.0	1.65	0.86	0.001	1.10	0.095	0.025	1.50
6.5	1.5	1.2	0.001	0.9	0.06	0.09	0.8
7.0	1.4	0.56	0.01	0.85	0.04	0.063	0.75
7.5	1.35	1.5	0.025	1.10	0.035	0.058	0.65
8.0	1.3	1.4	0.074	0.9	0.06	0.05	0.60
9.0	1.10	0.65	0.059	0.8		0.074	0.80
10.0	0.9	0.62	0.126	0.85		0.086	1.0
12.0	0.7	0.90		0.80			1.10
15.0	0.6	0.84		0.90			1.0
20.0	0.5	0.84					

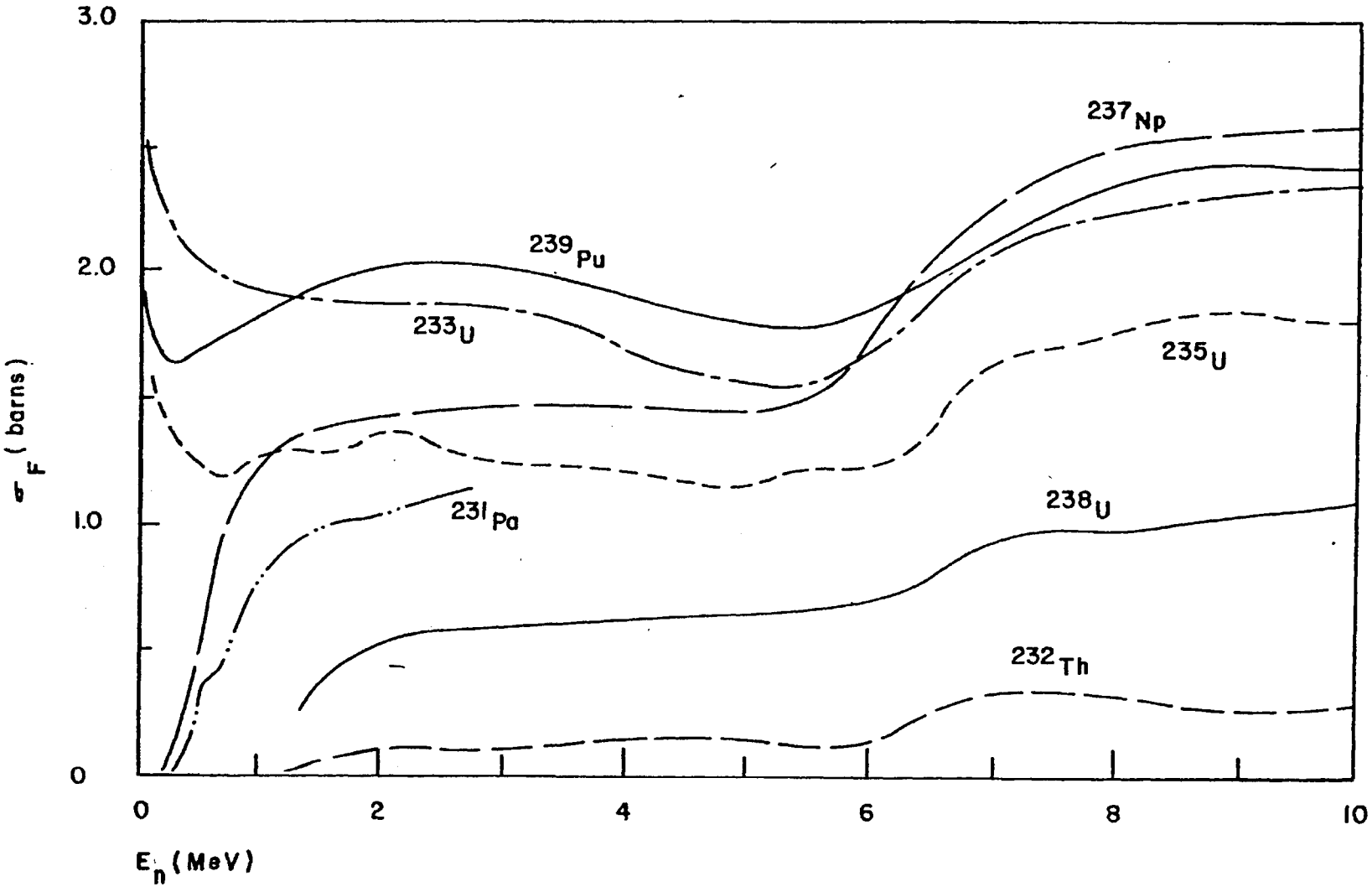


Figure C.1 Microscopic fission cross sections, σ_F for various isotopes as a function of neutron energy. Data from BNL-325

SOLID STATE NUCLEAR TRACK DETECTORS IN REACTOR PHYSICS PROBLEMS[1]

A. U. Haque*, C. B. Besant* and B. W. Hooton**

**Department of Mechanical Engineering, Imperial College of Science and Technology, London SW7, U.K.*
***Nuclear Physics Division, A.E.R.E., Harwell, Oxfordshire, U.K.*

ABSTRACT

Calibration of CA80-15 for fast neutron dosimetry in mixed radiation fields is described. For a fission source the sensitivity is $\simeq 1.4 \times 10^{-5}$ tracks per neutron. The experimental results are in sufficiently good agreement with the theoretical computations to consider CA80-15 as a good fast neutron integrating device.

KEY WORDS

Nuclear tracks; cellulose nitrate; fast neutrons; fission spectrum; neutron interactions; etchant; sensitivity.

INTRODUCTION

Solid state nuclear track detectors are being developed for the selective detection of fast neutrons in the presence of a high flux of gamma rays and low energy neutrons. This interest stems from a requirement to measure the fissile content of spent reactor fuel elements and the assay of fissile material for safeguards. The material selected for this purpose was cellulose nitrate CA80-15 due to its low registration threshold value ($dE/dx \simeq 0.4$ MeV cm^2/mg) which makes it sensitive to a wide range of particles produced in fast neutron interactions with the constituents of the plastic thus leading to a high sensitivity.

THEORETICAL CONSIDERATIONS

Recoil Nuclei

The following characteristics are of interest in the utilisation of this method. 1) The energy of the recoil nuclei produced at various neutron energies and the linear loss of energy of these particles at the beginning of their range. 2) The range of recoil ions in the detector as a function of energy. 3) The total number of recoils produced per unit area of the detector. The average energy, dE/dx, range and scattering cross sections calculated as a function of neutron energy are given in table 1 (Haque, 1979; BNL 325).

It is estimated that the minimum lengths of tracks produced in the detector must be $\simeq 2\mu$m to be visible in an optical microscope with usual methods of observation

[1]Research approved by A.E.R.E. Harwell.

(Fleischer, 1964; Rolarosy, 1969). For this reason and as a function of data in table 1 there exists a neutron energy threshold beyond which the tracks can be observed in the detector if the etching conditions have been chosen appropriately. The total number of tracks produced per unit area of the detector was calculated using the equation;

$$N = \sigma \Phi A C \qquad (1)$$

where: N = number of tracks per unit area (t/cm^2); σ = elastic scattering cross section (cm^2); C = concentration of particular nucleus (g/cm^2); A = Avogadros number (6.02×10^{23} mol^{-1}) and Φ = neutron fluence (n/cm^2).

Reaction (n, α) from C, N and O

The (n, α) reaction from C, N and O in the neutron energy interval which is of interest to us (fission spectrum) are endothermic (Evans, 1967; Segre, 1953). In table 2 the considered (n, α) reactions, Q values and threshold energies are listed. Table 3 shows the average energies of the particles produced in these reactions, the range of α-particles calculated as a function of neutron energy and the cross sections for these (n, α) reactions.

The sensitivity of CA80-15 as a function of neutron energy was calculated by substituting different parameters in equation 1, from tables 1 and 3. These results are shown in fig. 3, and table 4.

EXPERIMENTS

CA80-15 films were irradiated with mono-energetic fast neutrons from 0.2 to 17 MeV which were produced using the IBIS machine at A.E.R.E. Harwell. The fluence was measured with a BF_3 long counter calibrated on a $^{252}C_f$ neutron source. Neutrons were incident normally on the surface of the films.

After irradiation the CA80-15 films were etched in 6N KOH at $60^{o}C$ for different times. As control, the same plastic sample but unirradiated was treated with the same etching agents under the same etching conditions and some background tracks were detected.

RESULTS

Prolonged Etching Effects

The quantitative relation between the etching time and the number of tracks is shown in fig. 1. It was observed that tracks grow in size and number with etching time which can be explained as follows. 1) Very small features which were not originally perceptible are enlarged. 2) New tracks that began and ended beneath the original surface are encountered as material is removed. 3) The etching along a track having a low dip angle and damage that increases downwards reveals track partway along their lengths.

After some time the track density reaches a plateau which gives optimum etching conditions. This plateau is reached earlier as the neutron energy decreases. At long etching times some of the original tracks may be lost as their optical contrast is reduced. At higher energies the recoil tracks are longer and remain visible over much longer etching times. The thickness of the plastic surface removed as a function of etching time is shown in fig. 2, which reveals a linear relationship.

The Sensitivity Curve

The experimental sensitivity curve for CA80-15 at a particular etching condition (6N KOH at 60°C for 45 mins.) is shown in fig. 3. The sensitivity increases with neutron energy. The tracks observed up to E_n = 1.5 MeV are due to recoil protons as at E_n = 1.5 MeV the average energy of recoil protons produced is 0.75 MeV and protons having this energy produce readily observable tracks in CA80-15 (Haque, 1979). The tracks from E_n = 1.5 to 7 MeV are due to (n, α) reactions from C, N and O, while at neutron energies higher than 7 MeV C, N and O recoils are also present. The experimental and theoretical results are composed in table 4 and are in sufficiently good agreement.

The Effects of High Gamma Doses

An earlier study has shown that the bulk etching rate of CA80-15 at high gamma doses increases as shown in fig. 4, (Haque, 1977). Some of the neutron irradiated films were exposed to different gamma doses from 1 to 24 M Rads from a ^{60}Co source and the track density in these films is plotted in fig. 5. The track density starts decreasing at ∿ 6 M Rads, because the increase in bulk etching rate of CA80-15 makes the background surface roughened thus making it difficult to avoid the counting loss. However, when the etching times were reduced according to the increase in the bulk etching rate, the track density remained constant even at high gamma doses as shown in fig. 5. The results suggest that CA80-15 can be used successfully for the selective detection of fast neutrons in high gamma backgrounds provided etching conditions have been chosen appropriately.

REFERENCES

BNL 325 (1976). Vol. II, Brookhaven National Lab., New York.

Evans, R.D. (1967). The Atomic Nucleus. McGraw Hill, New York.

Fleischer, R.L., Price, P.B., and Walker, R.M. (1964). Track registration in various solid state nuclear track detectors. Phys. Rev., 133. A1443 - 1449.

Haque, A.U. (1979). Measurement of fast neutrons using nuclear track detectors. Imperial College report No. AERE/IC/3.

Haque, A.U. (1977). A study of solid state nuclear track detectors. M.Sc. Thesis. University of London.

Ralarosy, J. (1969). Journal de Phys. 30. p. 1.

Segre, E. (1953). Experimental Nuclear Physics. Vol. II, John Willey and Sons. New York.

TABLE: 1

Calculated Parameters of H, C, N and O Recoils

E_n	Hydrogen				Carbon				Nitrogen				Oxygen			
	$\bar{E}_H$	dE_H/dx	R_H	σ_{el_H}	$\bar{E}_C$	dE_C/dx	R_C	σ_{el_C}	$\bar{E}_N$	dE_N/dx	R_N	σ_{el_N}	$\bar{E}_O$	dE_O/dx	R_O	σ_{el_O}
(MeV)	(MeV)	$\frac{(MeV\ cm^2)}{mg}$	(μm)	(b)	(MeV)	$\frac{(MeV\ cm^2)}{mg}$	(μm)	(b)	(MeV)	$\frac{(MeV\ cm^2)}{mg}$	(μm)	(b)	(MeV)	$\frac{(MeV\ cm^2)}{mg}$	(μm)	(b)
1	0.5	0.36	5.8	4.0												
3	1.5	0.18	33	2.2												
5					0.71	1.82	1.23	1.6	0.62	0.43	1.1	0.65				
6					0.85	2.67	1.38	0.88	0.76	1.52	1.21	1.1				
8					1.15	3.9	1.58	1.4	0.98	3.18	1.5	0.9	0.89	2.03	1.16	0.6
10					1.44	4.72	1.85	0.68	1.25	4.25	1.74	0.85	1.11	3.32	1.3	1.0
12					1.8	5.34	2.03	0.9	1.5	5.10	1.98	0.8	1.32	4.41	1.4	1.0
15					2.14	5.8	2.3	0.85	1.86	5.92	2.2	0.9	1.65	5.6	1.6	1.0
20					2.85	6.26	2.65	0.85	2.5	6.85	2.55		2.21	6.8	2.4	

TABLE: 2

Q-Values and Threshold Energies for (n, α) Reactions

Reaction	Q-Value (MeV)	Threshold Energy (MeV)
$^{12}_{6}C + ^{1}_{0}n \rightarrow ^{4}_{2}He + ^{9}_{4}Be$	-5.7	5.75
$^{14}_{7}N + ^{1}_{0}n \rightarrow ^{4}_{2}He + ^{11}_{5}B$	-0.15	0.15
$^{16}_{8}O + ^{1}_{0}n \rightarrow ^{4}_{2}He \quad ^{13}_{6}C$	-2.20	2.21

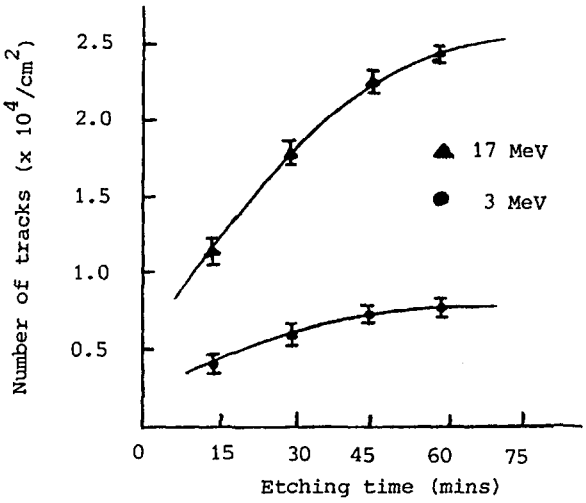


FIG. 1 Track density in Ca80-15 as a function of etching time (6N KOH at 60°C) for neutron energies 3 and 17 MeV

TABLE: 3

Cross Sections of (n, α) Reactions from C, N and O, Average Energies of Particles Produced and Range of α-particles as a Function of Neutron Energy

E_n		Carbon			Nitrogen				Oxygen			
(MeV)	$\bar{E}_{^9Be}$ (MeV)	$\bar{E}_\alpha$ (MeV)	R_α (μm)	σ_α (b)	$\bar{E}_{^{11}B}$ (MeV)	$\bar{E}_\alpha$ (MeV)	R_α (μm)	σ_α (b)	$\bar{E}_{^{13}C}$ (MeV)	$\bar{E}_\alpha$ (MeV)	R_α (μm)	σ_α (b)
1.0					0.16	0.69	3.0	0.001				
1.5					0.26	1.09	4.2	0.02				
2.0					0.36	1.49	6.0	0.05				
2.5					0.46	1.89	8.5	0.1				
3.0					0.56	2.29	20.25	0.2				
3.5					0.66	2.69	13.0	0.4	0.10	1.20	5.0	0.0
4.0					0.76	3.09	15.0	0.35	0.19	1.62	7.0	0.05
4.5					0.86	3.49	17.5	0.34	0.28	2.03	9.0	0.05
5.0					0.96	3.89	20.5	0.3	0.36	2.44	12.0	0.225
5.5					1.06	4.29	23.0	0.08	0.45	2.85	14.0	0.01
6.0		0.66	2.7	0.001	1.16	4.69	26.5	0.095	0.54	3.26	16.0	0.025
6.5		1.05	4.0	0.001	1.26	5.09	29.0	0.06	0.63	3.68	19.0	0.09
7.0		1.43	5.5	0.01	1.36	5.49	32.5	0.04	0.72	4.09	22.0	0.063
7.5		1.82	8.0	0.025	1.46	5.89	36.0	0.035	0.80	4.50	25.0	0.058
8.0	0.09	2.20	10.0	0.074	1.56	6.29	41.0	0.060	0.89	4.91	28.0	0.05
8.5	0.21	2.59	12.0	0.034	1.66	6.69	43.0	0.01	0.98	5.32	31.0	0.054
9.0	0.32	2.97	14.0	0.059	1.76	7.09	47.5	0.0	1.07	5.74	34.5	0.071
9.5	0.44	3.36	17.0	0.087	1.86	7.49	53.0		1.16	6.15	39.0	0.077
10.0	0.55	3.74	19.0	0.126	1.96	7.89	56.0		1.24	6.56	43.0	0.086

TABLE: 4

Theoretical and Experimental Sensitivity of CA80-15 as a Function of Neutron Energy

E_n (MeV)	Theoretical Sensitivity		Experimental Sensitivity	$\eta_{exp.}/\eta_{calc.}$
	$\eta_{calc.}$ ($\times 10^{-5}$ t/n)	Reactions Considered	$\eta_{exp.}$ ($\times 10^{-5}$ t/n)	
1.0	0.8	recoil protons	0.62	0.78
1.25	0.75	recoil protons	0.68	0.9
1.5	0.6	recoil protons	0.78	1.3
3.5	0.95	(n, α) from N	1.25	1.3
4.0	1.1	(n, α) from N and O	1.4	1.2
5.0	1.7	(n, α) from N and O	1.6	0.9
8.0	1.6	(n, α) from O, C and N recoils	1.8	1.1
10.0	1.75	C, N, and O recoils	2.0	1.14
12.0	1.7	C, N, and O recoils	2.12	1.24

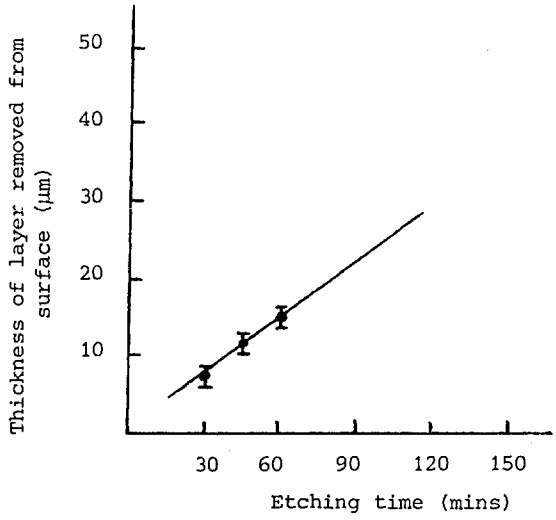


FIG. 2 Thickness of layer removed from surface as a function of etching time in 6N KOH at 60°C for CA80-15

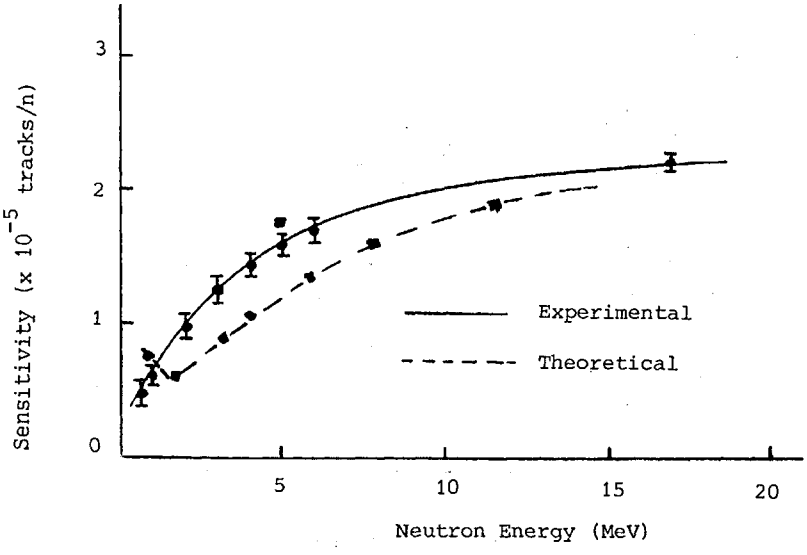


FIG. 3 Experimental and theoretical sensitivities of CA80-15

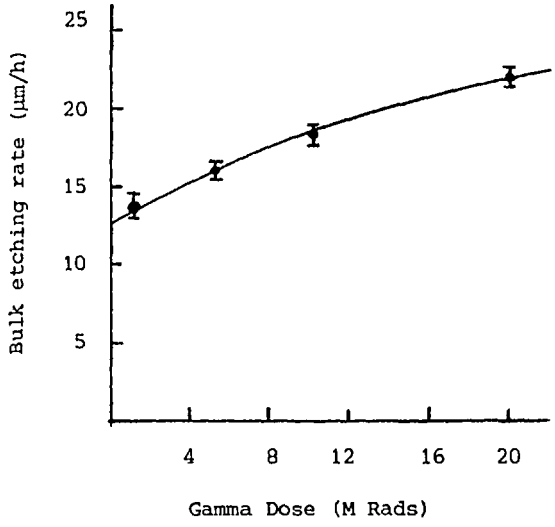


FIG. 4 Bulk etching rate in 6N KOH at 60°C for CA80-15 as a function of gamma dose

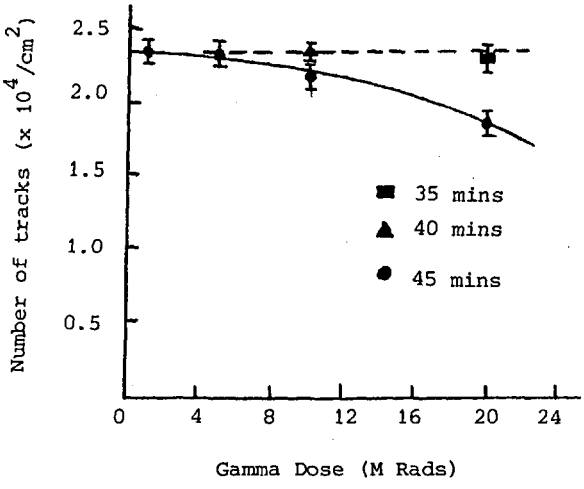


FIG. 5 Number of tracks from 17 MeV neutrons in CA80-15 as a function of gamma dose, etched in 6N KOH at 60°C for different times

Technical Notes

International Journal of Nuclear Medicine and Biology, Vol. 5, pp. 261–265. Pergamon Press Ltd 1978. Printed in Great Britain

Solid State Track Recorders in Nuclear Medicine

(*Received* 21 *October* 1977)

SEVERAL TYPES of fast particles including protons, neutrons, pions and heavy charged particles are currently being evaluated for applications in the radiation therapy and diagnosis of cancer. There is already evidence to indicate that some of these particles will prove superior to conventional X-rays and γ-rays in certain applications. Almost all studies with these new techniques are utilizing nuclear detectors, counters and photographic plates originally designed and constructed for nuclear reactor physics and engineering applications. For a variety of reasons these detectors and counters are not appropriate for adoption in wide-spread medical applications. It appears likely that as the clinical evaluation programmes proceed a demand will be created for medically practical particle detectors and counters. In this context, cellulose nitrate track recorders were evaluated for use in charged particle radiography for the investigation and location of tumours and regions of abnormal density in soft tissues and to assist in investigations of radiation dose for radiation therapy.

Introduction

Our previous work in the detection of charged particles using Solid State Track Recorders, was directed to the measurement of nuclear reaction rates in reactors and to the development of a neutron spectrometer via chemical etching.[1,2] As a result of this work and better understanding of the chemistry of cellulose and its derivatives, new techniques of track revelation, based on the nature of the latent tracks, have been discovered.

These techniques utilize the following:

(a) *Base-exchange*[3]

It was shown in Reference (3) that radiation damage in cellulose (and especially in cellulose nitrate) lead to oxidative reactions along the latent tracks and consequent formation of acidic groups. The exchange of the H^+ ion of the irradiated cellulose with the larger Ca^{2+} ion from the base exchange solution has also been shown to be proportional to the radiation dose and to be dependent on the pH of the solution. The amount exchanged is maximum in alkaline solution and minimum in acidic. Latent tracts are identified by the contrast of colour between the bulk plastic (a rosy colour) and the Ca^{2+} ion which is white (in fact this is similar to the grafting technique).

(b) *Free radicals (scavengers)*[4]

Free radicals are exceedingly common radiation products whose widespread existence in all irradiated organic solids has been demonstrated by EPR (electron paramagnetic resonance) techniques. Scavengers are substances which react with free radicals giving away their colour to form relatively stable compounds. Latent tracks are seen by this distinct colour contrast given by the scavengers, with the rosy bulk plastic background.

(c) *Colouring of the acidic group by methylene blue*

Large molecules of methylene blue will anchor themselves, giving away their colour, to the acidic group which had been formed in the bulk plastic due to irradiation.

Latent tracks are recognised, counted and measured by the blue conical damaged trails embedded in a rosy background.

One of the major drawbacks in extending the application of Solid State Track Recorders via etching technique to nuclear medicine has been the low optical contrast between the irradiated and un-irradiated regions of the SSTR. This has been overcome by colouring of the acidic group by methylene blue, which was very successful for revealing a charged particle radiograph as well as for the reaction rate measurements in nuclear reactor physics applications.

The usefulness of this technique lies in the ability to observe the individual tracks produced by the charged particles in the SSTR with a high optical contrast and resolution compatible with atomic and molecular scales. This technique is still in its infancy and needs better understanding and more quantitative data.

Charged Particle Radiography

Current methods in nuclear medicine employing gamma emitting radionuclides impose three major limitations on the usefulness of these methods, namely:

(i) Image contrast is severely reduced by activity contained in tissues surrounding the regions of interest. This activity which contributes noise to the image may vary spatially and is often so pronounced that only structures with a high radionuclide concentration can be differentiated from their surroundings.

(ii) In spite of the relatively high inherent resolution capabilities of certain nuclear medicine imaging devices, their effective resolution is limited by that of the collimator whose improvement must be weighed against the concomitant severe loss in detection efficiency. Since the resolution and sensitivity (for the imaging of sources in tissues) of collimators vary with distance, the perceptibility of small or low contrast structures is usually reduced with depth.

(iii) The widespread use of ^{99m}Tc in nuclear medicine limits the scope of this discipline. Although ^{99m}Tc is readily available, inexpensive, has a low energy–high proton yield and possesses some desirable chemical properties, there are two serious drawbacks to its use: (a) Because of the low energy gamma radi-

ation from ^{99m}Tc, detection efficiency varies significantly with depth and may be affected by the presence of bone overlying the organ of interest. (b) The chemical properties of ^{99m}Tc are less akin to physiological processes than those of many other radionuclides.

As a consequence of the above limitations and due to the failure of X-ray diagnostic techniques to accurately detect tumours and other regions of abnormal density in soft tissues, imaging in nuclear medicine has been primarily limited to morphological examinations; while recording physiological studies which should be possible in this field have been greatly restricted.

Conventional X-ray imaging does well in the evaluation of the chemical composition and large differences in density, such as bone, soft tissue and air. Artificial differences can be made by introducing air or iodine compounds. However, the diagnostic information of conventional X-rays is limited because the tissues of interest are obscured by superposition of over- or underlying tissues in the projected radiograph (Fig. 1). Also the response of the X-ray photographic films has unwanted halo effects due to the recording of unwanted electrons and charge secondaries.

In order to circumvent these problems and to increase the scope of nuclear medicine, methods have been developed, such as the EMI scanner, which is currently being used.

Present research with alpha particles is an attempt to improve on spatial resolution and density sensitivity (Fig. 2).

The Technique

A beam of monoenergetic charged particles (e.g. ^{16}O ions) is directed down a beam channel to a facility which houses the detection equipment and the biological object or patient (Fig. 3). The beam is brought to rest in a stack of plastic sheets, which in the present work were cellulose nitrate films. Particles traverse about the same mass thickness (g/cm^2) before coming to rest in a particular sheet, which gives information about the mass density along their path. The damaged regions in the plastics may either be preferentially etched using a suitable chemical to render the tracks visible under an optical microscope or these tracks may be revealed using methylene blue, which was highly successful for heavy ions.

Protons and alpha radiography is also of interest due to smaller radiation doses as compared to the radiation doses in the methods currently being used such as EMI. Present X-ray and EMI techniques deliver doses of 1000 mrad and 1600 mrad respectively and probably would not detect a compressed breast or skull tumour directly, compared to a 30 mrad dose from alpha particles with good resolution of the tumour. As a result of straggling and scattering, radiographs can be produced with heavy ions. The usefulness of this technique lies in the track revelation with a high optical contrast which has been achieved using methylene blue and is discussed in the next section. However, the application of heavy ion radiography is restricted to some extent by the need for high energy particles (several hundreds of MeV/nucleon).

Radiograph Development by Methylene Blue

The damage left by a charged particle in a SSTR consists of acidic groups (carboxyl) among other radiation products. In the present work it was found that the acidic groups in tracks can be coloured by a basic dye (methylene blue); thereby leading to a direct and convenient method of track revelation in a radiograph.

In a basic dye the colouring group (chromophore) is contained in the cation. Methylene blue is commonly used in histology for staining acidic structures of cells. It is particularly effective since its affinity for basic groups is very high. However, because of the relatively large size of the cation (~10 Å), it cannot easily penetrate cellulosic materials, where ions of up to ~8 Å diameter are admitted. Thus a swelling agent must be employed to expand the spaces between the molecules along the latent tracks in order to aid penetration. In the case of cellulose nitrate, it was found

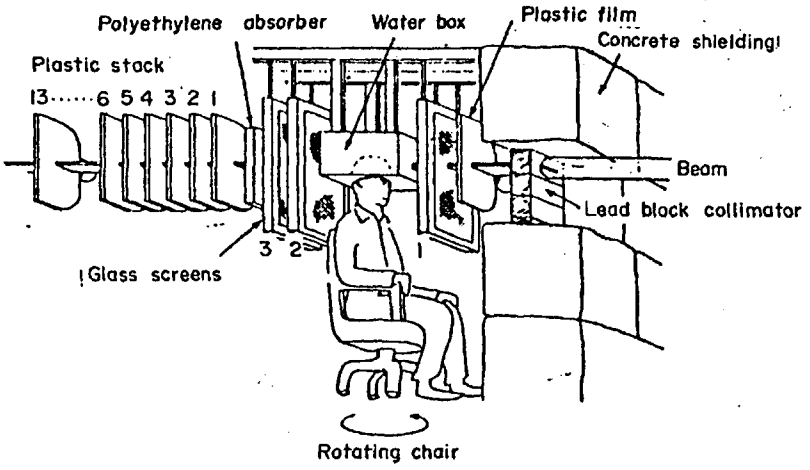
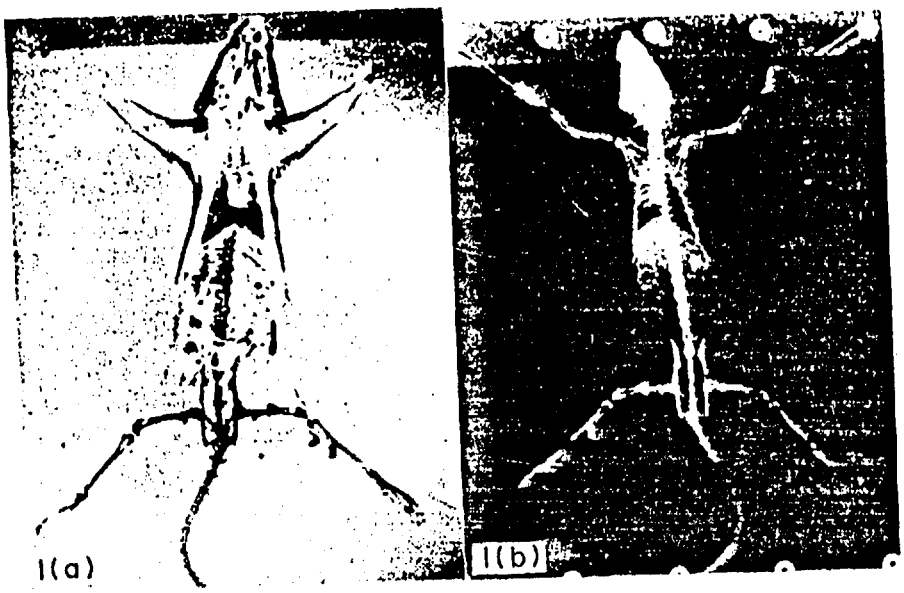


FIG. 3. Schematic diagram of helium ion transverse section imaging (the alpha Radiography Facility).



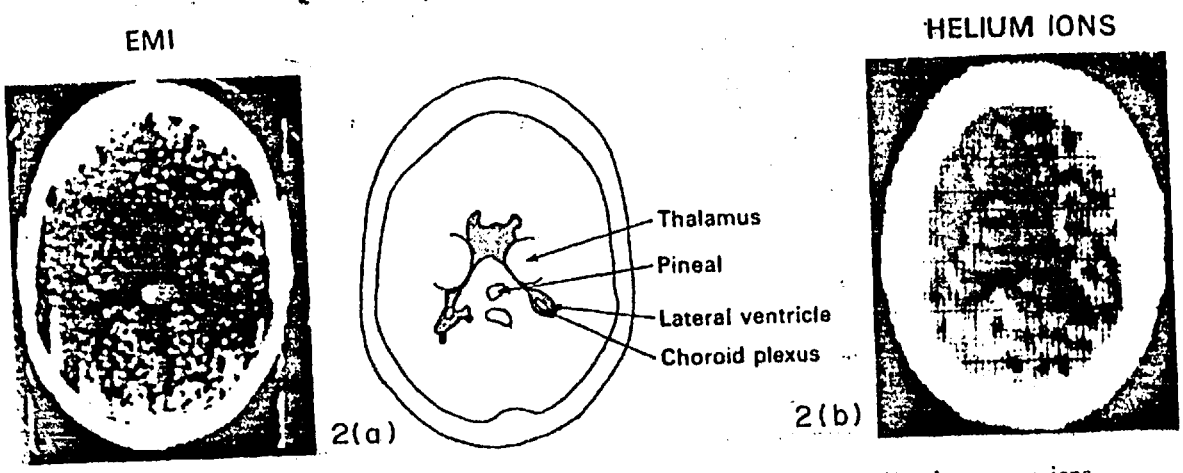


FIG. 1. Details of a long tailed rodent. (a) with X-rays; (b) with 400 meV/nucleon neon ions.

FIG. 2. (a) EMI scan of the brain consisting of 180 views and requiring a 1600 mrad dose to the subject. (b) Helium ion image of the same subject on SSTR consisting of 64 plastic sheets, requiring only a 30 mrad dose.

that an aqueous solution of methylene blue with constituents as given in the following formula (1) was effective. Formulae (2) and (3) were tried for heavy particles (fission fragments) with success but as yet have not been tried for light particles.

(1) *Acidic*
Methylene blue: 1 g
Glacial acetic acid: 1 ml
Ethyl alcohol: 20 ml
Distilled water: 82 ml

(2) *Basic*
Methylene blue: 0.3 g
Ethyl alcohol: 30 ml
0.01% KOH: 100 ml

(3) *Basic*
Methylene blue: 1 g
Borax: 1 g
Distilled water: 100 ml

The cellulose nitrate material used for the SSTR was a thin sheet (100 μ) CA 80–15 manufactured by Kodak Pathé. The CA 80–15 plastic was irradiated by heavy ions at various angles of incidence and various doses. The specimens were immersed in a solution of methylene blue for various lengths of time. Short times are preferable since the plastic becomes uniformly coloured blue due to the weaker affinity of methylene blue for the hydroxyl groups in the cellulose nitrate. The carboxyl groups absorb methylene blue much more rapidly.

The profile of the charged beam was revealed by a very short treatment (~5 min). Experiments were done to find the minimal dose which could be revealed to the human eye by an immersion in methylene blue. This minimal dose was found to be $\sim 10^5$ particles/cm^2 at an energy of ~35 MeV, which corresponds to a dose of 8.45 mrad at the surface of the plastic.

Further experiments were done on charged particle tracks at 30° to determine the amount of penetration of methylene blue dye into the tracks. This was found to depend on the swelling of the latent track. By using effective swelling agents such as chloride, the penetration could be increased by a factor of 2 to a distance of 64 μ.

The radiograph can be etched in sodium or potassium hydroxide after colouring, so that the results of dyeing can be checked by a post etching.

Conclusions

This work shows that the SSTRs can be successfully used in nuclear medicine and the resulting tracks can be revealed by dyeing with high efficiency. The major advantage of the method is the high contrast achieved between irradiated and unirradiated regions of the radiograph, which permits easy revelation of a beam profile of a diagnostic beam. Previously, dyes were used to fill etched tracks to achieve higher contrast. Also this work shows that techniques of histological staining are useful in charged particle radiography.

Acknowledgements—The authors gratefully acknowledge the advice and help given by Dr. B. VARGA and Dr. A. H. WINDLE. Thanks are also due to AERE Harwell for use of accelerator time and in particular to Mr. E. SPARROW whose assistance was most valuable.

A. Y. QAQISH
C. B. BESANT
A. U. HAQUE

Department of Mechanical Engineering,
Imperial College,
London SW7, U.K.

References

1. QAQISH A. Y. and BESANT C. B. *Nucl. Instrum. Meths.* **138**, 493 (1976).
2. BESANT, C. B., QAQISH A. Y. and VARGA B. B. *J. Radiat. Effects* No. 50 (1977).
3. QAQISH A. Y. PhD. Thesis, University of London (1977).
4. VARGA B. MsC. Thesis. University of London (1977).

Nuclear Instruments and Methods 173 (1980) 127–130
© North-Holland Publishing Company

Part V. Neutron physics

MEASUREMENT OF FAST NEUTRONS USING NUCLEAR TRACK DETECTORS

A.U. HAQUE, C.B. BESANT and B.W. HOOTON *

Nuclear Power Section, Department of Mechanical Engineering, Imperial College of Science and Technology, London SW7, England

The properties of solid state track detectors for neutron measurements in high gamma radiation fields are being investigated. The programme consists of:

1) Designing a neutron detector based on the tracks from recoil protons, (n, α) reactions or fission fragments.

2) Calculating the response of detectors to neutrons in the energy range 0–17 MeV.

3) Verification of the calculated response by measurements using mono-energetic neutrons.

4) Measuring the effect of a high gamma dose on the detector performance.

5) The application of automatic track counting techniques.

A measurement of recoil protons from neutrons in the energy range 0.1–17 MeV has been carried out for cellulose nitrate. The measurements were made using the IBIS accelerator and the Harwell Long Counter as an absolute measurement of neutron flux. The results shown in fig. 4 have been interpreted in terms of a simple model based on the (n, p) scattering cross section and a detection efficiency for protons which increases with energy. The agreement between experiment and theory is not yet satisfactory and has led to the realisation of a number of fundamental differences between neutron and charged particle detection in track recorders. These differences are:

1) Neutron induced tracks originate uniformly from within the body of the material.

2) Neutron induced tracks are not readily observed on the incident face because recoil protons are directed into the bulk of the material.

3) In contrast with charged particle tracks a chemical etch of the back surface of the material will reveal tracks which are caused by charged particles leaving the material. The characteristics of such tracks differ because the energy loss of the emergent particle in the material decreases as the etch penetrates into the material. The emerging recoil protons from the back surface will have a range of different energies and directions, even for mono-energetic neutrons.

Experiments on fission fragment tracks in Makrofol from (n, *f*) reaction in ^{238}U have to be carried out and the effect of gamma rays on track recognition has been measured for doses up to 24 MRad. Automatic track counting techniques, developed at Imperial College, are being applied to neutron induced track measurements and should help to overcome the subjective nature of human decisions on the number of tracks seen in an etched foil.

1. Materials

The substances subjected to examination as material for plastic detectors were cellulose nitrate (CA80-15, LR 115 and CA80-15 type B), cellulose triacetate, Makrofol and Cronar. After initial experiments cellulose nitrate (CA80-15) and polycarbonate (Makrofol) films were selected for detailed examination.

2. Irradiations

In preliminary experiments to select the suitable materials and to optimise the etching conditions a ^{252}Cf neutron source was used. In order to analyse the correlation between the neutron fluence and the number of tracks, it is desirable to use monochromatic neutrons with known energy, for which the elastic and inelastic scattering cross sections of the atoms consisting of the plastics are known.

It was decided to produce monoenergetic neutrons using the IBIS machine at A.E.R.E. Harwell. Neutrons from 0.2 MeV to 17 MeV were produced using D–D, D–T, P–T and P–Li reactions. The fluence of these neutrons was measured with a BF_3 long counter calibrated on a ^{252}Cf neutron source. Neutrons were incident normally on the surface of the films and 10 films were irradiated at one time.

The irradiated sides on all films were marked so as to compare the number of tracks on front and back surfaces. It was decided to have neutron fluence of about 10^9 n/cm^2, so as to have convenient track density for counting purposes.

* A.E.R.E. Harwell

3. Chemical etching

After irradiation with neutrons, the films were etched in potassium or sodium hydroxide aqueous solutions at 19°C or 60°C for different times.

As control, the same plastic sample but unirradiated was treated with the same etching agents under the same etching conditions, and some background tracks were detected. Therefore, in order to estimate the real number of tracks caused by the fast neutron irradiation, it was necessary to subtract the number of background tracks from the total number of tracks per unit area detected in the irradiated plastics.

4. Track observation and counting

The microscope used for most of the present work was a Reichert (Model MEF2) with oil immersed (140X or 150X) or dry (15X, 50X or 70X) objectives together with X8 or X12.5 oculars. The microscope stage and fine focus controls are equipped with dials so that the stage area can be scanned with precision. One eye-piece is equipped with a squared grid. The length of a side of the square was calibrated with a stage micrometer.

The microscope stage position is defined so that the same frame will not be counted more than once. At every frame position tracks in the field of view bounded by the square are counted from the top line of the square to the bottom. If the tracks cross left or top line they are not counted, whether they begin or end within the square. If they cross the right or bottom line they are counted, so that a proper statistical estimate of the track density can be obtained without deciding which is the beginning or end of the track. When the counting in one field is completed, the stage is moved so that a track or spot crossing the boundary is moved to the opposite boundary and the counting process is repeated. When counting all the tracks on the recorder, care is taken to move from one scanning path to another by displacing the scanning path one field of view after a given path is completed.

5. Results

5.1. Prolonged etching effects

The quantitive relation between the etching time and the number of tracks is shown in figs. 1 and 2. It

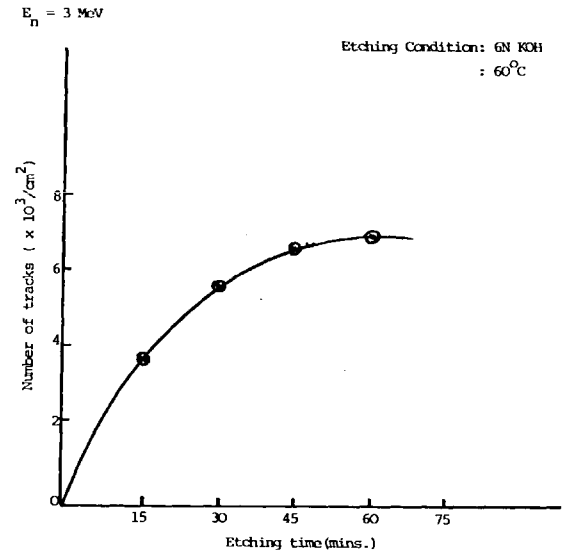


Fig. 1. Track density as a function of etching time.

was observed that the tracks grow in size and number with etching time and still remain detectable during the early period of etching. But beyond certain limits in etching times which depended on the etching condition, the background surface became so roughened as to make it difficult to avoid counting loss, which accounts for the bowing of the curves towards the

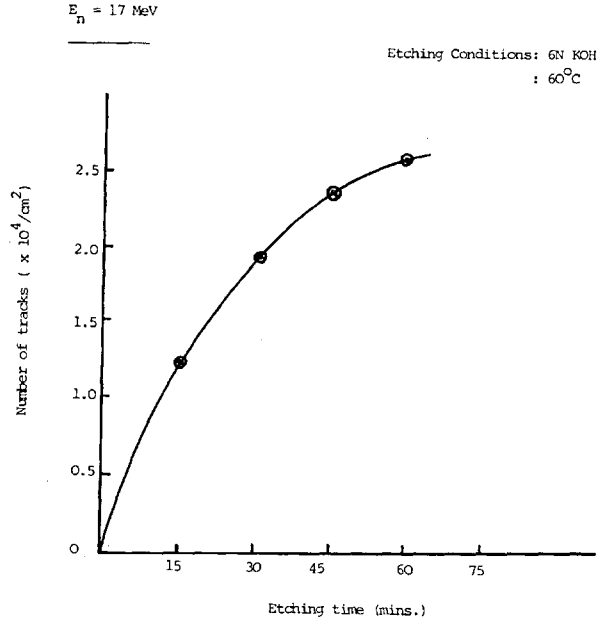


Fig. 2. Track density as a function of etching time.

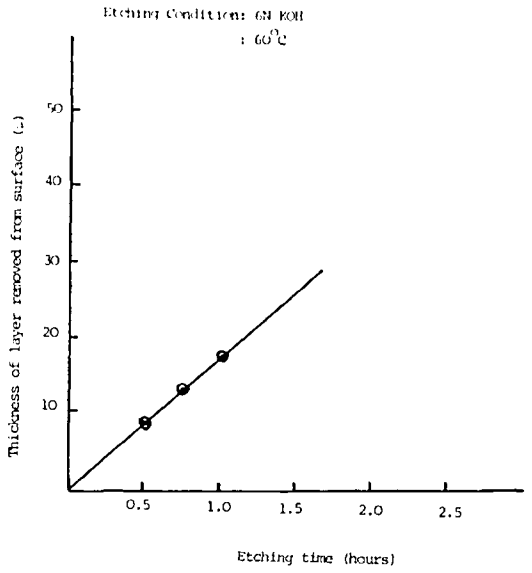


Fig. 3. Bulk etching rate.

end. The roughening of the background surface started quite early when aqueous solution of 25% KOH was used at 60°C.

Longer etches reveal more tracks for three major reasons [1]:

1) Very small features which were not originally perceptible are enlarged.

2) New tracks that began and ended beneath the original surface are encountered as material is removed.

3) The etching along a track having a low dip angle and damage that increases downwards reveals track partway along their lengths.

The use of fixed etching conditions and time (t) is essential, so that the thickness $V_B t$ of removed material is standardized. Otherwise, the total number of tracks will increase monotonically.

The thickness of the plastic surface removed by etching was also measured. The results are plotted against etching time in fig. 3. The figure reveals a linear relation between dissolved thickness and etching time.

5.2. The efficiency curve

The efficiency curve ($E_n V_s \eta$) for CA80-15 at a particular etching condition (6N KOH at 60°C for 45 min) is shown in fig. 4. It can be seen that the sensitivity of CA80-15 increases steeply with neutron energy till ~3 MeV after this increase is not too sharp. This can be explained as follows.

As the detector is thicker than the ranges of the maximum energy recoil protons (head-on collisions) till ~3 MeV; therefore the efficiency of the detector increases steeply with neturon energy until the elastic scattering cross section begins to drop significantly [2]. However, a thin detector has a somewhat different energy response. When the range of the maximum energy recoil protons equals the detector thickness the response begins to round off. Detectors of this

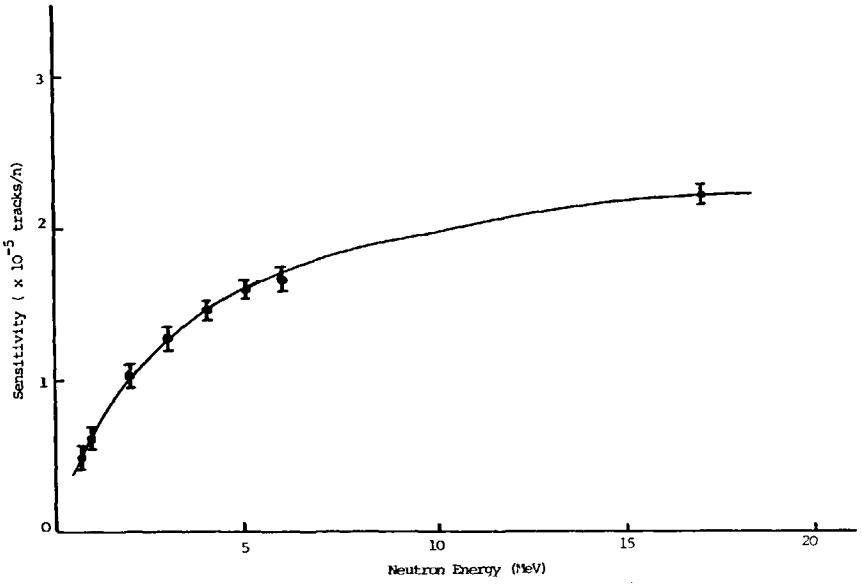


Fig. 4. Sensitivity as a function of neutron energy.

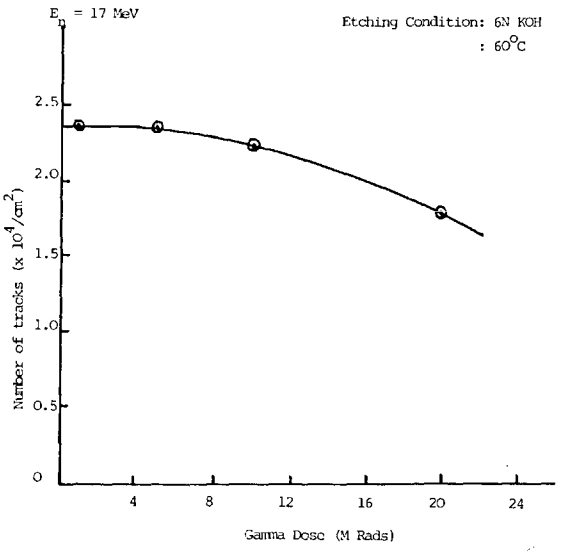


Fig. 5. Track density as a function of gamma dose.

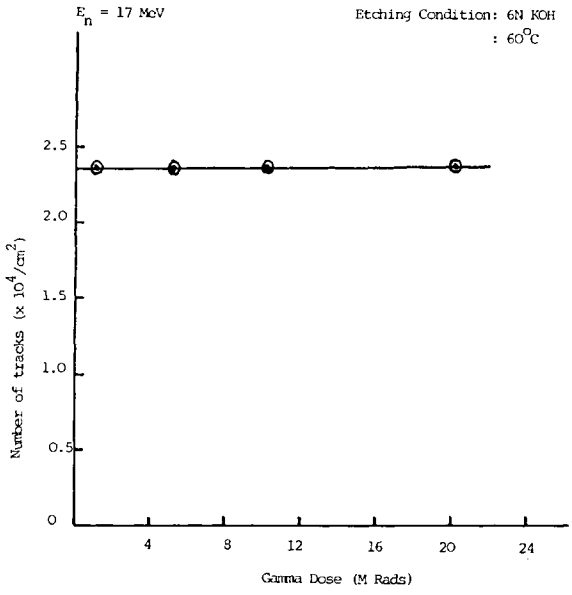


Fig. 6. Track density as a function of gamma dose for different etching times.

type are useful in that they sample lower neutron energies better, in comparison to higher energies, than do the thick detector types.

The fact that only a fraction of tracks are detected under the microscope means that the reproducibility of measurement of track densities is quite dependent on nuclear track detector sensitivity and on etching variables, time, temperature and solution strength.

It is difficult to estimate the number of visible tracks due to each type of neutron interaction separately, since many recoils will give rise to tracks similar to α-particles [3].

6. The effects of high gamma doses

The effects of high gamma doses on the reproducibility, efficiency etc., must be investigated before using them for selective detection of fast neutrons in mixed radiation fields.

Some of the neutron irradiated films were exposed to different gamma doses (1–24 MRad) from a ^{60}Co source.

Fig. 5 shows tracks/cm^2 as a function of gamma dose D for these films. The track density starts decreasing at about 6 MRad, this is due to an increase in the bulk etching rate V_B.

Fig. 6 shows tracks/cm^2 as a function of gamma dose D. These films were etched for different times at different gamma doses. The etching time was decreased for high gamma doses because of an increase in V_B.

The results suggest that cellulose nitrate can be used successfully for selective detection of fast neutrons in high gamma backgrounds but one has to select the proper etching conditions.

References

[1] R.L. Fleischer, P.B. Price and R.M. Walker, Nuclear tracks in solids (University of California Press, Berkeley, 1975).
[2] BNL 325, vol. 2 (1976).
[3] A.L. Frank and E.V. Benton, Proc. 7th Int. Colleq. on Corpuscular photography and visual solid detectors, Barcelona (1970) p. 441.